Detectores de Avalancha de Baja Ganancia Resistentes a la Radiación para la Medición de Tiempo con Alta Precisión para la Actualización de Alta Luminosidad del Experimento CMS

"Radiation-Hard Low-Gain Avalanche Detectors for High-Precision Timing for the High-Luminosity Upgrade of the CMS Experiment"

Efrén Navarrete Ramos

Director: Dr. Iván Vila Álvarez

Tutor: Dr. Gervasio Gómez Gramuglio

Doctorado en Ciencia y Tecnología
Universidad de Cantabria

Tesis doctoral para obtener el título de:
Doctor en Física

Instituto de Física de Cantabria
(CSIC-UC)

Febrero 2025

A mis padres Efrén y Andrea, mis hermanas Dulce y Dixie, a mi amada esposa Sulma, mi amada hija Eleonor y a mis familiares cruzando el oceano y la frontera de la vida.

Declaration

I hereby declare that except where specific reference is made to the work of others, the contents of this dissertation are original and have not been submitted in whole or in part for consideration for any other degree or qualification in this, or any other university. This dissertation is my own work and contains nothing which is the outcome of work done in collaboration with others, except as specified in the text and Acknowledgements.

Efrén Navarrete Ramos
Febrero 2025

Acknowledgements

En primer lugar a la familia, gracias por todo, en el amplio sentido de la palabra. Gracias a mis papás que me educaron con (mucha) paciencia y mucho amor, acompañado siempre de mis hermanas, compañeras durante todo el crecimiento; a mi amadísima hija Eleonor, que ha crecido muchísimo en todo este tiempo, pasando de bebé tierna a niña incansable, y a Sulma por todo lo compartido y por ser quien hizo posible esta etapa, logrando mucho, iniciando desde cero.

Ha sido retador el realizar una actividad lejos del país de origen, con todo lo que conlleva instalarse como familia, durante una pandemia, dentro de un contexto que no es el que dominas ni conoces, donde a pesar de tener prácticamente el mismo idioma, todo es diferente, la comida, las costumbres, las actividades cotidianas, el modo y estilo de vida, incluso el sentido del humor es diferente, así como la forma de socializar que de por sí no se me da bien ni en México. Ni hablar de lo que dejas atrás al emigrar, a 8950 km de distancia, sabiendo que cuando regreses, aunque suene ser poco éstos 4 años, las cosas habrán cambiado, sabes que han cambiado bastante y las cosas avanzaron sin ti. Por esto es que en esta parte agradezco infinitamente, nuevamente, a la familia, la que está en México (mis padres, hermanas, abuelos, tíos, primos, sobrinos, suegros, cuñados) y la que me acompañó todo este tiempo cruzando el atlántico: Sulma y Eleonor, por quienes esta aventura ha sido posible y motivo desde el inicio.

Gracias a todo el grupo de física de partículas e instrumentación del IFCA, por incluirme en su día a día, capacitarme, tenerme paciencia y en "traducirme" bastantes frases que ni idea tenía de su significado, muchas relacionadas con comida. A Iván, Marcos, Gervasio, Richard, Javier, Cristian, Agustín, Clara, Celia, Pablo, Pablo, Jordi, Pedro, David, David, Andrés, Rubén, Sergio, Brochero, Celso, Rocío, Alicia, Nuria, Alberto, Arteche, Silvia y todos con quienes aprendí, conviví, viajé y/o nos tomamos un café con una charla interesante. Jamás se debe olvidar el café de las 11:00, es una responsabilidad con la que hay que cumplir, a menos que colisione con alguna reunión, como la famosa reunión SIFCA de los martes, donde el éxito se planifica y los logros se comparten.

Destaco ahora a mis directores y asesores, que me han dado la oportunidad y confianza inicial sin saber a lo que se atenían al incluir a este mexicano en sus filas. Fuera de bromas,

gracias a Iván y Gervasio que me han apoyado desde el día -1 para realizar este doctorado, tanto a nivel académico, profesional y a veces hasta burocrático. A Marcos y su gran paciencia en transmitirme lo necesario en cuanto a análisis (haciendolo sangrar "e-tinta" varias veces), a Richard y Javi por enseñarme el fucnionamiento, montaje y pormenores de los setups del IFCA, aunque no pude evitar "romper" cosas, gajes del trabajo. Gracias también a los colegas del CNM, Salva y Jairo, por todo lo compartido, mayormente vía e-mail, siendo a quienes recurres cuando hay dudas.

Pasamos ahora a los testbeams, donde agradezco a los colegas con quienes se trabajó día, noche, madrugada o según se requiriera, para al terminar el turno, buscar un lugar abierto para cenar, comer o desayunar: Matías, Neil, Luca, Andrés, Leonardo, Murtaza, Datao, Grigory, Parisa, Rubén, Jongho, Cristóvão, Gregor, Roberta, Vagelis, Michael, Marcel, Ralf y muchos más que coincidimos en los testbeams en CERN y DESY, gracias. Ha sido una experiencia muy gratificante y de mucho aprendizaje, y en donde, citando: "si todo parece ir bien en el primer intento, es porque algo está saliendo mal" [**?**][1].

This work have been developed in the framework of "Ayudas para contratos predoctorales para la formación de doctores 2019", co-funded by the European Social Fund program "El FSE invierte en tu futuro" with grant reference: PRE2019-087514; and the *Plan Complementario en el Área de Astrofísica y Física de Altas Energías*, financed by Next Generation EU funds, including the Recovery and Resilience Mechanism (MRR), the Recovery, Transformation and Resilience Plan (PRTR) and the Autonomous Community of Cantabria.

This work was also developed in the framework of the CERN RD50/DRD3 collaboration and has been funded by the Spanish Ministry of Science and Innovation (with the reference MCIN/AEI/10.13039/501100011033/) and by the European Union's ERDF program "A way of making Europe". Grant references: PID2020-113705RB-C31, PID2020-113705RB-C32 and PID2021-124660OB-C22. Also, it was supported by the following European funding programs: the European Union's Horizon 2020 Research and Innovation (under Grant Agreement No. 101004761, AIDAInnova) and NextGenerationEU (PRTR-C17.I1).

Gracias.

[1] Ok, no recuerdo dónde lo escuché, pero sigue siendo válido.

Resumen

La actualización de Alta Luminosidad del Gran Colisionador de Hadrones (HL-LHC) será el experimento insignia de la física de partículas en la próxima década. Con el incremento en la luminosidad surgen nuevos desafíos técnicos, especialmente en la reconstrucción de los vértices primarios de las colisiones. Esto se debe a la ocurrencia de múltiples colisiones entre protones en un mismo cruce de haces, un fenómeno conocido como apilamiento (*pile-up*), que genera una gran densidad de interacciones superpuestas y complica la asignación precisa de las partículas al vértice primario del que proceden. Una asignación incorrecta de los vértices afecta la calidad de los datos reconstruidos, lo que se traduce en una importante reducción de la luminosidad efectiva del experimento.

Para afrontar este desafío, dentro del experimento *Compact Muon Solenoid* (CMS), en el cual se enmarca esta tesis, se ha propuesto la implementación de un nuevo concepto de detector, el *MIP Timing Detector* (MTD). Este detector permitirá medir los tiempos de producción de partículas cargadas mínimamente ionizantes (*Minimum Ionizing Particles*, MIP) con una alta resolución temporal, proporcionando una nueva dimensión en la identificación y separación de las colisiones superpuestas.

Más concretamente, esta tesis se centra en el desarrollo de la tecnología sensora para la región de cierre del MTD, conocida como *Endcap Timing Layer* (ETL). La tecnología de sensores seleccionada para estas capas de temporización son los *Low-Gain Avalanche Detectors* (LGADs), los cuales ofrecen una respuesta de señal ultrarrápida, una ganancia interna moderada y una excelente resolución temporal, características que los hacen ideales para el seguimiento de alta precisión en la era del HL-LHC.

En esta tesis doctoral, se presentan estudios de tolerancia a la radiación de sensores de silicio de avalancha de baja ganacia LGAD (Low Gain Avalanche Detectors), los cuáles serán empleados en el "Compact Muon Selenoid" (CMS) para la actualización de alta luminosidad del Gran Colisionador de Hadrones LHC (Large Hadron Collider). Para ello se han realizado diferentes campañas de caracterización sobre LGADs con distintas tecnologías: Fabricados en obleas con sustratos de tipo "Silicon on Silicon" (SiSi) y en sustratos crecidos "epitaxialmente" (Epi), además algunos sensores de éstas producciones fueron fabricados

con co-implantación de Carbono en la capa de multiplicación, con el objetivo de mejorar su tolerancia a la radiación, comparado con sensores estándard después de ser irradiados.

Como resultado, se concluye que entre los sensores LGAD fabricados en el Centro Nacional de Microelectrónica (CNM), los sensores SiSi con coimplantación de carbono (dosis de 9×10^{14} at/cm^2), tras ser irradiados con una fluencia de 15×10^{14} n_{eq} cm^{-2} cumplen los requisitos de resolución temporal del experimento CMS de menos de 50 ps al voltaje de operación, definido como el voltaje necesario para alcanzar una carga colectada de 8 fC, y por debajo del límite de 12 V/μm para el voltaje de polarización de estos dispositivos.

El Capítulo 1 proporciona una visión general del experimento CMS del LHC y el contexto de la actualización de alta luminosidad (HL-LHC). El Capítulo 2 sienta las bases de los detectores semiconductores. En el Capítulo 3 se revisa el estado-del-arte y las tendencias de I+D de los detectores semiconductores en la física de altas energías. En el Capítulo 4 se describen los métodos experimentales utilizados en las diversas campañas de caracterización, test-beams y las instalaciones de irradiación. En el Capítulo 5 se explican los daños específicos de los LGAD por radiación. Los resultados de la caracterización de LGADs para el CMS ETL se presentan en el Capítulo 6, y finalmente, el Capítulo 7 contiene un resumen y las conclusiones de esta tesis.

Posteriores investigaciones se pueden plantear en la optimización de la dosis de implantación y profundidad de la capa de ganancia, combinando el enriquecimiento con Carbono en sensores fabricados con tecnología epitaxial, así como la implentación de nuevas tecnologías en el diseño de sensores como el LGAD inverso con trinchera (Trenched iLGAD).

Abstract

The High-Luminosity upgrade of the Large Hadron Collider (HL-LHC) will be the flagship experiment in particle physics in the next decade. With the increase in luminosity, new technical challenges arise, particularly in the reconstruction of primary collision vertices. This is due to the occurrence of multiple proton-proton collisions within a single beam crossing, a phenomenon known as pile-up (*pile-up*), which generates a high density of overlapping interactions and complicates the precise assignment of particles to their corresponding primary vertex. An incorrect vertex assignment affects the quality of reconstructed data, leading to a significant reduction in the experiment's effective luminosity.

To address this challenge, within the *Compact Muon Solenoid* (CMS) experiment, which frames this thesis, the implementation of a new detector concept, the *MIP Timing Detector* (MTD), has been proposed. This detector will enable the measurement of the production times of minimally ionizing charged particles (*Minimum Ionizing Particles*, MIP) with high temporal resolution, providing an additional dimension for the identification and separation of overlapping collisions.

More specifically, this thesis focuses on the development of sensor technology for the forward and backward regions of the MTD, known as the *Endcap Timing Layer* (ETL). The selected sensor technology for these timing layers consists of *Low-Gain Avalanche Detectors* (LGADs), which offer an ultra-fast signal response, moderate internal gain, and excellent time resolution, making them ideal for high-precision tracking in the HL-LHC era.

In this PhD thesis, radiation tolerance studies have been carried out for LGADs, which will be used in the detector of the Compact Muon Selenoid Experiment (CMS) for the High-Luminosity (HL) upgrade of the Large Hadron Collider (LHC). For this purpose, different characterization campaigns have been carried out on LGADs produced with different technologies: Sensors fabricated on wafers with substrates called 'Silicon on Silicon' (SiSi) and on 'epitaxially' grown substrates (Epi), also some sensors from these productions were fabricated with the feature of Carbon enrichment, co-implanted in the multiplication layer, with the aim of improving the radiation tolerance of these devices, which is proved in this study by obtaining less degradation of the multiplication layer compared to standard sensors (without carbon) after being irradiated.

As a result, it is concluded that among the LGAD sensors manufactured at the National Center for Microelectronics (CNM), the SiSi sensors with carbon co-implantation (dose of $9 \times 10^{14}\,\mathrm{at/cm^2}$), after being irradiated with a fluence of $15 \times 10^{14}\,\mathrm{n_{eq}\,cm^{-2}}$, meet the time resolution requirements of the CMS experiment of less than 50 ps at the operating voltage, defined as the voltage required to achieve a collected charge of 8 fC, and below the limit of $12\,\mathrm{V/\mu m}$ for the bias voltage of these devices.

Chapter 1 provides an overview of the LHC CMS experiment and the context of the HL-LHC high-luminosity upgrade. Chapter 2 lays the groundwork for semiconductor detectors. The state-of-the-art and the R&D trends of the semiconductor tracking and vertex detectors are reviewed in Chapter 3. The experimental methods used in the various characterization campaigns, test-beams, and irradiation facilities are described in Chapter 4. The specific radiation damage to LGADs is explained in Chapter 5. The results of the characterization of LGADs for the CMS ETL are presented in Chapter 6, and finally, Chapter 7 contains a summary and the conclusions of this thesis.

Further research can be considered in the optimization of implantation dose and gain layer depth, the combination of carbon enrichment in epitaxially fabricated sensors, and the implementation of new technologies in the design of sensors such as the trenched iLGAD.

Related Publications

- E. Navarrete Ramos, J. Duarte-Campderros, M. Fernández, G. Gómez, J. González, S. Hidalgo, R. Jaramillo, P. Martínez Ruiz del Árbol, M. Moll, C. Quintana, A.K. Sikdar, I. Vila, J. Villegas, **Impact of neutron irradiation on LGADs with a carbon-enriched shallow multiplication layer: Degradation of timing performance and gain**, Nuclear Instruments and Methods in Physics Research Section A: Accelerators, Spectrometers, Detectors and Associated Equipment, Volume 1074, 2025, 170309, ISSN 0168-9002, https://doi.org/10.1016/j.nima.2025.170309

- E. Currás, A. Doblas, M. Fernández, D. Flores, J. González, S. Hidalgo, R. Jaramillo, M. Moll, E. Navarrete, G. Pellegrini, I. Vila, **Timing performance and gain degradation after irradiation with protons and neutrons of Low Gain Avalanche Diodes based on a shallow and broad multiplication layer in a float-zone** $35\mu m$ **and** $50\mu m$ **thick silicon substrate**, Nuclear Instruments and Methods in Physics Research Section A: Accelerators, Spectrometers, Detectors and Associated Equipment, Volume 1055, 2023, 168522, ISSN 0168-9002, https://doi.org/10.1016/j.nima.2023.168522

- E. Navarrete Ramos, J. Duarte-Campderros, M. Fernández, G. Gómez, J. González, S. Hidalgo, R. Jaramillo, P. Martínez Ruiz del Árbol, M. Moll, C. Quintana, I. Vila, J. Villegas, **Effects of Neutron Irradiation on LGADs with Broad Multiplication Layer and varied Carbon-Enriched Doses: A Study on Timing Performance and Gain Deterioration**. Under internal preparation.

- As a member of the "CMS Collaboration," contributed to 100+ papers (see ORCID profile).

Presentations

- Velkovska, Iskra. **Performance of Irradiated Ti-lgads at 160 Gev SPS Pion Beams**. Zenodo, February 4, 2025. https://doi.org/10.5281/zenodo.14926265

- Navarrete Ramos, Efren. **"Radiation Tolerance Study of CNM-IMB Run15973"**. Presented at the Last (43rd) RD50 Workshop on Radiation Hard Semiconductor Devices for Very High Luminosity Colliders (CERN) (RD50), Geneve, Switzerland, December 1, 2023. https://doi.org/10.5281/zenodo.14849900

- Liu, Tiehui, and Datao Gong. **ETROC2: The First Full Size, Full Functionality Precision Timing ASIC Prototype For lgad-based CMS Endcap Timing Layer (ETL) Upgrade.** Zenodo, October 3, 2023. https://doi.org/10.5281/zenodo.14850027

- Navarrete Ramos, Efren. **"Radiation Tolerance Study of Lgads for the CMS Encap Timing Layer Detector"**. Presented at the 18th "Trento" Workshop on Advanced Silicon Radiation Detectors (TREDI), Trento, Italy, February 28, 2023. https://doi.org/10.5281/zenodo.14849855

- Navarrete Ramos, Efren. **"Radiation Tolerance Study of CNM-IMB Run #15246"**. Presented at the 41st RD50 Workshop on Radiation Hard Semiconductor Devices for Very High Luminosity Colliders (RD50), Sevilla, Spain, December 1, 2022. https://doi.org/10.5281/zenodo.14849752

- Quintana San Emeterio, Cristian. **"Update on the Characterization of Neutron Irradiated IMB-CNM Sic Planar Diodes"**. Presented at the 41st RD50 Workshop on Radiation Hard Semiconductor Devices for Very High Luminosity Colliders (RD50), Sevilla, Spain, November 30, 2022. https://doi.org/10.5281/zenodo.14850357

- Villegas, Jairo. **Measurements on last IMB LGADs production**. Presented at the 40th RD50 Workshop on Radiation hard semiconductor devices for very high luminosity colliders (RD50), Geneve, Switzerland, June 23, 2022. http://hdl.handle.net/10261/280065

- Vila, Ivan. **"Radiation Tolerance Study of Aida2020v2 Lgads Manufactured at IMB-CNM"**. Presented at the The 38th RD50 Workshop, June 22, 2021. https://doi.org/10.5281/zenodo.14850256

Table of contents

Chapter 1

Introduction

1.1 HL-LHC upgrade and CMS experiment

The Large Hadron Collider (LHC) [1] has been in successful operation since late 2010 at the European Organization for Nuclear Research (CERN) in Geneva. The LHC is a circular collider that accelerates protons or lead ions. This apparatus propels bunches of hadrons or ions until they approach the speed of light, causing them to collide at four distinct points along their path. Each of these points hosts an experiment: ALICE, which investigates ion collisions in an attempt to comprehend the Universe's initial moments; LHCb [2], which studies b-particle physics and seeks to understand the asymmetry between matter and antimatter; and finally, CMS and ATLAS, which are general-purpose experiments.

The High-Luminosity (HL) upgrade of the LHC (HL-LHC) is scheduled to begin in 2030 and will deliver an integrated luminosity of up to $4000\,\mathrm{fb}^{-1}$ that is about ten times more than the current luminosity, and is planned to work over a 10-year period [1]. The HL-LHC upgrade will start with the called Long Shutdown 3 (2026–2029), which is a three-year period where the LHC accelerator will undergo improvements in order to reach the high-luminosity configuration. The HL-LHC will operate at a stable luminosity of $5.0 \times 10^{34}\,\mathrm{cm}^{-2}\,\mathrm{s}^{-1}$, with a possible maximum of $7.5 \times 10^{34}\,\mathrm{cm}^{-2}\,\mathrm{s}^{-1}$, with an average of $1.6\,\mathrm{collisions/mm}$ and up to 200 proton-proton (pp) interactions per bunch crossing (pile-up). In these conditions, disentangling the multiple collisions and correctly associating the reconstructed tracks to their primary production vertex will be a main challenge.

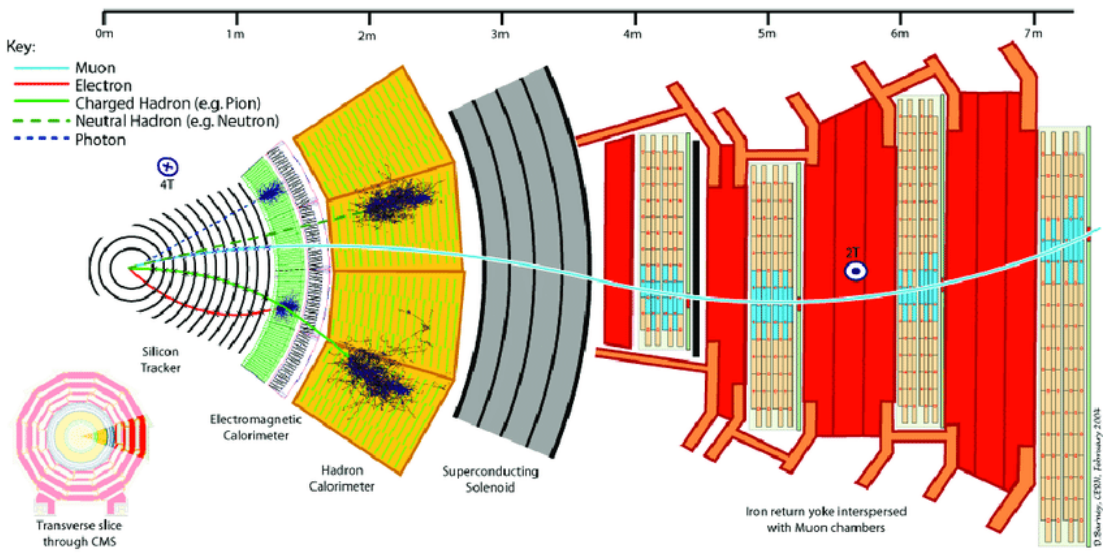

Fig. 1.1 CMS experiment in an transversal schematic slice where can be seen: The silicon tracker, electromagnetic and hadron calorimeters, the superconducting solenoid and the muon chambers, from left to right respectively. Taken from [3].

1.2 CMS High-Luminosity upgrade

The Compact Muon Solenoid (CMS) experiment [3], the central subject of this thesis, is structured with multiple layers that constitute the sub-detectors: The outermost layer is a muon spectrometer, succeeded by hadronic and electromagnetic calorimeters, and at the core lies the tracker, composed of several layers of silicon detectors. Figure 1.1 shows the different layers of the CMS experiment in an schematic view. The interaction of radiation with these various detector layers facilitates particle identification. For example, muons are highly penetrating particles and pass through all layers of the detector, including the tracker, the electromagnetic calorimeter, the hadronic calorimeter, and are finally detected in the muon detector; a photon interacts only with the electromagnetic calorimeter, and the trajectory of a hadronic particle ends at the hadronic calorimeter.

The aim of the High-Luminosity upgrade is to enable the CMS experiment to meet the conditions of the HL-LHC while maintaining its excellent performance in terms of signal resolution, selection efficiency and background discrimination. Therefore, the detectors need to be upgraded to cope with the high pile-up and large radiation conditions.

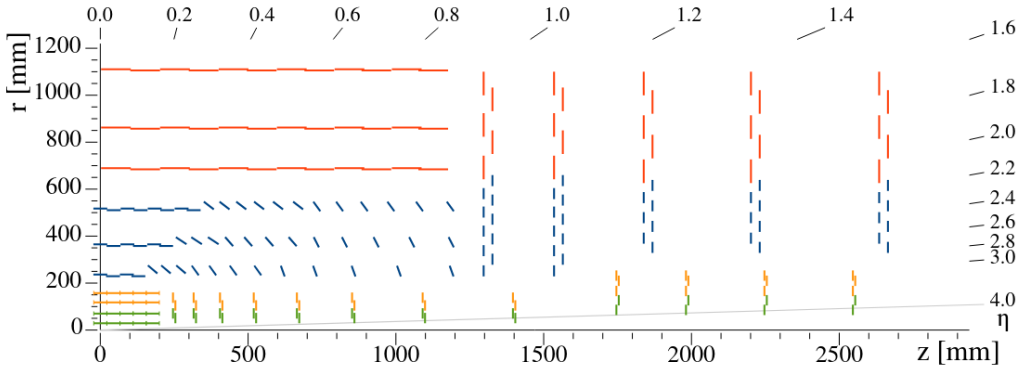

Fig. 1.2 Sketch of one quarter of the tracker layout. In the Inner Tracker the green lines correspond to pixel modules made of two readout chips and the yellow lines to pixel modules with four readout chips. The blue and red lines represent the two types of modules from the Outer Tracker. Taken from [4].

1.2.1 Tracker System upgrade

The entire silicon tracking system, consisting of pixel and strip detectors, will be completely replaced due to the significant damage and performance degradation they would suffer with the HL-LHC upgrade, and to cope with the more demanding operating conditions. The Tracker System upgrade [4], will consist of the Inner Tracker and Outer Tracker systems having increased forward acceptance, increased radiation hardness, increased granularity and compatibility with higher data rates and longer trigger latency, and is also intended to contribute to the L1T by using the Outer Tracker p_T modules. Its geometry will have a barrel and two end caps distributed as follows:

- The Inner Tracker: Consisting of pixels of $25 \times 100 \mu m^2$, organized in 4 barrel layers and 8 small discs + 4 large discs per each side.
- The Outer Tracker: Consisting of 174 million macropixels and 44 million strips, organized in 6 barrel layers and 5 discs per each side.

1.2.1.1 The Inner Tracker

The Inner Tracker is expected to exhibit the required radiation tolerance and deliver the desired performance in terms of detector resolution, occupancy, and tracking performance. Will consist of sensors and readout electronics, as well as a large data volume to be stored and sent out at high trigger rates. The inner Tracker will consist in thin silicon sensors with a thickness in the 100–150 µm range, segmented into pixel sizes of 25 μm^2. The design of the

Inner Tracker will allow to replace degraded parts over an extended year-end technical stop. Figure 1.2 is the sketch of

The detector consists of a four-layer barrel section called the Tracker Barrel Pixel Detector (TBPX), eight small double discs per side called the Tracker Forward Pixel Detector (TFPX) and four large double discs per side called the Tracker Endcap Pixel Detector (TEPX).

The pixel modules consist of a pixel sensor, pixel read-out chips (PROC), a flex circuit and a mechanical support, and form the basic unit of the inner tracker. The sensors are bump bonded to the readout chips. A thin, high-density interconnect (HDI) flex circuit is bonded to the sensor and wire-bonded to the PROCs. It carries the data, provides the clock, trigger and control signals and power distribution to the PROCs, and houses all other passive and active components.

One of the pixel sensor technologies selected for the Inner Tracker is the 3D sensor subsection 3.1.3. This is the base technology for the innermost region of the Inner Tracker, where radiation hardness is particularly important. The electrodes penetrate the bulk to form 3D columns and the distance between the electrodes is independent of the sensor thickness, allowing thicker sensors to generate a larger signal, low depletion voltages and efficient charge collection. The low charge carriers trapping gives an advantage over planar sensors by achieving higher radiation hardness. In addition, the lower operating voltage reduces the risk of edge sparking and lowers power consumption, making them less susceptible to thermal runaway.

1.2.1.2 The Outer Tracker

The Outer Tracker will be composed of p_T modules, that as mentioned before, will implementing the L1 trigger functionality. The p_T module is based on the parallel top and bottom strip sensors, with the strip direction being parallel to the z axis in the barrel and nearly radial in the endcaps, allowing the concept of "stereo strips" to be used to measure the z coordinate in the barrel and the r coordinate endcaps. Two versions of p_T modules have been produced: modules with two strip sensors (2S modules) and modules with one strip and one macro-pixel sensor "pixel-strip" (PS modules). The precision of the z coordinates provided by the PS barrel layers limits the origin of the trigger tracks to a portion of the illuminated region of about 1 mm, which is sufficiently precise to partially discriminate particles coming from different vertices.

The strips in the 2S (PS) modules have a length of about 5 cm (2.4 cm). Figure 1.3 is a sketch of one quarter of the Outer Tracker where blue (red) lines represent PS (2S) modules and also The three sub-detectors, named Tracker Barrel with PS modules (TBPS), Tracker

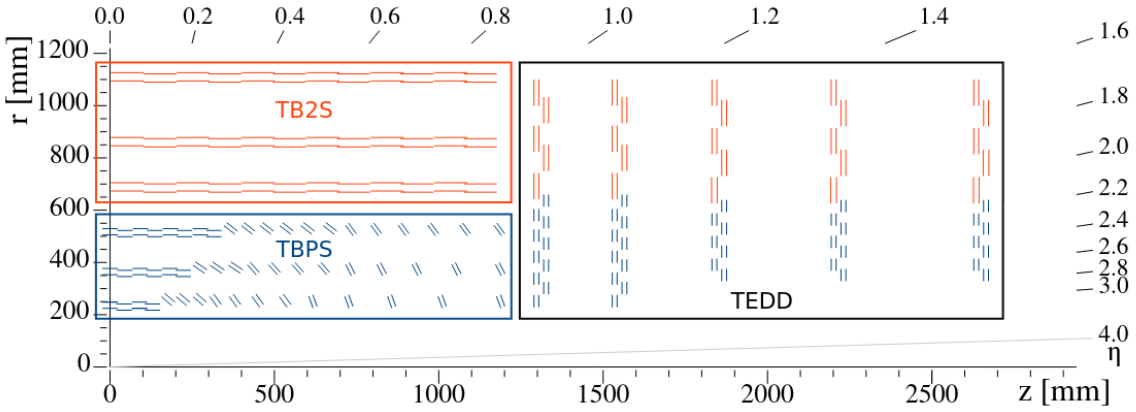

Fig. 1.3 Sketch of one quarter of the Outer Tracker. Blue (red) lines represent PS (2S) modules. The three sub-detectors, named Tracker Barrel with PS modules (TBPS), Tracker Barrel with 2S modules (TB2S), and Tracker Endcaps with double-disks (TEDD), are indicated. Taken from [4].

Barrel with 2S modules (TB2S), and Tracker Endcaps with double-disks (TEDD), can be identified.

1.2.2 High-Granularity Calorimeter

In the context of the CMS High-Luminosity upgrade, a novel calorimeter has been proposed, one which possesses the capability to measure position, energy and time. This calorimeter, designated as the High-Granularity Calorimeter (HGCAL) [5], is expected to fulfill several crucial requirements:

- To be a dense calorimeter, to allow for high compactness of the particle shower's lateral development and fine lateral and longitudinal granularity.
- Have capability of precisely measuring the time of the showers.
- Contribute to the Level-1 Trigger (L1T) selection.

The HGCAL will have a coverage in the $1.5 < \eta < 3.0$ region, will consists in electromagnetic (CE-E) and hadronic (CE-H) sections, segmented into 47 layers, with both sections structured as sampling calorimeters, that uses two types of sensors: hexagonal silicon cells and scintillators cells:

- CE-E: Consisting in 26 layers of silicon sensors and Cu and Pb absorbers.
- CE-H: Consisting in 7 layers of silicon sensors and 14 layers of silicon-scintillator sensors.

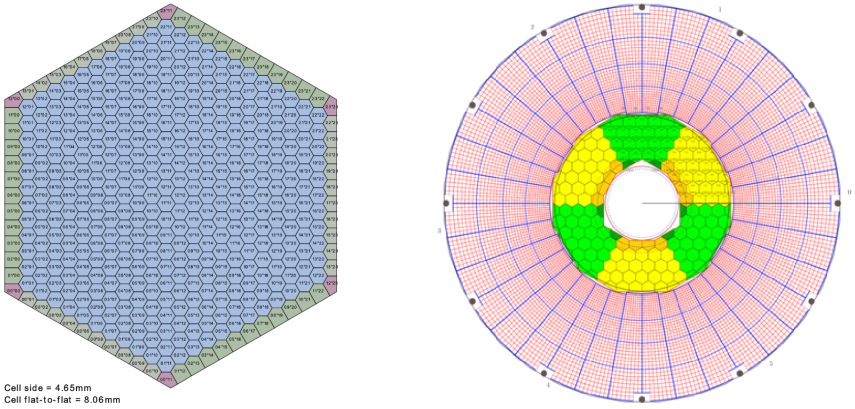

Fig. 1.4 Scheme of the arrangement of silicon sensors into an hexagonal module (left) and layout of layer 40, with hexagonal modules and scintillator cells (right). Taken from [6].

Figure 1.4 (left) is a scheme of the arrangement of silicon sensors into an hexagonal module and (right) is the layout of a layer with hexagonal modules and scintillator cells. The HGCAL ReadOut Chip (HGCROC) will be use for the sensor readout, providing fast signal shaping and about 25 ps timing resolution for an energy deposit equivalent to 50 fC and at the same time being radiation tolerant up to 2 MGy [5].

1.2.3 MIP Timing Detector

With the main motivation of o address the high pileup that will come with the High-Luminosity upgrade, the MIP timing sub-detector have been proposed [7, 8], which will provide a time resolution of 30 ps per track of Minimum Ionizing Particles (MIP). This sub-detector is expected to significantly improve the performance CMS detector by disentangling the high number of pileup events by adding precision timing and for instance increasing the identification efficiency and the time-of-flight measurement of different interactions.

The MTD will be covering the barrel and endcap regions as can be seen in Figure 1.5, distributed as:

- The Barrel Timing Layer (BTL): For lower radiation areas, is a cylindrical detector inside the tracker support tube, covering $|\eta| < 1.45$. Employing Scintillating lutetium-yttrium orthosilicate crystals activated with cerium (LYSO-Ce) and to be read out by silicon photomultipliers (SiPMs).

- The Endcap Timing Layer (ETL), consisting in a pair of disks located in front of the HGCAL thermal screen in the $1.6 < |\eta| < 3.0$ region. Employing the Low Gain

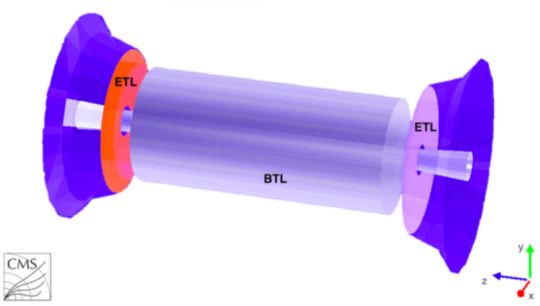

Fig. 1.5 Scheme of the MTD containing the Endcap Timing Layer (ETL) represented in orange disks (identified with the legend ETL.) and the Barrel Timing Layer (BTL) represented with the central blue cylinder. Taken from [9].

Avalanche Detectors (LGADs) silicon sensors, grouped in 16×16 arrays bump-bonded to the dedicated ETROC2 (Endcap Timing ReadOut Chip).

The number of tracks for pileup vertices that are erroneously associated with the hard interaction vertex can be mitigated by using the track timing information along with their corresponding beam line extrapolated z-position. Figure 1.6 contains simulated and reconstructed vertices in a bunch crossing with 200 pileup interactions, with an MTD of 30 ps time resolution scenario. The horizontal axis is the z position along the beam line. The time is in the vertical axis. The red dots are the simulated vertices. The vertical yellow lines indicate only 3D reconstructed vertices. The tracks are the black crosses and the vertices are the blue open circles, both reconstructed using a "4D" method [10].

Figure 1.7 is a simulated quantified reduction of the pile-up. showing the main number of incorrectly associated tracks to the primary vertex, as a function of the line density of collision vertices. In the case of 200 pile-up, the peak density located for a line density of 1.9 collisions per mm, The average number of incorrectly assigned tracks is about 20 without the use of time information. In this case, the time information from the MTD could be useful to restore the CMS performance close to the current.

1.2.3.1 The Endcap Timing Layer

The CMS Endcap Timing layer (ETL) is a sub-detector proposed to be built using Low Gain Avalanche Detectors (LGAD) with a pixel size of $1.3 \times 1.3\,\mathrm{mm}^2$. The ETL will cover the pseudorapidity range of $1.6 < |\eta| < 3.0$, with a total surface area of $14\,\mathrm{m}^2$. This sub-detector will be exposed to radiation levels up to $1.5 \times 10^{15}\,\mathrm{n_{eq}\,cm^{-2}}$ at $|\eta| = 3.0$ denominated as the high-fluence region. However, for 80 % of the ETL area, the fluence is less than

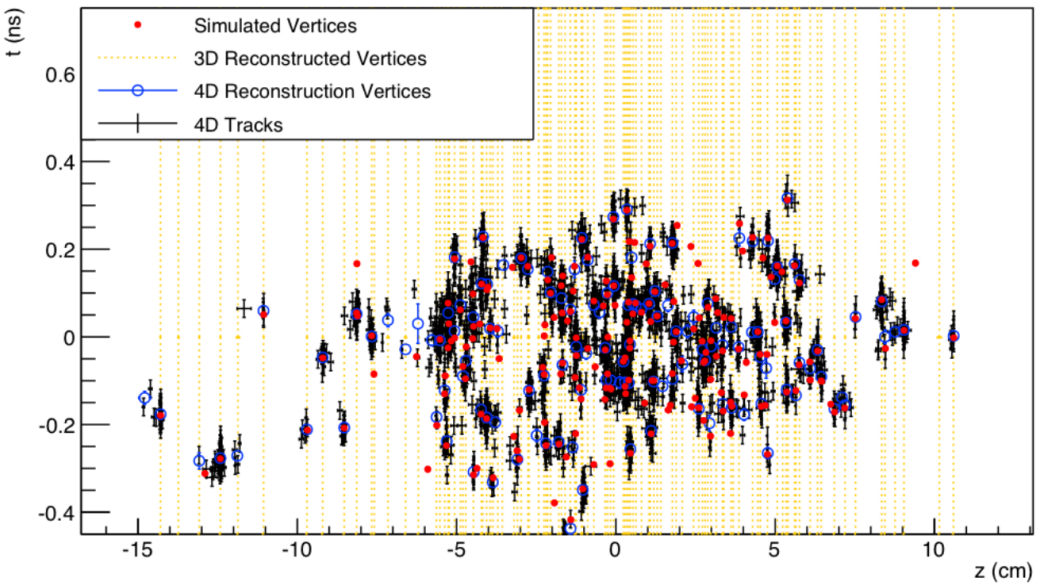

Fig. 1.6 Vertices (simulated and reconstructed)in a bunch crossing with 200 pileup interactions, with an MTD of 30 ps time resolution scenario. The horizontal axis is the z position along the beam line. The time is in the vertical axis. The red dots are the simulated vertices. The vertical yellow lines indicate only 3D-reconstructed vertices. The black crosses and the blue open circles represent tracks and vertices. Taken from [10].

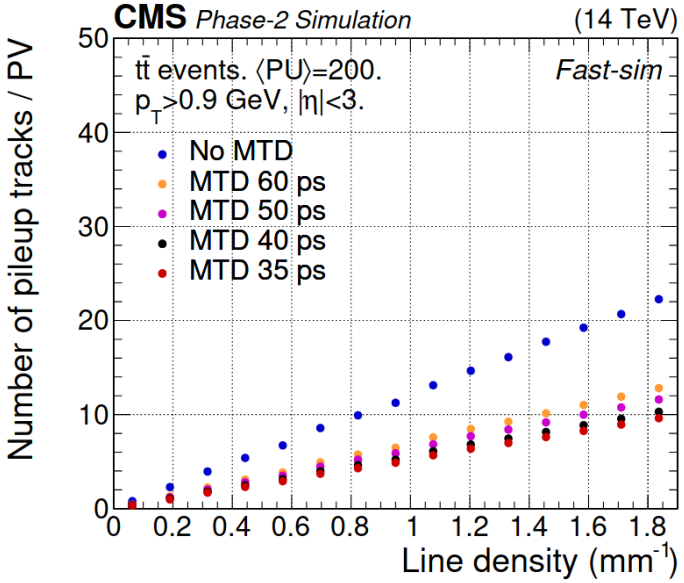

Fig. 1.7 Number of pileup tracks incorrectly associated with the hard interaction vertex as a function of the collision line density for different time resolutions. Taken from [10].

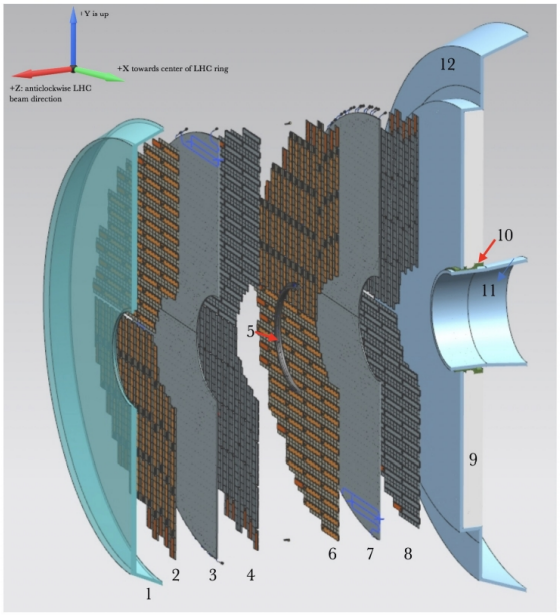

1: ETL Thermal Screen
2: Disk 1, Face 1
3: Disk 1 Support Plate
4: Disk 1, Face 2
5: ETL Mounting Bracket
6: Disk 2, Face 1
7: Disk 2 Support Plate
8: Disk 2, Face 2
9: HGCal Neutron Moderator
10: ETL Support Cone
11: Support cone insulation
12: HGCal Thermal Screen

Fig. 1.8 Scheme of the ETL containing the ETL disks with modules on both faces, along with the support structure. The neutron moderator (9), whose purpose is to shield the Tracker from back-scattered particles from the CE, and thermal screen of the CE (12), follow the ETL. The independent thermal screen of the ETL (1), is on the left. Taken from [10].

1×10^{15} $n_{eq}\,cm^{-2}$, being the low-fluence area. Therefore, these two fluence points are the ones of interest for the radiation tolerance study in this research. The ETL will consist of two separate disks, each composed of different layers like: thermal screens, support plates and cones, mounting brackets and the two faces of the two disks containing the modules with the silicon LGADs. The scheme of the ETL layers can be seen in Figure 1.8.

The LGAD sensors have intrinsic moderate gain of around 10-30 factor, provided by a gain layer, which helps to overcome capacitance and other noise sources and achieve a low-jitter fast-rising pulse edge required for precision timing reconstruction for MIPs. The LGADs will have a 50 µm active region, within a typical 300 µm thick silicon wafer. The readout chip to be used is the ETROC2, that uses timing of the leading edge of the pulse from the LGADs and contains amplifiers and discriminators followed by circuits to measure the Time-of-Arrival (TOA) of each particle and Time-over-Threshold (TOT) to measure the pulse height for time walk correction.

1.2.3.2 The Barrel Timing Layer

The BTL, as mentioned before, will be based on the LYSO:Ce scintillator crystals technology, with a final geometry of $3.75 \times 3.12 \times 54.7 mm^3$, distributed in arrays of 16 bar-like sensor

modules. This technology was selected by its fast response, having a 40 ns decay time, a high density ensuring a energy loss of about 0.86 MeV/mm for a MIP particle. The light signal produced by each crystal is read at each bar end by a SiPM, with a cell size of 25 µm.

The signal produced by the SiPMs is processed by a custom readout ASIC, the TOFHIR (Time-Of-Flight, HIgh Rate), providing high signal gain and noise filtering with a feature to have a Differential Leading Edge Discriminator [9].

1.2.4 The Muon System Upgrade

The muon system is crucial because one of the most sensitive signatures of the production of new particles is often one or more muons, so the CMS was built with several complementary sub-detectors to identify muons and measure their momentum and charge over a wide range of kinematics: The drift tube (DT) and the barrel resistive plate chamber (RPC) are divided into 5 wheels, complemented by the two endcaps which house the cathode strip chambers (CSCs) and the endcap RPCs where the particle rate is particularly high. The DT, CSC and RPC detector subsystems are very important for the identification and measurement of muons with the precision and accuracy required to fulfill the CMS objectives, and it is therefore necessary to ensure that their performance is maintained in High-Luminosity environments:

Drift Tube (DT) chambers: The DT chambers and on-chamber electronics should continue to operate at the HL-LHC. However, the "minicrate" electronics attached to each chamber will need to be replaced to ensure proper functionality for the HL upgrade.

The Cathode Strip Chambers (CSCs): The CSCs cover the CMS endcap regions corresponding to $0.9 < |\eta| < 2.4$, resulting in a larger radiation environment than for the in-barrel muon chambers. Although no significant degradation of key chamber parameters such as gas gain, detection efficiency, spurious signal rates, strip-to-strip resistance or dark currents has been observed [11], and it is expected that the CSCs can be used until the end of the HL-LHC operation, some CSC readout electronics boards will need to be replaced to accommodate the higher triggering requirements of L1 trigger rates and chamber occupancies by using high-speed optical output links and faster processors.

Resistive Plate Chambers (RPC): There are upgrades planned for the RPC system, although the current RPC chambers will be able to operate until the end of the High-Luminosity upgrade. These upgrades are to the link system that connects the front-end board to the trigger processors. This upgrade to the link system will make the RPC system robust to the high radiation environment.

1.2.5 The Data Acquisition and High Level Trigger upgrade

The CMS trigger and data acquisition system will continue to have two levels of triggering, with only one synchronous hardware-based Level 1 trigger, consisting of custom electronic boards and operating on dedicated data streams, and a second level, the High Level Trigger (HLT), which uses software algorithms running asynchronously on off-the-shelf computer hardware, and uses the full detector data to select events for offline storage and analysis.

The Level 1 trigger system will be completely redesigned, using tracking information and particle flow algorithms to select events at a rate of up to 750 kHz, compared to the 100 kHz current rate, in order to maintain the efficiency of signal selection at the level of the current performance [12].

The main purpose of the data acquisition system (DAQ) is to provide the data path and time decoupling between synchronous detector readout and data reduction, asynchronous selection of events of interest in the HLT, their local storage at the experiment site and transfer to permanent storage and analysis. The CMS data acquisition will be upgraded to collect data fragments for Level 1 accepted events from the detector backend modules at a rate approximately 5 to 7.5 times higher than the current rate. The total event network throughput required for the High-Luminosity upgrade is up to a factor of 32 higher, requiring a correspondingly larger buffer. In general, the computing power required for the HLT is estimated to be 24 times greater than today, based on simulations and the currently available HL upgrade reconstruction code [13].

Chapter 2

Semiconductor radiation detectors

Particle detectors are complex systems composed of multiple layers of sub-detectors, each consisting of various sensors. Collectively, these layers facilitate the acquisition of information about the particles to be detected. To gather the necessary data for Elemental Particle Physics events and to meet the practical requirements of each experiment, detectors are typically arranged in different layers. As seen in the previous chapter, a cross-sectional view of a detector system would reveal tracking devices (which provide information about the particle's path), calorimeters (which can be of Electromagnetic (ECAL) or Hadronic (HCAL) type and measure the energy of the particles), and particle identification detectors (which provide information to identify the resulting particle type).

The combined data from all layers of a detector enable the reconstruction, tracking, vertexing, and particle identification of the multiple events occurring in particle collision experiments. Each layer of a detector operates under specific principles, with silicon-based semiconductor sensors being one of the most prevalent.

Silicon-based detectors, essentially solid-state ionization chambers, are widely used due to their numerous advantages. These include compactness, excellent energy resolution, high speed, high granularity, low intrinsic noise, lower ionizing energy compared to other detectors (like gas-based), minimal sensitivity to high magnetic fields, and high production know-how since they are manufactured using standard semiconductor industry processes.

2.1 Semiconductors fundamentals

The silicon semiconductor structure is characterized by a tightly packed, periodic arrangement of atoms in a crystalline form. This proximity of atoms results in their outer shell atomic levels forming an energy band configuration that can be considered as a continuum. Concurrently, a forbidden energy band gap is generated as a consequence of this periodic arrangement,

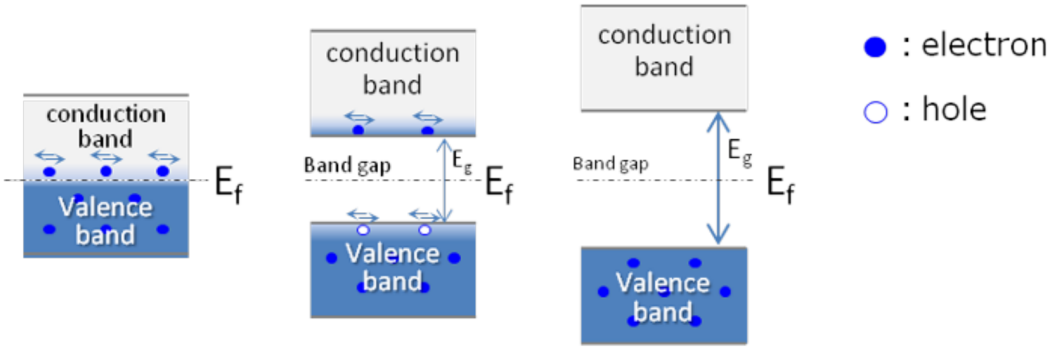

Fig. 2.1 Representation of the conduction band, valence band and the band gap from a metal, a semiconductor and an insulator. The Fermi level E_f and the energy gap E_g, are also represented, not scaled.

separating the conduction and valence bands. The primary distinction between the valence and conduction bands lies in their electron occupancy and mobility. The valence band is where electrons reside at zero temperature, while the conduction band contains electrons at higher energy levels, further from the nucleus. This results in weaker binding and greater mobility, allowing electrons to be promoted and generate currents.

The size of the band gap is instrumental in determining whether the material behave as an insulator, semiconductor, or conductor and the primary distinction of them lies in the energy gap: conductors have $E_g = 0\,\text{eV}$ overlapping valence and conduction bands, insulators have $E_g > 5\,\text{eV}$ and for semiconductors $E_g \simeq 1\,\text{eV}$. In a state of absolute zero temperature (0 K), electrons completely occupy the valence band, leaving the conduction band empty. Under these conditions, both semiconductors and insulators exhibit no electrical conductivity. However, when electrons gain sufficient energy to cross the gap and reach the conduction band, they become free to move within the crystal leaving behind a vacancy in the valence band, known as a hole. The electron and the hole together form what is known as an electron-hole pair. Both the free electrons in the conduction band and the holes in the valence band contribute to the electrical conductivity of the material.

A key parameter for determining the electron and holes concentration is the Fermi level, defined as the thermodynamic work required to add an electron to the structure. Mathematically, it is represented as the hypothetical energy level of an electron that would have a 50% probability of being occupied at any given time under thermodynamic equilibrium. Also known as the Chemical Potential, the Fermi level is situated almost midway between the valence and conduction bands for an intrinsic semiconductor. A representation of the band gap from metal, semiconductor and insulator material can be seen in Figure 2.1.

2.1.1 Doping

The conductivity of the semiconductor structure can be altered by introducing dopants. In other words, atoms of the semiconductor can be replaced with other elements of similar atomic size but different valence. Dopant impurities shift the Fermi level of the semiconductor away from its central position. Specifically, acceptors move the Fermi level to a lower energy, while donors move it to a higher energy. This shift affects the probability of having an occupied energy level in the conduction band $P_{occupation}$ changes according to the change in the Fermi level μ:

$$P_{occupation}(E) = \frac{1}{e^{-(\mu - E)/kT} + 1} \tag{2.1}$$

The resistivity properties of a material, which reflect the difficulty with which current passes through the material, are key determinants of its behavior. In semiconductors, these properties and other derived characteristics can be changed by controlling the concentration of the dopants.

Doping is a procedure in which the purity of crystalline silicon is intentionally changed, since the mono-crystal silicon used in semiconductor sensors (and other electronic components) has almost no impurities within its structure and only a few electrons are promoted to the conductive band by thermal excitation, so this mono-crystal is mostly insulator. This doping process can be done in silicon growth stage or in other manufacturing steps on localized areas, depending on what is desired as well as the doping can be done with different dopant types. If the dopants increase the effective concentration of electrons (holes) in the conductive (valence) band then the crystal silicon converts to a denominated *n-type* (*p-type*) silicon and this dopant is thus called a donor (acceptor).

After the doping process, the silicon lattice will have an increased amount of majority carriers according to the type: electrons in *n-type* and holes for *p-type*, that also changes the Fermi level mentioned in the previous section displacing it to the conductive or valence band. Since Silicon have 4 valence electrons on the outermost orbital, the most common elements used as dopants are those from III and V groups serving as acceptors or donors and the density of the carriers can be described with:

$$n = n_i e^{\frac{E_F - E_i}{kT}}, \; p = n_i e^{\frac{E_i - E_F}{kT}} \tag{2.2}$$

where n_i is the intrinsic density of undoped silicon, and E_F and E_i the Fermi levels displaced and undoped respectively.

2.1.2 p-n junction

A p-n junction, is created when p-type and n-type silicon are combined. Upon formation, a significant density gradient in both electron and hole concentrations emerges at the metallurgical boundary. The contact between the two types triggers a diffusion of carriers along the junction due to the density gradient. This process continues until an electric field, potent enough to halt diffusion, is generated by the charge disparity between the two materials. This field arises as a portion of the p-type silicon acquires a net negative charge, while the n-type silicon undergoes the opposite effect, culminating in the formation of the p-n junction with a space charge.

The two doped zones contain charge carriers that are inclined to reorganize along the junction via a diffusion current due to the concentration difference. As electrons in the n region start to diffuse into the p region, majority carrier holes from the p region similarly diffuse into the n region. Assuming uniform densities and comparable donor and acceptor concentrations in the p and n regions, the depletion region extends equally into both sides of the junction, and this junction is thus denominated to be abrupt.

As previously stated, the aggregate positive and negative charges in the n and p regions generate an electric field along the metallurgical junction from the n to the p region. This electric field expels all electrons and holes near the junction due to a drift current, thereby creating a region depleted of free charge. In this region, only ionized donor or acceptor atomic nuclei impurities persist, as they are anchored in the crystalline lattice. This area is known as the depletion region or space charge region. The boundaries of this depleted region are defined by the points where the drift and diffusion currents balance each other.

The electric field $E(x)$ in crystalline structures depends on the charge space as, and can be determined by applying the Poisson equation and integrating it for both n and p zones of the junction, resulting in:

$$\begin{aligned} E(x) &= \frac{-eN_a}{\varepsilon_{Si}}(x+x_p)+C_1;\ x_p < x < 0 \\ E(x) &= \frac{eN_d}{\varepsilon_{Si}}(x_n-x)+C_2;\ 0 < x < x_n \end{aligned} \tag{2.3}$$

with e the electron charge, ε_{Si} the relative permitivity of the silicon (11.68 at room temperature) and x_p and x_n being the depletion widths on the p and n sides of the junction.

In the scenario where no external voltage is applied to the p-n junction, it is deemed to be in thermal equilibrium and implies a constant Fermi energy level throughout the junction region. The difference between the intrinsic Fermi levels in both the p and n regions can

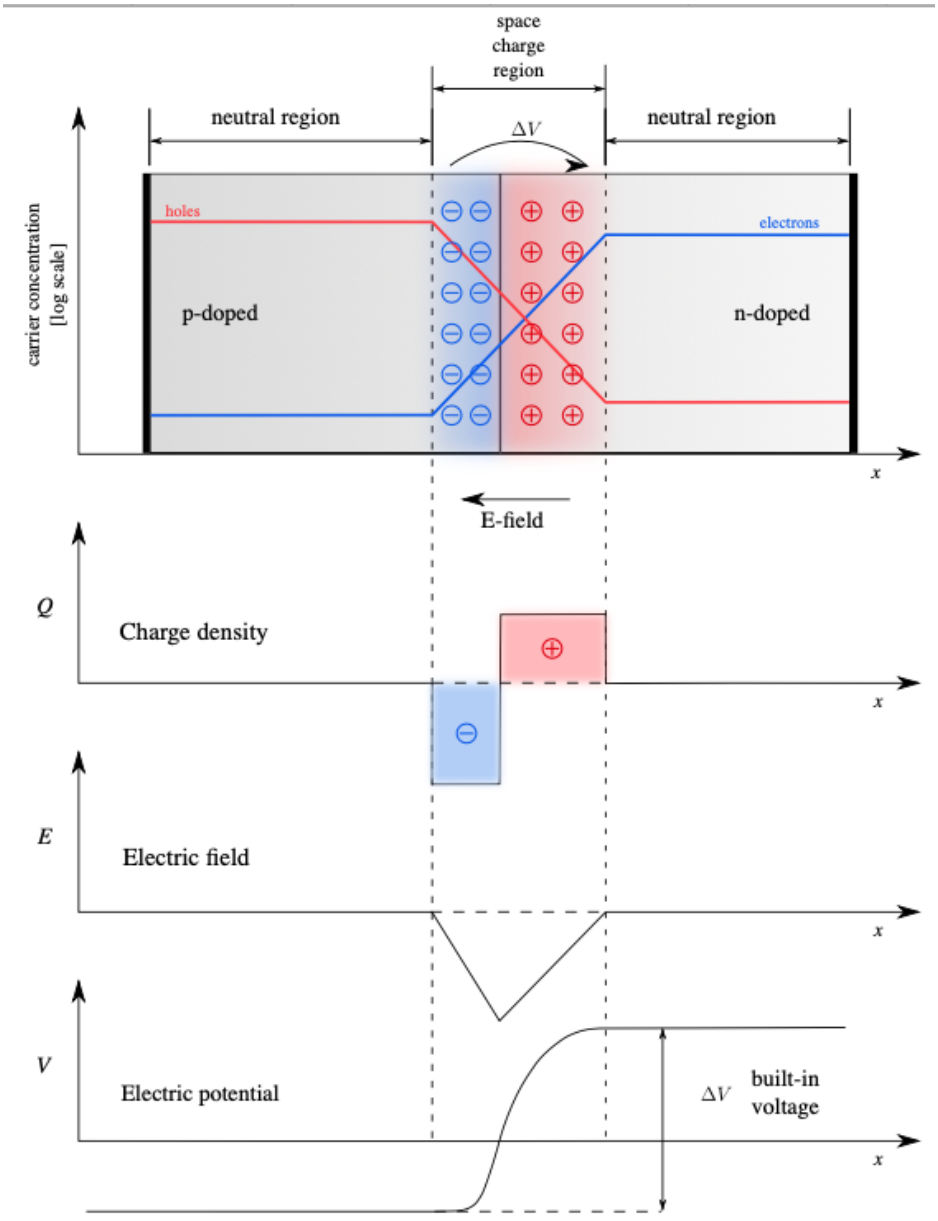

Fig. 2.2 Representation of an abrupt p-n junction showing the carrier concentration for the p-type and n-type regions, as well as the space charge region formed without external bias, with the corresponding charge density, electric field and electric potential. Taken from [14].

be determined as the generated built-in potential barrier, denoted as V_{bi}. This barrier is exemplified as the obstacle that electrons in the conduction band of the n region encounter when attempting to transition to the conduction band of the p region. This built-in potential is equal to the difference of the Fermi levels of each p and n regions $V_{bi} = E_{Fn} - E_{Fp}$ and depends logarithmically on the doping concentrations.

$$\Delta E_F = -kTlog\frac{N_a N_d}{n_i^2} \tag{2.4}$$

Corresponding to an electric potential:

$$\Delta V_F = \frac{1}{q_e}\Delta E_F = V_{bi} \tag{2.5}$$

We also can determine the depleted region using the effective carrier density $N_{eff} = N_d - N_a$ like:

$$W = \sqrt{\frac{2\varepsilon_0\varepsilon_{Si}}{e}\frac{V_{bi}}{|N_{eff}|}} \tag{2.6}$$

Again with no external voltage applied, this depleted region is usually of some micrometers and the V_{bi} is just around 0.5 V to 1 V. The Figure 2.2 schematically shows an abrupt p-n junction with the corresponding charge density, electric field and electric potential. In the next subsection the case where an external bias voltage is applied will be analyzed.

2.1.3 Biasing

The application of potential between the p and n regions disrupts the equilibrium condition, leading to a non-constant Fermi energy level throughout the semiconductor structure. The bias voltage can either increase or decrease the junction's barrier potential, depending on whether the polarization is forward or reverse.

In the case of forward bias, an external positive potential is applied to the p-region and negative to the n-region, reducing the potential barrier. This reduction in barrier potential causes the current carriers to return to the depletion region and recombine. As the voltage applied at the p-n junction increases, the large number of electrons and holes further diminishes the depletion region. Consequently, the electric current in the p-n junction increases, and the depletion region decreases with increasing voltage. On the other hand, when an external voltage is applied in reverse bias, the Fermi level on the n side falls below the Fermi level on the p side, and this difference equates to the applied voltage. This applied

voltage signifies the reverse-biased condition, and the total potential barrier, denoted by V_{total}, increases following:

$$V_{total} = V_{bi} + V_{bias} \tag{2.7}$$

V_{bi} is the built-in potential barrier in thermal equilibrium of Equation 2.4, V_{bias} is the magnitude of the reverse-biased potential.

The magnitude of the electric field in the depleted zone escalates beyond the thermal equilibrium value due to the applied voltage. As the electric field intensifies, the number of positive and negative charges increases, given that the electric field is the gradient of the potential. Therefore, the width of the space charge, W_{dep}, increases as the square root of the applied voltage V_{bias}, being:

$$W_{dep} = \sqrt{\frac{2\varepsilon_0 \varepsilon_{Si} V_{bias}}{e_0 |N_{eff}|}} \tag{2.8}$$

Under the single-sided junction approximation, where the doping concentration of the bulk is significantly smaller than the doping concentration of the implanted region, the width of the space charge decreases with the square root of this concentration. If the width of the space charge region expands until the sensor is entirely depleted to the full volume, with d defined as the distance between the detector electrodes with different doping type, we can then define the depletion voltage in planar sensors like:

$$V_{dep} = \frac{d^2 e_0 N_{eff}}{2\varepsilon_0 \varepsilon_{Si}} \tag{2.9}$$

2.1.4 Current and capacitance of a Si sensor

2.1.4.1 Capacitance

The region of depletion between electrodes can be conceptualized as a capacitor, with the electrodes functioning as the anode and cathode, and the depleted region serving as the dielectric. This is known as the junction capacitance.

Any fluctuation in the charge within a p-n junction due to a change in the applied voltage V_a, results in a capacitance C, which is related to the depletion charge $Q(V_a)$, following:

$$C(V_a) = \left| \frac{dQ(V_a)}{dV_a} \right| \tag{2.10}$$

Since this capacitance can be described in terms of the area A of the diode-like that is depleted to a width W_{dep} from Equation 2.8, we can write Equation 2.10 like:

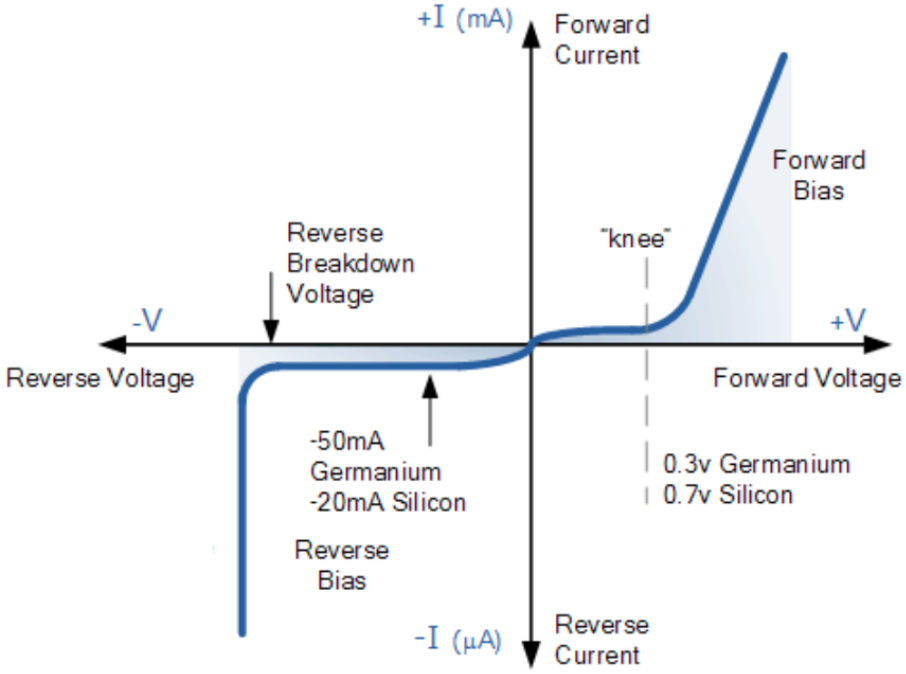

Fig. 2.3 The current as a function of the forward and reverse bias voltage applied to a semiconductor sensor, where the reverse or dark current due to the applied reverse bias is shown as an example until it reaches breakdown as a result of avalanche multiplication. Taken from [14].

$$C = \frac{\varepsilon_0 \varepsilon_{Si} A}{W_{dep}} = A\sqrt{\frac{\varepsilon_0 \varepsilon_{Si} N_{eff}}{2V_{bias}}} \tag{2.11}$$

The expression for the junction capacitance appears to be analogous to that of a parallel plate capacitor, with the key distinction being that the depletion width, and consequently the capacitance, is dependent on the voltage. It diminishes as the square root of the bias voltage until full depletion is achieved, at which point the capacitance attains a minimum value and subsequently remains constant.

2.1.4.2 Leakage current

In the case when a semiconductor sensor is reverse-biased, an small current is generated due to recombination of minority carriers and by diffusion. This current is known as leakage current or reverse current. Since electron-hole pairs are produced thermally, this current is also temperature dependent following:

$$I(T) = I_0(\frac{T}{T_0})^2 exp(\frac{E_g}{2kT_0} - \frac{E_g}{2kT}) \tag{2.12}$$

with k being the Boltzmann constant and again E_g the band gap energy of about 1.1 eV. This current is small and will be increasing according to the bias voltage if we increase it, similar to the behavior of a diode. If the bias voltage is high enough, the electric field will also increase and free carriers will be so accelerated that they could ionize the bonded electrons and generate secondary electron-hole pairs in the depleted region, in an *avalanche* effect, culminating in breakdown of the sensor. This avalanche effect due to the reverse biasing is important for the type of sensors studied in this thesis.

In general, the current of a semiconductor sensor follows the diode equation or also known as the Shockley equation [15] that considers the components of the diffusion current due to holes J_p and electrons J_n, describing the current-voltage characteristics under the reverse and forward biasing:

$$J = J_n + J_p = J_0(e^{q_e V/kT} - 1), \tag{2.13}$$

where

$$J_0 = q_e n_i^2 \left(\frac{D_n}{N_a L_n} + \frac{D_p}{N_d L_p} \right). \tag{2.14}$$

With D_n and D_p being the diffusion constant for electrons and holes, L_n and L_p the corresponding n and p diffusion lengths and n_i the intrinsic carrier concentration.

Figure 2.3 shows the current as a function of the bias voltage applied to a semiconductor sensor, where the reverse current due to the applied reverse bias is shown as an example until it reaches the so-called breakdown voltage. This is the voltage at which the reverse current increases in orders of magnitude in just a few volts as a result of avalanche multiplication.

2.1.5 Silicon sensors

The silicon sensors structure includes an intrinsic electric field generated by a p-n junction, a depleted semiconductor bulk that acts as an ionizing medium, and electrodes where a current is induced as charge carriers traverse the bulk. The construction of the sensitive zone of silicon-based sensors requires the depletion of the silicon structure of charge carriers. A sensor substrate made of doped silicon can be depleted when an external reverse bias is applied to the electrodes, then a depleted region and a large electric field are generated, forming the ionization chamber.

When a minimum ionizing particle (MIP) traverses a silicon detector, it undergoes energy loss via ionization, thereby generating electron-hole pairs along its trajectory. In a similar vein, when a photon permeates the detector, it is absorbed, resulting in the liberation of an excited electron that is promoted to the conduction band and leaves a hole in the valence

band. If the diode is fully depleted, the generated electrons and holes will drift towards the electrodes under the influence of the electric field, inducing a measurable signal. Owing to the small energy gap of silicon, a substantial quantity of charge carriers is generated in comparison to other types of ionizing radiation detectors. On average, one electron-hole pair is created for every 3.6 eV of energy deposited.

2.2 Sensors manufacturing

Semiconductor sensors are typically made from silicon crystals that are sliced and arranged into thin wafers using high-precision processes to achieve the desired characteristics for each application. In most cases, the sensor manufacturing process starts with sensor designs, which are recorded using various techniques. The recorded designs are then imprinted onto each silicon wafer through a complex sequence of physical and chemical processes. These processes include etching, thin film deposition, ion implantation using photolithography, diffusion, atomic layer deposition and so on. During these processes, the different layers of the design are deposited, grown or removed as many times as necessary to achieve the desired functionality.

2.2.1 Silicon wafer manufacturing

All developments related to the production of silicon devices begin with essential steps to obtain the raw material: silicon wafers. A simplified description of silicon wafer production is given in this subsection.

Although silicon (Si) is the second most abundant element on the surface of the Earth, it occurs naturally in silicates. However, these silicates are useless without a purification process. This process involves isolating silicon from high-purity silica (SiO_2) found in quartz and quartzite, which contain relatively few metallic impurities [16]. After a series of steps, this purified silicon is known as 'metallurgical grade silicon' (MG-Si) after the reaction:

$$SiO_2 + C \rightarrow Si + CO_2 \tag{2.15}$$

However, MG-Si is not pure enough for electronic applications. It requires an additional multi-step process. First, it reacts with anhydrous hydrochloric acid gas (HCl) at high temperatures in special reactors to form trichlorosilane $(SiHCl_3)$ (TCS) in a fluidized bed reactor (FBR)[17], as shown in the reaction:

$$Si + 3HCl \rightarrow SiHCl_3 + H_2 \tag{2.16}$$

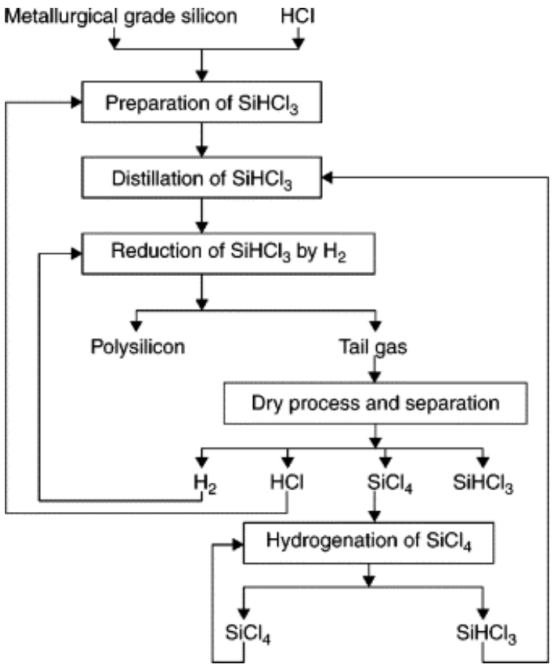

Fig. 2.4 Schematic of the Siemens process. The reuse of by-products that is a common practice, is also shown. Taken from [18].

The resulting gas is fractionally distilled to further purify it, eventually forming solid polycrystalline silicon. This purification process, known as the 'Siemens process' [18], in where the the TCS is broken down in a reducing atmosphere at around 1000 °C and adding hydrogen to finally depositing the formed polycrystalline silicon by the reverse reaction in a chemical vapour deposition reactor:

$$SiHCl_3 + H_2 \rightarrow Si + 3HCl \tag{2.17}$$

The modified Siemens process, which involves additional multi-stage processing, is shown in Figure 2.4.

Once this electronic-grade polycrystalline silicon has been obtained, it can be melted and then grown into a large single silicon crystal using various growing methods used in the industry.

2.2.1.1 Czochralski process

The Czochralski (Cz) process, named after Jan Czochralski, is the most common method of producing single crystal silicon. The process is carried out in an vacuum chamber, commonly called a "crystal puller", which contains a large crucible, usually made of quartz. Semiconductor grade polycrystalline silicon is charged into the crucible along with precise

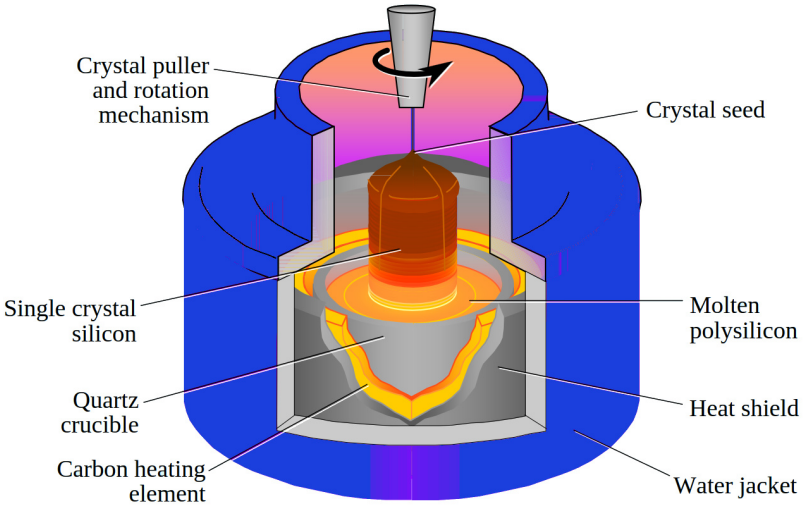

Fig. 2.5 Sketch of the Czochralski process with the main components shown. Adapted from [19].

amounts of dopants, such as phosphorus or boron, in the concentrations required to produce p-type (B) or n-type (As, P) polycrystalline silicon.

The charged crucible is electrically heated to a temperature sufficient to melt the polycrystalline silicon, above 1421 °C. Once the silicon is fully molten, a small seed crystal mounted on a rod is lowered into the molten silicon. The seed crystal is typically about 5 µm in diameter and up to 300 µm long. It acts as a "starter" for the growth of the larger silicon crystal from the melt. A single silicon crystal seed is placed on the surface with a known crystal facet oriented vertically in the melt. The crystal facets are defined by "Miller indices" which refer to the x, y or z plane axis, with 100, 110 or 111 being the typical indices used. Crystal growth from the melt will conform to this initial orientation, giving the final large single crystal a known crystal orientation.

The seed crystal is slowly pulled out of the melt at a rate of a few centimetres per hour. This pulls the molten silicon out of the melt and allows it to solidify from the seed into a continuous single crystal. The pulling speed determines the final diameter of the large crystal. Both the crystal and the crucible are rotated during crystal pulling to improve crystal homogeneity and dopant distribution. The temperature and pulling speed are carefully adjusted to eliminate dislocations in the crystal. The final large crystal is cylindrical in shape and is called a "boule". Figure 2.5 shows a schematic diagram of the Czochralski process.

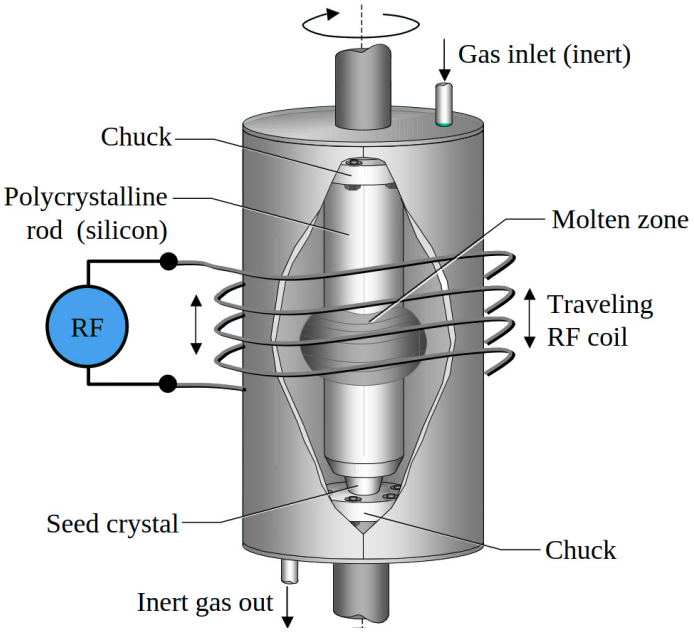

Fig. 2.6 Scheme of the float-zone (FZ) process with the main components shown. Adapted from [19].

2.2.1.2 Float-zone process

Float-zone (FZ) refining is a process developed to achieve higher purity in the silicon, consisting in mounting the polycrystalline silicon vertically inside the growth chamber and ensuring an inert atmosphere or even under vacuum and preventing the ingot from being in contact with other components. The molten zone is then held between two vertical solid bars by its own surface tension, giving the method its name [20].

The polycrystalline silicon ingot has a seed crystal at its base, again knowing its orientation with the Miller indices. Then radio frequency (RF) coils[1] are used to heat the ingot without contact, creating a molten region of about 2 cm thickness that is moved along the ingot length to push out the impurities and leave just refined single crystal silicon. Here it is important to note that in the float zone process, dopants and other impurities are rejected by the growing silicon crystal. A rotation movement is also applied to improve the homogeinity in the final crystal. The float zone (FZ) process scheme can be seen in Figure 2.6, which shows the main elements involved.

[1] RF coils are the most common, but there are several other heating methods such as optical, electron beam, laser and resistance heating [20].

2.2.2 Wafer type for sensors

There are several types of wafers used in the manufacture of semiconductor sensors, most commonly classified by the manufacturing process used to produce the wafer. In this subsection only two types of wafers used for sensors will be reviewed: the epitaxial (epi) wafers and the silicon-on-silicon (SiSi) wafers.

2.2.2.1 Epitaxial wafers

Epitaxy refers to the deposition of a crystalline layer on a crystalline semiconductor substrate or surface. It involves the growth of new crystalline layers with well-defined orientations relative to the seed layer. The deposited crystalline film is called an "epitaxial layer" [21]. For most technological applications, single-domain epitaxy, where the overlying crystal is aligned with the substrate crystal, is preferred. Epitaxy plays a crucial role in semiconductor manufacturing, particularly in the growth of epitaxial layers on semiconductor substrate wafers.

Silicon epitaxy is used to create epitaxial devices on silicon wafers consisting of thin nano-layers of semiconductor crystals. By combining different semiconductor materials and dopants, "epi wafers" determine the performance of photonic and radio frequency (RF) semiconductor devices. The energy required to grow the epitaxial layers depends on the chemical sources and hydrogen as the carrier gas. Once formed, the layers can be patterned into desired shapes. Silicon epitaxy can be homoepitaxial (same material as the substrate) or heteroepitaxial (different material), depending on the composition of the layers.

Epitaxial silicon film growth involves the deposition of a thin layer of monocrystalline silicon on a monocrystalline silicon substrate. The very simplified process [22] can be broken down into the following steps:

- Melt formation: A melt containing molecules of the starting substrate and a low-melting is created. This melt is heated to partially dissolve the surface of the substrate, resulting in a high resistivity layer.

- Layer formation: Next, a thin layer of another material is formed. This step is critical in creating semiconductor devices. Chemical vapour deposition (CVD) is used to create the second layer. Another methods are the Vapor-Phase Epitaxy (VPE) a modification of CVD, and Molecular-Beam Epitaxy (MBE) that is mainly for compound semiconductors.

- Thermal oxidation: The third layer is then produced by thermal oxidation. The silicon layer achieves a uniform thickness.

2.2.2.2 SiSi wafers

Silicon on Silicon (SiSi) wafers are based on the silicon bonded to silicon-on-insulator (SOI) wafers, involves the bonding of two silicon layers with no oxide in between. Typically, a high resistivity silicon layer is bonded to a low resistivity wafer. SiSi wafers are used as an alternative to thin film epitaxial growth.

The advantages of SiSi over thin film epitaxy include cost effectiveness. Technically, SiSi enables the fast manufacture of PIN diodes as an alternative to thin epitaxial layers.

Direct wafer bonding technology enables the production of silicon substrates containing multiple layers of monocrystalline silicon. These layers can have resistivity ranging from 1 mΩcm to 10 kΩcm, for both n-type and p-type, and different crystal orientations, a feature not achievable with conventional epitaxial wafers. In addition, the transition between high and low doping levels can be either sharp or gradual, depending on the specific application or customer requirements. The SiSi bonding process produces high quality wafers with low leakage, minimal warping and low defect density. Film thickness variations can be as low as $\pm$ 0.5 µm [23].

2.2.3 Microfabrication of sensors

The microfabrication of silicon sensors is a multifaceted process involving several key stages, which are based on fundamental concepts. These include the addition and removal of materials from the semiconductor, in order to create specific functional regions and/or layers. Etching is employed to selectively remove material from the silicon wafer, while deposition and implantation involve the addition of layers of material and the modification of the wafer's properties. Deposition techniques are employed to add thin films to the wafer, while ion implantation introduces dopants. Photolithography is a process that involves the use of light to define intricate patterns on a wafer. This patterning method serves as a foundation for subsequent etching or deposition steps, ensuring precise and accurate fabrication of the sensor's components. The combination of these processes enables the creation of highly functional and precise silicon sensors.

2.2.3.1 Photolithography

Lithography, from Ancient Greek $\lambda\iota\theta o\varsigma$ (lithos) meaning "stone", and $\gamma\rho\alpha\varphi\varepsilon\iota\nu$ (grafein), meaning "to write" [24], is originally derived from the concept of the process of printing on a flat surface (originally on metal or stone plates) in which a previous preparation of the material allows only the desired pattern to be inked. Following this concept, applied to the manufacture of silicon detectors, the surface is the silicon wafer and the printing is performed

by the various methods of deposition and etching processes to obtain the desired elements of the detector. Photolithography is a technique that can be applied to form precise patterns in a variety of materials [25], including metal, nitride, oxide, and semiconductors. It employs precise optical exposures to achieve high precision in the patterns required for the fabrication of detectors.

Photolithography is a critical process in semiconductor manufacturing, used to transfer intricate patterns onto the wafer with high precision. This process begins by coating the wafer with a light-sensitive material called photoresist. The wafer is then exposed to ultraviolet (UV) light through a photomask that contains the desired pattern. The exposure to UV light induces chemical changes in the photoresist, making it either more soluble (positive photoresist) or less soluble (negative photoresist) in the developer solution. After development, the remaining photoresist forms a mask that protects certain areas of the wafer during subsequent etching or deposition processes.

Advanced photolithography techniques, such as extreme ultraviolet (EUV) lithography, enable the creation of patterns with sub-wavelength resolution, essential for modern semiconductor devices with feature sizes in the nanometer range. Additionally, multiple patterning techniques, such as double patterning and quadruple patterning, are employed to further enhance resolution and achieve the high-density integration required for cutting-edge semiconductor technologies.

The combination of photolithography and patterning processes ensures the precise definition of device features, enabling the fabrication of complex integrated circuits and advanced semiconductor devices.

2.2.3.2 Deposition and implantation

Deposition and implantation are critical processes in semiconductor fabrication that enable the creation of various layers and modifications needed for electronic devices. Deposition involves the addition of thin films or layers of materials onto the semiconductor wafer, and can be achieved through several methods, including:

- Chemical Vapor Deposition (CVD): Involves the reaction of gaseous precursors to form a solid film on the substrate.
- Physical Vapor Deposition (PVD): Uses physical processes such as sputtering or evaporation to deposit materials.
- Atomic Layer Deposition (ALD): Offers precise control over layer thickness by using sequential, self-limiting chemical reactions.

Implantation involves the introduction of ions, such as boron or phosphorus, into the semiconductor substrate to modify its electrical properties. This process, known as ion implantation, allows for the precise control of dopant concentration and depth, enabling the formation of p-type and n-type regions essential for the operation of transistors, diodes, and other semiconductor devices. The combination of deposition and implantation techniques ensures the accurate formation of complex multilayer structures and the fine-tuning of electronic properties.

2.2.3.3 Etching

Etching is a fundamental step in the fabrication of semiconductor sensors, essential for creating precise patterns and structures on the wafer surface. The etching process can be classified into two main types:

- Wet etching involves the use of liquid chemicals to selectively remove material from the wafer. This method is typically used for isotropic etching, where the material is removed uniformly in all directions. Wet etching offers advantages such as high etch rates and good selectivity, but may lack the precision required for intricate patterns.
- Dry etching, on the other hand, utilizes plasma or reactive gases to etch the material and provides greater precision and control. Techniques such as reactive ion etching (RIE) and deep reactive ion etching (DRIE) are commonly used in dry etching. RIE combines the effects of chemical and physical etching to achieve high-resolution patterns with anisotropic profiles, while DRIE is specifically designed for deep etching, making it ideal for creating high-aspect-ratio structures.

The choice of etching technique depends on factors such as the desired resolution, aspect ratio, material compatibility, and the specific requirements of the sensor design.

2.3 LGAD technology

Low Gain Avalanche Detectors (LGAD) are semiconductor sensors whose operational function is based on that of a typical silicon sensor as described in subsection 2.1.5, but whose structure is designed to have a moderate gain by incorporating a multiplication region and a design intended to operate over a wide range of reverse bias voltages before breakdown.

The process of charge multiplication in LGAD is achieved by the addition of a moderately doped p-type diffusion layer situated beneath the highly doped n-type electrode. This results in an increase in the doping concentration in the vicinity of the p-n junction (see

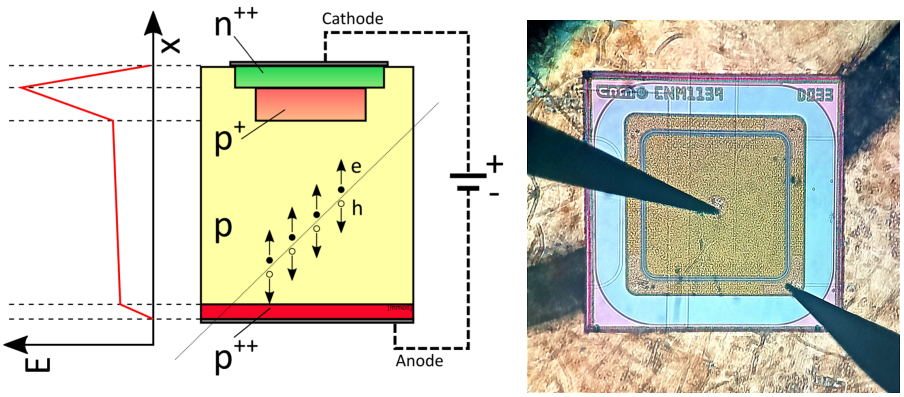

(a) LGAD scheme (b) Top view of an LGAD

Fig. 2.7 (a) is the simplified schematic cross section of the basic structure of the core of the LGAD (without the periphery structures). The n^{++}, p^{+}, p layers, the anode and cathode, and the electric field of the sensor are shown. When a particle passes through the active region, electron-hole pairs are created and collected. Taken from [26]. (b) is the top view of a real single pad of 1.3×1.3 mm^2 LGAD from CNM. The main central pad and the guard ring are contacted by the needles of the probe station (black shapes).

subsection 2.1.2), in comparison to the highly resistive substrate. As a consequence of p-well diffusion, the electric field at the junction increases under reverse bias conditions. This allows electrons generated by the incident radiation to generate avalanche multiplication due to the impact ionization mechanism before being collected. Figure 2.7 (a) illustrates an LGAD core components and the charge multiplication. In this regard, the performance of LGAD is analogous to that of the Avalanche Photo Diode (APD) but at lower gain values on the output signal, typically in the order of 10, compared to the APDs that can achieve gain levels above 100.

The RD50 collaboration [27] has been involved in the development of radiation sensors for the HL-LHC upgrade over the last few years and has been closely involved with the LGAD. Although LGADs are an excellent option to meet the requirements of the HL-LHC experiments, LGADs face major challenges such as:

- Radiation hardness: As LGADs will be will be exposed to a harsh radiation environment, which will degrade detector performance. In this sense, studies [28] have reported an increase in radiation hardness by enriching the multiplication layer with carbon (see section 5.2).

- Safe operating range: The sensors must operate above full depletion voltage and below the breakdown voltage while maintaining an optimum operating range between the desired gain and a safe operating voltage.

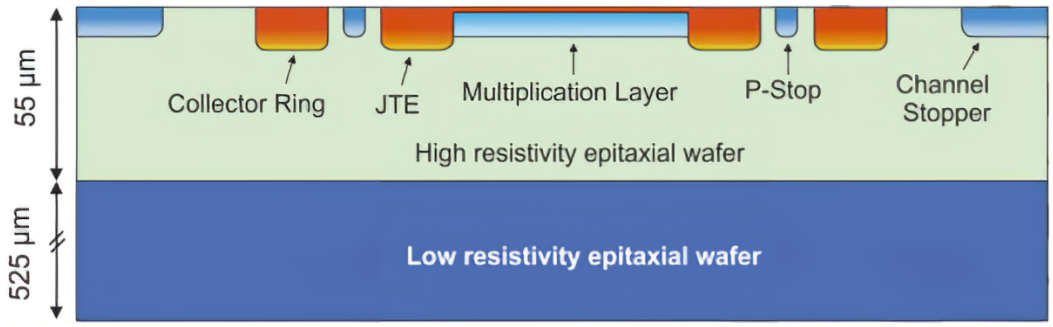

Fig. 2.8 Scheme of the cross-sectional structure of an LGAD [28] manufactured in an epitaxial wafer. The Collector Ring, Channel Stopper, P-Stop, Multiplication Layer, and the Junction Termination Extension (JTE) are illustrated. The thickness of the active volume, low resistivity wafer, and component distributions are just for example, not in proportional scale.

- Fill factor: Sensors represent a non-enhanced region where particles are not multiplied. In this sense, the main LGAD manufacturers have developed novel structures such as iLGADs, AC-LGAD, TI-LGAD or Trench iLGAD to improve this fill factor

In this aspect, the design of LGADs incorporates additional structures that are responsible for ensuring the suitability of these sensors for high-energy experiment applications. Figure 2.8 depicts a schematic cross-section of an LGAD, illustrating the principal structures that constitute the typical design, which encompasses both the core and periphery.

2.3.1 Gain layer

The characteristic feature of LGADs is their multiplication region, which consists of the $n^{++}/p^{+}/p$ structure, where the highly doped p^{+} layer is added to create a very high electric field region. This electric field produces avalanche multiplication of the primary electrons, creating additional electron-hole pairs.

The gain layer is created by an initial boron implantation followed by high temperature annealing. As a result, a deep p-well diffusion with a peak concentration in the range of $1 \times 10^{16} cm^{-3}$ and a shallow n^{+} electrode diffusion to form the $n^{++}/p^{+}/p$ structure. When this multiplication region is reverse biased, the electric field in the p-n junction increases strongly until the impact ionisation mechanism responsible for the charge multiplication is enabled.

In order to guarantee the complete depletion of the detector at relatively low voltage, the utilisation of an extremely high resistivity substrate is imperative. It is of particular importance to ensure that the electric field is increased at the edges of the p-n junction,

as these edges often exhibit a rounded curvature. This curvature causes the electrostatic potential to concentrate at the junction curvature, resulting in an increase in the local electric field in this region.

Without a suitable design at these edges, the charge carriers collected at the edge may exhibit a different multiplication value than those collected in the core region, where the electric field is uniform. This underscores the importance of maintaining uniform electric field distribution within the core region of the sensor through effective edge termination of the p-n junction. Some technologies has been developed to face the uniformity of the electric field and stability of the sensor when reverse biased.

2.3.2 JTE

In order to improve the operating voltage performance with a full depletion voltage lower than the breakdown voltage, a variety of elements have been incorporated into the design of the LGADs. The Junction Termination Extension (JTE) is a structure located at the periphery of the gain layer. Its purpose is to improve the stability of the sensor at high voltages by preventing the accumulation of electrostatic potential at the edges of the p-n junction and to improve gain homogeneity [26]. This is important because the edges of the p-n junction always have a rounded termination, which is responsible for the accumulation of electrostatic potential, as can be seen in Figure 2.9 (a), where the equipotential lines show the crowded electrical distribution at the edge of the p-well, which can cause premature breakdown.

This extension, in the case of LGADs from CNM [29], is implemented by exceeding the shallow n^+ electrode diffusion beyond the mask limits of the p-well in such a way that it overlaps the original curvature of the p-n junction (Figure 2.9 (b)). As a consequence of this diffusion occurring through the lowly doped substrate rather than through the higher doped p-well, a deeper n^+ junction is formed in the overlapping region. Furthermore, this extension is enhanced by the addition of a deep n-type diffusion (Figure 2.9 (c)), which goes deeper and reduces the crowded electric distribution at the edge of the junction thus preventing early breakdown of the p-n junction edges.

2.3.3 Guard-ring

It has been demonstrated [31] that in order to enhance the signal-to-noise ratio (SNR) in LGADs, it is essential to minimise the leakage current originating from the surface, as this current represents a significant source of noise. In order to achieve this, numerous LGAD designs have incorporated the use of an additional electrode positioned in the periphery of

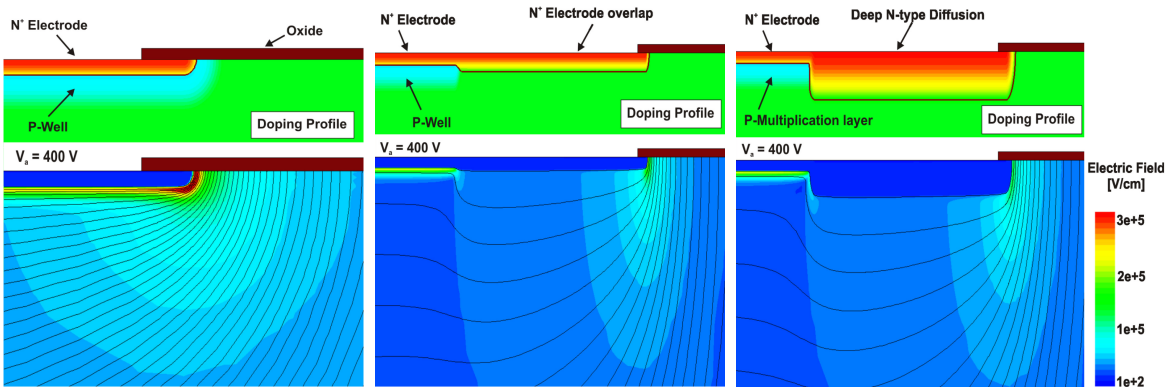

(a) No edge termination (b) N^+ electrode overlap (c) N-type deep diffusion

Fig. 2.9 Simulated doping profile (top) and equipotential lines (bottom) of the electric field at the edge of the p-n junction of fully depleted LGADs from CNM [29] without an edge termination (a), with an n^+ electrode overlapping the p-well layer (b) and with the addition of an deep n-type diffusion (c). Modified from [30].

the sensors, surrounding the active areas. When this additional electrode is biased, it extracts the surface leaked current.

This biased electrode is commonly designated as a "guard-ring" (GR), although some manufacturers, have designated it as a "collector-ring" due to the existence of a different structure, the "floating guard-ring," which serves a similar purpose to the JTE in enhancing the homogeneity of the multiplication junction.

There are numerous designs of GRs, with each manufacturer developing their own unique configuration. However, the most prevalent type of GR present in LGADs for the HL-LHC, which will be the focus of this study, are electrodes constructed using N-type diffusion. In principle, when biased to the same bias voltage as the main pad in order to preserve homogeneity of the electric field, the GR is capable of extracting the surface leakage current and a the portion of the current in the bulk that originates outside the active region of the sensor [30], thereby leaving the current generated by the active region of the sensor to be extracted exclusively by the n^+ electrode.

2.3.4 P-stop and P-spray

Parasitic current paths can develop along the peripheral surface due to positive fixed charges typically present within the so-called field oxide. The field oxide serves as an implantation mask to protect the LGAD surface from additional undesired impurity and dopant penetration. These positive fixed charges induce a concentration of negative charges along the peripheral

region's surface, resulting in the formation of an inversion layer in the very low doped P-type substrate.

With the presence of the GR surrounding the detection electrode (main pad) on the surface, there is a possibility that these two components could electrically contact each other through the inversion layer. To mitigate this, two implementations have been considered:

- P-Spray: This approach involves an initial shallow implantation of boron (low dose and low energy) across the entire surface. It creates a low-doped P-type layer at the surface, preventing the inversion layer from forming.
- P-Stop: Similar to the P-Spray, the P-Stop also prevents the inversion layer by using an highly doped implantation process. However, the P-Stop implementation is more effective in eliminating surface current paths.

2.3.5 Channel stopper

As the reverse bias is increased, the LGAD substrate is depleted in both the vertical and lateral directions. The lateral depletion of the substrate becomes relevant subsequent to the full depletion in the vertical direction, when the sensor is fully depleted and the additional supplied voltage is then supported by the lateral spread of the depletion region. If the peripheral region is insufficiently long, the depletion region may eventually reach the edge of the chip, resulting in a significant current injection from the sensor borders.

A channel stopper [32] is a highly doped silicon region with the same metallurgical character as the substrate, designed to halt the lateral spread of the depletion region at the silicon surface. Additionally, a common "design rule" [30] to circumvent this undesirable effect is to extend the peripheral length by a factor of at least two times the thickness of the substrate.

2.4 Radiation damage

Silicon detectors are of paramount importance in high-energy physics experiments. They are employed in a variety of applications, including track reconstruction, momentum measurement in magnetic fields, and the identification of secondary or decay vertices. Furthermore, silicon detectors are utilised as active layers in sampling calorimeters in certain experimental procedures.

The prolonged exposure of radiation causes damage to silicon sensors due to defects induced by the particles traversing the lattice. These defects modify the electric field and the

structure of the energy band, the leakage current of the devices increases and other effects caused by radiation damage. This section will present a review of the negative radiation effects on silicon sensors. More specific radiation damage on LGADs will be discused in chapter 5.

2.4.1 Displacement damage

The displacement of silicon crystal atoms from their normal lattice sites results in the formation of defects within the detector bulk. A so-called "Frenkel" defect occurs when hadrons or higher-energetic leptons displace an atom out of its lattice site by an inelastic collision, leading to the formation of a silicon interstitial and the creation of a vacancy in a process called Primary Knock-on Atom (PKA). This displacement in silicon requires approximately 25 eV to generate. This particular defect in silicon forms a "Frenkel pair," which is constituted by the interstitial silicon atom and its vacancy.

The introduction of these defects results in the formation of new energy levels within the silicon band structure, which in turn alters the electrical characteristics of the bulk. To illustrate, deep-level defects within the bandgap have the potential to act as generation centers for electron-hole pairs, which may result in an increase in reverse current.

It is important to note that bulk defects with energy levels in the silicon bandgap can cause electrically macroscopic effects. This depends on the position of the defects in the bandgap, the number of defects N_t and where they are in relation to the bandgap. A contribution to the space charge modification can result from positively charged donors or negatively charged acceptors, which also affects the depletion voltage. The trapping of charge carriers produced by ionizing particles passing through the bulk is another consequence that is reflected in the reduction of the sensor signal amplitude, and another important effect is the leakage current increase due to current generation by levels close to the center of the band gap. These three main effects of defect levels can be seen in Figure 2.10.

2.4.1.1 The NIEL hypothesis

The Non-Ionising Energy Loss (NIEL) hypothesis is a model that proposes a proportionality between the non-ionising energy loss by a particle within the sensor and the resulting displacement damage in the silicon. In this way the radiation damage produced by different particles with different energies can be scaled. This implies that the radiation damage incurred is dependent on both the particle type and its energy. The loss of energy by slow charged hadrons is primarily due to ionisation, whereas fast charged hadrons possess sufficient energy

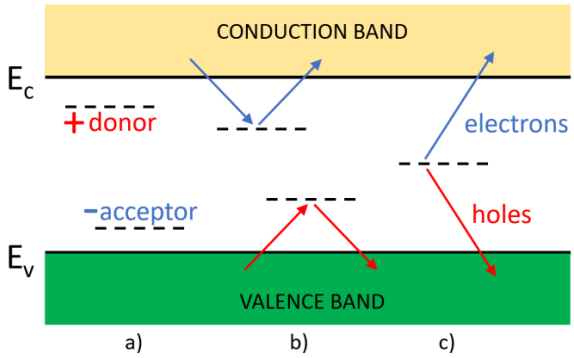

Fig. 2.10 Schematic of the main defects with macroscopically effects: Space charge modification in (a), charge carrier trapping in (b) and leakage current increase in (c). Adapted from [33]

to create Frenkel pairs and large clusters in silicon. In contrast, neutral hadrons interact exclusively through inelastic collisions with lattice atoms.

The NIEL hypothesis proposes that each collision at energy E, defined as the energy of a particle ν, has a probability $f_\nu(E,E_R)$ of producing a PKA with E_R being the recoil energy. Considering all the cross sections $\sigma_\nu(E)$ represents all possible interactions between the incident particle (with energy E) and the silicon atoms in the crystal, which result in lattice displacements. The probability of an additional atom being dislocated can be represented by the Lindhard [34] partition function $P(E_R)$. By considering the cross-section for all possible non-ionising interactions of particles with energy E, the NIEL can be calculated as the displacement damage function (cross-section) D(E):

$$D(E) = \sum \sigma_\nu \int_0^{E_R} f_\nu(E,E_R) P(E_R) dE_R \tag{2.18}$$

In order to normalize the damage, it is necessary to rescale the displacement damage cross section so that it produces a reference value produced by a mono-energetic beam of neutrons of 1 MeV.

This enables the definition of a proportionality constant, designated as the "hardness factor" k, as follows:

$$k = \frac{\int D(E)\phi(E)dE}{D(E_n = 1MeV)\int \phi(E)dE} \tag{2.19}$$

where $\phi(E)$ is the fluence in particles/cm^2 of energy E.

Using this hardness factor, we can re-scale to 1 MeV neutron equivalent fluence ϕ_{eq} any fluence of other particle type that produces equivalent displacement damage, using:

$$\phi_{eq} = k\phi = k \int \phi(E) dE \tag{2.20}$$

This hypothesis is based on the assumption that the detector damage scales with the accumulated energy transferred to displacement in silicon.

2.4.2 Leakage current increase

In silicon sensors, bulk current arises from two primary contributions: Generation current and diffusion current, with the first one being the dominant contribution in fresh and irradiated sensors. Defects located near the middle of the bandgap play a crucial role in generating and recombining electron-hole pairs through thermal excitation. Consequently, the reverse current increases linearly with irradiation fluence, reflecting the NIEL energy deposited by radiation following:

$$\Delta I = \alpha \Phi_{eq} V \tag{2.21}$$

Where the α is the proportionality factor, the increment in reverse current ΔI after the irradiation normalized by the diode volume V and the irradiation fluence is denoted by ϕ_{eq}. Importantly, this parameter is strongly temperature-dependent since in radiation damaged diodes the generation current dominates, also with low fluence levels, and the reverse bias current $I_R(T)$ can be rescaled to different temperatures using the equation:

$$I_R(T) \propto T^2 e^{(-\frac{E}{2kT})} \tag{2.22}$$

This scaling of the current with temperature is a good parameter to cross-check the temperature variation by measuring the change in reverse current experimentally.

2.4.3 Space charge modification

The depletion voltage in unirradiated silicon sensors is directly related to the effective doping concentration N_{eff}. However, radiation-induced defects can alter this relationship as they can act as donors or acceptors that can be fully ionised at room temperature if their energy level is close enough to the valence or conduction bands. When a detector is biased, deeper defects can change the effective doping concentration, leading to changes in the depletion voltage.

In highly irradiated silicon sensors, an intriguing phenomenon occurs: a collected charge higher than expected for the sensor thickness and irradiation doses. This unexpected behaviour is attributed to an avalanche multiplication process, similar to what occurs in

avalanche photodiodes (APDs). This process involves charge multiplication within the device. The underlying mechanism involves a very high effective doping concentration (N_eff), which leads to an intense electric field in a localised region. Impact ionisation compensates for the charge lost due to irradiation effects, resulting in higher than expected collected charge.

A double junction effect can occur in irradiated silicon sensors. This effect results from the activation of defects near the two implanted regions when the detector is biased, effectively creating two separate junctions. Consequently, the depletion process in an irradiated silicon sensor involves the contribution of two distinct space charge regions, which eventually merge into one when the sensor is fully depleted. In particular, one of these regions may dominate the behaviour. For example, an almost complete inversion of the space charge sign is observed in n-type FZ silicon. Studies of [35] have introduced a model to describe this effect and its evolution with irradiation.

Acceptor or donor removal, is an effect that occurs when dopants are displaced from their interstitial positions and subsequently deactivated. This effect in a macro and microscopic way and its implications in LGADs are discussed in detail in section 5.1.

2.4.4 Charge carrier trapping

Crystalline defects introduce localized energy levels within the silicon bulk. These defects have a high capture cross section, which affects re-emission times. When charge carriers encounter these defects, they can become trapped. Consequently, the usual signal integration times expected in high-energy physics (HEP) experiments (typically tens of nanoseconds) may not apply. Trapping is a significant source of signal degradation in irradiated silicon detectors, especially after exposure to high fluences.

The lifetime of carriers directly correlates with the crystal's purity. While silicon exhibits low concentrations of original crystalline defects, radiation-induced defects can significantly enhance trapping effects. A parametrization of trapping effects has been proposed [36], where the inverse of the lifetime relates to NIEL-related bulk damage and fluence as follows:

$$\frac{1}{\tau} = \frac{1}{\tau_i} + \phi K \tag{2.23}$$

with K being a constant that depends on the carrier type (hole or electron) and the particle used in irradiaiton (charged hadrons or neutrons), τ_i is the instrinsic lifetime of the carriers of orders of milliseconds.

2.4.5 Damage on the surface

Surface damage in silicon detectors arises primarily from ionisation effects within the SiO_2 passivation layers. When defects are introduced into these layers, electrons escape from the oxide while positive ions remain, creating a positive space charge. This situation can lead to premature breakdown and avalanche effects due to the high local electric field. Segmented devices, such as microstrip and pixel detectors, are more susceptible to surface damage, while non-segmented devices (such as diodes) may experience negligible effects. To mitigate oxide damage in n-on-p detectors, common strategies include the implementation of:

- P-stop isolation: A p-type silicon barrier surrounds the electrodes, minimising the effect of surface damage.
- P-spray isolation: An additional p-type layer is added between the passivation layers and the sensor bulk, further reducing surface damage.

2.4.6 Annealing

Defect annealing in silicon plays a critical role in understanding the behavior of crystalline defects. Since temperature affects the mobility of defects, it has a significant effect on the annealing process. In particular, both primary and secondary defects evolve during annealing. Secondary defects, like primary defects, are mobile and can migrate or form complex structures. The annealing process can be categorised into three types:

- Complex formation: In complex formation (see subsection 5.1.1), a defect migrates to another lattice site by acquiring sufficient energy to overcome the potential barrier anchoring it in place. This migration typically occurs during thermal excitation.
- Defect migration: Defects become mobile and move through the silicon lattice until they encounter sinks (such as dislocations or grain boundaries). The extent of migration is strongly temperature dependent.
- Dissociation: In dissociation, a multi-component defect complex breaks down into its constituent parts.

The probability of interactions during annealing is described by a balance equation:

$$-\frac{dN_x}{dt} = kN_x \tag{2.24}$$

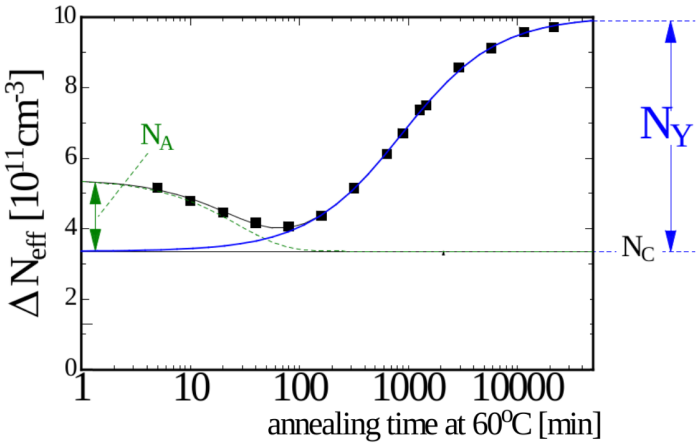

Fig. 2.11 Effective doping concentration N_{eff} as a function of the annealing time. Annealing of 60 °C and data taking at room temperature. Adapted from [33].

With N_x the concentration of defects of "X" type and k the rate constant of the process: Additionally, the rate constant for these processes is temperature-dependent and follows the Arrhenius relation:

$$k = k_0 exp\left(-\frac{E_A}{k_B T}\right) \tag{2.25}$$

With E_A being the energy of activation of the process, T the absolute temperature and k_B the Boltzmann constant.

By examining defect annealing behavior, researchers can identify the nature of specific defects. Remarkably, the annealing process can persist for years after irradiation, and changes may still occur during this extended period. As already mentioned, the strong dependence of the leakage current on the temperature makes it necessary to cool the irradiated devices in order not to change the behaviour of the irradiated devices during characterisation. For this reason, all facilities that handle irradiated silicon sensors have low temperature areas to store and operate the irradiated samples and to prevent unwanted annealing.

After irradiation, the effective doping concentration evolves with time. Since annealing accelerates the defect reactions in the bulk of irradiated silicon devices, it has been investigated [33] the beneficial effect of annealing on irradiated sensors in terms of a slow increase in their effective doping concentration N_{eff}.

This effect has been studied in n-type (phosphorus) doped devices, resulting in a positive space charge, that after irradiation induced the formation of a negative space charge, reducing the initially positive space charge according to the fluence until the space charge becomes negative at the so-called "type inversion" or "space charge sign inversion" point, and continuing to become negative until it converts into a permanent p-type device. The long-term

annealing that increases the N_{eff} of this type of sensor is then called "reverse annealing", and the increase in the N_{eff} after a comparatively short annealing time is called "short term" or simply "beneficial annealing".

Figure 2.11 shows the effective doping concentration N_{eff} as a function of the annealing time of an irradiated n-type silicon sensor, with an annealing of 60 °C and data taking at room temperature. The change of the effective doping concentration ΔN_{eff} is:

$$\Delta N_{eff}(t) = N_{eff,0} - N_{eff}(t) \tag{2.26}$$

with $N_{eff,0}$ ($N_{eff}(t)$) being the value before (after) irradiation. The time dependence can be parameterized with:

$$\Delta N_{eff}(t) = N_A(t) + N_c + N_Y(t), \tag{2.27}$$

where N_c is the called "stable damage" (do not change with time), $N_A(t)$ the "short term annealing" and N_Y the "reverse annealing".

Chapter 3

Semiconductor tracking and vertex detectors in HEP: State-of-the-art and R&D trends

High energy physics (HEP) experiments involve various subsystems equipped with different types of detectors designed for specific applications and purposes. Among these detectors, silicon sensors play a key role in particle physics experiments due to several advantageous characteristics. These include compactness, suitability for large-scale production, and excellent energy, spatial and temporal resolution, compared to other technologies [37]. In addition, the well-established manufacturing processes for semiconductor devices facilitate research and development, enabling the design of detectors that meet stringent requirements.

Conceptually, semiconductor detectors consist of three essential components: the sensor, the readout electronics and their interconnections. Two different architectures are commonly used in HEP experiments: hybrid and monolithic technologies. In the hybrid architecture, the sensor and read-out chip (ROC) are fabricated independently and then interconnected. Conversely, monolithic designs integrate the sensor and readout functionalities within the same silicon substrate, providing a streamlined and compact solution for high energy particle detection.

In this chapter, we will briefly review the state of the art of the semiconductor-based detectors used in the HEP experiments for tracking and vertexing, and introduce some of the most promising R&D towards the implementation of 4D tracking.

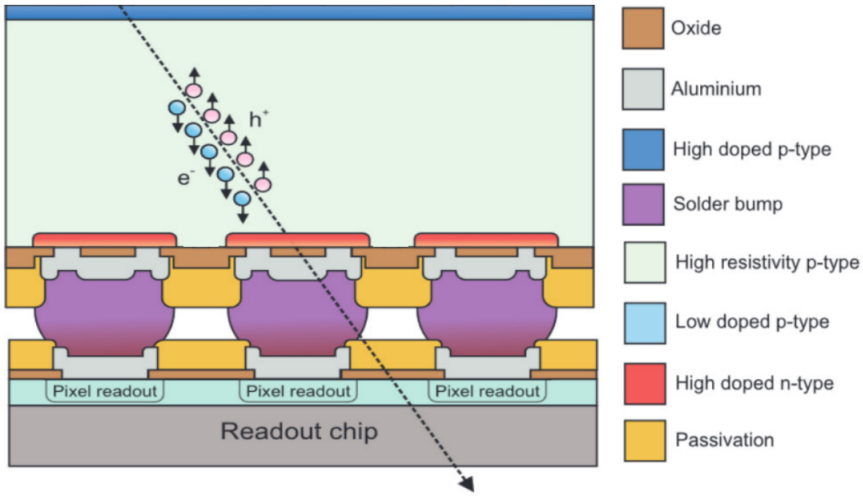

Fig. 3.1 Scheme of the cross-sectional configuration of a hybrid detector. This example comprises an pixelated n-in-p LGAD, a read-out chip and bump-bondings employed for interconnection between these components. The doted line represents a charged particle crossing the sensor, generating electron-hole pairs. Adapted from [39].

3.1 Hybrid detectors

Hybrid sensors, a crucial component in modern particle physics experiments, result from the integration of two essential elements: the sensor and the readout application specific integrated circuit (ASIC) [38]. This architecture allows independent optimisation of the readout ASIC and the sensor, but requires an interconnection process to assemble the final detector. Various bonding techniques facilitate this interconnection, including the well-established wire bonding technique, the more recently introduced bump bonding technique and the emerging Solid Liquid Inter-Diffusion (SLID) technique. Figure 3.1 is the cross-section scheme that exemplifies a hybrid pixelated detector composed of an pixelated n-in-p LGAD, a read-out chip and bump-bondings employed for interconnection between these components.

- Wire bonding [40]: Wire bonding creates electrical connections between semiconductor-based devices and silicon chips using bonding wires made of materials such as gold and aluminium. In segmented sensors, however, wire bonding is limited to segmented sensors with a dedicated readout (typically read by strips). Ultrasonic and thermosonic wire bonding are widely used in microelectronics due to their flexibility and cost effectiveness. Ultrasonic Wedge Bonding (US Bonding) is used to bond gold or aluminium wire, while Thermosonic Ball Wedge Bonding (TS Bonding) uses heat, pressure and ultrasonic energy to weld a gold, copper or silver ball to the chip surface.

- Bump bonding: Bump bonding is used for flip chip applications: mounting a chip upside down directly onto a substrate or second chip. No additional wire is used, and contact is made solely by means of pre-applied bumps. This method is very compact and has low inductance due to the short lead lengths. The recent limits of the hybridization with bump-bondings it is around of 25 µm pitch. It is also possible to stack several chips on top of each other. Despite its robustness, bump bonding is complex and requires wafer pre-processing for underbump metalisation. The bump bonding process can be summarised in three main steps [41]:
  - Underbump metalisation: A layer of metal compound is deposited on the metal contact for each unit cell or pixel.
  - Reflow: Controlled heating melts the metal mix and surface tension transforms it into a metal ball.
  - Flip chip and reflow: The sensor and read-out chip (ROC) are aligned and bonded, followed by a secondary reflow step to stabilise the bond. The surface tension during melting ensures self-alignment between sensor and ROC.

Recent R&D initiatives have been developed novel alternatives to the hybridization. Some of them are:

- Solid Liquid Interdiffusion (SLID) [42]: Investigated as an alternative to bump bonding has been studied within the ATLAS pixel upgrade R&D groups. This technique, in a simplified description, involves the following steps:
  - A benzocyclobutene (BCB) coating provides planarisation and isolation on the last metal layer of the wafer.
  - Both the ROC and the sensor require a 100 nm thin TiW diffusion barrier.
  - Electroplating deposits a 5 µm Cu layer on both components, with an additional 3 µm Sn layer on one side.
  - Alignment and heating 240–320 °C causes the tin to melt and diffuse into the copper, forming a Cu_3Sn alloy.
- Hybridization of Pixel detectors with Anisotropic Conductive Films (ACF) [43]: It is an alternative to standard flip-chip technology. The ACF technique uses 3 µm Ni-Au plated polymer beads embedded in an adhesive film 18 µm thick, requiring a pre-cure at 100 °C, then a final cure at 150 °C for 18 s, creating an anisotropic vertical connection between the sensor and ASIC pixels. These balls contact the raised metallised contact pads and are then deformed during bonding to establish electrical contact.

The following subsections provide a general description of the most developed technologies for semiconductor-based sensors that are part of the hybrid detectors used in particle physics: Pixelated planar sensors, microstrips sensors and 3D pixel sensors.

3.1.1 Planar sensors

In the context of collider tracker detectors, achieving optimal granularity while maintaining a reasonable material budget is crucial. Pixels offer excellent granularity, but their one-to-one read-out requirement poses challenges. The interconnection process and data handling become more complex, and additional material is introduced in the sensitive area (such as read-out chips and bumps), leading to increased technology costs. Consequently, pixel technologies are not practical for covering large detector areas. Typically, pixel detectors are positioned in the innermost layers near the interaction point to resolve secondary vertices, while micro-strip detectors occupy the outer layers of the silicon tracker.

Pixelated planar sensors manufactured using standard microelectronics processes are the prevailing technology. Planar pixel sensors serve as the standard choice for high-energy physics (HEP) tracking and vertex detectors. They also form the baseline technology for upgrading vertex detectors to handle high luminosities while maintaining fluences below $1 \times 10^{16}\,\mathrm{n_{eq}\,cm^{-2}}$.

These planar sensors consist of a matrix of silicon diodes, with each cell (matrix element) read-out by an Application-Specific Integrated Circuit (ASIC) cell. The ASIC could include amplification, discrimination, and read-out functionalities, necessitating a one-to-one connection for efficient data retrieval. The manufacture of planar sensors is relatively straightforward as they rely on standard planar semiconductor processes. Planar sensors are currently used in the trackers of the CMS and ATLAS experiments and remain the main technology for the future CMS ETL subdetector, which is the focus of this thesis.

The Low Gain Avalanche Detectors (LGAD) provide an illustrative example of another planar sensors, having been selected as the principal technology for the timing layers subdetectors ETL and HGTD of the particle experiments CMS and ATLAS, respectively. For further details about LGAD technology, please refer to section 2.3.

These planar sensors are based on the well-known semiconductor manufacturing technology, as described in subsection 2.1.5, the reason is the concurrence of its features like for example the LGADs, which provide excellent time resolution below 30 ps and significant radiation resistance up to fluences of $1 \times 10^{15}\,\mathrm{n_{eq}\,cm^{-2}}$ [44] with a small material budget with an active silicon thickness of only 50 µm, which is important as both detection and charge collection efficiencies have been found to be strongly dependent on sensor thickness [45]. Another advantage of the latest LGADs is that, because they are fabricated according to

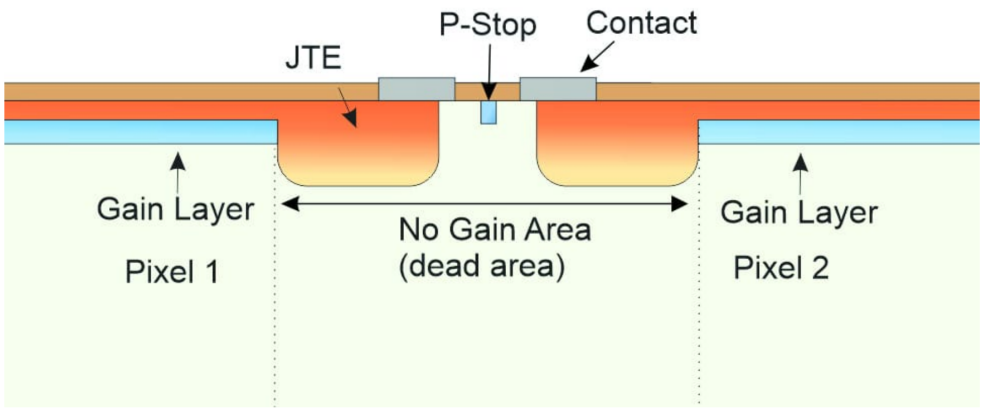

Fig. 3.2 Scheme representing two adjaccent planar pixels to illustrate the no-gain area in an LGAD, defined as the zone between the outer edge of the gain layer from the neighbor pixels. Courtesy of CNM.

the n-in-p structure, irradiation does not cause the well-known undesirable "type inversion" mentioned in subsection 2.4.6.

While LGAD sensors offer a number of advantages, they are not without limitations in terms of their capacity for segmentation. The high granularity of pixel sensors necessitates the utilization of a considerable number of readout channels, which can prove to be a significant drain on available resources. Furthermore, a significant challenge is the enhancement of the "fill factor" that affects LGAD sensors and which refers to minimize the non-sensitive area generated at the intersections between neighboring pixels or pads causing the so-called "small pixel problem" [46]. This Fill-Factor can be define as the ratio of the gain area A_{gain} and the total area A_{total} of the sensor:

$$Fill - Factor = \frac{A_{gain}}{A_{total}} \tag{3.1}$$

In the case of the recent LGAD sensors, the non-gain area is delineated like the distance between the outer edges of the multiplication layers of adjacent active regions (see subsection 2.3.1). Consequently, particles traversing these regions will produce smaller signals (without gain) since the ionization charges produced in this region will not be collected through multiplication layer. An example of this no-gain area can be seen in the scheme of Figure 3.2

Nevertheless, ongoing research and development is aimed at overcoming these challenges and improving the performance of planar sensors, with the aim of implementing sensors with high granularity and high fill factor, while maintaining excellent time resolution, leading to the paradigm of 4D tracking systems. Recent goals are focused on adding temporal layers to particle experiments to provide time tagging to identify individual particles. Going one step

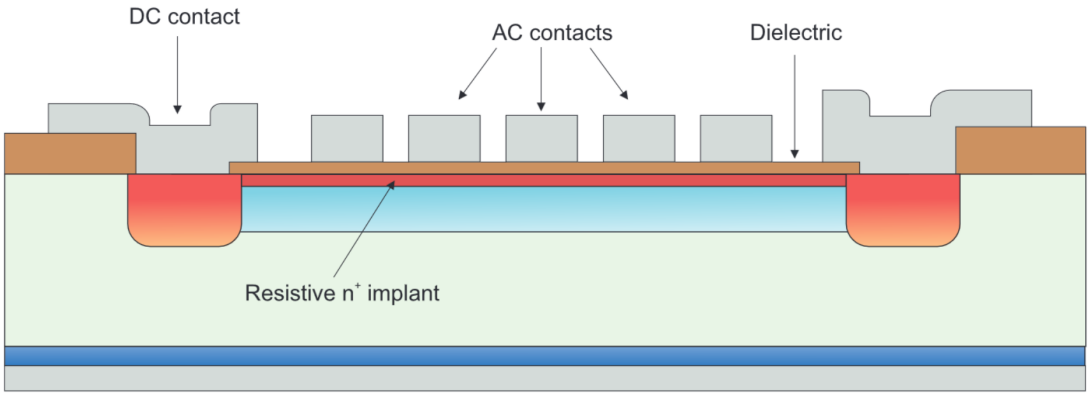

Fig. 3.3 Scheme of the cross-sectional configuration of an AC-RSD-LGAD with the main components of this design. Not scaled. Adapted from [39].

further, we could imagine a tracker in which each plane is able to measure the activation time of each pixel, thus becoming a true 4D tracking system. The following proposals represent some of the most promising avenues of research:

3.1.1.1 AC-coupled RSD-LGAD

Resistive Silicon Detector LGAD (RSD-LGAD), represents a technological advancement in the production of an LGAD that is capable of achieving a 100% fill factor through its intrinsic design, as well as a significant charge sharing between the various readout electrodes, which can be leveraged for enhanced spatial resolution, even in the case of perpendicular incidence. The technology is based on the LGAD, but with the key distinction of featuring an AC-coupled readout through a dielectric and a $n+$ resistive implant. Consequently, the $n+/p$ region remains unsegmented, and it is through this n+ resistive implant that the DC-coupled signal is measured, and segmentation is performed by creating small electrodes that are AC-coupled pads located on the surface of the sensor.

It is of great importance to control the various parameters in order to achieve the desired properties of these AC-coupled RSD-LGADs, including the capacitance that couples the AC electrodes to the sensor through the dielectric layer, which can be tuned by making it thinner or thicker, and the resistivity of the $n+$ layer, which can be tuned by adjusting the doping level. In this context, a lower doping level will result in a higher resistivity. It is desirable to have a large coupling capacitance and a higher resistivity in order to achieve a larger signal.

The cross-sectional configuration of the AC-RSD-LGAD is illustrated in Figure 3.3. Electron-hole pairs are created in the p-type bulk of the sensor, where the electrons drift to the gain layer in a manner analogous to that observed in a conventional LGAD, resulting in multiplication. Subsequently, the electrons will reach the resistive $n+$ implant, where they

will be directed towards the AC electrodes since offer the smallest impedance to ground. The $n+$ layer and the AC electrodes act as multiple RC circuits, connected to their respective read-out electrodes. Each AC electrode then collects a certain amount of charge, dependent on the distance to the position where ionization occurs.

Through this "charge sharing" process, the position of the hit of the particle can be calculated from charge imbalance algorithms [47]. The AC coupling induces a positive charge in the electrodes, which constitutes the signal that is to be read out. Subsequently, the electrons accumulated by each electrode are gradually discharged via the DC contact positioned at the periphery of the $n+$ layer.

Different manufacturers have been produced and tested AC-RSD-LGADs like the IMB-CNM [48], or production and testing conducted by the Brookhaven National Laboratory (BNL) [49], as well as by the Fondazione Bruno Kessler (FBK) and the Italian National Institute for Nuclear Physics (INFN) [50]. Some RSD-LGADs devices from FBK-RSD2 have been studied [51], resulting in spatial resolutions of about 5 µm with pixels size up to 200 µm. The temporal resolution, evaluated at testbeam with protons of 120 GeV/c has been measured to be of around 40 ps.

Another variant approach of this technology are the DC-coupled sensors that has the main difference of not to have the dielectric layer and thus the metal contacts being DC-coupled. This DC-coupled approach has the main advantage over the AC-RSD design of the ability to control the signal spread. In DC-RSD, the read-out electrodes are directly embedded in the n+ resistive layer and the use of low-resistivity strips connecting the electrodes improves spatial accuracy From these sensors maintaining an excellent time resolution of around 30–40 ps [52].

3.1.1.2 TI-LGAD

The Trench Isolated LGAD (TI-LGAD) represents a novel design that incorporates trenches at the inter-pad regions between two pixels. This approach allows for the fabrication of an LGAD that minimises the non-gain area while maintaining a similar sensor design. The TI-LGAD has been proposed by FBK [53] as a means of improving the LGAD design by reducing the inter-pad distance (IPD) to values of few micrometres.

The isolation between adjacent pads is achieved by etching trenches in the substrate using the deep reactive ion etching (DRIE) technique [54], which is then filled with an isolating material, such as the commonly used SiO_2. This technology is referred to as deep isolation technology (DIT), thus replacing the implementation of the JTE and p-stop structures (see section 2.3) at the periphery of the pixels.

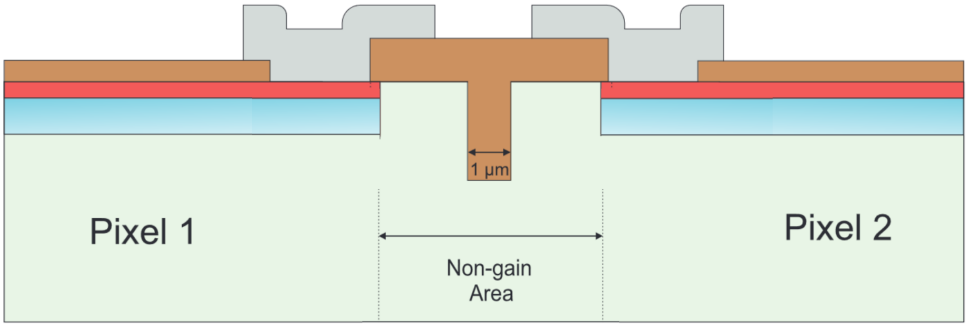

Fig. 3.4 Scheme of the cross-sectional configuration of an TI-LGAD where the trench placed between two adjaccent pixel can be seen, replacing the JTE and p-stop structures for pixel isolation. Adapted from [39].

Figure 3.4 depicts the cross-sectional configuration of the region between two pixels, illustrating the implementation of the TI technology. It can be observed the vertical trench, which can have a width of the order of 1 µm and a depth of 10 µm, that serves to isolate the pixels and leads to a no-gain area of up to 6 µm [55]. This allows for the segmentation of LGADs with a pixel pitch of 50 µm and a fill factor that is higher than that achieved by standard LGAD designs [46].

While not reaching 100%, this technology employs suitable existing technology, as seen in the majority of LGAD designs. Modifications to TI-LGADs have been proposed, including the use of boron-doped trenches [56], with the aim of implementing the gain mechanism also in the IP regions and potentially achieving a fill factor of 100%.

Some TI-LGAD carbon-infused devices, with small pixels of 375 µm $\times$ 250 µm and with single trench etched in Si substrate manufactured at FBK, have been characterized in a 160 GeV SPS pion test-beam campaign (see section 4.6), at temperature of $-25\,^{\circ}$C, in order to evaluate their time resolution, efficiency and inter-pad performance. The results of this campaign [57] indicate that unirradiated TI-LGADs biased to 164 V have a time resolution of approximately 46 ps. Samples irradiated to $1.5 \times 10^{15}\,\mathrm{n_{eq}\,cm^{-2}}$ biased at 400 V reached a time resolution of about 58 ps, at the same time as being fully efficient up to 94.2% at 530 V.

3.1.1.3 iLGAD

One of the proposed solutions to the fill-factor problem of LGADs is the inverse LGAD (iLGAD) [59]. The initial approaches entail the segmentation of pixels occurring in the p++ ohmic contact, rather than in the gain layer. Consequently, each pixel's response must be read out by the backside plane. This requires then, a double-sided process representing a

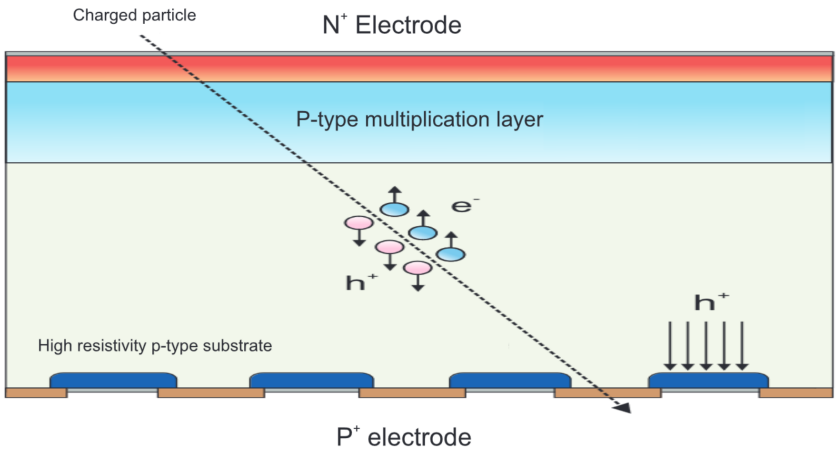

Fig. 3.5 Scheme of the cross-sectional configuration of a doubled sided inverse LGAD (iLGAD), with the main elements indicated remarking the segmentation made in the backplane of the sensor. Adapted from [58].

disadvantage in that it necessitates a complex double-sided process in the manufacturing phase, which also translates into additional costs.

In comparison to a standard LGAD, it is to be expected that the electrical characteristics, features and performance of this new device will be very similar. Given that the gain layer remains unsegmented in the case of iLGAD, it is reasonable to posit that uniformity will increase and that the no-gain area will be avoided, resulting in a 100% fill factor.

One of the key distinctions is that, after the creation of electron-hole pairs due to the incidence of a charged particle, the iLGAD technology is capable of collecting holes instead of electrons. This is illustrated in the cross-sectional diagram of a double-sided iLGAD in Figure 3.5. The multiplication layer is situated in the superior region of the sensor, situated beneath the N+ electrode. The segmentation is performed with the p+ pixels located in the inferior region of the sensor.

In an effort to reduce the active thickness of the sensors to a target depth of around 50 µm (allowing a high time resolution), which it is not possible for the double-sided fabrication process of iLGAD sensors, a novel prototype of a single-sided iLGAD technology has been developed, based on the same concept but with a significantly simplified single-sided manufacturing process, comprising approximately 50% fewer fabrication steps. This design incorporates trenches filled with polysilicon to isolate the active zone, situated above the support wafer and allowing to make the fine segmentation on the surface of the sensor with p+ pixels. This technology is also referred to as the Trench iLGAD concept [60], which was developed by CNM. The scheme of this proposed technology that combines the trench isolation and the iLGAD concept can be seen in Figure 3.6.

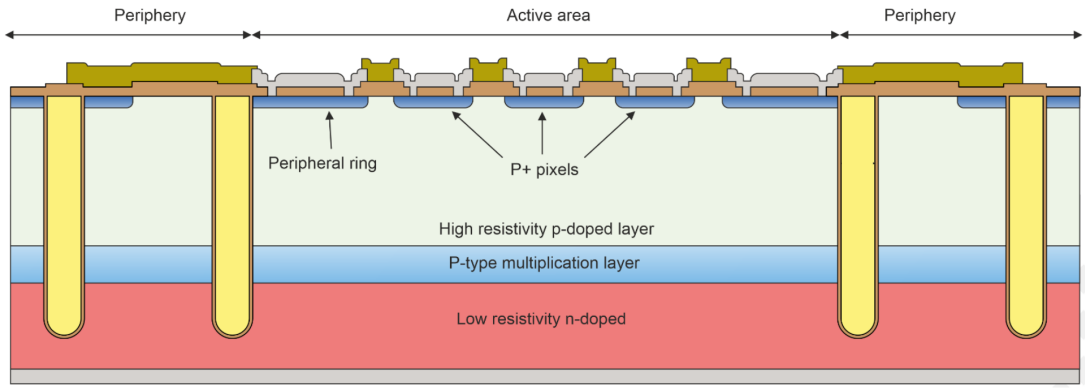

Fig. 3.6 Scheme of the cross-sectional configuration of the single-sided trench iLGAD concept, which combines the iLGAD and the trench isolation technologies. Adapted from [58].

3.1.2 Microstrips sensors

Microstrip detectors employ a readout system where each strip interfaces with an Application-Specific Integrated Circuit (ASIC), typically positioned at one end of the strips. The interconnection process between the sensor and the readout chip relies on ultrasonic wire bonding—a cost-effective standard technique widely used in the semiconductor industry. In the case of binary readout, the resolution along the transverse coordinate of the strip is determined by the strip-to-strip distance or pitch (p), with an accuracy up to $\sigma = p/\sqrt{12}$ [61].

As an illustrative example within tracker colliders, the CMS (Compact Muon Solenoid) tracker employs single-sided AC-coupled silicon strip sensors with polysilicon bias resistors and a single guard ring structure. These strip sensors, measuring 10×10 cm, are commonly used in current strip detectors. Their pitch is typically 80 µm, resulting in a geometrical resolution of approximately $\sigma \simeq 20$ µm [62]. To enhance position measurement precision, charge sharing between adjacent strips allows for interpolation. Neighboring strips may also exhibit analog signals due to effects like diffusion, capacitive coupling (inter-strip), Lorentz angle, or inclined tracks. Leveraging these effects, cluster-finding algorithms further refine position determination.

The CMS Silicon Strip Tracker (SST) [63] contains a total of 15148 individual detector modules and an active area of 200 m^2 of silicon, distributed in various sub-structures: The Tracker Inner Barrel (TIB), which contains four layers of silicon modules between 25.5 cm and 49.8 cm. The Tracker Outer Barrel (TOB), which contains six layers ranging from 60.8–108 cm. In front of the SST are two disc-like sub-detectors perpendicular to the beam: The Tracker Inner Disks (TID) complement the TIB coverage in the forward region with three discs containing three concentric rings of silicon modules. The SST is completed by two Tracker End Caps (TEC) with 9 discs of silicon modules.

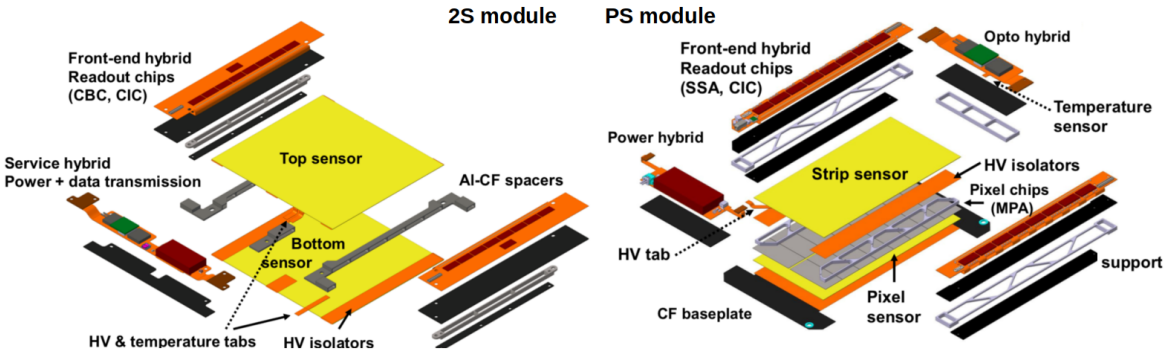

Fig. 3.7 Scheme of the two types of modules for the Outer Tracker of the SST: 2S module (left) and PS module (right). Both type of modules will be using n-in-p type silicon sensors. Adapted from [64].

The first two layers of the TIB and TOB and two rings of the TID (TEC) contain double-sided "stereo modules", where two detector modules are glued back-to-back and in one of them the strips have a rotation by 100 mrad, allowing them to provide a 3D reconstruction. The spatial resolution for the reconstructed clusters is estimated using a "pair method", which only considers hits when two detector modules have sufficient overlap to be traversed by the same particle trajectory, thus reducing the effects of multiple scattering. Only tracks with a transverse momentum greater than 3 GeV/c and more than six hits in layers of the SST and the pixel detector are considered.

The CMS Phase II Outer Tracker will be constructed from two types of modules [64]:

- Strip-Strip (2S) modules: 10×10 cm, 2 sensors (top and bottom) each with 2 rows (left and right) of 5 cm long strips, 90 µm pitch.
- Macro-Pixel Strip (PS) modules: 5×10 cm, 2 sensors (top and bottom): top sensor with 2 rows of 2.3 cm long strips and bottom sensor with 1467 µm long macro pixels, 100 µm pitch.

The both type of modules will be using the n-in-p type (that also avoid the type-inversion after irradiation) silicon sensors with 200 µm of active thickness. Figure 3.7 shows the scheme of the two types of modules for the Outer Tracker of the SST: 2S modules (left) and PS module (right).

3.1.3 3D pixel sensors

The concept of 3D pixel sensors was first proposed in 1997 as a new architecture for solid-state radiation detectors [65]. Unlike planar technology, where the electrodes are parallel to

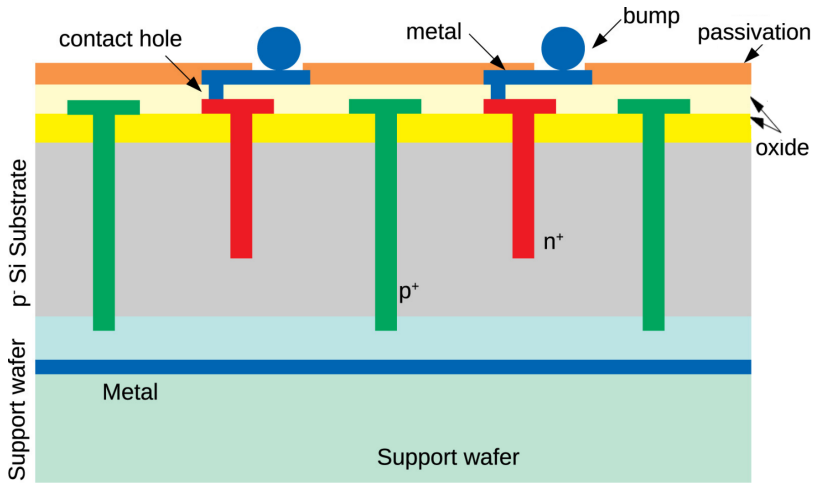

Fig. 3.8 Scheme of the cross-sectional configuration of a single sided 3D-sensor.

the sensor surface, 3D pixel sensors have electrodes arranged as columns perpendicular to the surface. The interface between the n+ implant and the p-type bulk forms the p-n junction, while the p+ implant defines the ohmic contact. Electric field lines extend from the p-n junctions to the ohmic contacts.

When a particle passes through the sensor, it creates charge carriers (electrons and holes). These carriers follow the electric field and eventually reach the electrodes. As they move, they induce a current in the electrodes, resulting in a measurable signal. In particular, the 3D architecture incorporates intrinsic slim edge technology, where peripheral ohmic columns stabilize the electric field at the dicing edge unlike planar sensors, which require guard rings to prevent failure due to mechanical damage during wafer dicing.

A strong electric field exists between the n-column and the p-column in 3D sensors, facilitating the rapid drift of excess carriers towards collection points. Bump bonding connects each pixel of the sensor to the channels of the readout chip. A key advantage of 3D sensors is the decoupling of sensor thickness and inter-electrode spacing. Unlike planar pixel sensors, where closer electrodes reduce the active volume, 3D architectures maintain the active volume even with reduced electrode spacing. In addition, 3D sensors operate at significantly lower depletion bias voltages of around 6 V (and can be operated to until around 30 V) when non-irradiated, minimizing thermal dissipation and preventing problems such as thermal runaway and sparking.

The shorter drift path for charge carriers further reduces collection time, overcoming a limitation faced by planar pixel sensors at high fluences. As baseline technology for the innermost layers of the upgraded CMS and ATLAS vertex detectors, optimized 3D sensor

designs feature reduced pixel cell sizes ($25 \times 100\,\mu m^2$ and $50 \times 50\,\mu m^2$), thinner active layers (around 150 µm), and narrower, closely spaced columns (diameters around 5 µm [66]).

Ongoing research continues to enhance 3D sensor technology, addressing challenges and exploring novel applications. The unique electrode arrangement and improved performance characteristics position 3D pixel detectors as promising tools for advancing particle physics experiments. Their suitability for high-energy physics experiments, such as the upgraded CMS and ATLAS detectors for the HL-LHC upgrade.

Test beam characterization campaigns at DESY and CERN SPS on 3D pixel modules have been successfully performed [67], using the CMS read-out chip (CROC) bump-bonded to the pixel sensor with a linear front-end and a matrix of 145152 pixel channels. 3D pixel modules with a pitch of 50 µm were measured, samples non-irradiated and irradiated to a fluence of $1 \times 10^{16}\,n_{eq}\,cm^{-2}$, which is approximately half the fluence expected for the upgraded CMS tracker in its innermost layer after 10 years of operation. The unirradiated modules were biased to the minimum stable voltage of 6 V and to a higher value of 30 V, and a bias of 150 V was used for the unirradiated modules.

The resulting best spatial resolution for the 50 µm pitch irradiated module is about 5.7 µm, obtained at 20° of incident track and a 99% hit efficiency, and for the non-irradiated 3D pixel module a resolution of about 5 µm was obtained for a 20° rotation angle.

3.2 Monolithic detectors

Monolithic detectors play a crucial role in high-energy physics experiments. Unlike hybrid detectors, which combine separate sensor and readout components, monolithic detectors integrate both functionalities into a single piece of silicon. This integration reduces material volume, allows for thin detector layers (down to 50 µm), and achieves fine pixel pitches. The lack of hybridization between sensor and readout also contributes to cost savings and simplifies assembly. The main lines of research within particle physics experiments from the monolithic detectors are:

3.2.1 DEPleted Field Effect Transistor (DEPFET)

These DEPFET detectors incorporate a Metal Oxide Semiconductor Field Effect Transistor (MOSFET) that has been designed to operate in a depleted region of the semiconductor substrate for the amplification of electronic signals. The use of a fully depleted sensor substrate results in a detector with radiation detection and amplification in each pixel, exhibiting low noise and high spatial resolution, as well as low power consumption. The

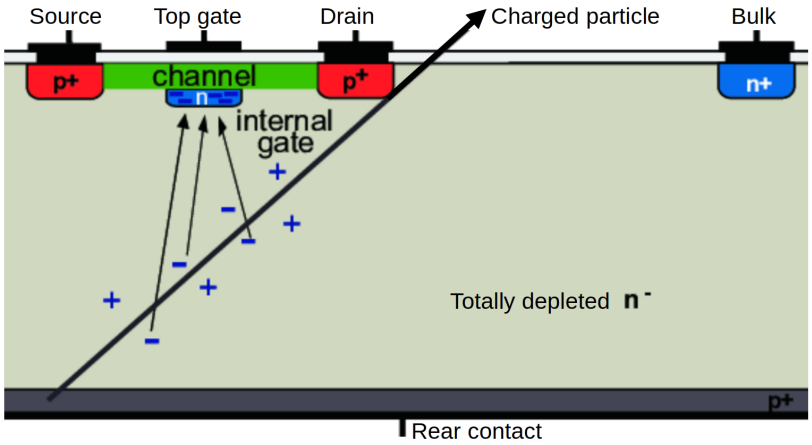

Fig. 3.9 Scheme of the cross-sectional configuration of a DEPFET pixel sensor with intrinsic amplification. Adapted from [68]

concept was first proposed in 1987 [69]. One of the most crucial parameters in a DEPFET sensor is the intrinsic amplification.

DEPFET pixels are employed in particle physics experiments, for instance, these detectors are incorporated into the BELLE II experiment in their pixel layers. The experiment has reported [70] the production of 6000 electron-hole pairs in a 75 µm silicon layer when a minimum ionising particle (MIP) traverses the sensor. Additionally, the experiment has reported a hit detection efficiency of 99.5%, an intrinsic resolution of 12 µm and a signal-to-noise ratio of between 20 and 40 per MIP. Furthermore, the experiment has demonstrated that the sensor is capable of a working read-out time of 20 µm.

3.2.2 CMOS Pixel Sensor (CPS)

In the 1990s, Complementary Metal-Oxide Semiconductor (CMOS) technology was proposed as a basis for the development of a Complementary Metal-Oxide Semiconductor (CPS). In the context of particle physics experiments, Monolithic Active Pixel Sensors (MAPS) were introduced, comprising a single device integrating the sensor and read-out electronics where each pixel is a photodiode CMOS pixel. In the previous case of DEPFET, the integration process encompasses solely the initial amplification stage within the sensor cell. In contrast, the integration of CPS involves the implementation of a sophisticated CMOS circuit, which integrates both analog and digital processing, in conjunction with the sensor.

MAPS are constructed with an epitaxial layer that is grown on a substrate wafer and serves to host the CMOS circuitry. In conventional CPS, the p-type epitaxial layer that is not fully depleted, serves as the sensitive volume, while charge is collected by diffusion in an n-well implant. After the charge collection, it is store in the diode-parasitic capacitance and

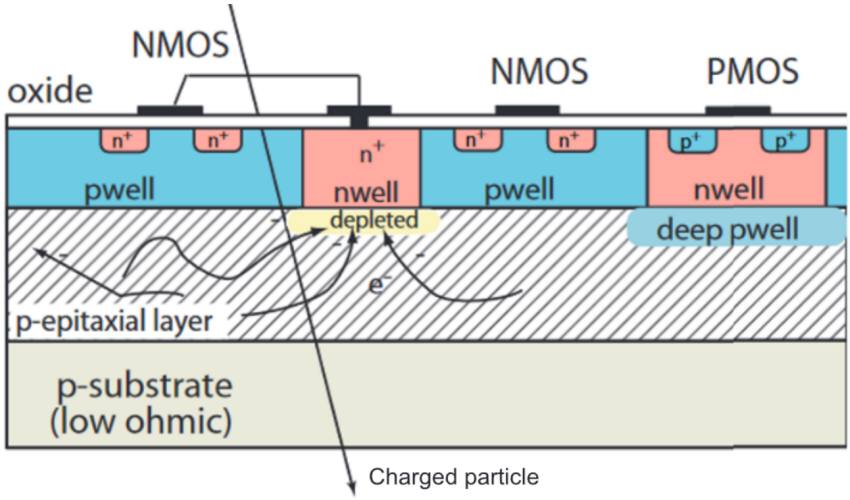

Fig. 3.10 Scheme of the cross-sectional configuration of a CPS sensor commonly called MAPS. Adapted from [71]

the voltage drop is amplified. This technology has the potential to reach a pixel size below the 10×10 µm^2, which would allow for excellent position resolution while maintaining sufficient radiation tolerance and low power dissipation. They are employed primarily in ion collider experiments, such as the STAR experiment at RHIC [72].

Due to the thin epitaxial layer of around 10–40 µm, the CPS can achieve a very low material budget and, as it can be operated at room temperature, additional cooling systems are not required. The implementation of high resistivity to the epitaxial layer in CMOS processes has allowed the charge collection time and radiation tolerance to be improved to 1×10^{15} n_{eq} cm^{-2}. The CPS technology has been implemented in the so-called MIMOSA-28 suitable for the STAR-PXL detector, consisting of a pixel array of 960×928, a pixel pitch of 20.7×20.7 µm and capable of a spatial resolution of 3.6 µm and a time resolution of 185.5 µs [73].

The principal disadvantage of CPS technology is that while the n-type transistors (NMOS) can be situated within the active area, the p-type transistors (PMOS) must be isolated by n-wells that could act as parasitic anodes. This has the effect of affecting the read-out response and limiting the capabilities of the integrated circuit. Moreover, CPS display a slow readout when compared to alternative technologies utilized in timing applications.

3.2.3 High Voltage CMOS

For high-rate, high-radiation environments (such as the LHC environment), fast and complete collection of charge by drift in an electric field is required. To achieve this, a new technology

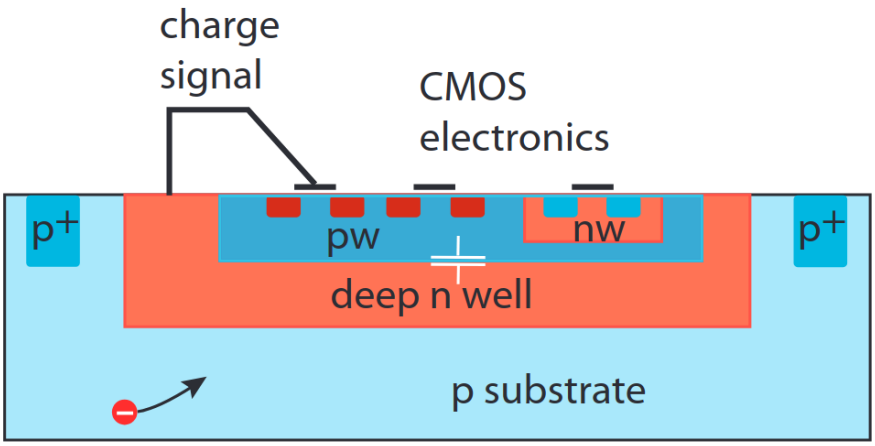

Fig. 3.11 Scheme of the cross-sectional configuration of an HV-CMOS. a deep n-well is required for both the collection electrode and to protect the electronics from the applied high voltage (HV). Adapted from [74]

has been implemented that allows higher voltages to be applied, so that the depletion region below the collection electrode can be increased to around a typical range of 25–150 µm to provide a sufficiently large and fast signal in the so-called depleted MAPS, "DMAPS" [74].

It was also necessary for this technology to provide multiple wells to allow shielding of the wells from charge, and to provide full CMOS circuit functionality by decoupling the use of both NMOS and PMOS transistors decoupled from the substrate. This variant of the sensors based on CMOS technology then comprises a CMOS circuit integrated in an HV deep n-well. This technology allows the implementation of CMOS in the pixel electronics, facilitating the production of fast and radiation tolerant sensors with a good signal-to-noise ratio. The embedded electronics can include a charge amplifier, shaper, comparator and other components.

These sensors are capable of achieving high spatial resolution of about 4 µm and maintaining good performance even after irradiation at fluences of $1 \times 10^{15}\,\mathrm{n_{eq}\,cm^{-2}}$ [75]. The main disadvantage of this technology is the considerable crosstalk generated by the active CMOS logic gates and other integrated electronics. Figure 3.11 is the cheme of the cross-sectional configuration of an HV-CMOS.

HV CMOS sensors are typically reverse biased at voltages above 60 V, the depletion zone is either created from the top surface only or, by applying backside processing. Also, due to the average drift distance that the charges needed to reach the collection electrode is short and the trapping probability is therefore reduced, the Radiation tolerance is also enhanced in this type of sensors.

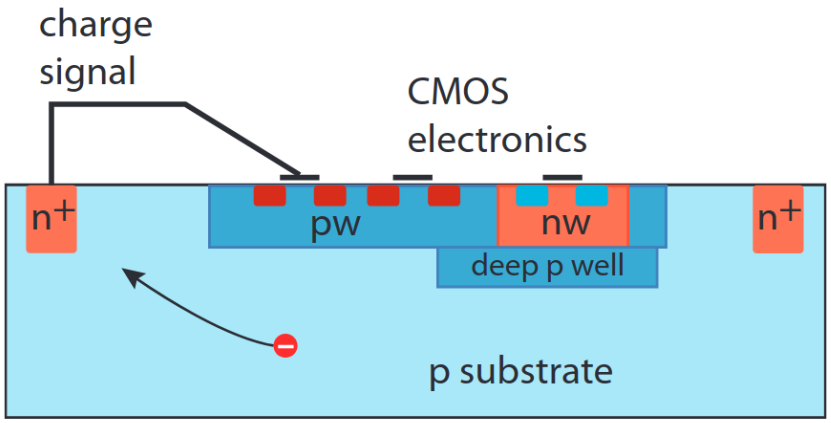

Fig. 3.12 Cross-sectional configuration of a small charge collecting electrode variant of a DMAP. Adapted from [74]

Figure 3.12 shows an alternative design that includes a small charge collection electrode (n well) apart from the CMOS electronics, allowing a very small collection capacitance of only 5–20 fF, which is desired to improve noise and timing performance. However, radiation tolerance is more difficult to achieve than in the design of Figure 3.11, as the average drift distances to the collector are longer for the same pixel cell size, resulting in a higher probability of trapping. Therefore, small pixel sizes are preferred for small electrode designs.

Chapter 4

Experimental methods

In this chapter, we delve into the various experimental setups, functional principles and characterisation techniques, emphasizing those conducted at the Instituto de Física de Cantabria (IFCA) and test-beam facilities employed during different sensors characterisation campaigns. These experimental setups are:

- Electrical Characterisation: This technique involves analyzing the electrical properties of the devices. Measuring parameters such as current-voltage and capacitance-voltage characteristics to understand the behavior of the devices.
- Radioactive Source setup: In this method, a radioactive source is used to study the interactions between radiation and the material and extract valuable information about its response.
- Laser illumination characterisation, using the Transient Current Technique (TCT) . Involves exposing a sample to a laser light and measuring the resulting transient current response. This technique provides insights into charge carrier, and can be used to study the sensor jitter.
- Test-Beam Characterisation: Use particle beams to probe the response of detectors. Test-beam facilities allow precise measurements of sensors performance.

Additionally, the chapter covers common data processing and analysis methodologies related to these experimental techniques. These methods play a crucial role in extracting meaningful information from the collected data to study the sensors response and their radiation tolerance after being irradiated in dedicated facilities. Overall, the chapter provides a comprehensive overview of the tools and approaches used for characterisation.

4.1 Data acquisition system

All the data acquisition (DAQ) systems employed in this thesis have a similar read-out structure. The sensor's analog signal is conditioned using an analog front-end, which may include an amplification stage. The conditioned analog signal is digitized by a high-bandwidth Digital Store Oscilloscope (DSO). The resulting digitized waveform data is then transferred to a personal computer (PC) via high-speed interfaces such as Universal Serial Bus (USB) or Ethernet for further analysis, storage, and visualization using a dedicated software application running on a PC.

The DAQ system is further complemented by a set of instrumentation, including: trigger logic for event selection; power supplies for biasing the devices under test and the front-end electronics; as well as additional equipment for environmental monitoring (such as temperature or humidity sensors); and motorized displacement stages, all of which are controlled or read-out via field buses such as General-Purpose Instrumentation Bus (GPIB) or USB, enabling comprehensive control and integration of the entire measurement setup.

4.1.1 Signal conditioning: high-bandwidth low-noise amplifier

The devices under test were mounted in passive printed circuit boards (PCB) designed at CERN (PCB version 15) and adapted at IFCA (PCB version 16) in where the LGAD sensors are attached and wire-bonded to provide the connectors required for read-out and a terminating resitor of 50 Ω. The sensor can be then connected to an amplifier for signal conditioning.

When we characterise silicon sensors, one of the main objectives is to obtain information about their signal response, but usually this response signal is very weak, even more so in the case of timing applications where the thickness of these silicon LGADs are intended to be about 50 µm, and therefore we need to use an amplifier stage to properly monitor and store the data for later analysis. To successfully characterise the time resolution, which is a critical parameter to satisfy, it requires large signals with short rise time and minimal noise. Therefore, the amplifier should have low noise, reduced jitter (see subsection 4.2.4), high gain and sufficient bandwidth to accept fast pulse responses and a wide dynamic range.

The chosen CIVIDEC C2-TCT Amplifier [76], has an integrated "Bias-Tee" that is a device that allows both biasing and read-out through a single line, effectively decoupling the High Voltage (HV) required for the sensor from the readout response. This amplifier, characterised by its low noise current gain, has an analogue bandwidth of 10 kHz - 2 GHz and a nominal gain of 40 dB. This amplifier has the following connections:

- +12V connector, for powering the amplifier.

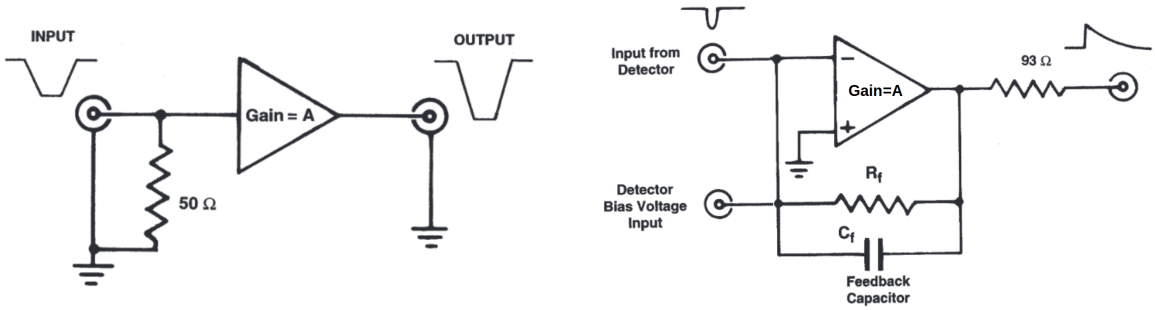

(a) Current-Sensitive amplifier (b) Charge-Sensitive amplifier

Fig. 4.1 Simplified schematic of a Current-Sensitive amplifier (a), and a Charge-Sensitive amplifier (b). The main elements of both amplifiers can be seen.

- HV connector, for the biasing, sourced by a sourcementer.
- IN connector, that directs the HV for biasing the sensor and receives its response.
- OUT connector, for transmitting the response signals to the oscilloscope.

There are two common amplifiers used for silicon sensor characterisation: current-sensitive and charge-sensitive. In the first case, the output voltage is proportional to the rate of change of the charge signal with respect to time, and in the case of charge-sensitive amplifiers, this voltage output is proportional to the charge signal [77]. In Figure 4.1 The schematics of both types of amplifier are shown in a simplified form [78].

4.1.1.1 Current-sensitive amplifiers

In this type of amplifier a properly terminated 50 Ω input impedance of the current-sensitive amplifier converts the current pulse from the detector to a voltage pulse. If the rise time of the amplifier is negligible compared to the detector rise time, and the voltage gain of the amplifier is A, with I_{in} being the amplitude of the current pulse from the detector, the amplitude of the voltage pulse at the amplifier output will be:

$$V_{out} = 50 I_{in} A \tag{4.1}$$

In this current sensitive amplifier (Figure 4.1 (a)), the dominant factor limiting timing resolution is the fluctuation in transit times of electrons as they cascade through the detector. This results in a jitter in the arrival time of the pulse at the detector output. However, in instances where the detector signals are sufficiently weak to necessitate the use of a current-sensitive amplifier, it is imperative to consider the impact of amplifier input noise on time resolution.

4.1.1.2 Charge-sensitive amplifiers

The charge sensitive amplifier (Figure 4.1 (b)) has a parallel resistor and capacitor to form the feedback of the amplifier, but in this type the resistor prevents the saturation of the amplifier output and the amplification is mainly determined by the feedback capacitor and the integration of the current in this capacitor allows the output to be proportional to the charge signal.

As previously discussed, the primary parameters of interest in most applications are the charge and the Time of Arrival (ToA). A charge-sensitive amplifier can provide either or both of these parameters. It integrates the charge on the feedback capacitor, making its gain unaffected by alterations in detector capacitance. Ideally, the output pulse's rise time matches the width of the detector's current pulse. The amplifier's output voltage possesses an amplitude V_o, and a decay time constant τ_f which are given by:

$$\begin{aligned} V_{out} &= \frac{Q_D}{C_f} \\ \tau_f &= R_f C_f \end{aligned} \tag{4.2}$$

Here, Q_D represents the charge discharged by the detector, C_f denotes the feedback capacitor, and R_f signifies the feedback resistor.

4.1.1.3 Amplifier gain

It is important to note that the performance of an amplifier is not constant across all signal frequencies. Therefore, it is necessary to measure the amplifier's output power, or more commonly, output voltage against frequency [79]. This results in a graph known as a response curve, which displays the relative output throughout the amplifier's operational frequency band. Typically, response curves employ a logarithmic frequency scale on the x-axis. This approach accommodates a broader frequency range than a linear scale would permit. The vertical y-axis uses linear divisions but employs the logarithmic units of decibels. The one-tenth of a Bel unit was initially created for quantifying telephone cable losses, now is the preferred logarithmic unit for most electronic applications.

The gain at various frequencies are compared to a specific reference frequency called the mid-band frequency. The difference at the mid-band frequency and any other measured frequency is also expressed in decibels, either greater (+dB) or lesser (-dB) than the mid-band frequency, which is assigned a value of 0dB.

The conversion of a power gain ratio to dBs involves multiplying the log of the ratio by 10:

$$Power(dB) = 10\log\left[\frac{P_2}{P_1}\right] \tag{4.3}$$

with P1 being the power at mid-band, and P2 the measured power.

Decibels are suitable for comparing an amplifier's output at different frequencies since all output power or voltage measurements are taken across the same impedance. It's widely accepted to describe voltage gain in decibels [80] and the conversion of voltage ratios to dBs uses $P = V^2/R$:

$$\begin{aligned} dB_v = 10log\left[\frac{V_2^2/R}{V_1^2/R}\right] = 10log\left[\frac{V_2^2}{V_1^2}\right] = 10log\left[\frac{V_2}{V_1}\right]^2 \\ dB_v = 20\log\left[\frac{V_2}{V_1}\right] \end{aligned} \tag{4.4}$$

and in the same way for current ratios, using $P = I^2R$:

$$\begin{aligned} dB_i = 10log\left[\frac{I_2^2R}{I_1^2R}\right] = 10log\left[\frac{I_2^2}{I_1^2}\right] = 10log\left[\frac{I_2}{I_1}\right]^2 \\ dB_i = 20\log\left[\frac{I_2}{I_1}\right] \end{aligned} \tag{4.5}$$

Following this relation, we can know that the nominal gain of the CIVIDEC C2-TCT amplifier of 40 dB delivers a gain factor 100, which also has been confirmed experimentally:

Measurements were taken on an FBK LGAD without an amplifier and after with the CIVIDEC amplifier connected in order to calculate the gain of the system in a real environment and, importantly, at the real operating frequency. Figure 4.2 shows the comparison of the measurements of an LGAD in the TCT setup (see Figure 4.21), calculated for two data sets: without (a) and with amplifier (b), and then calculating the gain of the amplifier by dividing the amplitude of the amplified pulses by the non-amplified, at different bias voltages after the depletion (above 50 V) of the sensor and before the breakdown (less than 160 V) depicted in (c). The calculated gain factor remains close to the nominal gain factor of 100.

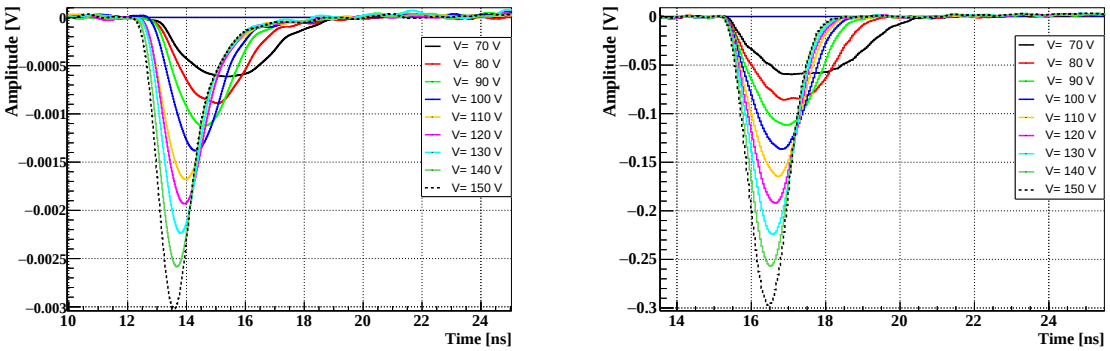

(a) Waveforms without amplifier

(b) Waveforms with CIVIDEC C2-TCT

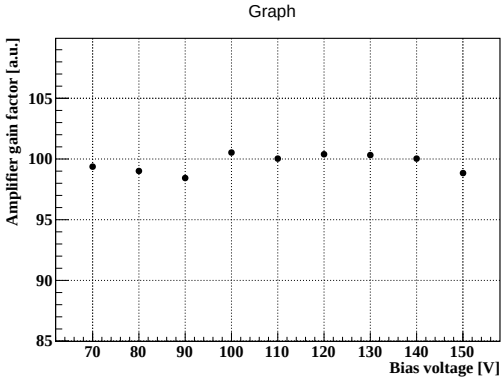

(c) Amplifier gain per different voltages

Fig. 4.2 Waveforms of an FBK LGAD without (a) and with (b) the CIVIDEC amplifier. (c) is the calculated gain at the different voltages.

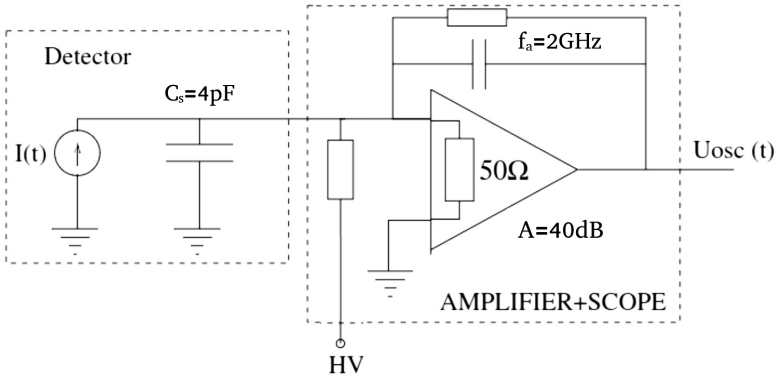

Fig. 4.3 Equivalent circuit of the read-out system with the sensor, amplifier and oscilloscope.

4.1.2 Real-time waveform capture: Digital Storage Oscilloscope

Once the sensor is connected to the amplifier and biased, its response can be monitored in real-time using an oscilloscope, allowing the user to view and record the response as waveforms. In order to achieve the optimal waveform capture, it is essential to be aware of the main parameters of the oscilloscope.

The sampling rate of a digital oscilloscope determines the level of accuracy of the signal, that is, how many samples an oscilloscope can capture, usually expressed in gigasamples per second (GS/s).

The "bandwidth" refers to the range of frequencies that it can consistently capture. An oscilloscope with a wide bandwidth and fast rise time (see subsection 4.2.3) signal processing is excellent for applications that require precise timing analysis, such as those performed in LGADs. The resolution of an oscilloscope is the ability to detect and display subtle changes in a signal by dictating the smallest voltage rise that can be faithfully displayed [81].

The oscilloscope used to make the sampling of the waveforms is a Digital Storage Oscilloscope (DSO) YOKOGAWA DL9140 [82], that is a digital oscilloscope with basic performance that features 4-channel analog input, a maximum sampling rate of 5 GS/s, a maximum frequency bandwidth of 1 GHz, and a maximum recording length of 6.25 MWord. This oscilloscope have active probes capable of observe signals with frequencies higher than 500 MHz and can continuously acquire waveforms at a maximum trigger rate of 9 kHz.

The threshold level set in the oscilloscope will depend on the relation of the amplitude of the pulses, as a guide we can consider that the threshold have to be about three times higher than the baseline noise level. For example in most of the cases, when characterising LGADs with an amplifier of 40 dB, the baseline noise in our setups are of about 3 mV, that means that a threshold level of 10 mV should be enough to take optimal data.

The resulting equivalent circuit of the read-out system, including the sensor, amplifier and oscilloscope can be seen in Figure 4.3. Here the frequency domain of the circuit can be obtained employing the equation to calculate the cut-off frequency [83]:

$$\nu_s = \frac{1}{2\pi R C_s} \tag{4.6}$$

knowing that the capacitance of a full depleted LGAD with area of 1.3×1.3 mm^2 and a width of the active thickness of 50 µm, following Equation 2.11, we calculate the sensor capacitance C_s of about 4 pF, and using $R = 50\,\Omega$ as the input impedance of the equivalent circuit, we obtain that the cut-off frequency of the circuit $\nu_s = 795$ MHz that is less than the cut-off frequency of the amplifier of 2 GHz and less than the bandwidth of the oscilloscope of 1 GHz.

4.1.2.1 Oscilloscope comparison

To ensure that the data sampling was optimal enough to use for the timing characterisation of the LGADs, a comparison was made with another oscilloscope, using a Tektronix MSO70404C Mixed Signal Oscilloscope (MSO), which supports features such as a frequency bandwidth of 4 GHz, 25 GS/s on its 4 analogue channels, and low noise and jitter for timing analysis [84].

The comparison of the measurements of a CNM LGAD using the two oscilloscopes was made in the radioactive source setup (see section 4.5), using the same configuration in both oscilloscopes, such as the same number of points to be sampled, threshold level, vertical resolution and time scale. After filtering the waveforms (see section 4.2) from the two datasets, 801 events from the Yokogawa oscilloscope and 738 events from the Tektronix oscilloscope were processed. The comparison of the averaged waveforms, rise time distributions, amplitude distributions and collected charge (see section 4.2) at different bias voltages for the same LGAD sample is shown in Figure 4.4.

As it can be seen, there is no significant difference between the results obtained by the two oscilloscopes: The amplitude is slightly higher in the Yokogawa by just under a 1 mV; the rise time is different by about 15 ps and the calculated collected charge is also very close between the two results and for the different bias voltages, with a difference of less than 1 fC for the higher bias voltage measured. This exercise was carried out on three different samples, each measured at different bias voltages, and a similar behaviour was found for all results. As previously demonstrated, both oscilloscopes are equipped with the requisite capabilities to ensure accurate characterisation during characterisation campaigns.

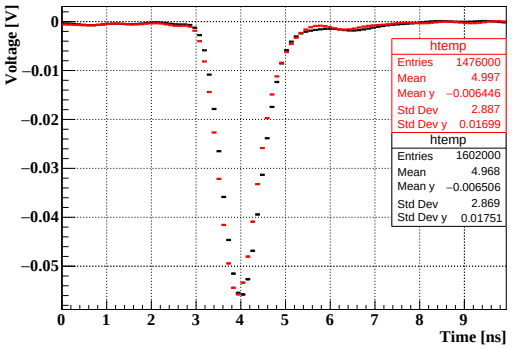

(a) Waveform comparison at 185V

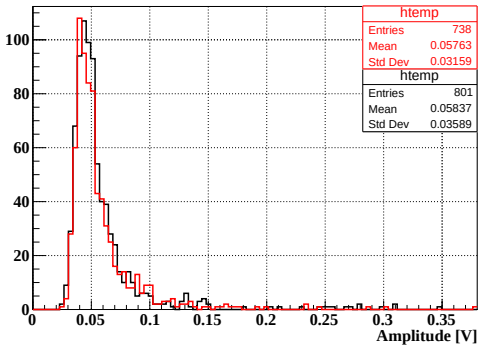

(b) Amplitude comparison at 185V

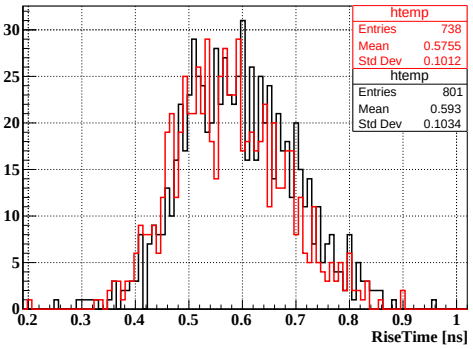

(c) Rise time comparison at 185V

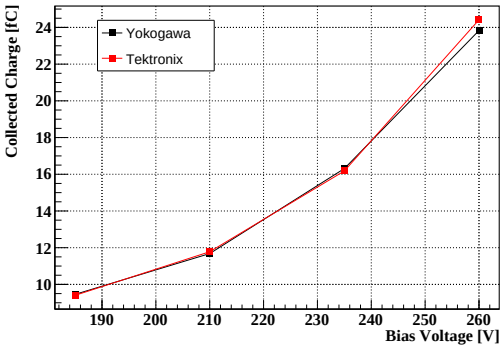

(d) Collected charge at different bias

Fig. 4.4 Comparison of the Yokogawa (black) and Tektronix (red) oscilloscopes for the waveform profile (a), amplitude (b), rise time (c) and collected charge (d) from an CNM LGAD.

4.1.3 Data acquisition software

The data acquisition interface is managed by a computer software. This computer is connected to all the instruments and allows them to be controlled by special software developed at IFCA. This software allows automated data acquisition, programming of different bias voltages and other characterisation parameters such as the number of waveforms to be recorded, trigger delay, sampling rate and setting of a current compliance. This software is also used to move the axis motor stages to properly focus the laser beam in the case of the TCT setup (see section 4.4).

Once the data has been taken, it can be processed to obtain the different parameters that are the main objectives of each characterisation campaign. Most of the analyses were carried out using the software based on the open-source data analysis framework *CERN Root* [85], such as *TRICS* [86] and *CVIV 101* [87], both developed within the IFCA High Energy and Instrumentation Group [88].

4.2 Waveform processing

Once the data have been stored from the different setups, they can be read using the *TRICS* software, which converts the data file (which may be in most text formats) to a root "tree" class (a list of independent columns called "branches") that contains both a "branch" with the raw events and a "branch" with the waveforms processed with the variables needed to perform the data analysis. In order to analyse the raw data correctly, it is necessary to filter the events that pass certain filters based on the parameters that are to be studied. This is done in order to ensure good quality in the results.

After the data file has been converted to a root format, it is possible to plot the key parameters described below. This allows for a second conversion to root format with the filtered events, after which the data analysis can be continued. In the case of the radioactive source setup, since data are taken in a three-sensor stack (see section 4.5), the data filtering should be conducted independently for each of the three channels (one per sensor of the stack). However, when reprocessing the root file, only those events that pass the cuts in the three channels will remain. The *TRICS* software is designed to store the results of the filtering process in a configuration file which is readable by the software, which executes the cuts. Additionally, this configuration file enables the user to set, enable, disable, or modify a number of other variables that are crucial to the analysis.

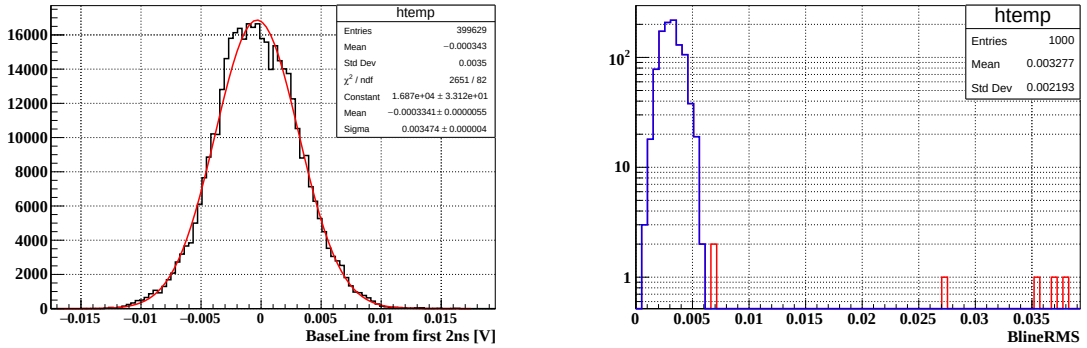

(a) Distribution of the first 2 ns of the waveform (b) Distribution of the BaseLine RMS

Fig. 4.5 Distribution of the BaseLine of the waveform taken form the first 2 ns (a) and the distribution of the BaseLine RMS showing in the red the events that are outside the expected range of noise and in blue the distribution after applying cuts in noise. Events from one non-irradiated sample from CNM Run15973 at 110 bias voltage.

4.2.1 BaseLine noise

The baseline noise can be extracted from the selected first nanoseconds of the waveform, as this region is devoid of signal information. Figure 4.5 (a) shows the distribution of the first 2 ns that corresponds to the BaseLine. This BaseLine noise includes the noise of the sensor itself and the contribution of the setup electronics. For each event recorded, we can compute its effective value, the root mean square (RMS) of that region (BaseLine RMS), and then visualise this distribution of BaseLine RMS as in Figure 4.5 (b). Using the central limit theorem, this BaseLine RMS noise can be approximated by a Gaussian distribution [89]. With the BaseLine RMS we can then set a cut level to ensure that noisy events from many different sources outside the expected parameters are removed.

This filtering on the basis of the BaseLine noise also removes events caused by electromagnetic noise that exceeds the threshold set in the data acquisition phase and that, in most cases, does not represent a true triple coincidence of the three sensors in the "stack" of the radioactive source setup. This procedure should be done for the three channels corresponding to a different sensor and for all the bias voltage steps recorded in the dataset.

4.2.2 Amplitude

The amplitude of the waveform is defined as the maximum voltage measured of every waveform. As the BaseLine noise is added to the signal pulse, the amplitude should be calculated after correcting for the BaseLine noise, this can be done by subtracting the BaseLine mean from the amplitude, for all waveforms.

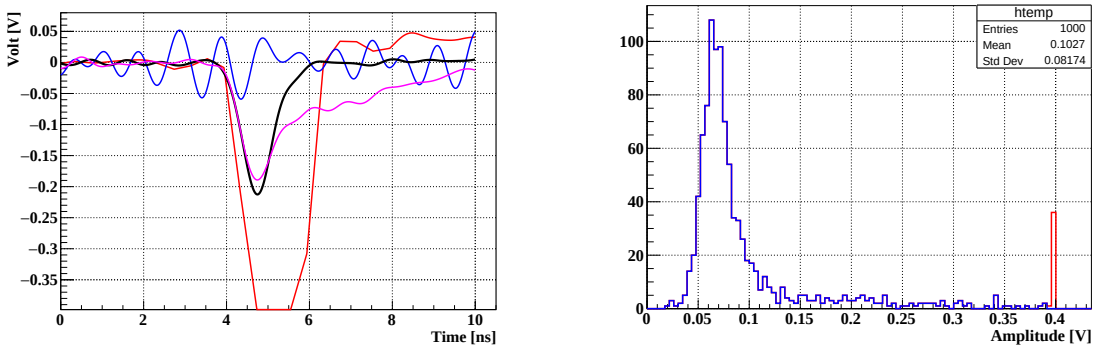

(a) Waveforms from the RS setup

(b) Distribution of amplitudes

Fig. 4.6 Plot (a) shows an example of the expected waveform (black), a waveform with micro-discharges (pink), an amplitude-saturated waveform (red) and electromagnetic noise (blue). Plot (b) is the distribution of amplitudes corrected by the baseline, showing in red the total number of events recorded and in blue the events after filtering out these "saturated" events.

Because the amount of charge deposited by the particles in each sensor is different (in the case of the radioactive source characterisation), in some cases there will be waveforms recorded that do not match the expected behaviour. To illustrate this, Figure 4.6 (a) shows in red a waveform with an amplitude greater than the selected vertical resolution in the scope, these saturated amplitude waveforms must be discarded to avoid miscalculating the amount of charge collected; in pink there is a waveform that has an increase in its current and pulse duration attributable to the presence of "micro-discharges" [90]; in blue there is an example of electromagnetic noise, and in black is an example of an expected waveform. To visualise the saturated amplitude waveforms, we can plot the amplitude distribution of the waveforms as in Figure 4.6 (b).

The aforementioned amplitude filtering must be implemented for all three sensors and for all bias voltages. However, the occurrence of a saturated event, noisy events, or the presence of micro-discharges in one sensor will result in the rejection of that event across all three channels.

4.2.3 Rise time, slew rate and signal-to-noise ratio

From the waveforms, it is possible to extract the main parameters used in the analysis of time resolution of electronic devices, such as the slew rate (SR), which represents the rate of change of the voltage amplitude of the signal over time: $\frac{dV}{dt}$ that is determined by the gradient of the pulse.

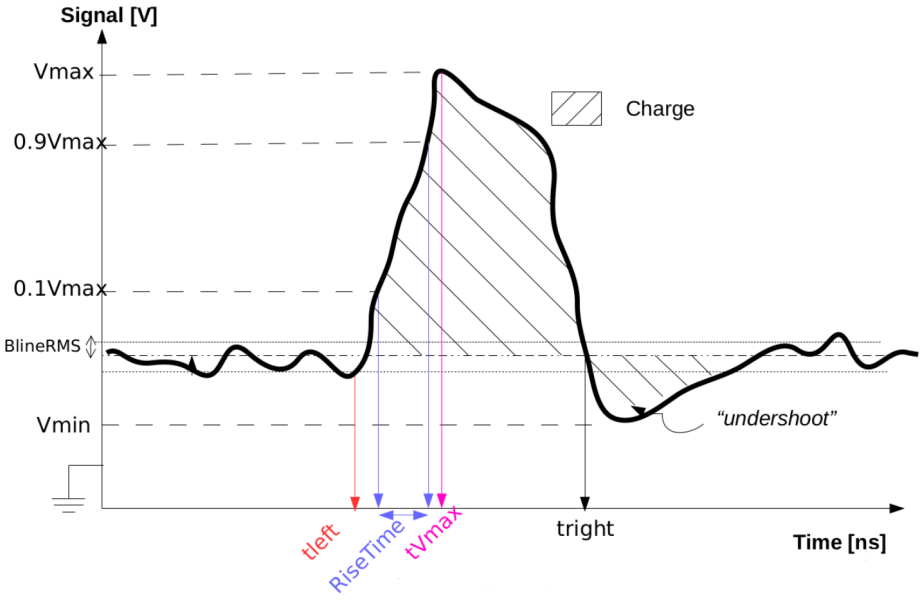

Fig. 4.7 Sketch of a waveform to illustrate the most commonly used parameters in waveform processing: Amplitude, Rise Time, Charge, Baseline (Bline). Sketch adapted from [92]

The rise time (RT) is defined as the time taken for a signal to change from a specified low value to a specified high value. It is typically expressed as a ratio or percentage [91]. In the field of electronics, these percentages are typically expressed as 10% and 90% of the signal amplitude S. RT is a fundamental parameter in high-speed electronics, as it is a measure of a circuit's ability to respond to fast input signals. The SR can thus be expressed in terms of the RT and the amplitude of the signal S as: $SR = S/RT$.

The signal-to-noise ratio (SNR) is a measure of the relative amount of signal and noise present in a waveform. As the name implies, it is simply the ratio and is an important parameter that affects the performance and quality of systems that process signals. A high SNR indicates a clear and easily discernible signal, whereas a low SNR suggests a signal that is more susceptible to noise and may be challenging to distinguish. Signal-to-noise ratio (SNR) can be enhanced through a variety of techniques, including the amplification of the signal, which is a common approach employed by LGAD sensors.

Figure 4.7 illustrates the common parameters that can be calculated from the waveform processing. It can be observed that the main pulse is used to calculate the amplitude, which reaches a maximum voltage, designated here as "Vmax". The BaseLine, designated as "Bline," is also depicted, as is the so-called "undershoot" from which the minimum "Vmin" is determined. Furthermore, the values of "tleft," "tVmax," and "tright," which can be obtained from the matching values in time, are illustrated. Finally, the SR, RT, and SNR can be calculated from these parameters.

4.2.4 Sensor jitter

Statistical (Landau) and noise fluctuations represent significant sources of timing fluctuations. These fluctuations are amplitude-dependent variations in time resolution, resulting from the fact that the signals do not always trigger at the same point. This phenomenon is referred to as sensor jitter.

Sensor jitter can be calculated using the adapted TCT setup described in subsection 4.4.2. This setup employs a split signal from the laser to illuminate the sensor, which is then recorded as a waveform containing a double peak. This is illustrated in Figure 4.8.

In this configuration, the measurement of two signals from the same laser shot and the recording of both pulses on the same oscilloscope channel and in the same event eliminates the external sources of jitter, including those from the oscilloscope, laser, or amplifier. The difference between the two pulses is calculated, leaving only the sensor jitter as the main contribution to the time resolution in this setup. Sensor jitter is then defined as the variance of the threshold crossing time due to noise variations, and divided by $\sqrt{2}$ according to the procedure of Equation 4.7.

The time difference of the two pulses $\Delta_t = t_1 - t_2$ is used to compute the σ that is proportional to the jitter of the sensor that give us:

$$\begin{aligned} \sigma_{\Delta_t}^2 = \sigma_1^2 + \sigma_2^2 = 2\sigma_t^2 \\ \sigma_t = \frac{\sigma_{\Delta_t}}{\sqrt{2}} \end{aligned} \tag{4.7}$$

Due to the noise nature of the sensor jitter, it is also proportional to the following relationships:

$$\sigma_t = \frac{\sigma_n}{\frac{dV}{dt}|_{V_T}} = \frac{N}{SR(T)} \tag{4.8}$$

Wherein, $\frac{dV}{dt}$ represents the slew rate (SR), and N is the noise. Using the relation $SR = S/RT$, and finally using $SNR = S/N$, we can reformulate Equation 4.8 as:

$$\frac{N}{SR(T)} \sim \frac{N}{\frac{S}{RT}} = \frac{RT}{SNR} \tag{4.9}$$

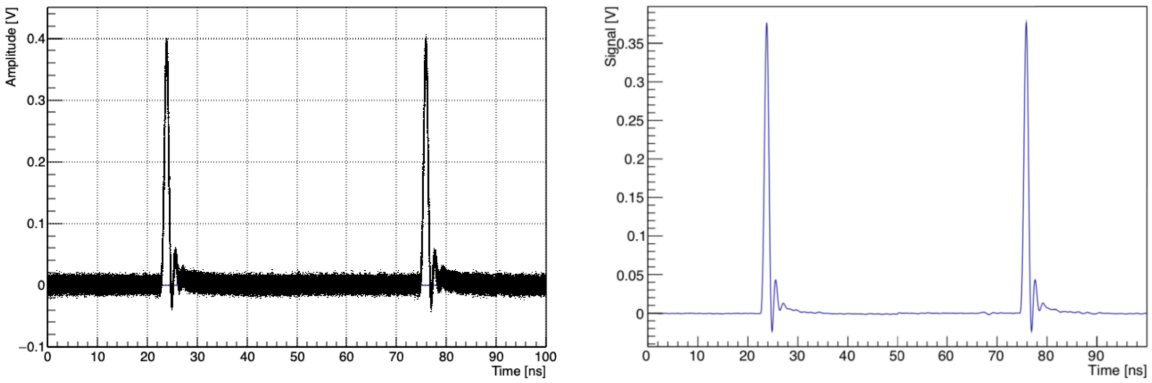

(a) 1000 double pulse waveforms (b) Averaged double pulse waveform

Fig. 4.8 Figure (a) depicts the amplitude versus time plot of 1000 non-averaged shots taken at 150 volts for a LGAD (W11-DB10). Figure (b) represents the average of those 1000 events. It is notable that the second pulse occurs approximately 52 nanoseconds after the first pulse.

This equation is significant because it emphasises that sensors can be fine-tuned for timing applications by reducing their time resolution by reducing their RT or increasing their SNR. This is exemplified in the case of the LGADs, as discussed in section 2.3.

4.2.5 Time-walk correction

The time-walk is a delay that occurs when pulses of different amplitudes cross a fixed threshold at different times. This is because larger amplitude pulses reach the threshold earlier than smaller ones, even if they were emitted at the same time [93]. This can introduce inaccuracies in time measurement systems, especially those that rely on precise timing information.

The Constant Fraction Discriminator (CFD) is a time pickoff technique designed to ascertain the arrival time of an event, irrespective of its amplitude. This method is analogous to the mathematical procedure of locating a maximum by identifying the zero of its derivative. Given that signal pulses possess similar rise time and peak shapes, the CFD enables triggering based on a constant fraction of the total peak height rather than a fixed threshold. This approach mitigates the effects of time-walk and results in trigger times that are independent of peak heights, as can be observed in Figure 4.9.

The operational principle of the CFD hinges on the detection of the "zero-crossing" point of a combined pulse (in electronics it is easier to find the time when the pulse crosses zero), which is derived through the following sequence of steps:

1. The signal is partitioned into three components: Input, Delay, and Fraction. The Fraction component results from an attenuation factor denoted by k.

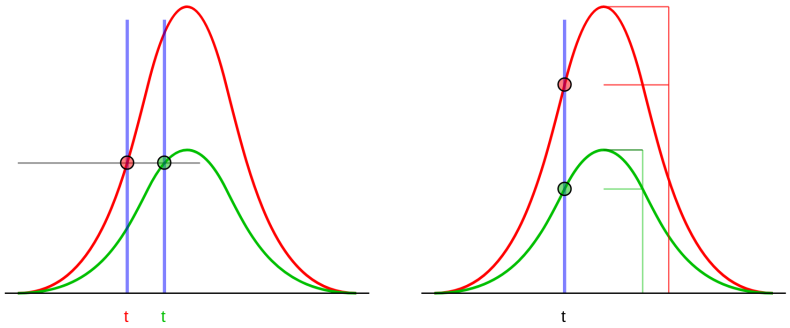

Fig. 4.9 Comparison between the time of arrival of two pulses (green and red) using a time over threshold (left) and a Constant Fraction Discrimination (right). The time-walk effect can be observed in the left plot.

2. One of the components is inverted, typically the Fraction component, as indicated by the negative sign of the k factor.

3. The attenuated and delayed signals are then combined through an addition operation.

4. A trigger is generated when the resulting combination intersects zero, a point referred to as the zero-crossing point (In other cases without inverting any signal, the trigger is generated when the Delayed and Attenuated signals intersect).

The CFD ensures a consistent trigger time, regardless of the amplitude of the input signal. The *TRICS* software has a built-in CFD algorithm that provides the peak time of the event pulses for different values of the attenuation factor k, from 0.1 to 0.9 in decimal increments. This CFD algorithm is available in *TRICS* for TCT and RS setup datasets.

4.2.6 Charge collection

After the data taking and filtering of the many events recorded, we can extract the information about the sensor like the collected charge of the sensor as a result of the crossing MIPs. The collected charge of a sensor can be determined by integrating the current of all the waveforms recorded, over the time duration of the pulse:

$$Q_{tot} = \int_{t_1}^{t_2} I(t)\,dt \tag{4.10}$$

Where the start and end times of the pulse, designated as t_1 and t_2, respectively, are to be considered. It should be noted that the current in question must be determined from the waveform, taking into account the resistive termination connected to the passive printed

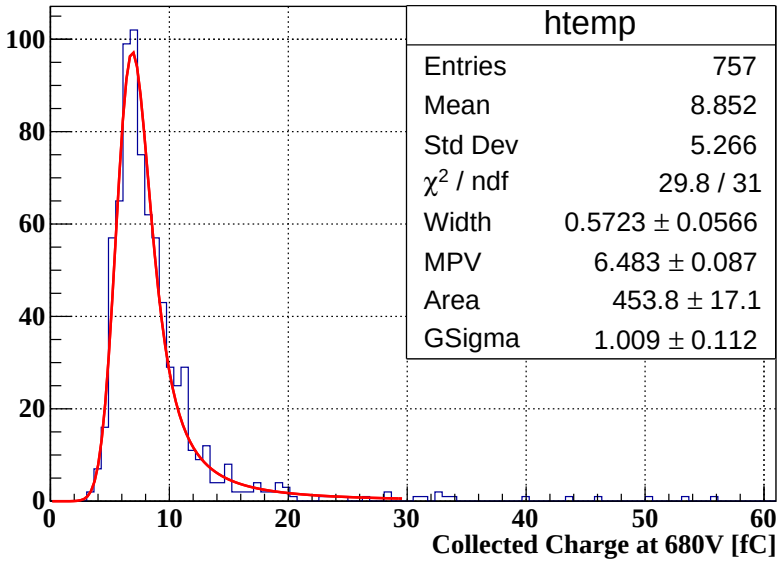

(a) Collected charge.

Fig. 4.10 Distribution of collected charge calculated from the integration of the waveforms of an LGAD biased to 680 V. The Most Probable Value (MVP) can be extracted from the convoluted Gauss-Landau fit.

circuit board (PCB) with a resistance of 50 Ω and the amplifier's gain factor, which in this case is 100. Consequently, the calculation of the collected charge is as follows:

$$Q_{collected} = MPV \left(\frac{\int_{t_1}^{t_2} V(t)\, dt}{Gain_{amp} \times 50\,\Omega} \right) \tag{4.11}$$

The total charge distribution for a single detector is fitted by convoluting a Landau function with a Gaussian, and the Most Probable Value (MPV) of this distribution serves as an estimate of the charge collected. Figure 4.10 depicts the distribution of the calculated collected charge resulting from the integration of the waveforms acquired in the radioactive source setup. The convoluted Gauss-Landau fit is depicted in red, and the MVP value is taken as the collected charge value.

4.2.7 Time resolution

From the radioactive source setup data, we can calculate the Time of Arrival (ToA) that is determined as the moment a pulse crosses a certain threshold. Given that pulses of varying amplitudes will cross a threshold at different times (due to the time walk effect), these arrival

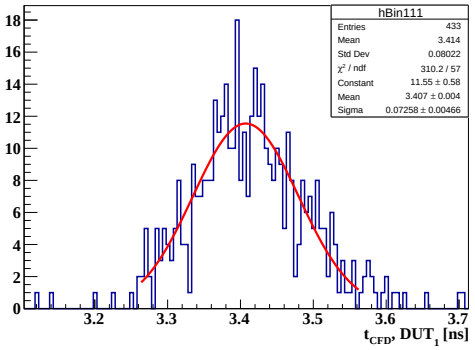

(a) t_{CFD} from DUT_1

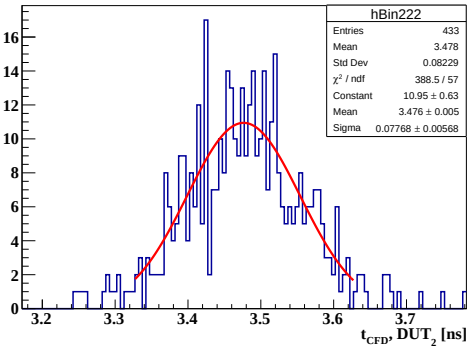

(b) t_{CFD} from DUT_2

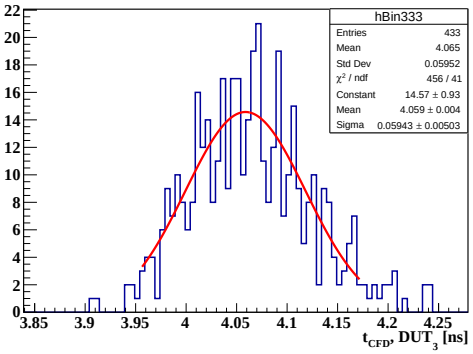

(c) t_{CFD} from DUT_3

Fig. 4.11 Distribution of the arrival time after time-walk correction t_{CFD} for three Devices Under Test (DUT) (a), (b) and (c) from CNM RUN15973 measured in Radioactive Source.

time of the pulses is determined using the Constant Fraction Discrimination (CFD) time pickoff method described in subsection 4.2.5 to determine the time-walk corrected arrival time t_{CFD}. An example of the distributions of t_{CFD} from three different samples arranged in a "3-stack" configuration (see section 4.5) can be seen in Figure 4.11 (a), (b) and (c).

The time resolution of a sensor can be determined by the standard deviation of the distribution of time-of-arrival (ToA) differences relative to a known reference. If such a reference is not available, three detectors can be simultaneously measured [94], and the individual time resolutions σ can be computed from the three pairwise differences: $\Delta t_{1,2}$, $\Delta t_{1,3}$ and $\Delta t_{2,3}$. In Figure 4.12 there are examples of the distributions of these differences.

These distributions are fitted to a Gaussian function and the fitted widths $\sigma_{1,2}$, $\sigma_{1,3}$, and $\sigma_{2,3}$ resulting are utilized to ascertain the time resolution of the three sensors (σ_1, σ_2, σ_3) by solving the corresponding system of equations:

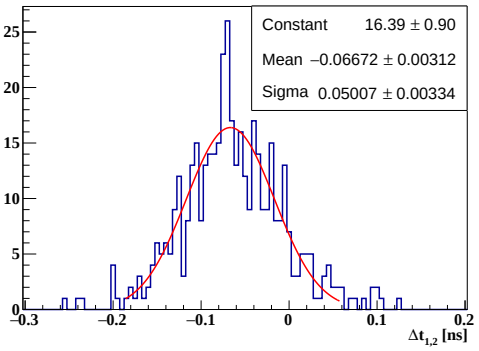

(a) Distribution of $\Delta t_{1,2}$

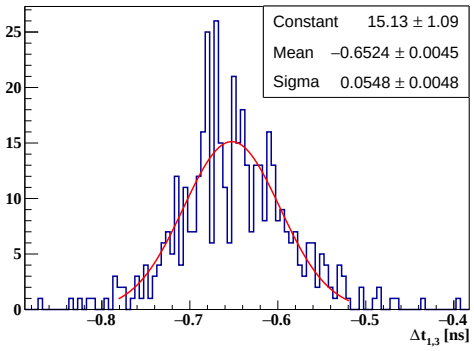

(b) Distribution of $\Delta t_{1,3}$

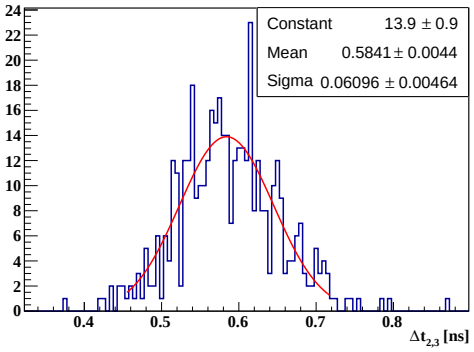

(c) Distribution of $\Delta t_{2,3}$

Fig. 4.12 Distribution of the differences between t_{CFD} from pairs of three samples from CNM RUN15973: pair 1-2 in (a), 1-3 in (b) and 2-3 in (c). These distributions are fitted to a Gaussian function from which the width σ is calculated.

$$\begin{aligned}
\sigma_1 &= \left(\frac{1}{2}(\sigma_{2,1}^2 + \sigma_{1,3}^2 - \sigma_{3,2}^2)\right)^{\frac{1}{2}}, \\
\sigma_2 &= \left(\frac{1}{2}(\sigma_{2,1}^2 - \sigma_{1,3}^2 + \sigma_{3,2}^2)\right)^{\frac{1}{2}}, \\
\sigma_3 &= \left(\frac{1}{2}(-\sigma_{2,1}^2 + \sigma_{1,3}^2 + \sigma_{3,2}^2)\right)^{\frac{1}{2}},
\end{aligned} \tag{4.12}$$

and we can calculate the errors (δ_1, δ_2 and δ_3) using:

$$\begin{aligned}
\delta_1 &= \frac{\left((\sigma_{2,1}\delta_{2,1})^2 + (\sigma_{1,3}\delta_{1,3})^2 + (\sigma_{3,2}\delta_{3,2})^2\right)^{\frac{1}{2}}}{2\sigma_1}, \\
\delta_2 &= \frac{\left((\sigma_{2,1}\delta_{2,1})^2 + (\sigma_{1,3}\delta_{1,3})^2 + (\sigma_{3,2}\delta_{3,2})^2\right)^{\frac{1}{2}}}{2\sigma_2}, \\
\delta_3 &= \frac{\left((\sigma_{2,1}\delta_{2,1})^2 + (\sigma_{1,3}\delta_{1,3})^2 + (\sigma_{3,2}\delta_{3,2})^2\right)^{\frac{1}{2}}}{2\sigma_3},
\end{aligned} \tag{4.13}$$

where $\delta_{i,j}$ is the error in the value $\sigma_{i,j}$.

4.3 Electrical characterisation

The electrical characterisation of the samples is based on the extraction of the main parameters of interest from the different devices when they are operated at reverse bias voltages. This allows the evolution of the sensors' behaviour when biased to be monitored. Furthermore, this characterisation provides a quality control between the different samples of the same production run and is intended to verify that the specifications are met and in concordance with the corresponding detector requirements.

The electrical characterisation is currently conducted within the clean room of the IFCA utilising a probe station. This probe station comprises six needles, three of which are equipped with coaxial connectors for current measurements and three with triaxial connectors for capacitance measurements. To perform the measurements, one needle is required to make contact with the metalisation of the main pad from each device, another needle to contact the Guard-Ring, and a third needle to contact the ohmic contact (backplane) of the device through the chuck of the probe station (see the following sub-section for further details). For this reason, the measurements were only made over single-pad tests in relation to the number

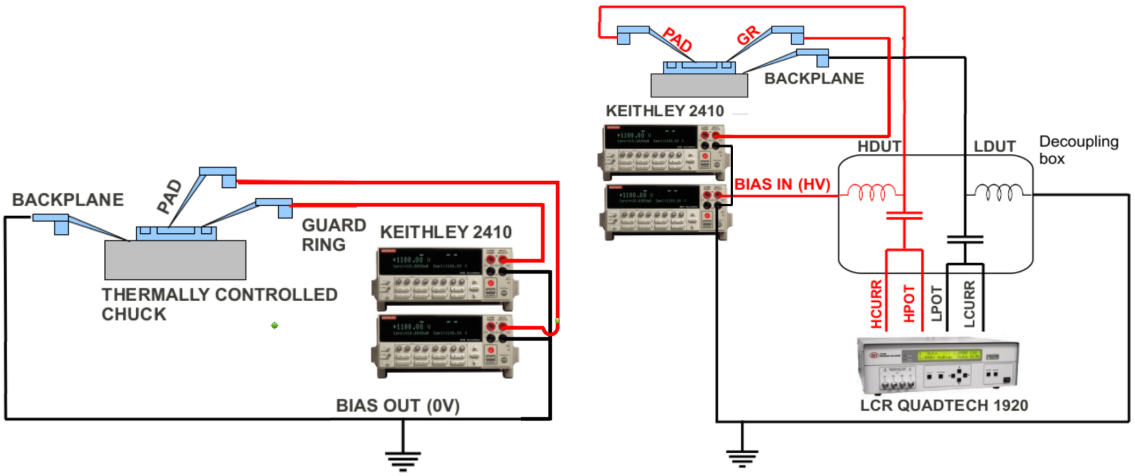

(a) Scheme of the IV setup (b) Scheme of the CV setup

Fig. 4.13 Sketch of the two configurations of the probe-station connections used for the IV (a) and CV (b) measurements at IFCA. Example samples and needles are illustrated in blue.

of pads of the different samples, with the exception of a few devices with an array of 16×16 pads, which were measured in their entirety using an elastomer system developed by the INFN Torino group.

4.3.1 Current-Voltage characteristics

The dark current mentioned in subsection 2.1.4 is measured as a function of the reverse bias voltage to extract the so-called IV curve of the devices. IV curves give us various information about the behaviour of the devices and are important for determining operational parameters by analysing the shape of these curves.

As seen in Equation 2.12, the leakage current is temperature dependent and therefore we need to control the temperature for all these measurements to extract the IV curves. In the case of the probe station, there is a programmable thermal chuck to maintain the desired temperature of the measurements.

In the probe station for electrical characterisation at IFCA, the current is measured using Keithley 2410 sourcemeters [95], which allow the high voltage to be applied to the samples and the current to be measured at the same time. For the IV measurements, the guard-ring and main diode currents were measured independently using two different sourcemeters. The cathode and the guard-ring are connected to high voltage (HV) and the ohmic contact side (backside) of the sensors is connected to ground, according to the sketch of Figure 4.13 (a), which shows the equipment and connections to the samples of the IV setup.

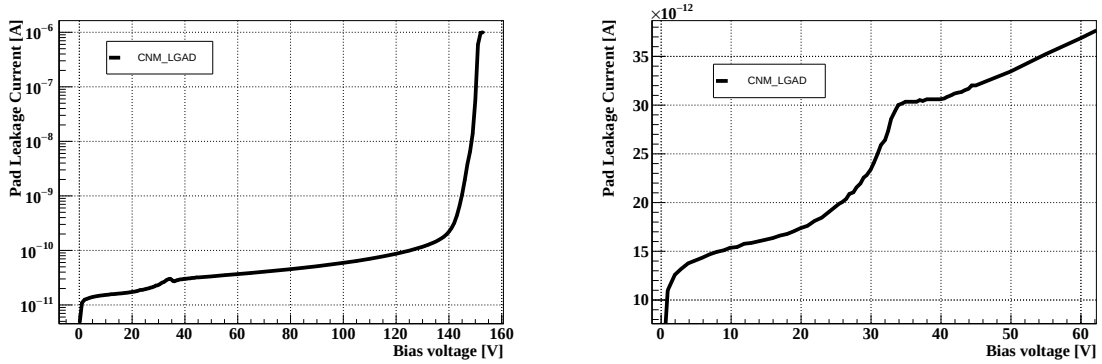

(a) IV curve from an LGAD

(b) Gain-layer region of IV curve

Fig. 4.14 Pad leakage currents as a function of the reverse bias from an LGAD non irradiated. (a) is the complete IV curve untill the breakdown voltage in log scale, and (b) is a zoomed view of the gain layer region in lineal scale.

In Figure 4.14 we can see an IV curve of a non-irradiated LGAD. In (a) the IV curve shows the increase of the dark current of the main pad as the applied bias voltage increases. As this example is an LGAD with a highly doped gain layer, the first voltages are required to deplete this multiplication layer and the amount of leakage current increases rapidly between 0 V and 30 V as we can see in Figure 4.14 (b), which is an enlarged view of this region, then the increase of the current is slower and continues like this until about 300 V, this region being the one that corresponds to the depletion of the bulk, to finally have another rapid increase of the current of orders of magnitude in just a few more volts at about 305 V, indicating the breakdown of the sample (Figure 4.14 (a)).

4.3.1.1 V_{GL} and V_{BD} determination

One of the important parameters that we can extract from the electrical characterisation is the gain layer depletion voltage V_{GL} (only in the case of LGADs or similar devices), which is the voltage required to deplete this multiplication layer. Another important parameter is the voltage at which the breakdown V_{BD} of the device occurs, since the dark current increases rapidly by orders of magnitude in just a few volts.

The aforementioned two parameters can be determined by estimating the changes in slope that the IV curves show with respect to the bias applied. These changes in slope can be determined using a variable called *kbd*, that is the derivative of the current weighted by the ratio of current to voltage Equation 4.14, introduced in [96] initially as an estimator of the breakdown voltage V_{BD} and later adapted [97] to identify the transition between the region corresponding to the gain layer V_{GL} and the bulk region.

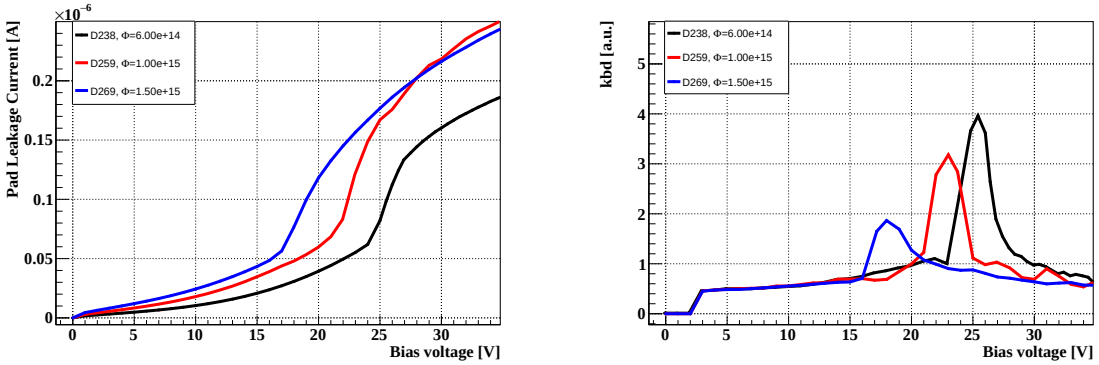

(a) IV curve from CNM samples

(b) *kbd* variable versus bias voltage

Fig. 4.15 IV curve of samples from CNM RUN15246 irradiated at different fluences (a) and its *kbd* of these samples (b). The peak in *kbd* indicates the transition point from the gain layer to the bulk, which is used as the V_{GL}.

$$\text{kbd} = \frac{dI/dV}{I/V} \tag{4.14}$$

This determination of V_{GL} is also used to better characterise the sensors after irradiation, since irradiation deactivates the dopants of the gain layer, as we will see in section 5.1. In Figure 4.15 we can see an example of the IV curves of three samples of LGADs from CNM Run15246 at three different irradiation fluences (a) and the variable *kbd* as a function of the applied bias voltage for the same samples (b). The peaks in the curve of (b) indicate the transition point of the slope caused by the gain layer, which allows us to determine the V_{GL} in this point for these sensors.

4.3.2 Capacitance-Voltage characteristics

The capacitance of silicon sensors behaves in a simplified approximation as a variable capacitance capacitor when the bias voltage is applied, since the depletion width W_{dep} changes as seen in subsection 2.1.4. As with IV curves, CV measurements consist of recording the capacitance of the devices as a function of the reverse bias applied, in order to later evaluate their characteristics. Figure 4.13 (b) shows the connections of the CV setup, which again uses sourcemeters for the HV supply and employs a Quadtech 1920 LCR meter [98], used to read the capacitance of the sensors connected via a decoupling box used to isolate the HV and LCR signals as shown in (b).

The LCR meter, like other instruments used to characterise electronic components, materials and circuits, uses the impedance $|Z|$ [99], which is the opposition that a device

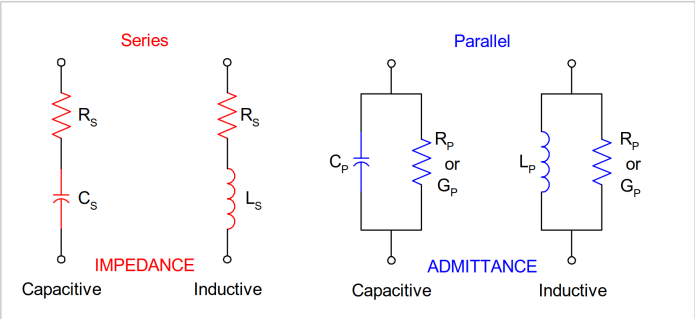

Fig. 4.16 The equivalent circuits for both capacitive and inductive impedances are presented in series and parallel configurations. [99].

or circuit offers to the flow of ac current at a particular frequency. Since this is neither a pure reactance nor pure resistance, it can be represented through its "equivalent circuit" by a combination of resistance and reactance, at any frequency and in a series or parallel arrangement.

The equivalent circuits available on the LCR Quadtech 1920 are shown in Figure 4.16 with L being the inductance, R the resistance, G the conductance, C the capacitance, and the subscripts indicate parallel (p) or series (s). We utilise the parallel configuration of the LCR meter in our characterisations. Once the impedance is measured, the embedded computer of the Quadtech 1920 mathematically converts it to capacitance.

This LCR meter also permits the frequency of the input signal employed to read the capacitance to be selected, which is crucial in irradiated devices, as the capacitance-voltage curve exhibits a dependence on this signal frequency. This phenomenon, designated "the small signal trapping effect", is observed when a signal is introduced into a device containing defects. It is attributed to the irradiation-induced changes in the effective doping density, N_{eff} [100]. Furthermore, in order to obtain accurate capacitance measurements, a correction must be applied by subtracting the capacitance of the entire circuit in the absence of samples (open circuit correction). However, this correction is stored locally within the LCR meter and only needs to be performed once per characterisation campaign.

4.3.2.1 V_{GL} and V_{FD} determination for fresh sensors

From the CV curve we can calculate the voltage at which the gain layer is depleted V_{GL}, and the voltage at which the sensor is fully depleted V_{FD} can be also addressed.

Figure 4.17 (a) is an example of a CV curve from an LGAD and the behaviour of the capacitance is noticeable: It starts at the maximum value of the capacitance due to the depletion of the unbiased NP junction and then this capacitance decreases as the depleted

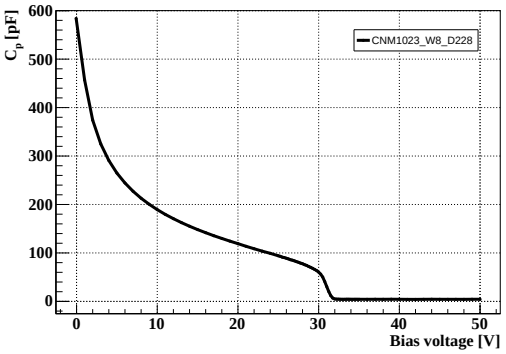

(a) CV curve from an LGAD

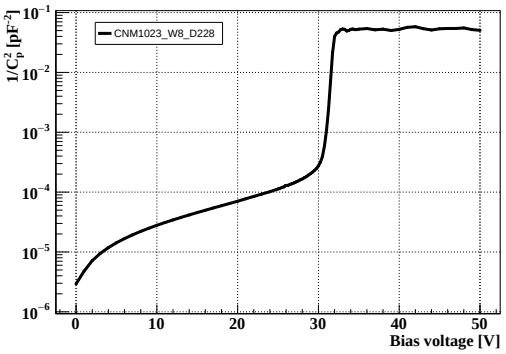

(b) $1/C^2$ plot from an LGAD

Fig. 4.17 The following figures illustrate the capacitance versus voltage curve (a) and the inverse of the capacitance squared ($1/C^2$) in logarithmic scale (b) from an LGAD non-irradiated sample. The subscript p denotes the utilisation of the internal parallel circuit of the LCR meter.

region increases. This decrease in capacitance is smooth due to the highly doped gain layer, which requires a large amount of reverse bias compared to that required to deplete the bulk. Then, around the 30 V, the capacitance starts to decrease at a greater rate, indicating that the multiplication layer is now depleted V_{GL} and the bulk is now depleting faster, and finally this capacitance stops decreasing indicating the V_{FD}. Finally, the capacitance continues to decrease until it reaches a constant value, C_{end}, which is now solely dependent on the active width of the device.

Since the C_{end} is reached when the device is fully depleted, regardless of the voltage applied above the V_{FD}, and from Equation 2.8, we can rewrite the relationship of the sensor capacitance to distinguish when the V_{bias} is below or above the V_{FD} as follows:

$$\frac{C}{A} = \begin{cases} \sqrt{\frac{e\varepsilon_0\varepsilon_{Si}|N_{eff}|}{2V_{bias}}} & \text{if} \quad V_{bias} < V_{FD} \\ \frac{\varepsilon_0\varepsilon_{Si}}{d} & \text{if} \quad V_{bias} \geq V_{FD} \end{cases} \tag{4.15}$$

and since the area A of the sensors are fixed, we can use the following relation:

$$\frac{1}{C^2} \propto \begin{cases} V_{bias} & \text{if} \quad V_{bias} < V_{FD} \\ d^2 & \text{if} \quad V_{bias} \geq V_{FD} \end{cases} \tag{4.16}$$

This relationship of the inverse of the squared capacitance $1/C^2$ versus the V_{bias} is most commonly used as an empirical method for determining the V_{FD} by simply fitting the fast rising part of the curve and the flat part separately and finding the intersection between them. The V_{GL} can be determined in this way, computing the intersection between the starting part

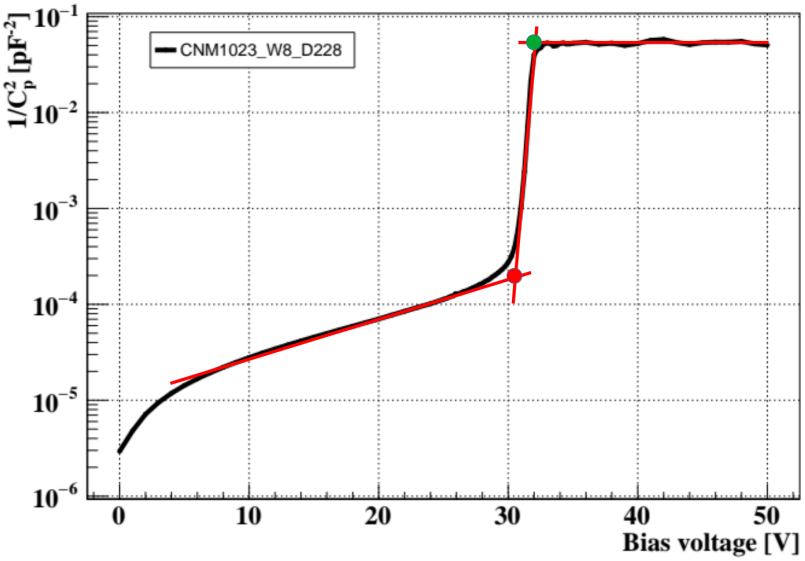

Fig. 4.18 Inverse of the capacitance squared $1/C^2$ in log scale with the V_{GL} (around the 31 V) and V_{FD} (around the 32 V) are represented in red and green respectively

of the curve and the region when the slope increases fast. An example of $1/C^2$ versus V_{bias} is shown in Figure 4.18 where the V_{GL} (red point) and V_{FD} (green point) for this example are represented.

4.3.2.2 V_{GL} determination for irradiated sensors

The irradiation of the samples modifies the V_{GL} in correlation with the irradiation fluence. Given that the measured capacitance depends on the depleted thickness of an LGAD, and the irradiation damage also alters the space charge of the gain layer in the devices, the CV curves exhibit a transformation in shape post-irradiation. To observe this effect in the V_{GL} region more precisely [101], CV measurements were conducted in our setup at a temperature of 10 °C with a low frequency of 100 Hz configured in the LCR-meter, as this effect is not observed at higher frequencies for irradiated devices.

For the irradiated devices, the CV curves demonstrate an increase in capacitance up to a local maximum, which has been deduced to be linked with the presence of the multiplication layer and the effects of the irradiation over it [102]. Figure 4.19 depicts the curves of samples from CNM RUN 15246, exhibiting this shape and where a decrease in V_{GL} is also observed as a result of irradiation. From these CV characteristics, it can be observed that the effect in question is present at low frequencies, though not at high frequencies. As a result, the method for calculating the V_{GL} for irradiated devices has been modified. The V_{GL} is now determined

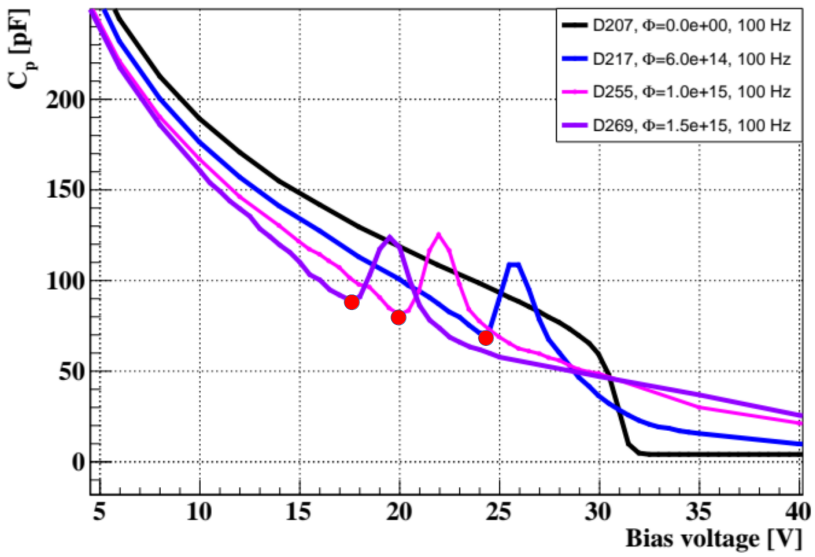

Fig. 4.19 Pad capacitance after irradiation as a function of the reverse bias. A CV curve from a non-irradiated sample added for comparison (black). Displacement of the V_{GL} as result of the irradiation damage is observed. Red points represents the V_{GL}

to be the one corresponding to the local minimum capacitance before the peak in the curve, as this value aligns with the V_{GL} determined from the IV measurements. Furthermore, this point in the curve is more consistent than the maximum of the peak, which in some measurements exhibited a deformed shape.

4.3.3 Doping profile

In some cases, as a quality control or simply to confirm the density distribution of doping across the active thickness of the sensor, the doping profile can be extracted from the CV characteristics, more precisely from the derivative of the $1/C^2$ parameter. Knowing the geometric area of the sensor (pad-like for planar sensors), and using the W_{dep} relation from Equation 2.8, we can use Equation 4.16 to write the expression for the effective dopant concentration in terms of the derivative of $1/C^2$ [103] as follows:

$$N(w) = \frac{2}{q\varepsilon A^2} \frac{1}{d(1/C(V)^2)/dV} \tag{4.17}$$

where A is the area of the sensor and w is the depth, which can be rewritten as follows:

$$w = \frac{\varepsilon A}{C(V)} \tag{4.18}$$

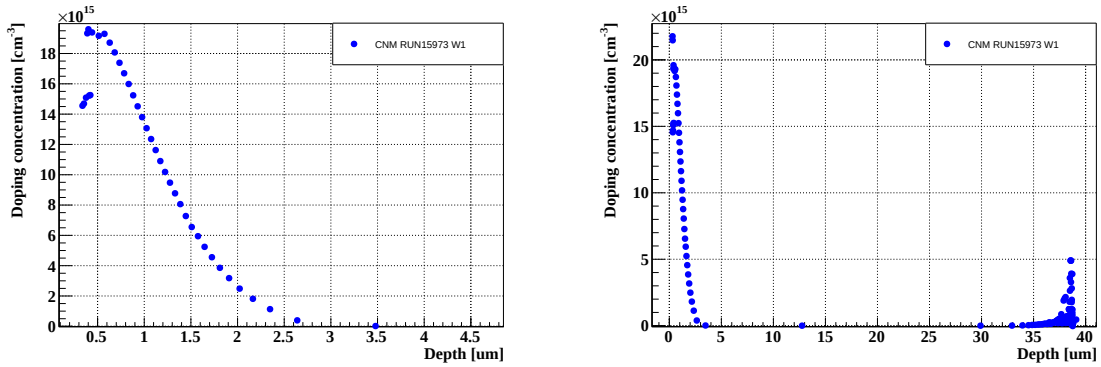

(a) Doping profile gainlayer

(b) Doping profile complete

Fig. 4.20 Doping profile of LGAD sensors from CNM RUN15973. The dopant concentrations are shown as a function of depth. (a) is the magnified view of the first micrometers where we can observe the maximum concentration at about 0.5 µm and (b) shows the same profile over the total computed depth.

Figure 4.20 depicts the doping profile of an LGAD from Run 15973. The figure illustrates the concentration of the dopant as a function of sensor depth, calculated from the capacitance data obtained from the CV characterisation.

It is important to note that the capacitance of a sensor depends on the depleted thickness of the sensor, which in turn depends on the applied bias voltage. This means that for a better extraction of the doping profile of the gain layer, which is important in LGADs, it is necessary to take the CV curves with a finer granularity at the very first bias voltages applied,for example, in steps of 0.05 V for the first few bias voltages).

In Figure 4.20 (a), it can be observed that the maximum dopant concentration is situated at approximately 0.5 µm in depth, which aligns with the intended implant configuration of the gain layer for these sensors and the behaviour of this implant (see subsubsection 6.2.1.2). In (b), the profile is shown over the total depth of the sensor, calculated from the CV curve, and how this depth corresponds to the approximated real active thickness of these sensors.

4.4 TCT characterisation

The Transient Current Technique (TCT) is an optical characterisation of semiconductor detectors that gives us information about the electric field by measuring the signal of the induced current due to the movement of the charge carriers as they cross a silicon sensor. To create the electron-hole pairs inside the silicon sensors, the usual procedure is to illuminate the active area of the sensors with a laser. The laser used for characterisation in our optical

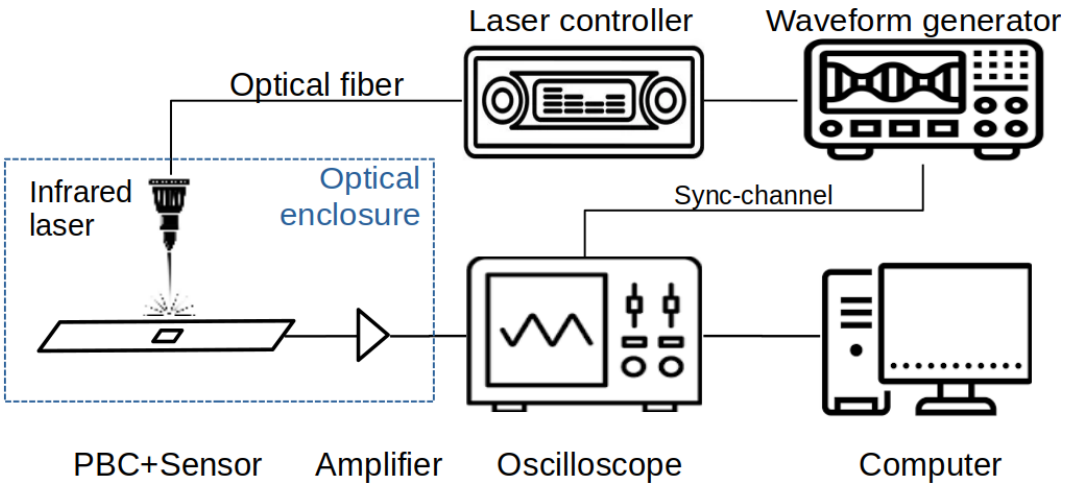

Fig. 4.21 TCT setup scheme. In this scheme we can observe the main components of the TCT setup at IFCA and the connections between them. The PCBs containing the sensors are mounted on the thermally controlled support inside the optical enclosure; the sensor are illuminated with a laser connected to its controller and the waveform generator; the response signal of the sensor is amplified and then read-out by an oscilloscope and recorded with the data acquisition software on a computer.

setup is infrared, since this laser wavelength traverses the entire silicon sensor, unlike the red laser, which only reaches a few microns inside the silicon lattice.

The infrared laser is also the most commonly used wavelength in characterisation to approximate a real Minimum Ionising Particle (MIP) passing through the sensor thickness, since the laser power can be tuned and, with the aid of a reference photodiode, the signal intensity can be normalised to the charge deposited by a MIP [104]. For this correction, the laser output is transmitted into a single mode optical fibre. Using an inline fibre splitter, the laser beam is split into two different beams, each of which passes through separate fibre outputs. One of these outputs is directed to the reference photodiode and the second fibre output is used to illuminate the sensor.

To control the laser, it is connected to an EIG1000D digital control unit [105], which allows some parameters to be set, such as the tuning of the laser pulse intensity. The external frequency is controlled by a Keithley 3390 Waveform Generator [106], set in a pulsed mode with the desired amplitude and shape. This waveform generator provides a sync output channel which can be connected to the oscilloscope if it is to be used as a trigger. The scheme of this laser setup for TCT applications can be seen at Figure 4.21.

The samples to be measured are mounted on a support inside a light blocking chamber to protect them from external light and some possible external noise. This support is mounted on three-axis electronic stages that allow the laser output to be moved along the sensor

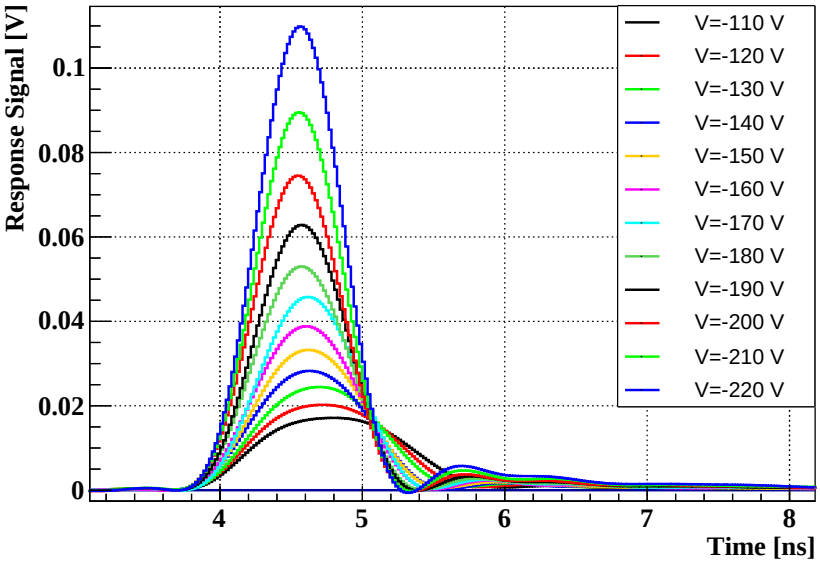

(a) LGAD waveforms from TCT setup

Fig. 4.22 Example of the waveform as a response of the illuminated LGADs biased at different voltages. We can observe the evolution of the shape and amplitude as a function of the bias.

surface and in the direction perpendicular to this plane with a displacement accuracy better than 10 µm. In addition, this support has a thermal chuck connected to a cooling system necessary to control the temperature and to prevent condensation of humidity on the sensors, a constant flow of dry air is circulated inside the chamber.

The sensors to be illuminated by the laser must be wire-bonded on a PCB to be then read by the oscilloscope and record the response waveforms as described in subsection 4.6.5.

4.4.1 Laser focusing

A prerequisite for laser illumination is the presence of optical windows on the sensors. These are non-metallised areas that allow the laser to penetrate the silicon of the sensor.

The first step in the sensor illumination process is to accurately position the sensor, which is wire-bonded to the PCB, within the laser output area. This is achieved by securing the sensor in the mechanical fixture and using the computer-controlled stages for a preliminary rough alignment. With the chamber closed, the sensor can be biased and its response monitored on the oscilloscope when the laser is activated. The next stage is to fine-tune the alignment of the laser spot close to the optical window. It's important to note that the

oscilloscope only registers a signal response when light enters the window, and that the intensity of the incident beam follows a Gaussian distribution.

A pre-programmed routine can then be used to scan the surface of the sensor within a user-defined area. This routine involves a series of illumination steps and moving a predetermined number of microns each time, as defined in the routine, to create a heat map grid of the currents across the scanned area. The final step is to adjust the stages to position the laser spot at the centre of the window, which should correspond to the area of maximum recorded current.

By aligning the laser within the optical window of the sensor, the aim is to maximise light deposition and achieve high area resolution. To achieve this, the laser beam must be focused so that its beam waist, which is the location where the beam radius has a minimum, coincides with the sensor surface. This is achieved by adjusting the position along the z-axis using the micrometer stages. The optimum position is determined when the amplitude of the signal is at its maximum. We can then select the position over the sensor area of interest to be illuminated.

4.4.2 TCT for timming

The IFCA TCT setup can be configured for use as a laser timing characterisation setup. Timing resolution is the smallest time interval that can be accurately measured by a system using sensors. The resolution of a system can be measured by calculating the time difference between two pulses with a fixed time delay. To generate these two pulses, the TCT setup is adapted by adding an optical splitter that divides the laser beam into two 50% (not exact) beams, one of which is passed through a 10 m optical fibre to delay the pulse by about 52 ns [14]. The two laser beams are then reunited by a combiner and used to illuminate the sensor to record events with two pulses separated by this time delay. A diagram of this configuration is shown in Figure 4.23.

There are a some considerations in the design of this timing characterisation configuration. The use of a laser implies that there will be some fluctuations on the laser power from one event to another. This fluctuation, and the fact that the splitting ratio is not exactly 50%, leads to amplitude fluctuations that result in the time-walk effect, which can be corrected using Constant Fraction Discrimination (CFD) algorithms (see subsection 4.2.5 for time-walk explanation and correction).

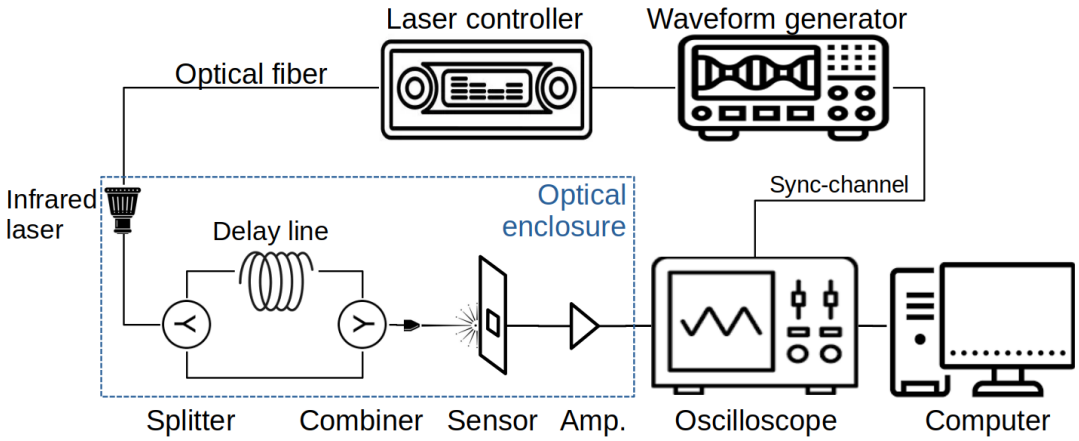

Fig. 4.23 Time resolution configuration of the TCT setup. This setup is based on the one described in Figure 4.21 but includes a splitter, a 10 m fibre optic delay line added in the path of one of the split laser beams and a combiner to use both beams before using them to illuminate the sensor.

4.5 Radioactive source characterisation

The use of radioactive sources for characterisation involves recording the signal responses of semiconductor devices by exploiting the emission of beta radiation. This radiation generates changes in the sensor's response as it passes through the material, creating electron-hole pairs in a manner similar to illuminating the sensor with a laser but with a slower event rate.

However, there are key differences between using a radioactive source and a laser. When using a radioactive source, the emitted particles deposit varying amounts of charge in the sensor at different times of incidence, depending on their impact rate. In contrast, laser illumination allows precise control over the amount of incident light, its position, and rate, with an absence of significant Landau noise in the rising edge of the pulse.

Radioactive source characterisation provides a closer approximation to a real radiation environment of an experiment, compared to laser-based techniques such as Transient Current Technique (TCT). However, it requires recording a larger number of events to obtain sufficient statistical data for computing representative characterization parameters. Furthermore, the characterisation with radioactive source permits the attainment of a realistic time resolution of the system when the particles traverse different sensor planes in a single occurrence (see subsection 4.2.7) and with a behaviour similar to that of a MIP.

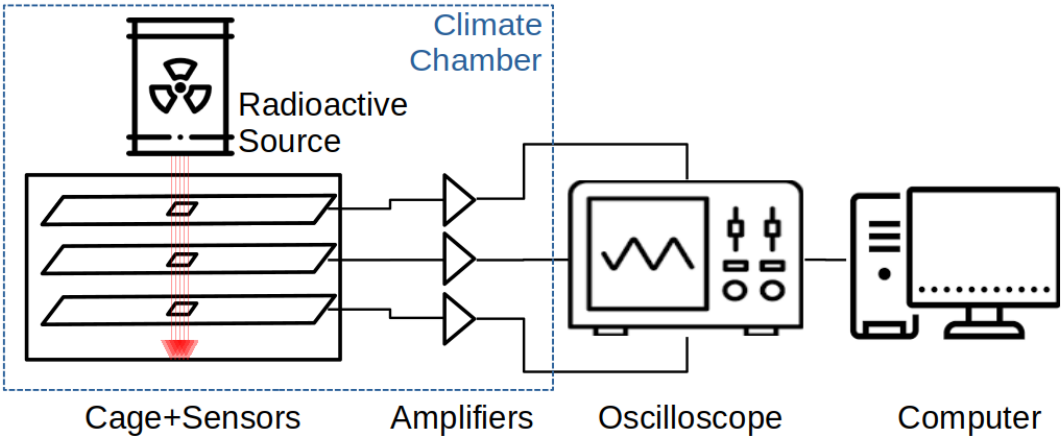

Fig. 4.24 Radioactive setup scheme. In this scheme we can observe the main components of the radioactive source setup: The ^{90}Sr source that is placed on top of the 3-stack of sensors, each one mounted on carrier PCBs, current amplifiers, the oscilloscope that records the response waveforms and a computer with the data acquisition software.

4.5.1 Radioactive source

The radioactive source chosen is an encapsulated strontium-90 (^{90}Sr), a radioactive isotope with a half-life of 29.1 years. Strontium-90 decays by β-decays to Yttrium-90 (^{90}Y) and finally to a stable Zirconium-90 (^{90}Zr), which is why ^{90}Sr is used commercially as an electron emitter in medical and industrial applications with an end-point energy of 0.546 MeV [107]. ^{90}Sr is commonly used in the characterisation of silicon devices when it is desirable to study the response of this type of device to minimum ionising particles (MIPs).

4.5.2 3 sensor stack setup

The experimental setup at the IFCA was designed to accommodate a metal enclosure containing a stack of three sensors. Each sensor is wire-bonded and mounted on a passive circuit board that facilitates the necessary electrical connections. This enclosure is housed in a climate chamber that controls the target temperature conditions and prevents condensation due to humidity. An encapsulated ^{90}Sr radioactive source with a nominal activity of 3.7 MBq is strategically positioned at the top of the sensor stack to ensure no direct contact with the samples, as shown in the Figure 4.24 sketch. The alignment of the sensors within the stack is maintained by bonding the devices to the PCBs in a consistent position using a mechanical template.

To quantify the induced current, external low-noise current CIVIDEC amplifiers are used, operating as described in section 4.4. The readout is performed on the oscilloscope described

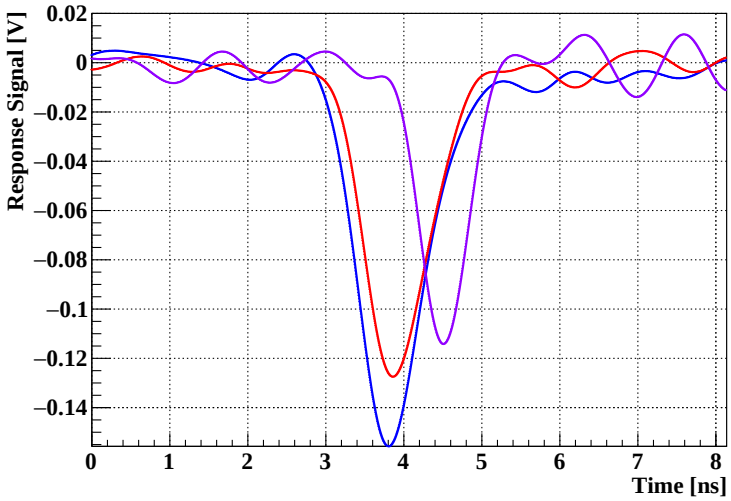

(a) LGAD waveforms.

Fig. 4.25 Example of a triple coincidence event showing the voltage versus time of a pulse from three different LGAD samples, each connected to a different channel on the oscilloscope.

in subsection 4.1.2 with a sampling rate of 5 GS/s. The occurrence of events is dependent upon a triple coincidence logic between the oscilloscope channels, which are subsequently recorded as events by the data acquisition software installed on a dedicated computer.

In the triple coincidence setup, each recorded event is expected to contain three different waveforms, each corresponding to a different sensor connected to an oscilloscope channel. The final rate of triple coincidence events is subject to variation and is influenced by a number of factors, including the alignment between the sensors and the radioactive source, sensor depletion and measurement conditions. Consequently, this rate of triple coincidence events may be either lower or higher, but the final number of events will be reduced following the offline selection process, which have been described in section 4.2.

An illustration of an event exhibiting a triple coincidence, with a single waveform per sensor, can be observed in Figure 4.25, which plots data from three distinct channels of the same event.

It is possible to make certain variations in the radioactive source setup, depending on the aspect that is to be studied. To study noise, for instance, the most fundamental approach is to record events without biasing the sensors and examine the baseline noise. Alternatively, to measure the amplitude of spurious pulses, it is necessary to remove the radioactive source and apply a bias voltage sufficient to record (if they occur) "dark counts" generated not by a MIP. Furthermore, to ascertain the frequency of these spurious pulses, it is sufficient to

replace the oscilloscope with NIM electronics (see next subsection) to count them at different bias voltages.

4.5.3 Spurious pulses

The so-called "dark counts" or "spurious pulses" refers to recorded events in the absence of any incident minimum ionizing particles (MIPs). The rate of this dark counts establishes the minimum count rate at which the signal is predominantly due to real particles, with the majority of false detection events being thermally induced. To verify the functionality of the sensors, a noise analysis can be conducted to identify and quantify these spurious pulses.

These spurious pulses are thermally induced, thus eliminating the need for an external excitation source such as a radioactive source. Instead, the sensor is biased slightly above the normal operating bias voltage (determined based on the requirements) but below the breakdown regime and then make an scan in search of these spurious pulses. The amplitude of these spurious pulses is measured for both fresh and irradiated sensors at each fluence, similar to measurements taken with a radioactive source. The charge of the spurious pulses can be computed using the amplitude-to-charge correlation from the measurements taken in radioactive source.

Given that the spurious pulse rate may be constrained by the digital oscilloscope maximum trigger rate of 9 kHz, we can employ NIM [108] electronic: A Discriminator that converts the analog pulse to a digital signal; a Timer that obtains the occurrence of signals; and a Counter, to ascertain the pulse rate of the Dark Counts capable of a maximum counting rate of 250 MHz [109]. The discriminator's minimum threshold is -25 mV, which is higher than the -15 mV used with the oscilloscope. Then the frequency of the spurious pulses can be obtained.

4.6 Test-beam characterisation

Test-beams constitute the most realistic environments for conducting sensor tests. Two facilities have been visited for the purpose of characterising sensors and modules of read-out chips with bump-bonded sensors, these two facilities has the advantage of using telescopes that have been designed to be compatible between research centres inside the European collaboration.

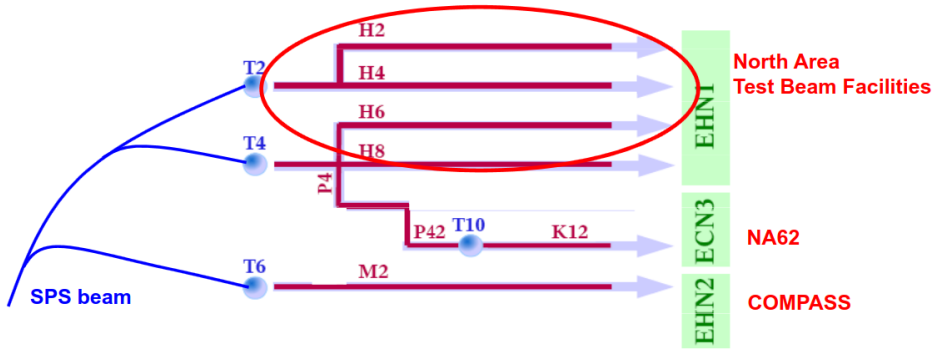

Fig. 4.26 Schematic sketch of the beam lines that are passed to targets (T). The test-beam areas (H) are circled in red [111], H6 contains the EUDET-telescope (see subsection 4.6.2).

4.6.1 Facilities

4.6.1.1 CERN SPS

The characterisation of the different campaigns was conducted using multiple test beams at two distinct facilities. One of these facilities was the North Area of the CERN Super Proton Synchrotron (SPS) [110] at the Prevessin area. In this location, the extracted beam from SPS is passed to the primary targets T2, T4 and T6, which are used to provide beam lines. The T4 target supplies the designated H6 beam line with a beam comprising electrons, hadrons and muons, which are subject to testing. This area has been utilised by various research groups, including the AIDAInnova and the ETL group, for the testing and characterisation of semiconductor sensors, such as the LGADs under investigation in this study.

4.6.1.2 DESY II

The other facility where test beams were done, employing lower energy levels was the Deutsches Elektronen-Synchrotron (DESY). DESY manages a beam testing infrastructure that includes three distinct beam lines (21, 22, and 24) located in Experimental Hall 2 (Building 27) on the Bahrenfeld campus in Hamburg. In Figure 4.27 shows the beam generation at DESY: A beam of bremsstrahlung is produced by a carbon fiber situated within the circulating beam of the electron/positron synchrotron DESY II. The resultant photons undergo conversion into electron/positron pairs via a metallic plate converter. Subsequently, the beam is spread out into a horizontal fan-like with a dipole magnet, and finally, it is shaped with a collimator. These beams can contain up to 1000 particles per cm^2 and have energies ranging from 1 to 6 GeV [112].

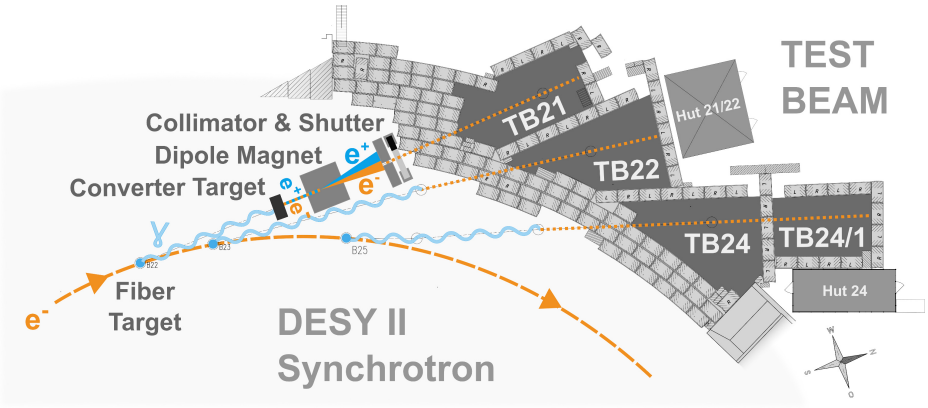

Fig. 4.27 Schematic layout of the beam generation at the DESY test beam facility. Not scaled. Taken from [112].

4.6.2 Telescope infrastructure

This category of beam telescope has its origins in the European network for detector R&D (EUDET) project [113] that utilised Mimosa26 sensors, capable of 2.2 cm^2 sensitive surface with a readout speed of 10,000 frames per second [114]. Replicas of this pixel telescope are operational at CERN, the Stanford Linear Accelerator Center (SLAC) [115], and in the Electron Stretcher Accelerator (ELSA) [116].

These telescopes offer high-precision beam tracking (approximately $2\mu m$), a sufficient event rate (approximately 2 kHz), and a straightforward integration capability of DUTs. They are operated by the EUDAQ framework (DAQ software) and analysed with either the legacy EUTelescope or Correyvreckan [117] offline reconstruction software. Consequently, these telescopes provide a comprehensive infrastructure for detector testing.

As mentioned, the EUDET-type telescope is an arrange of six-planes, three upstream of the beam and three downtream, and between them there is the dedicated area to place the DUTs. In order to control the temperature of the DUTs to perform low temperature characterization of irradiated samples, the DUT planes are disposed inside a cold-box coupled to a mini-chiller and with a constant flux of nitrogen as to prevent condensation.

Figure 4.28 is an scheme of the main infrastructure setup for the test-beam characterisations. It is important to note that in addition to the common telescope infrastructure, each test beam campaign has its own complex, interconnected subsystems and instruments that are planned (prior) and tested (during) each campaign.

The particle beam travels from the left (upstream) to right (downstream) crossing the Mimosa26 telescope sensors meanwhile the DUTs are placed inside the cold box in the middle space of the telescope. At the extremes of the telescope there are two pairs of photo-

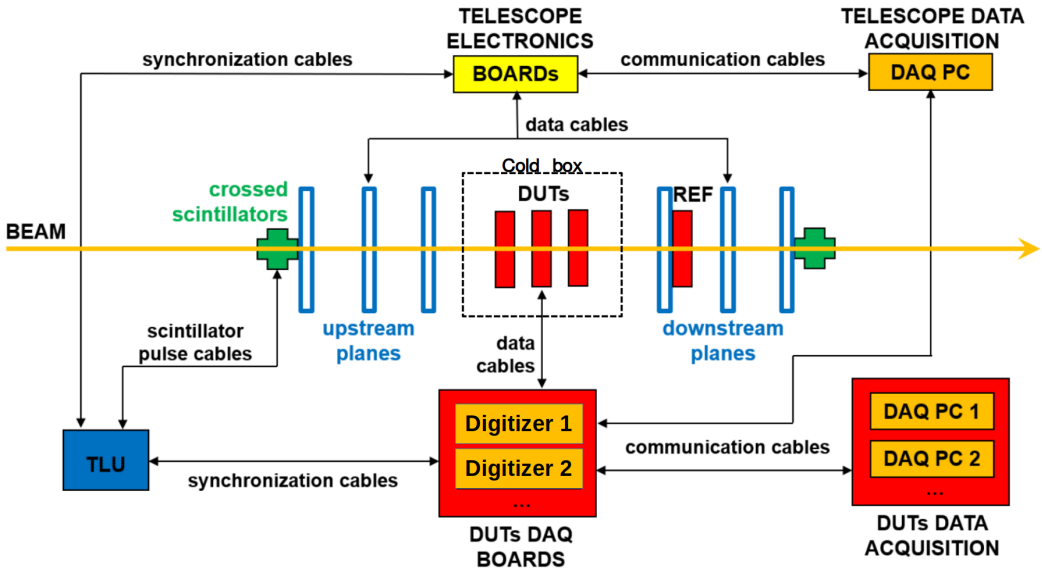

Fig. 4.28 Scheme of the standard test-beam setup at SPS-CERN with the main components and its interconnections. The particle beam travels from the left (upstream) to right (downstream) crossing the Mimosa26 telescope sensors and the DUTs placed in the middle. Scheme adapted from [118]

multiplier tubes (PMTs) scintillators called "scalers" that detects the arrival of the particles and generates a signal that is passed to the Trigger Logic Unit (TLU, see subsection 4.6.4).

4.6.3 DAQ system

In all our test-beam campaigns, we utilize EUDAQ2, a modular, open-source licensed data acquisition software framework [119]. This system was initially designed for data readout from EUDET-type pixel telescopes. The software facilitates the connection of individual detector readout systems, simplifying the integration of multiple DUTs. It supports various triggering and event building modes, which proved to be highly beneficial when the DAQ system was integrated into EUDAQ2. This integration allowed for successful combination of the DUTs data with the telescope data, based on global trigger identification.

EUDAQ2 itself performs various functions so-called "roles":

- The *RunControl* acts as the system's core and provides an interface to manage the START/STOP commands of the data taking and allow to load the initialization *.ini* and configuration *.conf* files.
- The *Producers* control all the subsystem hardware.
- The *DataCollector* merges the producers and stores the data.

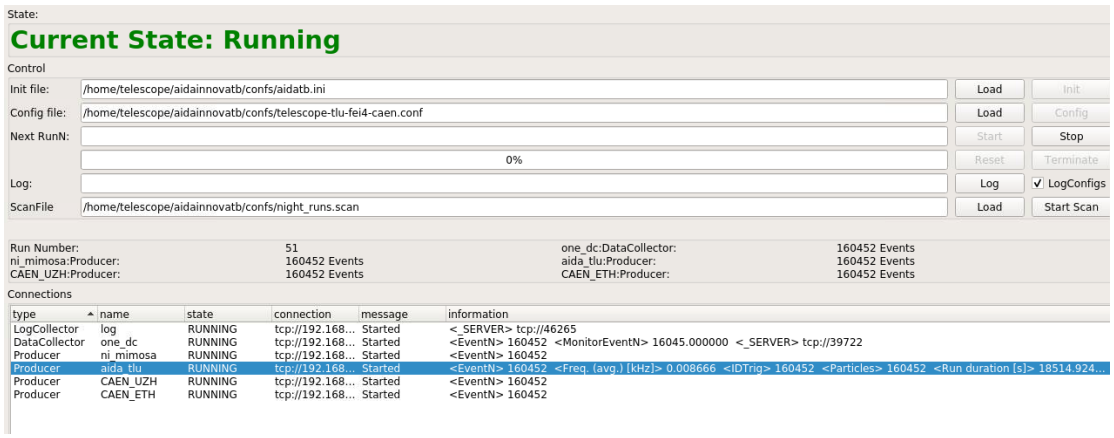

Fig. 4.29 Example of the EUDAQ2 interface *RunControl*. The commands, load files fields, connections (*Producers*) and status are visible.

- The *LogCollector* handles the system's relevant messages.
- The *Monitor* ensures online data quality by allowing to display useful histograms, hitmaps and waveforms, to mention some of these functionalities.

Every new sub-system hardware is added to the setup, a producer have to be developed and added to the EUDAQ2 system in order to be integrated. Figure 4.29 is an example of the EUDAQ2 *RunControl* interface during a test-beam data run.

4.6.4 Trigger

The TLU, specifically designed for high energy physics test-beams and developed by the particle physics group at the University of Bristol [120], is responsible for managing the trigger between the different subsystems of the readout hardware. The TLU's operating mode controls its ability to accept busy signals or other veto signals from the DUTs and to respond appropriately, preventing further triggers until all busy signals have been cleared. Each global trigger generated by the unit is accompanied by a 48-bit coarse timestamp. Each trigger defines an event, with the collection of measured hits from all sensors being stored together under the same event of a run.

Once receiving compatible signals from the scalers, the TLU generates a trigger and uses a simple handshake protocol to maintain synchronisation between the different detector systems. The detector systems assert busy signals on different lines, inhibiting triggers from the TLU until all lines are cleared. The TLU refrains from sending new triggers until all sensors have cleared their busy lines, ensuring synchronous triggering and reading of sensors.

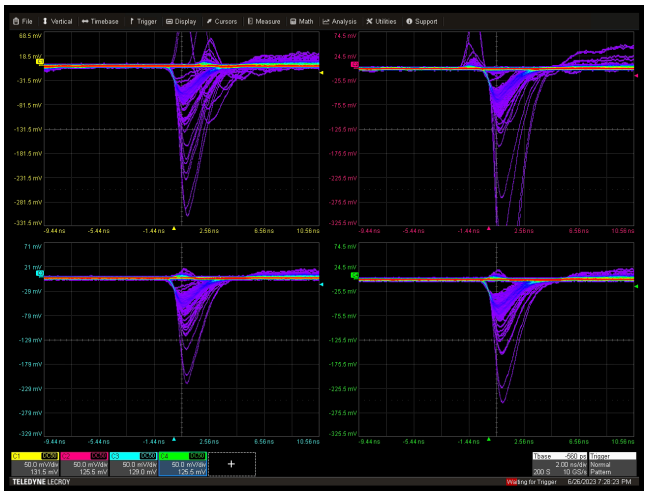

Fig. 4.30 Screenshot of the four channels of the oscilloscope, where an 2×2 pads LGAD is connected one pad to each channel to serve as a trigger for the TLU and digitizers.

In the case of the test beams from the AIDAInnova group, since the silicon detectors are fast enough, some additional systems were adapted for triggering: Basically, the use of a $20\,\mathrm{GS/s}$, 1 GHz oscilloscope capable of operating in the so-called sequence mode with a high number of segments to detect events and generate a signal to be split, one split of this signal as input to the TLU that controls the telescope and the other split signal as trigger for the digitizers. Since an oscilloscope was used as a trigger, a fast planar sensor can be used in this setup, as can be seen in Figure 4.30, where a 2×2 LGAD was used, with one pad connected to each oscilloscope channel configured with an "OR" logic acquisition.

4.6.5 DUT planes and Readout

The coldbox, placed in the centre of the telescope, is able to contain inside different support frames, which are solid plates mounted on independent motorised stages, in order to move along the coordinates of the plane perpendicular to the beam and to obtain a better alignment between the different planes and the beam. Figure 4.31 is the scheme of an example of the arrangement used in one of the test beams carried out in the CERN-SPS area. In this scheme we can see the Mimosa26 planes and the coldbox containing the support frames. In most cases, each support frame can contain two planes of DUTs, one per side, which is practical if we want to measure as many DUTs as possible per test batch.

The DUTs can be mounted and wire-bonded to the so-called "carrier boards", which are connected by "pogo pins" to the special Chubut 2 readout boards [121], designed for LGAD type sensors, which, in addition to good electrical characteristics, focus on simplifying mounting, transport and connections in the laboratory, such as test-beams. Chubut 2 boards are

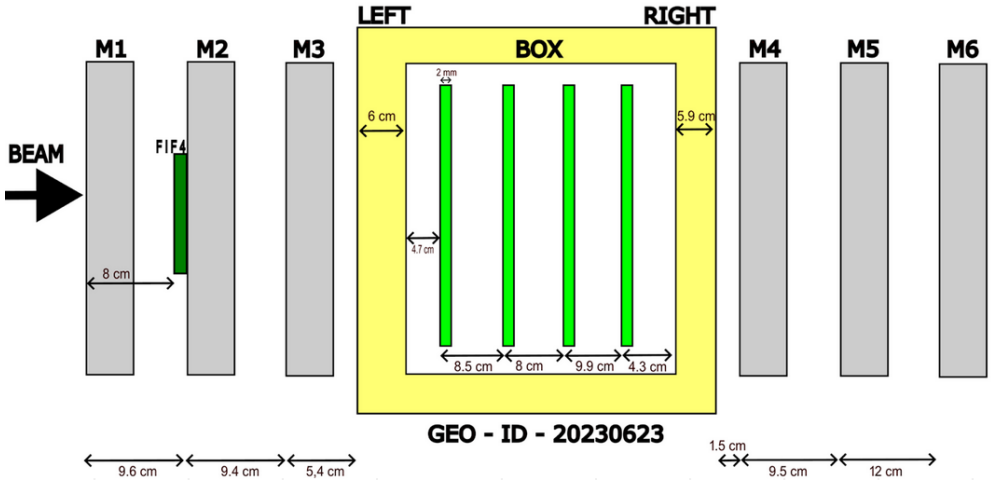

Fig. 4.31 Scheme of the distribution of the telescope planes (grey) and the frames (green) supporting the sample planes inside the coldbox (yellow).

able to support 4 channels[1] with two independent amplification stages, giving a total voltage gain of $\sim 40\,\text{dB}$ with $50\,\Omega$ input and output, and an effective measured transimpedance of $5050 \pm 250\,\Omega$. A rendering of the Chubut 2 can be seen in Figure 4.32 (a), showing the top and bottom views. Figure 4.32 (b) is a real Chubut 2 and a carrier board.

When a trigger is initiated, the DUT's responses are then readout using CAEN $16+1$ channels (the additional analogue input is designed for fast triggering), 12-bit, $5\,\text{GS/s}$ switched capacitor digitizers [122], which have an acquisition window of $\sim 200\,\text{ns}$ and a technology consisting of a series of 1024 capacitors in which the analogue input signal is circularly sampled while a digital memory allows subsequent events to be stored. If required, multiple digitizers can be added to the setup, according to the Figure 4.28 scheme.

4.6.6 Alignment method

The correct alignment of planes and samples with respect to the beam spot is a critical task and requires a methodology to ensure that this alignment is good enough for successful characterisation. In test beam campaigns this alignment is done in steps: The very first step starts with the design and planning of all components such as mounts, platforms, adjustable tables, support frames, readout boards, sensor geometry, cold box dimensions and in-situ telescope dimensions. This part is done by the collaborative group before each test beam.

Once in the test-beam areas, after a correct installation and connection of all the sub-systems that will be part of the test-beam like instruments, cables, etcetera, a visible laser alignment can be done with the purpose of making an initial alignment of the planes and

[1] Also a 4×4 *Chubut 16ch* and carrier boards are available.

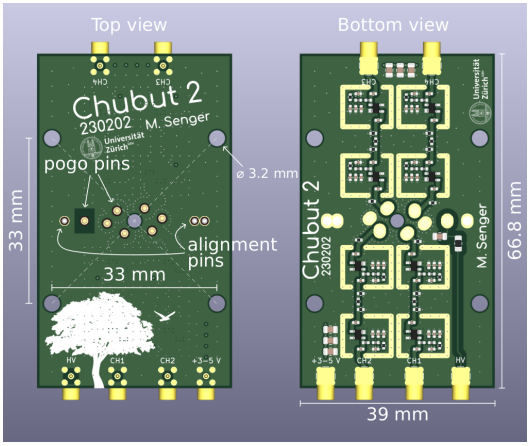

(a) Rendering of Chubut 2 board.

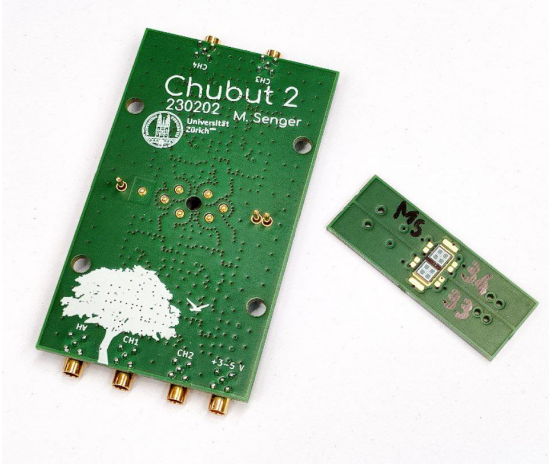

(b) Chubut 2 and carrier board.

Fig. 4.32 (a) is a render of the Chubut 2 board designed for LGAD samples. The high voltage, low voltage and the four channel connectors are also visible. (b) is a real Chubut 2 board and a carrier board with 2 2×2 LGADs attached to it. Taken from [121]

crosschecking that the telescope maintains in line with the beam. Both facilities have fiducial marks of the beam trajectory.

Fine alignment can then be carried out using data from the telescope itself, using a method called "shadow trigger alignment". This method requires that the telescope and the DUTs to be aligned are operational and is based on the fact that since the trigger signal is made by a sensor when it is hit by particles, regardless of the system registering a large amount of incident particles, there will always be a large accumulation of recorded hits that traverse this trigger sensor and this can be seen in the tracks recorded by the different Mimosa26 sensors of the telescope. This helps to know where the sensor trigger is in relation to the beam spot and, if necessary, to move the independent piezoelectric stages of their support frame.

A hitmap of a Mimosa26 plane is shown in Figure 4.33, where in (b) we can clearly see this accumulation of hits, which follows the same shape, like a shadow, of the pads of the 2×2 LGAD used as trigger (a).

The next steps in this alignment method are to swap the connection of the trigger sensor with the DUT of another plane to be aligned and then compare its shadow with the shadow of the original trigger and move it if necessary. In this part, I have personally verified that a more time-efficient alternative is to take only two of the trigger sensor's pads, preferably pads of a diagonal, and swap them with two pads (or sensors) of the plane that we want to align, thus obtaining four shadows to be aligned at the same time. Finally, this method must be repeated for all the DUT planes, each time the sensor batch is changed and each time there is a significant change in temperature (e.g. from room temperature to a low temperature).

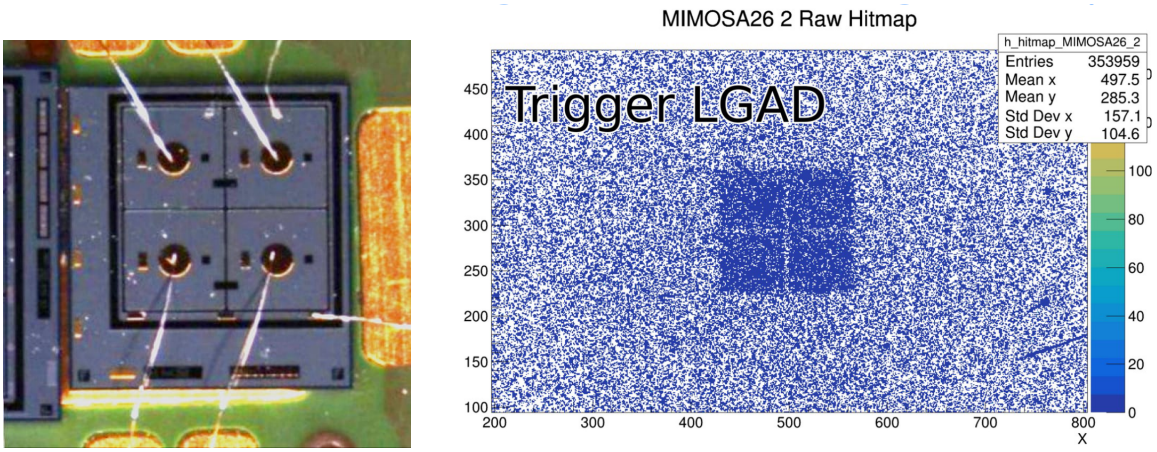

(a) 2×2 LGAD as trigger

(b) Shadow of an 2×2 HPK over a MIMOSA plane

Fig. 4.33 (a) is an example of a 2×2 HPK LGAD used as a trigger in a test-beam campaign. (b) is a hitmap recorded over a Mimosa26 plane in an alignment run. There is an observable clustering of hits corresponding to the "shadow" of the trigger.

4.7 Irradiation facility

The objective of all preceding characterisation methods has been the study of semiconductor sensors and the effects of radiation on their response and performance. In order to study the effects of radiation over the course of the various campaigns, the scientific collaboration has made use of external, specialized irradiation facilities, as irradiation is not part of the working methodology. However, working with irradiated sensors does have significant implications for the methodology.

In the case of this thesis, all irradiations were conducted using a nuclear reactor capable of delivering high radiation fluences ranging from $4 \times 10^{14}\,\mathrm{n_{eq}\,cm^{-2}}$ to $1.5 \times 10^{16}\,\mathrm{n_{eq}\,cm^{-2}}$. The neutron irradiation facility was the Reactor Centre at the Jožef Stefan Institute (JSI) [123] in Ljubljana, Slovenia. This facility utilises a TRIGA Mark II reactor, which has a maximum flux of approximately $2 \times 10^{13}\,\mathrm{n\,cm^{-2}\,s^{-1}}$ [124] at its centre. The neutron energy spectrum extends up to 10 MeV, with an accuracy of the fluence assured within 10% [83].

It is imperative that the sensors be maintained at a temperature of approximately $-20\,^{\circ}\mathrm{C}$ for the rest of their useful life in order to prevent the phenomenon known as "annealing" (see section). All centres that work with irradiated silicon sensors, including IFCA, CNM, DESY and CERN, are equipped with low-temperature storage space, climate-controlled chambers for measurements and possess the requisite experience in shipping sensors in cold "gel packs".

Chapter 5

Radiation-induced damage in Low Gain Avalanche Detectors

This chapter is an introduction to the radiation damage suffered by the LGADs designed for the HL-LHC upgrade experiments. In addition to the well-known effects of the irradiation on semiconductor sensors, such as leakage current increase, signal carrier trapping or spatial charge modification (see section 2.4), this chapter describes the specific effects of radiation on LGADs: The first section describes the radiation damage specific to LGADs, including the microscopic effects of radiation, the defect complexes involved, and the effect of resistivity on acceptor reactivation. The second section explains how carbon enrichment increases the radiation hardness of LGADs. Finally, the third section describes the destructive single-event burn-out that affects irradiated LGADs.

5.1 Irradiation-induced gain degradation in LGAD: Acceptor Removal mechanism

As previously reviewed, LGADs feature a thin, highly p-type doped layer that generates a strong electric field with sufficient strength to induce impact ionization for traversing electrons. This gain layer (p+) results from Boron implantation, which penetrates deeper into the silicon bulk than the shallow phosphorus implant (n++) constituting the cathode of the device.

Like all silicon-based sensors, LGADs experience the effects described in section 2.4 due to irradiation, including carrier trapping, increased leakage current, and modifications to space charge. Moreover, LGAD sensors experience a reduction in gain after being irradiated with charged hadrons or neutrons [104]. This reduction is due to the *acceptor removal mechanism*,

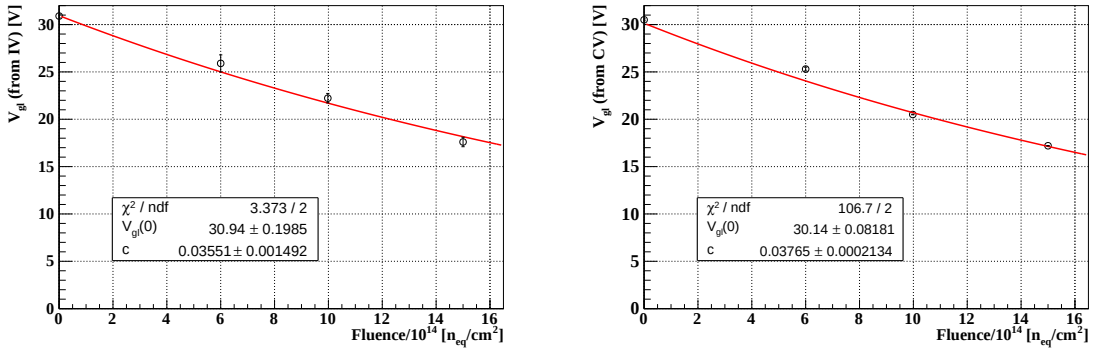

(a) V_{GL} computed from IV

(b) V_{GL} computed from CV

Fig. 5.1 Gain-layer depletion voltage (V_{GL}) from IV (a) and from CV (b) as a function of the fluence and the respective fit (red) from where the acceptor removal coefficient is calculated and being $c[10^{-16}\,\mathrm{cm}^2] = 3.6$ from IV, and $c[10^{-16}\,\mathrm{cm}^2] = 3.8$ from CV.

which involves the deactivation of the acceptors that form the gain layer (GL) [125]. In this context, boron (B) is specifically affected. The deactivation of boron reduces the effective doping of the gain layer. As a result, the primary effect is a suppression of the LGAD gain, caused by a smaller electric field peak in the gain layer.

As the irradiation process deactivates the boron implanted in the GL of LGAD sensors, the reverse bias required to fully deplete this gain layer V_{GL}, decreases relative to the pre-irradiation (fresh) state. This decrease in V_{GL} serves as an indicator of the residual active boron within the GL. Assuming uniform boron removal at a constant rate throughout the multiplication layer, we can represent V_{GL} as proportional to the boron concentration using the following equation:

$$V_{GL}(\Phi) \approx V_{GL}(\Phi = 0) \times e^{-c\Phi} \tag{5.1}$$

In this equation, c denotes the acceptor removal coefficient and V_{GL} is the gain layer depletion voltage corresponding to the specified fluence Φ. The coefficient c serves as an indicator of the degradation suffered by the multiplication layer, thus a lower c value indicates a more radiation-hardened sensor.

The acceptor removal can then be calculated using the V_{GL} from either the CV or IV data sets, as explained in subsection 4.3.1 and subsection 4.3.2. Figure 5.1 shows the V_{GL} values from IV (a) and CV (b) measurements of fresh and irradiated sensors from CNM RUN15946 plotted as a function of their irradiation fluence and fitted with Equation 5.1 to obtain the c coefficient that is $c[10^{-16}\,\mathrm{cm}^2] = 3.6$ from IV, and $c[10^{-16}\,\mathrm{cm}^2] = 3.8$ from CV for this example.

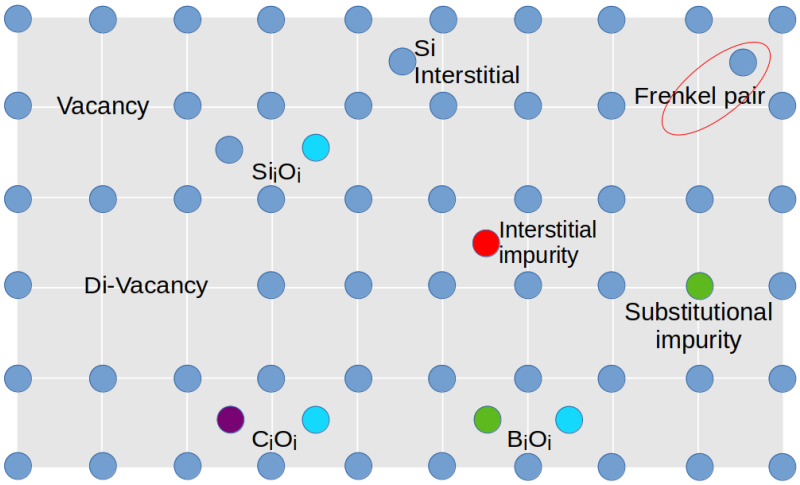

Fig. 5.2 Two-dimensional scheme of a silicon lattice section illustrating the main defects and complexes caused by irradiation-induced displacement damage. Adapted from [126].

5.1.1 Acceptor removal: microscopic description

At the microscopic level, active boron atoms located in the lattice sites (referred to as substitutional boron, B_s) are displaced from these nodes to interstitial positions (referred to as interstitial boron, B_i) and/or form defect complexes, such as 'Boron interstitial-Oxygen interstitial' (B_iO_i) or 'Boron substitutional-Silicon interstitial' (B_sSi_i). These complexes result in the removal of the original acceptor level associated with B_s and, in some cases, lead to the creation of a Boron Containing Donor (BCD) [127]. Figure 5.2 exemplifies in a two dimensional scheme some of the defects and complexes formed due to irradiation.

The formation of the B_iO_i defect has been tentatively identified as the primary mechanism for the gain degradation on LGADs [126]. When irradiated with highly energetic particles, defect clusters including silicon interstitials Si_i (denoted as I), and vacancies form within the silicon crystal lattice and exhibit mobility at temperatures near room temperature. The so-called Watkins replacement mechanism [128] allows interstitials I to reach lattice sites with boron substitutional atoms and follow the reaction:

$$I + B_s \rightarrow B_i \tag{5.2}$$

These boron atoms become interstitials B_i, migrating through the lattice for further react with oxygen interstitials (O_i), which are abundant in silicon crystals to finally leading to the formation of B_iO_i defect complexes by the reactions:

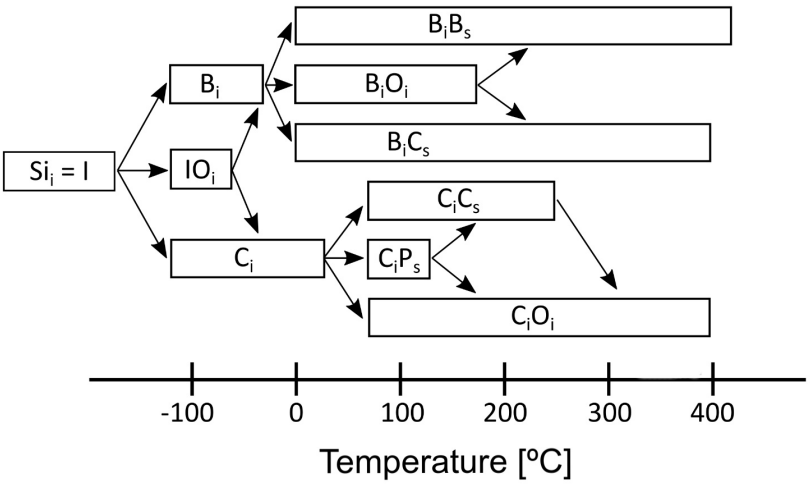

Fig. 5.3 Silicon interstitial defect reactions with impurities. The temperature scale shows the stability of the defects under quiescent condition. Adapted from [129].

$$B_i + O_i \rightarrow B_iO_i \tag{5.3}$$

that are stable at room temperature. The intermediate complex IO_i is not stable at room temperature. Figure 5.3 exemplifies the ideal reaction scheme of silicon self-interstitial defect reactions with impurities and the temperature at which the defects complexes are stable.

The donor energy level associated with B_iO_i can be readily detected using techniques such as Deep Level Transient Spectroscopy (DLTS) and Thermally Stimulated Currents (TSC) after charge injection through forward-biased devices. This complex features a donor level situated at 0.23 eV below the silicon conduction band edge of silicon [129]. Consequently, each B_iO_i defect formed results in the removal of one shallow acceptor (Bs) and the generation of a charged donor since contributes as positive in the space charge. Thus for every removed Boron (acceptor) and a B_iO_i (donor) created, a net acceptor removal rate should have a factor two.

5.1.2 Bi-stable behaviour of BCDs

Evidence from [130] reveals that even when using consistent vendors, processes, and experimental setups, the data scattering of the measured B_iO_i concentration becomes noticeable for irradiation fluences exceeding 10^{12} n/cm^2. Surprisingly, this scattering occurs even when measuring the same sample. The unusually large spread of results in boron-doped

silicon samples suggests that it is not solely due to measurement errors or material variations. Instead, it may result from inherent sample manipulation.

The low reproductibility of the B_iO_i concentration measured can be attributed to the bi-stable nature of the B_iO_i defect and in a more general sense, of the BCDs. These complexes exhibits at least two configurations, labeled as A and B. Bi-stability can occur when a stable configuration of a defect in the lattice changes with its charge state. The two configurations A and B are:

- Configuration A (BCD_A^+): The basal state behaviour of the complexes, with conditions of equilibrium that contribute with positive charge to the space charge and a donor level of 0.23 eV. This configuration contributes to the acceptor removal mechanism twice by deactivating the B_s acceptor and creating a BCD donor.

- Configuration B (BCD_B^0): The state of non-equilibrium conditions due to the trapping of one electron, observed indirectly by the variations of the A configuration with a not electrically active behaviour. This configuration minimizes the effect of the acceptor removal mechanism, since it just contributes to the deactivation of the B_s acceptor but it does not introduce an additional donor level.

And then, by considering these two behaviours of the B_iO_i complex in competing with the substitutional Boron, then the rate of the defect introduction $g_{B_iO_i} = g_{B_iO_i{}^A} + g_{B_iO_i{}^B}$ contributes to the rate of the acceptor removal following:

$$g_B = 2 \times g_{B_iO_i{}^A} + g_{B_iO_i{}^B} \tag{5.4}$$

The study conducted by [127] revealed that the transition between these configurations can occur in the following ways:

- From A to B: After exposing n-in-p pin diodes to an excess of carriers achieved through forward biasing, thermal treatments at moderate temperatures, or exposure to ambient light during sample manipulation before dark electrical measurements, a transition between configurations was observed. This transition was reflected in the shift of the full-depletion voltage (V_{FD}), which correlated with changes in the effective doping of the p-type substrate.

- From B to A: Returning the samples to a dark environment caused V_{FD} to revert to its previous equilibrium value. However, this reversal process is much slower compared to the transition from A to B.

The samples investigated in [130] permitted the determination that the samples reached a steady state within a period of seven hours, and that electrical measurement performed before presented different results. The bi-stable behavior of the BCDs defect fully accounts for these variations.

5.1.3 Effect of the resistivity on the acceptor removal and reactivation

It is important to note the effect of the resistivity level of the fabrication substrate on the acceptor removal mechanism and consequently the acceptor recovery potential. It has been studied [131] that the doping concentration (which inversely changes the resistivity) has a correlation with acceptor removal such that for devices with high initial doping concentrations (low resistivity), the fraction of acceptors removed by irradiation is lower, or in other words, the higher the doping concentration, the lower the acceptor removal.

Once the devices have been irradiated, not only the initial doping concentration affects the acceptor removal, but also the possible acceptor recovery, but in a different sense: According to the previous results concerning the transitions from the state BCD^{A+} to the state BCD_B^0, which is beneficial by reducing the acceptor removal effects, the results obtained in [130] on samples with different resistivity, after injecting the same small forward current at 20 °C, were observed:

- An increase of approximately 6.3 V in the V_{FD} was observed for sensors with high resistivity of 12 kΩcm.
- An increase of around 2.3 V in the V_{FD} for sensors with intermediate resistivity of 250 Ωcm.
- No reactivation of acceptors (change in the V_{FD}) was seen in samples with low resistivity of 50 Ωcm.

The efficiency of transitions from A to B states (by forward current injection), which is desired to reactivate acceptors, increases in direct proportion to the resistivity of the sample. This is attributed [127] to the differences in the volume containing greater density of free electrons over holes $n > p$: in low resistivity samples in which no acceptors reactivation was observed, there is a smaller volume containing $n > p$, while in high resistivity samples the volume where $n > p$ is greater.

5.2 Enhancing Radiation Hardness of LGADs through Gain Layer Carbon Enrichment

The enrichment of the gain layer of LGADs with co-implanted carbon has been proposed [132] with the aim of mitigating or reducing the undesirable effects of radiation associated with the gain reduction of these devices. Carbon enrichment has been investigated as a method of improving the radiation hardness of low gain avalanche detectors and it has been shown that a moderate addition of carbon concentration within the gain layer can reduce the acceptor removal rate [103], thereby improving the radiation hardness.

What happens microscopically with carbon co-implantation is that carbon competes with boron for the binding of highly reactive oxygen, here carbon acts as a trap for interstitial oxygen atoms, making them unavailable and therefore helping to reduce the formation of the B_iO_i defect, the primary cause of the acceptor removal mechanism, as described above. However, an excessive concentration of carbon atoms in the gain layer can be counterproductive as it could promote the formation of B_iC_s complexes which contribute to boron deactivation. In the following sections we will explore the optimal level of carbon enrichment in LGAD gain layers to improve their radiation resistance.

5.3 Permanent LGAD damage: Single-Event Burn-Out (SEB)

Single Event Burnout (SEB) is a breakdown phenomenon caused by thermal runaway resulting from the interplay of impact ionization and lattice heating in silicon sensors exposed to high electric fields. While SEBs impact not only Low-Gain Avalanche Diodes (LGADs), recent requirements for LGAD in High Energy Physics experiments have made SEBs more common in irradiated samples biased at voltages exceeding 600 V during test beams. This destructive breakdown manifests as a visible crater with a characteristic star-shaped burn mark on the sensor surface as can be seen in Figure 5.4.

SEBs are a well-known limitation for high-voltage power diodes and avalanche diodes used in High Energy Physics. They arise from high local currents initiated by ion strikes, which, in principle, do not provide sufficient energy or duration to cause permanent damage to the crystal. However, if the sensor operates within a bias voltage range corresponding to a reverse current twice that contributed by the heavy ion, positive feedback occurs due to avalanche gain, leading to device heating [133]. Several factors can influence the occurrence of thermal runaways, including the physical dimensions of the device, thermal conductivity

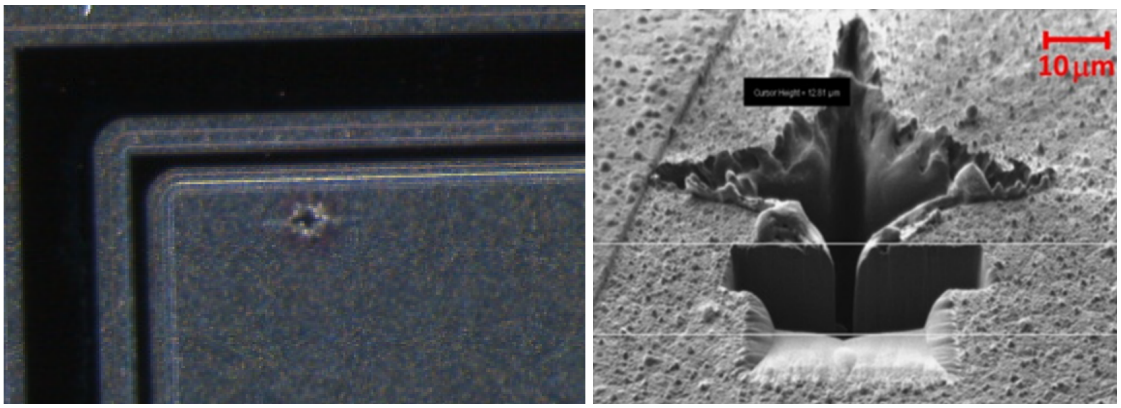

(a) LGAD with a crater due to SEB (b) Microscopic photograph of the crater

Fig. 5.4 (a) is a typical star-shaped mark due to SEB on a HPK-P2 LGAD irradiated to $2.5 \times 10^{15}\,\mathrm{n_{eq}\,cm^{-2}}$ during a DESY beam test. (b) is the microscopic photograph of a burn mark of a SEB of a CNM LGAD sensor. Images courtesy of [29].

to the heat sink, material heat capacity, and the geometry of charge deposition. Avalanche diodes become more susceptible to SEBs due to gain.

During test beams, LGADs can experience energy depositions of up to 100 MeV from a single charged hadron [134]. This generates a high carrier density, which screens carriers from being swept away, altering local resistivity converting sensor conductive. The field collapses in regions of high free carrier density, causing an increased voltage drop where density is lower. This intensified field leads to avalanche breakdown. The stored charge on the sensor electrodes and the high-voltage (HV) filtering capacitor discharges through the sensor. The resulting energy release can melt the silicon, creating a crater and permanently damaging the sensor.

Research by [135] suggests that LGAD failures are not due to design flaws but rather to the intensity of the electric field. They propose a "safe zone" of operation where the electric field is kept below $12\,\mathrm{V/\mu m}$. Indirectly, carbon enrichment also helps reduce the occurrence of SEB by lowering the required operating voltage for irradiated sensors.

Chapter 6

LGADs for the Endcap Timing Layer detector of CMS

This chapter presents a detailed analysis of the radiation tolerance (to neutrons and protons) of LGADs manufactured at Instituto de Microelectrónica de Barcelona - Centro Nacional de Microelectrónica (IMB-CNM), Hamamatsu Photonics K.K. (HPK), and Fondazione Bruno Kessler (FBK).

The first section describes the requirements that the sensors must meet according to the ETL sub-detector of the CMS, in terms of geometry, electrical properties and performance such as time resolution for all LGADs, before and after irradiation. The second section presents the radiation tolerance studies of LGADs produced at IMB-CNM, detailing specific manufacturing runs (#12916, #15246, and #15973). The third section deals with the LGADs manufactured at HPK, particularly examining the HPK2 production. Finally, the fourth section discusses the studies conducted on LGADs from FBK, highlighting the UFSD4 production. Special focus has been placed on understanding the effect of carbon co-implantation on reducing the acceptor removal.

6.1 Design and requirements of the LGAD for the Endcap Timing Layer detector of CMS

As mentioned in section 1.1 on the HL-LHC, this upgrade will have a greater amount of luminosity than the existing performance of the LHC and therefore an increase in the radiation to which the detectors will be exposed, including the sub-detectors of the CMS experiment. The initial plan[136] for the CMS MIP Timing Detector Endcap considers the mounting of an active element consisting of about 39000 sensors, of which about 32000 are expected

to be exposed to a radiation fluence of 1×10^{15} $n_{eq}\,cm^{-2}$ and the rest of 7000 sensors to be placed the high fluence region of 1.5×10^{15} $n_{eq}\,cm^{-2}$.

The hybrid sensors for the ETL will consist of an "assembly" which is the combination of the ASIC and the bump-bonded LGAD sensor which has a 16×16 pads of 1.3×1.3 mm^2 to operate in a working environment of -25 °C.

With regard to the requirements of LGAD sensors, the various manufacturers must carry out several characterization campaigns to certify that their LGAD technology meets the specifications of the ETL sub-detector of the CMS experiment, which are collected in documents such as the so-called "Market Survey" [136], in which also important parameters are defined, such as the breakdown voltage (V_{BD}), defined as the voltage at which the current increases by an order of magnitude in less than 5 V, and the so-called $V(8\,\text{fC})$, which is the bias voltage required for the LGAD to collect 8 ± 2 fC per MIP, as well as the time resolution requirements of the sensors.

Table 6.1 Summary of the geometric specifications for LGAD n-in-p sensors to comply with the Market Survey. Adapted from [136].

Geometric specification for the LGAD sensors	
Nominal thickness D of the active volume	45–65 µm
Overall thickness	200–800 µm
Number of pads (for the "large size sensor")	16×16
Dimension of each pad	1.3×1.3 mm^2
Sensor edge (distance from the outermost pad to the physical edge)	< 1000 µm on the 4 sides
Pad opening for needle probing	min 80×150 µm^2
Bump-bonding pad opening	50–150 µm diameter
Max chipping at the sensor edge	< 20 µm

The geometric specifications for the Market Survey are summarised in Table 6.1. The electrical characteristics and performance of the sensors to be operated at -25 °C are given in Table 6.2, for fresh (non-irradiated) and irradiated sensors, which also includes the specifications for the samples with a carbon-enriched gain layer, since carbonation alters some properties of LGADs, as discussed in section 5.2.

Table 6.2 Summary of the electrical properties and functionality requirements of the LGAD sensors at $-25\,^{\circ}\mathrm{C}$, fresh (non-irradiated) and irradiated to comply with the Market Survey. Adapted from [136].

Fresh (non-irradiated) sensors	
Bulk depletion voltage	$< 50\,\mathrm{V}$
V_{BD} due to gain with all pads and GR connected to ground	130–250 V
Time resolution at V(8 fC) for single pad sensor in RS-telescope	$< 50\,\mathrm{ps}$
Pad isolation	$> 0.1\,\mathrm{G\Omega}$
No-gain distance between pads	$< 140\,\mu\mathrm{m}$
Micro discharge noise at the V(20 fC) working point	Absent
Max leakage current for large-size standard (carbonated) gain layer sensor at V(8 fC)	$1\,\mu\mathrm{A}$ ($10\,\mu\mathrm{A}$)
After irradiation of $1 \times 10^{15}\,\mathrm{n_{eq}\,cm^{-2}}$ or $1.5 \times 10^{15}\,\mathrm{n_{eq}\,cm^{-2}}$	
Bias to reach (8 fC)/active thickness (V(8 fC)/D)	$< 12\,\mathrm{V}/\mu\mathrm{m}$
V_{BD} due to gain with all pads and GR connected to ground	> V(8 fC)+30 V
Time resolution at V(8 fC), for single pad sensor in RS-telescope	$< 50\,\mathrm{ps}$
Pad isolation	$> 0.1\,\mathrm{G\Omega}$
Micro discharge noise at the V(8 fC) working point	Absent

6.2 Radiation tolerance studies of LGAD manufactured at IMB-CNM

The *Instituto de Microelectrónica de Barcelona - Centro Nacional de Microelectrónica* (IMB-CNM), part of the *Consejo Superior de Investigaciones Científicas* (CSIC), is the largest centre in Spain dedicated to research and development in micro and nano technologies for electronic applications[29]. The IMB-CNM carries out activities related to the design and manufacture of integrated circuits, semiconductor devices and materials. The CNM pioneered the introduction of the LGAD sensor for HEP applications [58].

In this section, the radiation tolerance study of the LGADs produced at the IMB-CNM will be described. This study is focused on two different manufacturing technologies: sensors from Silicon on Silicon (SiSi) wafers (as described in subsubsection 2.2.2.2) and sensors from Epitaxial grown wafers (see subsubsection 2.2.2.1). The motivation for exploring LGAD sensors manufactured with the two different types of wafers mentioned before was the limited availability of the the SiSi wafers. This type of wafers have *a priori* a more accurate and uniform doping concentration with respect to epitaxial wafers, however the turnaround time of the SiSi provider was so large that the study of, more available, epitaxial wafers was needed.

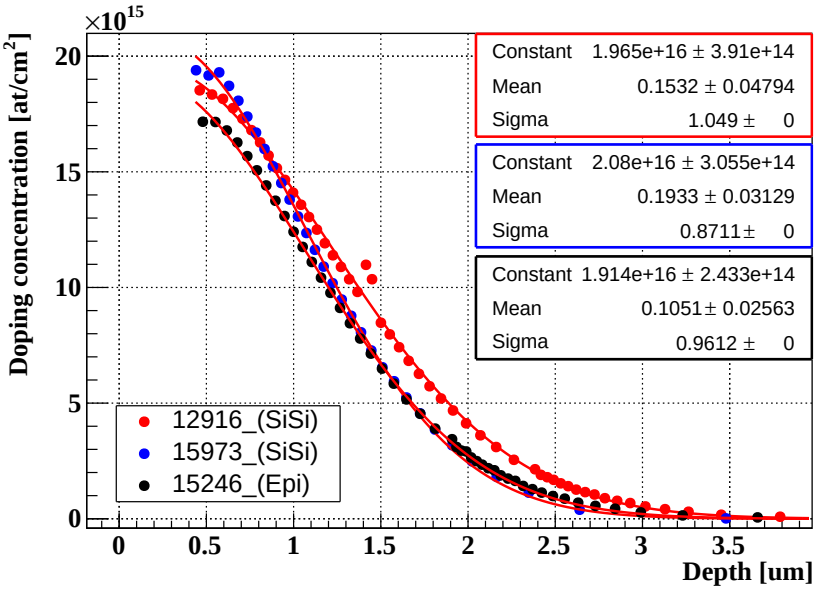

Fig. 6.1 Doped profiles of the gain layer of the non-carbonated samples from run #15973 (blue), run #15246 (black) and run #12916 (red), produced at the CNM. The sensors from run #15246 and run #15973 are very similar in shape and width, but the sample from run #12916 is slightly wider than the other SiSi run. The red line is the Gaussian fit of the profiles for the three runs.

Two types of gain layers are implemented: standard gain layer with solely Boron as dopant, and a second type with a co-implantation of carbon for increasing the radiation hardness (section 5.2) denominated as *carbonated*. The boron doping profile of the gain layer for all the LGADs studied presents a maximum close to the interface between the Si and the SiO_2; this is why it has been denominated *shallow* junction implantation.

Figure 6.1 is a comparison of the doping profiles from the three manufacturing runs characterized and their corresponding fits. The sensors from run #15246 (epitaxial) and run #15973 (SiSi) have the same doping shape, but the sample from run #12916 (SiSi) is slightly wider than the others runs, with a width (sigma) of 1.05 µm, compared to the 0.87 µm and 0.96 µm for the runs #15973 and #15246 respectively, assuming gaussianity. This small difference in the width will be use to differentiate between the two runs fabricated with the SiSi technology, using, indicating if the doping profile width is "Narrow (N)" or "Broad (B)" and using a "Production ID" which is an internal name used only in this thesis for the better identification of the samples that comprises the Producer_Wafer-Type_Implant-Type_Co-Implant-Dose.

Table 6.3 is a summary of the sensors from the different runs produced at IMB-CNM, including the boron and carbon doses, the wafer type, the temperature and dry oxidation

time (DOT) for the impurities drive-in, the implantation energy and the irradiation fluences studied.

Table 6.3 Summary of the LGADs samples from the runs manufactured at IMB-CNM on SiSi and epitaxial wafers. The data set includes information on the boron and carbon doses, the type of gain layer, and the dry oxidation time (DOT) and temperature for the drive-in, as well as the irradiation fluences under study. The implantation energy for all the wafers was 100 keV. The superscripts "R" and "N" indicates if the a "Radioactive Source" and/or "Noise" characterization was carried over the samples of that wafer. The production ID is an internal name used only in this thesis for the better identification of the samples that comprises the Producer_Wafer-Type_Implant-Type_Co-Implant-Dose.

RUN	Wafer	Production ID	B. Dose $[10^{13} cm^{-2}]$	C. Dose $[10^{13} cm^{-2}]$	Dopant Drive-in [°C / min]	Fluences $[10^{14}\ \mathrm{n_{eq}\,cm^{-2}}]$
12916	$W2^{R}$	CNM_SiSi_B	2.1	0	1150/90	0, 4, 8, 15, 25
15246	$W8^{RN}$	CNM_EPI_C	1.9	10	1100/180	0, 6, 10, 15
	$W10^{R}$	CNM_EPI	1.9	0	1100/180	0, 6, 10, 15
15973	$W1^{R}$	CNM_SiSi_N	1.9	0	1100/180	0, 4, 8, 15, 25
	W2	CNM_SiSi_N_C1	1.9	10	1100/180	0, 4, 8, 15, 25
	W3	CNM_SiSi_N_C2	1.9	20	1100/180	0, 4, 8, 15, 25
	$W4^{RN}$	CNM_SiSi_N_C3	1.9	30	1100/180	0, 4, 8, 15, 25
	W5	CNM_SiSi_N_C6	1.9	60	1100/180	0, 4, 8, 15, 25
	$W6^{RN}$	CNM_SiSi_N_C9	1.9	90	1100/180	0, 4, 8, 15, 25

6.2.1 LGAD on Silicon-on-Silicon substrates

Silicon-on-Silicon (SiSi) wafers were the initial choice for LGAD substrates, primarily due to the benefits of wafer-to-wafer bonding. This method allows for the use of high-resistivity wafers as the active substrate, which offers improved consistency in wafer-to-wafer uniformity compared to the variations typically seen in epitaxial manufacturing processes. During this study, two separate SiSi LGAD production runs were executed, each utilizing gain layer implantation profiles of different widths, as seen in Figure 6.1. For the narrower gain layer, carbon co-implantation was also performed at various dose concentrations to evaluate its effect on the radiation hardness of the LGADs.

In this section, we will present the characterization results of the wide boron implant (run #12916) and the narrow implant (run #15973) and conduct a comparative study of the effect of the doping profile width and carbon co-implantation on the radiation tolerance of the LGADs.

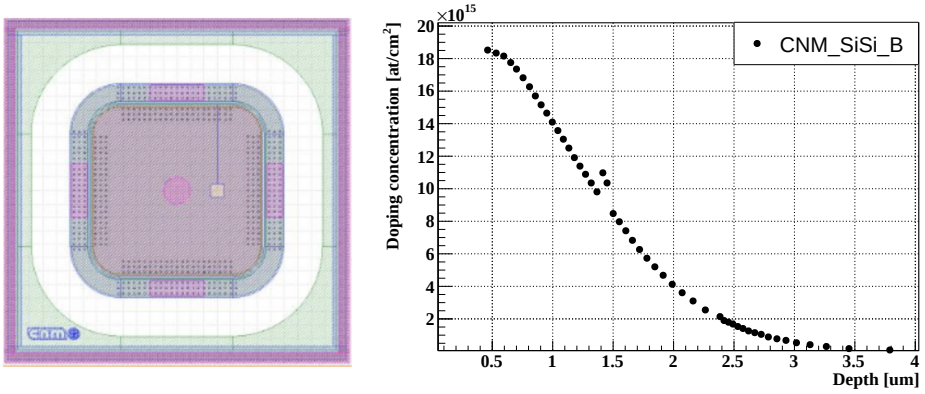

(a) Top view layout (b) Doping profile of the GL

Fig. 6.2 (a) is the top view of a single pad sample characterised. The main pad of the sensor is visible at the center (magenta) and the GR (dark green) is located around the main pad. The optical window is the small square at the right of the center. In (b) we can see the gain layer doping profile extracted from the electrical characterization for these devices.

6.2.1.1 Broad gain layer in standard SiSi substrates

Samples description: The LGAD Run #12916 (CNM_SiSi_B) was manufactured on silicon-on-silicon wafers, with 10 cm in diameter and an active thickness of 50 µm and 300 µm thick of low resistivity support wafer bonded to the active wafer of high resistivity. The samples used for this study were single pad devices with a total area of 2.6×2.6 mm^2 including the guard-ring (GR) and an active area of 1.3×1.3 mm^2. The samples have an optical window, that is an opening in the metallization of 100×100 µm^2 allowing direct illumination of the silicon with a laser for characterization with TCT. Figure 6.2 shows a top view of the single pad samples (a) used for this study and (b) is the gain layer doping profile extracted from the electrical characterization (see subsection 4.3.3 for calculation methodology) for these devices. These sensors were designed with an inter-pad (IP) distance, which is the distance between the end of the $p+$ gain layer of two adjacent pads, of 57 µm.

Before irradiation a total of 11 LGAD samples were characterised and from these samples, 6 were irradiated in the 250 kW TRIGA Mark II reactor at the Jožef Stefan Institute (see section 4.7): two samples at a irradiation fluence of 4×10^{14} n_{eq} cm^{-2}, two at 8×10^{14} n_{eq} cm^{-2}, one at 15×10^{14} n_{eq} cm^{-2} and one to a fluence of 25×10^{14} n_{eq} cm^{-2}.

IV characteristics: The leakage current of the main pad of the devices was measured before the irradiation at -25 °C, the expected operating temperature of the ETL detector, and following the procedure described in subsection 4.3.1. Figure 6.3 contains the IV curves from these samples, which exhibit a low current for all samples with minimal dispersion

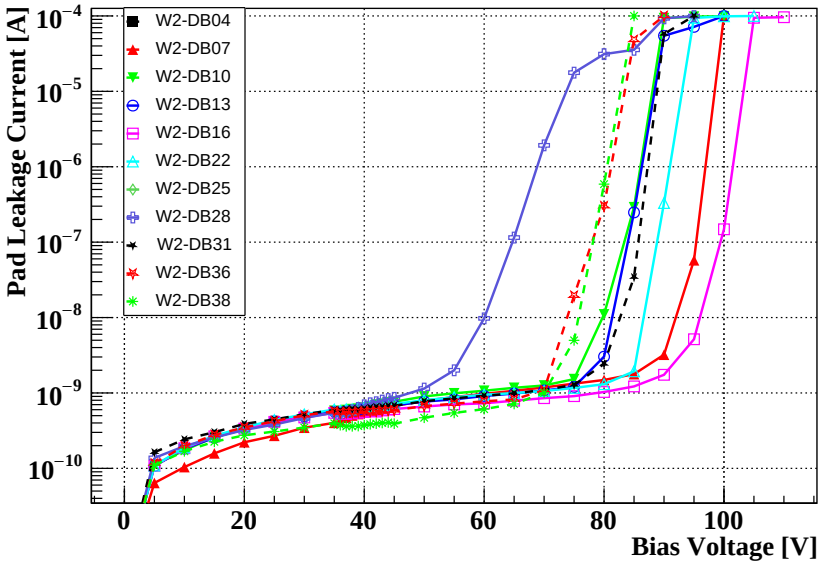

Fig. 6.3 Leakage current at $-25\,^{\circ}\mathrm{C}$ from the main pad as a function of the bias voltage applied of the LGADs from run #12916 (CNM_SiSi_B). The V_{BD} of the samples have values in the range of 60–95 V

between them. In contrast, the case of the breakdown voltage V_{BD} values have a high degree of dispersion, spanning a wide range of approximately 60–95 V. Conversely, the calculation of V_{GL} for the non-irradiated samples was not feasible due to the limitations of the current resolution of the sourcemeter employed and the selected voltage granularity. This was evidenced by the absence of a clear *kink* that is characteristic of gain layer depletion (e.g. Figure 4.14).

The IV curves of the irradiated samples are shown in Figure 6.4 (a) and an enlarged view of the region containing the junction between the multiplication layer and the bulk in Figure 6.5. The irradiation damage to the multiplication layer is clear as the voltage at which the breakdown starts (V_{BD}) are higher and the V_{GL} of the samples are lower compared to the values obtained prior the irradiation. It is also clear that these changes are different depending on the fluence at which the samples were irradiated.

The V_{BD} values per irradiation fluence (mean) resulting are listed in Table 6.4, and the V_{GL} calculated from the IV characterization are written together with the calculated from the CV curves in Table 6.5.

CV characteristics: The CV characterization before the irradiation of the samples were conducted at $20\,^{\circ}\mathrm{C}$. We can see the CV curve in Figure 6.6 and an enlarged view of the gain

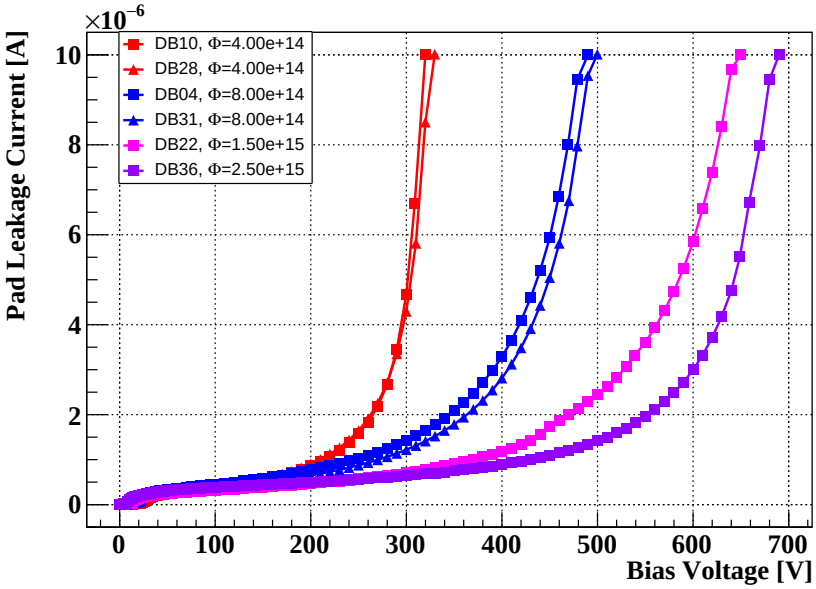

Fig. 6.4 Pad leakage current at −25 °C after irradiation as a function of the reverse bias of the CNM_SiSi_B samples. A clear radiation damage can be seen according to the irradiaiton fluence.

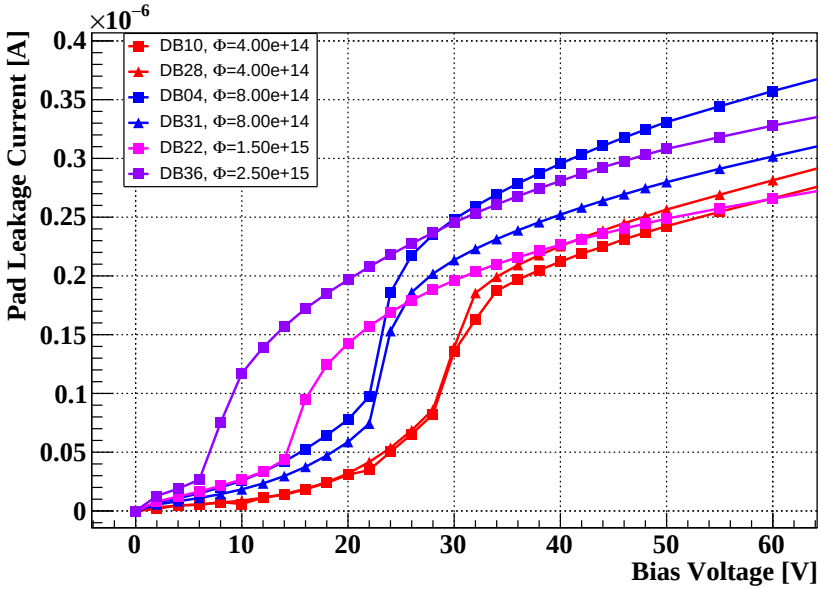

Fig. 6.5 Pad leakage current at −25 °C after irradiation as a function of the reverse bias of the CNM_SiSi_B samples. Enlarged view of the gain layer region of the IV curves where the characteristic *kink* corresponding to the gain layer and bulk transition can be seen.

Table 6.4 Summary of the break-down voltages V_{BD} at $-25\,^{\circ}$C calculated from the IV curves, at the different irradiation fluences ($n_{eq}\,cm^{-2}$), from the CNM_SiSi_B samples.

	V_{BD} from IV at different fluences ($n_{eq}\,cm^{-2}$)			
Fresh	4×10^{14}	8×10^{14}	15×10^{14}	25×10^{14}
60–95 V	270 V	400 V	550 V	560 V

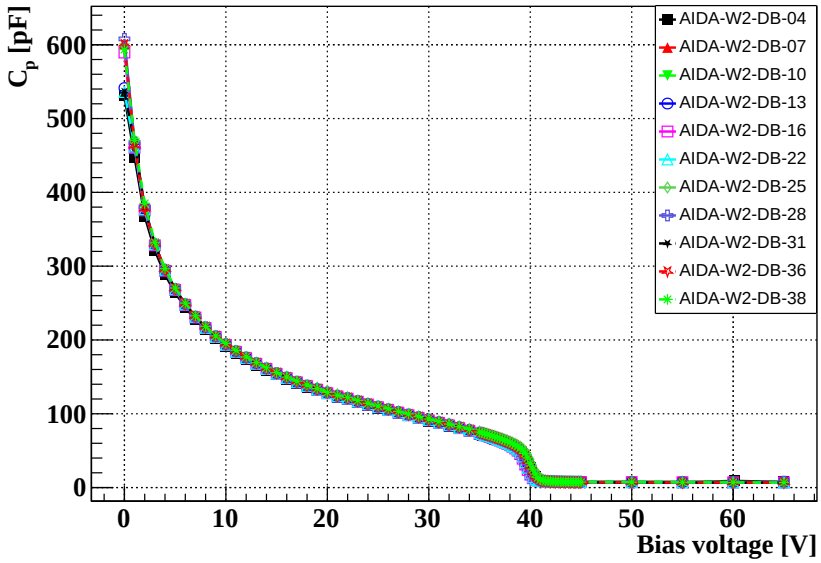

Fig. 6.6 Capacitance of the main diode is shown as a function of reverse bias before irradiation of the LGDAs from W2 of the CNM run #12916 (CNM_SiSi_B), measured at 10 °C.

layer region can be seen in Figure 6.7. The V_{GL} and V_{FD} were calculated yielded values of approximately 39 V and 42 V respectively with good homogeneity among the samples measured as can be seen in Figure 6.7. The final capacitance C_{end} was found to be of approximately 4.5 pF above the V_{FD}, which is in accordance with the expected value given the geometry of the devices.

The CV curves after irradiation of the samples can be seen in Figure 6.8 and an enlarged view of the gain-layer region in Figure 6.9, showing the peaks that are only visible at low frequency when measuring irradiated sensors (subsubsection 4.3.2.2). There is a clear decrease in V_{GL} with fluence, which is an indicator of radiation damage, and these V_{GL} are summarised in Table 6.5. The C_{end} remains the same as before the irradiation at a bias above 60 V.

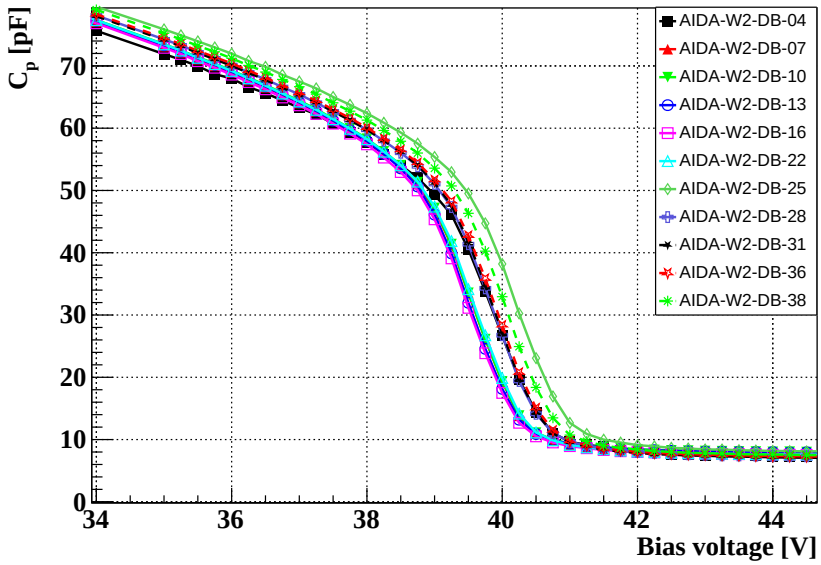

Fig. 6.7 CV curves before irradiation of the LGDAs from W2 of the CNM run #12916 (CNM_SiSi_B), measured at 10 °C. Enlarged view of the gain layer region. The V_{GL} and V_{FD} are of around 39 V and 42 V respectively

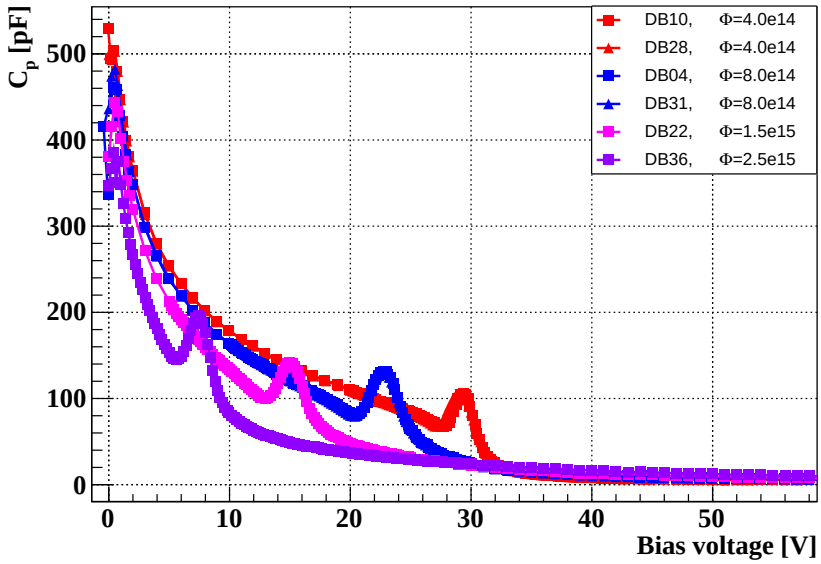

Fig. 6.8 CV curves are shown as a function of reverse bias after irradiation, measured at 10 °C of the LGDAs from W2 of the CNM run #12916 (CNM_SiSi_B).

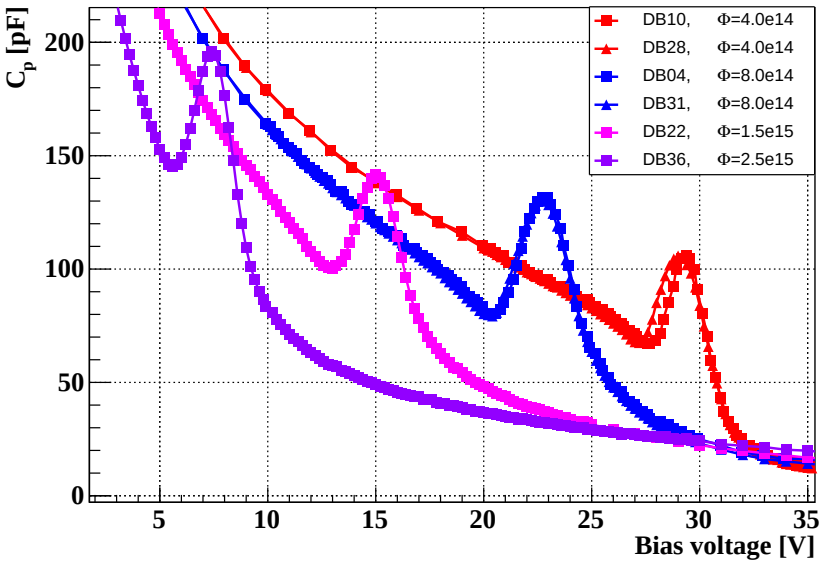

Fig. 6.9 CV curves after irradiation of the LGDAs from W2 of the CNM run #12916 (CNM_SiSi_B), measured at 10 °C. An enlarged view of the gain layer region is shown in. The different radiation damage depending of the fluence can be seen by the shift of the peak. The V_{GL} is determined following the procedure of subsubsection 4.3.2.2.

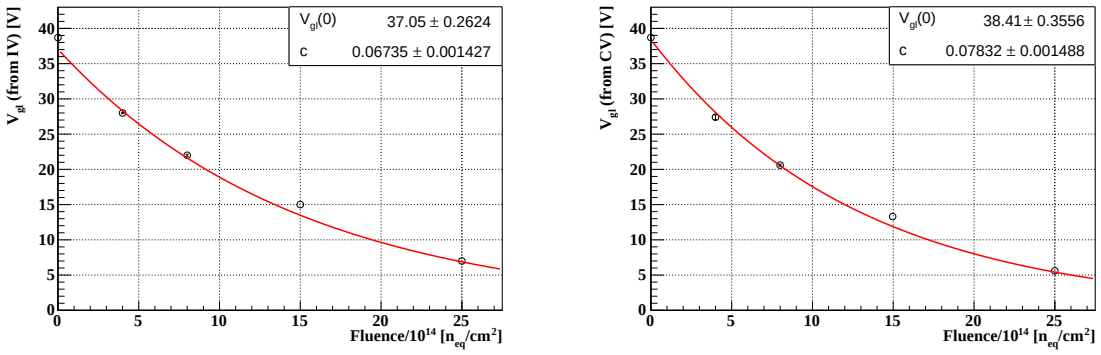

(a) V_{GL} from IV vs. fluence

(b) V_{GL} from CV vs. fluence

Fig. 6.10 Gain-layer depletion voltage of the CNM_SiSi_B samples from IV (a) and CV (b) as a function of the fluence and their respective fits (red) from which the acceptor removal coefficient is calculated: $c[10^{-16}\,\mathrm{cm}^2] = 6.7$ calculated from IV and $c[10^{-16}\,\mathrm{cm}^2] = 7.8$ from CV.

Acceptor removal coefficient: The V_{GL} obtained from both IV and CV are summarized in Table 6.5 for the fresh and irradiated samples at the different fluences studied. The difference in V_{GL} obtained from the two types of electrical characterization is not large in most cases, around 1 V. With these values of V_{GL} plotted against the irradiation fluence, we can fit the resulting curve and calculate the acceptor removal coefficient as described in section 5.1. Since V_{GL} cannot be calculated from the IV curves, I decided to take the value of the same V_{GL} from the CV curves, which were also seen to be very close to IV in the other CNM runs (section 6.2.2 and section 6.2.1.2).

Table 6.5 Summary of the V_{GL} values calculated from the electrical characterization of capacitance and current of the CNM_SiSi_B samples, before and after irradiation.

Fluence ($n_{eq}\,cm^{-2}$)	V_{GL} from IV	V_{GL} from CV
0	-	39.1 V
$4 \times 10^{14}\,n_{eq}\,cm^{-2}$	27.1 V	27.4 V
$8 \times 10^{14}\,n_{eq}\,cm^{-2}$	21.9 V	20.6 V
$15 \times 10^{14}\,n_{eq}\,cm^{-2}$	15.1 V	13.2 V
$25 \times 10^{14}\,n_{eq}\,cm^{-2}$	6.8 V	5.6 V

Figure 6.10 shows the V_{GL} values versus the irradiation fluence of the CNM_SiSi_B samples, calculated from the IV curves (a) and from the CV curves (b) and their respective fit (red). From the fit of the two plots then the acceptor removal coefficient can then be calculated, resulting in $c[10^{-16}\,cm^2] = 6.8$ calculated from the IV and $c[10^{-16}\,cm^2] = 7.7$ from the CV characteristics.

Charge collection:

Time resolution: Timing measurements were conducted using the RS setup (see section 4.5) on the irradiated LGADs. Figure 6.11 illustrates the charge and Figure 6.12 the time resolution obtained for the neutron-irradiated LGADs at fluences of $4 \times 10^{14}\,n_{eq}\,cm^{-2}$, $8 \times 10^{14}\,n_{eq}\,cm^{-2}$ and $15 \times 10^{14}\,n_{eq}\,cm^{-2}$. The doted lines are the limits for the ETL requirements: a charge above 8 fC and a time resolution below 50 ps, both at a bias voltage less than $12\,V/\mu m$. The results for non-irradiated LGADs are not included in these plots but these samples exhibited a charge exceeding 15 fC with a time resolution of ≈ 30 ps at low temperature, which falls within the expected range. However, for the irradiated LGADs, a clear degradation in both charge and time resolution is observed as a function of fluence.

Considering the requirements for the LHC phase II upgrade experiments, achieving a time resolution below 50-70 ps at a maximum bias voltage of 600 V is only possible for

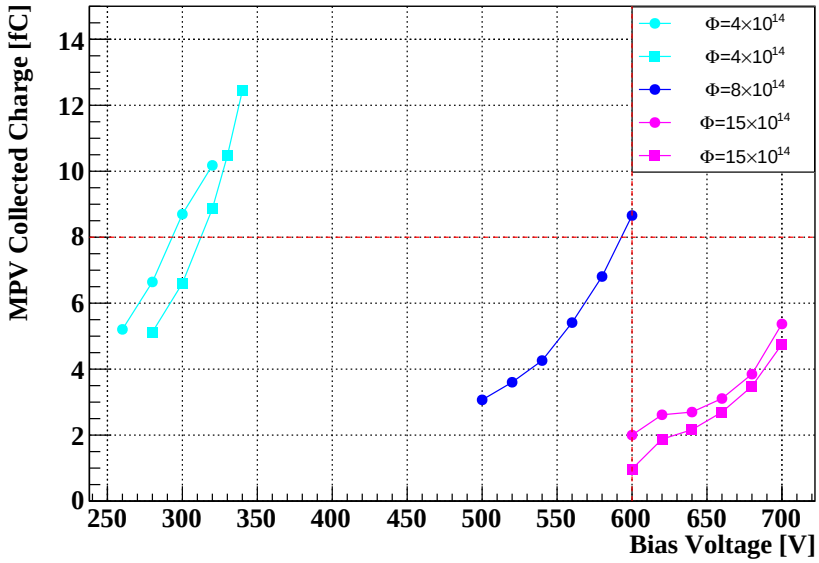

Fig. 6.11 Collected charge resulting from the radioactive source characterization setup for the run #12916 (CNM_SiSi_B) samples at $4 \times 10^{14}\,\mathrm{n_{eq}\,cm^{-2}}$ (turquoise), $8 \times 10^{14}\,\mathrm{n_{eq}\,cm^{-2}}$ (blue) and $15 \times 10^{14}\,\mathrm{n_{eq}\,cm^{-2}}$ (red) fluences. Unirradiated samples are not plotted, nor are samples irradiated to $25 \times 10^{14}\,\mathrm{n_{eq}\,cm^{-2}}$ which cannot be biased at higher voltages. The doted lines are the limits for the ETL requirements: a charge above 8 fC at a bias voltage less than $12\,\mathrm{V/\mu m}$

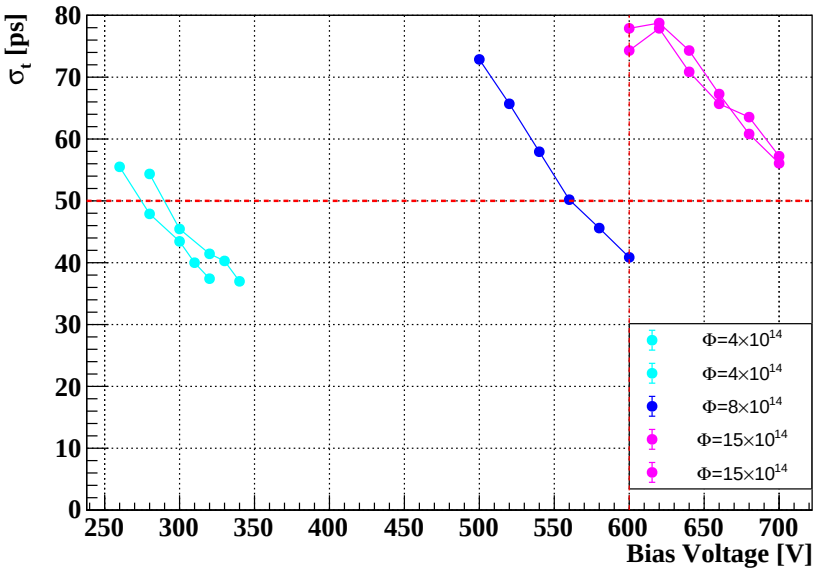

Fig. 6.12 Time resolution resulting from the radioactive source characterization setup for the CNM_SiSi_B samples at $4 \times 10^{14}\,\mathrm{n_{eq}\,cm^{-2}}$ (turquoise), $8 \times 10^{14}\,\mathrm{n_{eq}\,cm^{-2}}$ (blue) and $15 \times 10^{14}\,\mathrm{n_{eq}\,cm^{-2}}$ (red) fluences. Unirradiated samples are not plotted, nor are samples irradiated to $25 \times 10^{14}\,\mathrm{n_{eq}\,cm^{-2}}$ which cannot be biased at higher voltages. The doted lines are the limits for the ETL requirements: a time resolution below 50 ps at a bias voltage less than $12\,\mathrm{V/\mu m}$

fluences of $4 \times 10^{14}\,\mathrm{n_{eq}\,cm^{-2}}$ and $8 \times 10^{14}\,\mathrm{n_{eq}\,cm^{-2}}$. At the fluence of $15 \times 10^{14}\,\mathrm{n_{eq}\,cm^{-2}}$, the degradation in time resolution is more severe, and below the 600 V the time resolution exceeds 80 ps. Unfortunately, results for the highest fluence of $25 \times 10^{14}\,\mathrm{n_{eq}\,cm^{-2}}$ are not included in the present analysis. This is due to the fact that the samples in question were required to not be biased to voltages above the safe range in order to prevent the occurrence of fatal Single Even Burnouts (SEBs, see section 5.3).

6.2.1.2 Narrow gain layer in standard and carbonated SiSi substrates

Samples description: Building on the findings from the first Silicon-on-Silicon (SiSi) run discussed earlier, a second SiSi manufacturing run #15973 (CNM_SiSi_N) was carried out to enhance the radiation tolerance of LGADs. This run focused on implementing a reduced annealing (temperature) and doping dose, in order to reduce the initial gain, as previous experimental observations had shown improved radiation resistance of the gain layers. Additionally, carbon co-implantation was introduced with varying doses, aiming to further boost radiation hardness. While carbon co-implantation had been attempted in a previous IMB-CNM production, it failed to yield the anticipated improvement in radiation tolerance [137]. This unexpected outcome was attributed to excessive thermal annealing of the carbon impurities, which were implanted too early in the production sequence. The exposure to complete sequence of annealing steps led to excessive diffusion, significantly reducing the concentration of carbon atoms around the gain layer. To address this issue, the second SiSi production modified the implantation process. Carbon atoms were introduced after the boron implantation, ensuring they underwent the same thermal annealing as the boron used to create the gain layer. This adjustment aimed to maintain a higher concentration of carbon atoms in the critical region, potentially enhancing the radiation tolerance of the resulting LGADs.

The LGADs were manufactured on SiSi wafers with a diameter of 15 cm, this was the first LGAD fabrication run at IMB-CNM with such wafer diameter. The device wafer thickness is of 50 µm, defining the LGAD active width, while the handling wafer is 350 µm thick, acting as ohmic contact. The handle wafer resistivity is in the 0.001–1 Ω cm, while the device wafer resistivity is approximately 2 kΩ cm. These sensors were designed with an inter-pad (IP) distance, which is the distance between the end of the $p+$ gain layer of two adjacent pads, of 47 µm.

The fabrication parameters for this production, including the boron and carbon implantation doses, are detailed in Table 6.6. The main difference between the production wafers is the varying carbon dose.

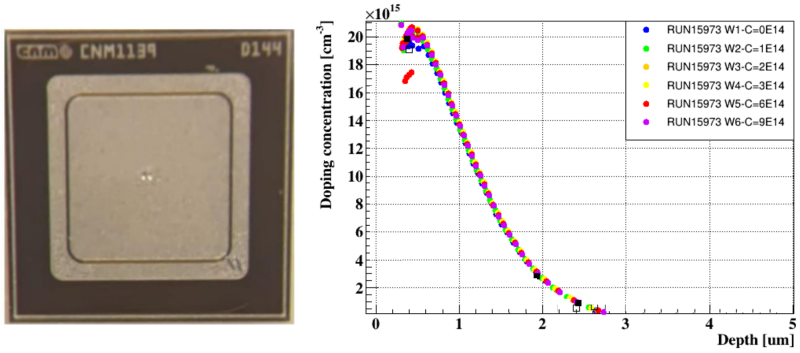

(a) LGAD top view (b) Doping profile of the GL

Fig. 6.13 (a) is the top view of a single pad sample of the CNM_SiSi_N sensors. (b) is the doping profile obtained from the electrical characterization. The labels in this plot indicates the carbon dose per every wafer.

Table 6.6 Differences carbon and boron doses for the different wafers employed on the run #15973 (CNM_SiSi_N).

Wafer	W1	W2	W3	W4	W5	W6
Boron energy (keV)	100	100	100	100	100	100
Boron dose (1×10^{13} cm^{-2})	1.9	1.9	1.9	1.9	1.9	1.9
Carbon energy (keV)	150	150	150	150	150	150
Carbon dose (1×10^{14} at/cm^2)	0	1	2	3	6	9

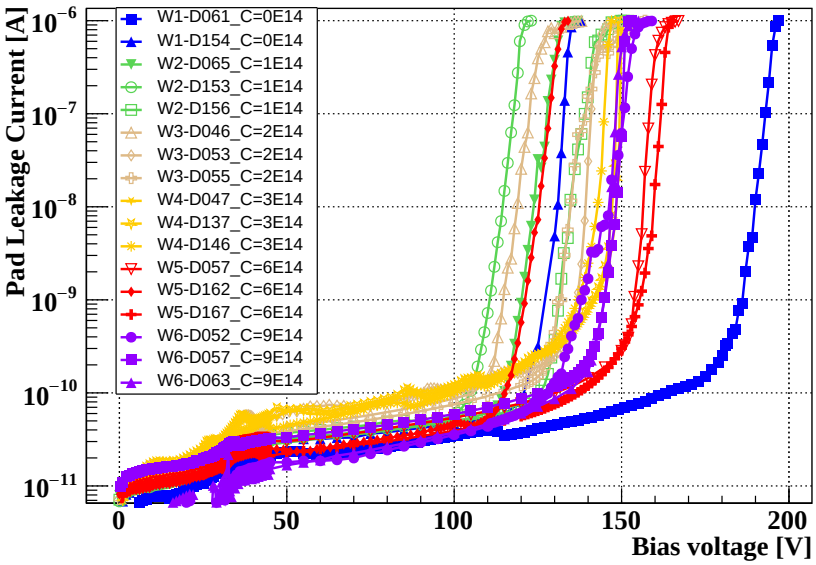

Fig. 6.14 Leakage current of the main diode as a function of the reverse bias voltage before irradiation for the run #15973 (CNM_SiSi_N) samples.

For this radiation tolerance study, the same type of single pad sensors as the one used for the broad gain layer SiSi production where used with the exception of the lack of the optical window. Figure 6.13 shows in (a) a top view of a single pad device from this run, where the main central pad and the GR around it are visible and (b) is the doping profile obtained from the capacitance-voltage characteristics.

18 non-irradiated LGAD samples were characterised: 3 samples for each of the 6 carbon doses. For the study with irradiated samples, a total of 48 samples were characterised: two samples from each carbon dose and per every of the 4 fluences, irradiated with neutrons to: $0.4 \times 10^{15}\,\mathrm{n_{eq}\,cm^{-2}}$, $0.8 \times 10^{15}\,\mathrm{n_{eq}\,cm^{-2}}$, $1.5 \times 10^{15}\,\mathrm{n_{eq}\,cm^{-2}}$ and $2.5 \times 10^{15}\,\mathrm{n_{eq}\,cm^{-2}}$, in the 250 kW TRIGA Mark II reactor at the Jožef Stefan Institute (JSI) in Ljubljana Slovenia. Non-irradiated devices were measured at room temperature, while irradiated devices were evaluated at a temperature of $-25\,^{\circ}\mathrm{C}$.

IV characteristics: Figure 6.14 shows the main diode leakage current versus bias voltage for the different sensor types before irradiation and at room temperature. The current of all samples is below the nano-ampere level over most of the bias voltage range before breakdown.

The breakdown voltage V_{BD} is around 120–150 V, except for one of the non-carbonated samples which has an unexpectedly large V_{BD} of about 190 V. The V_{BD} from this production

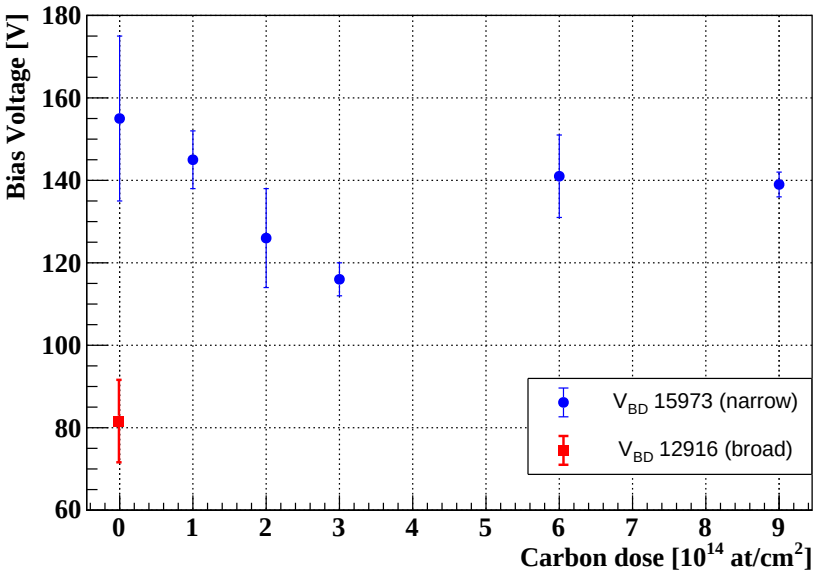

Fig. 6.15 Comparison of the V_{BD} before irradiation from run #15973 (CNM_SiSi_N) with narrow gain layer for the different carbon doses (CNM_SiSi_N_CX) in blue markers and added the run #12916 (CNM_SiSi_B) with broad standard gain layer in red marker for reference.

are systematically larger than V_{BD} obtained for the broad gain layer that is a clear indication of relative smaller gain of this production as we can see in Figure 6.15. The leakage current of the carbonated sensors is higher than that of the standard sensors, but this is not the case for the high carbonated sensors which appear to have less current, similar to the standard sensors. This is an expected results since the higher the defect concentration, the higher the leakage current.

The electrical characterization was performed on the irradiated samples at $-25\,^{\circ}\mathrm{C}$, from which two sensors for each carbon dose and fluence were measured. The pad leakage current of the sensors for the different carbon doses studied can be seen as a function of the reverse bias in Figure 6.16, Figure 6.17, Figure 6.18 and Figure 6.19 for the fluences of $4 \times 10^{14}\,\mathrm{n_{eq}\,cm^{-2}}$, $8 \times 10^{14}\,\mathrm{n_{eq}\,cm^{-2}}$, $15 \times 10^{14}\,\mathrm{n_{eq}\,cm^{-2}}$ and $25 \times 10^{14}\,\mathrm{n_{eq}\,cm^{-2}}$ respectively.

The shift of the V_{BD} towards higher values after irradiation is clearly visible in the case of the standard samples, starting from about 540 V for the fluence of $4 \times 10^{14}\,\mathrm{n_{eq}\,cm^{-2}}$ and about 740 V for those irradiated at $15 \times 10^{14}\,\mathrm{n_{eq}\,cm^{-2}}$.

The increase in V_{BD} for all samples indicates the suppression of the avalanche multiplication due both to the reduced mobility of the electrons and, specifically for the LGADs, the reduction of peak electric field around the gain layer. For the carbonated sensors in

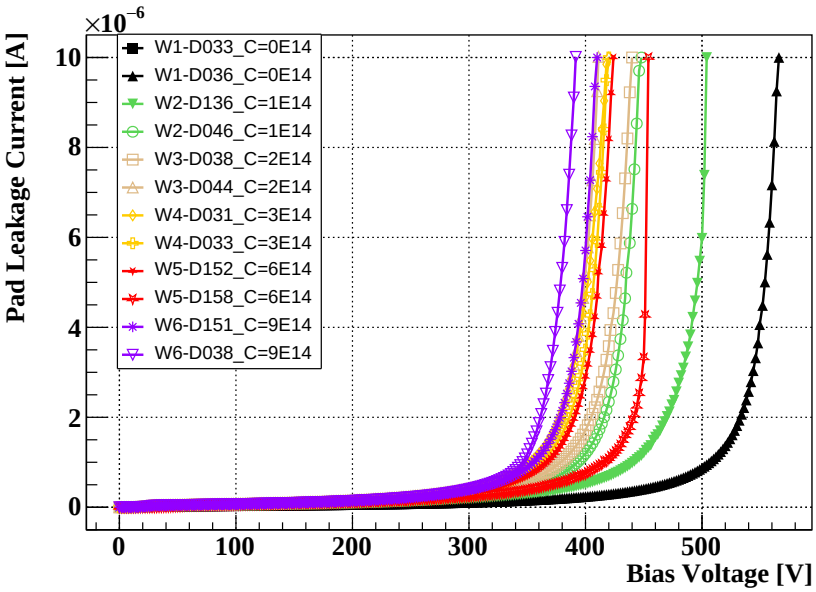

Fig. 6.16 The leakage current of the main pad after irradiation as a function of the reverse bias is shown for the standar CNM_SiSi_N and carbonated CNM_SiSi_N_CX samples of run #15973. Samples irradiated at 4×10^{14} $n_{eq}\,cm^{-2}$ are shown.

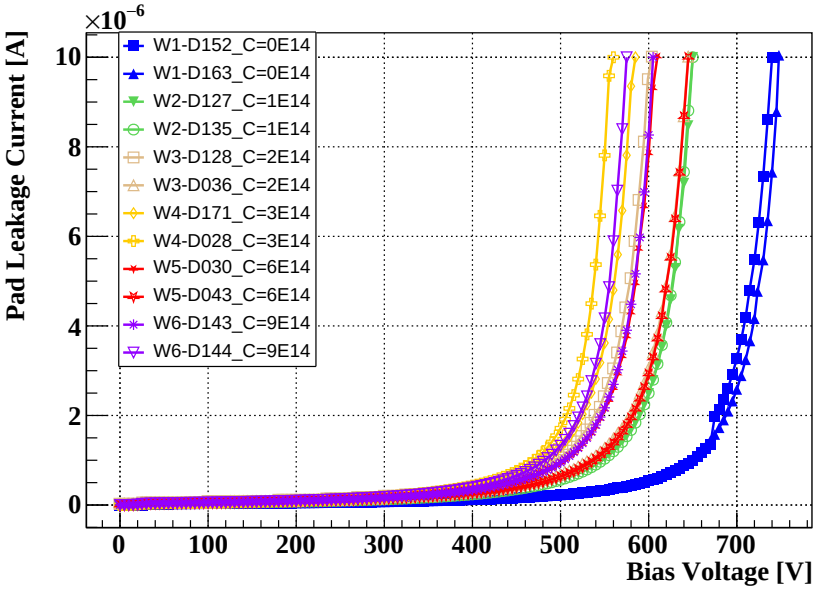

Fig. 6.17 The leakage current of the main pad after irradiation as a function of the reverse bias is shown. Samples irradiated at 8×10^{14} $n_{eq}\,cm^{-2}$ are shown.

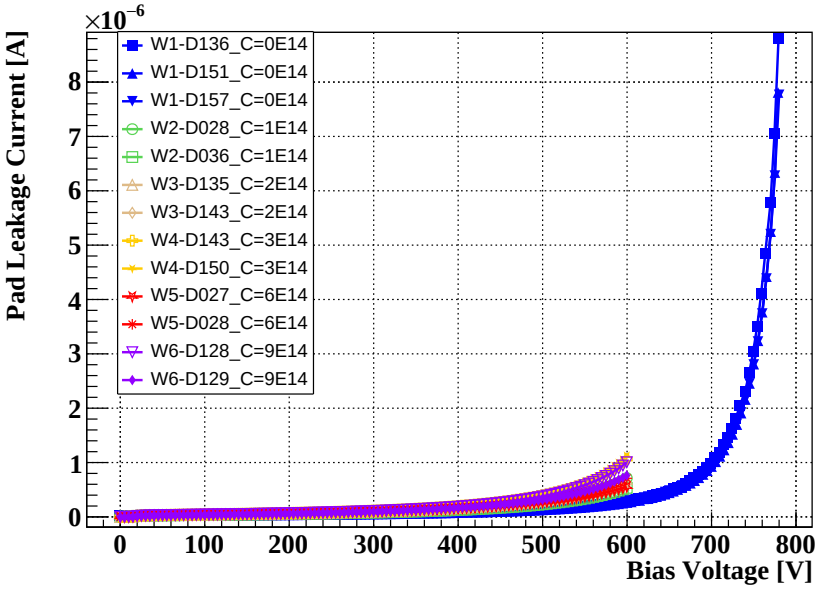

Fig. 6.18 The leakage current of the main pad after irradiation as a function of the reverse bias is shown for the standar CNM_SiSi_N and carbonated CNM_SiSi_N_CX samples of run #15973. Samples irradiated at 15×10^{14} n_{eq} cm^{-2} are shown.

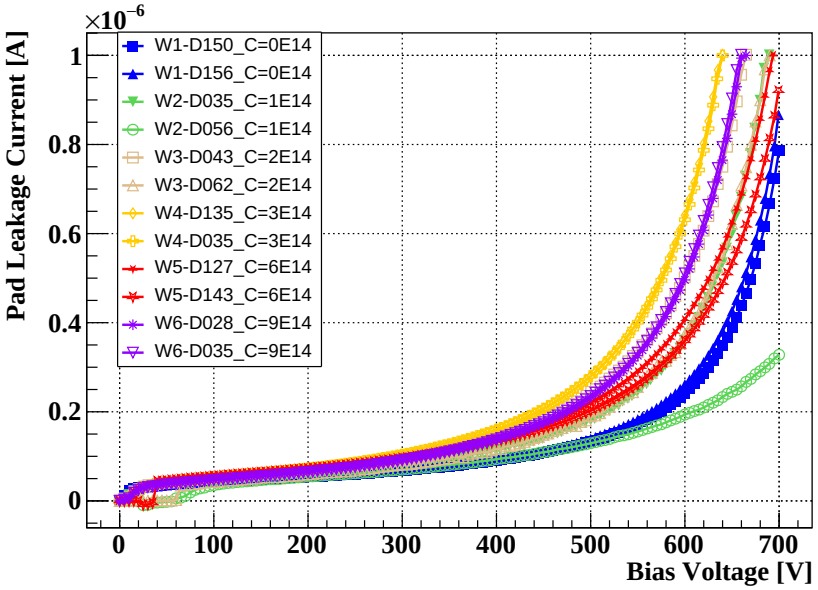

Fig. 6.19 The leakage current of the main pad after irradiation as a function of the reverse bias is shown for the standar CNM_SiSi_N and carbonated CNM_SiSi_N_CX samples of run #15973. Samples irradiated at 25×10^{14} n_{eq} cm^{-2} are shown.

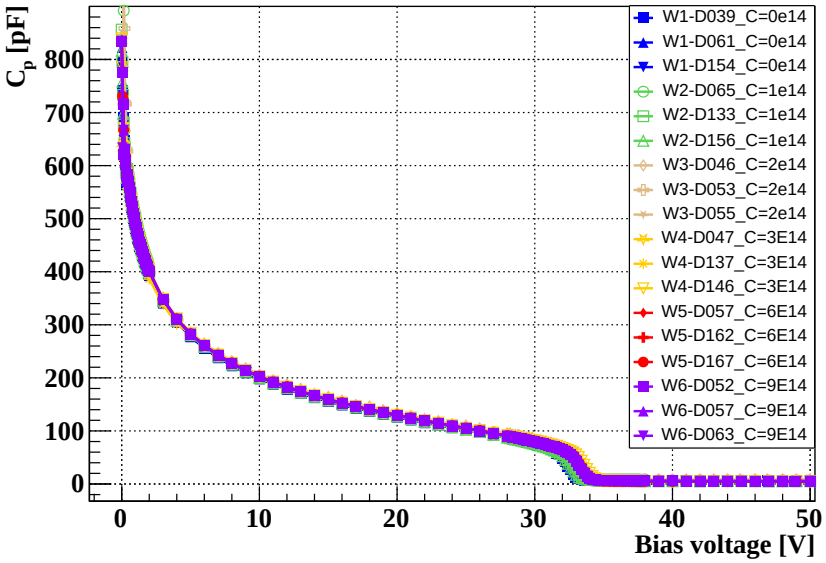

Fig. 6.20 Pad capacitance before irradiation as a function of the reverse bias for the standar CNM_SiSi_N and carbonated CNM_SiSi_N_CX samples of run #15973. The characteristic kinks in the curves due to the gain layer and bulk depletion can be observed.

Figure 6.18 the noise increased significantly before reaching the V_{BD} and the measurements had to be stopped at 600 V and not go to higher voltages to avoid damaging them.

CV characteristics: The CV characteristics of the samples prior to irradiation are illustrated in Figure 6.20 and an enlarged view of the gain layer region in Figure 6.21. Analysis of these curves revealed a V_{GL} of 31 V for standard samples and approximately 32 V for carbonated samples, as detailed in Table 6.7. We observed a final capacitance of about 4 pF at bias voltages exceeding 34 V for standard samples and 35 V for carbonated samples, with consistent results across sensors from the same wafer.

The reduced gain in this production, initially suggested by the higher V_{BD}, was corroborated by capacitance measurements. The V_{GL} value for the narrow gain layer is approximately 7 V lower than that of the broad gain layer. This decrease in V_{GL} can be attributed to the significantly narrower gain layer, which overcompensates for the increased boron implantation dose.

Related with the carbon co-implantation, the V_{GL} shows an increment from non-carbonated to carbonated sensors up to a dose of 3×10^{14}, but then it suffers a decrement when more carbon is added. This phenomenon has also been reported by other groups[138].

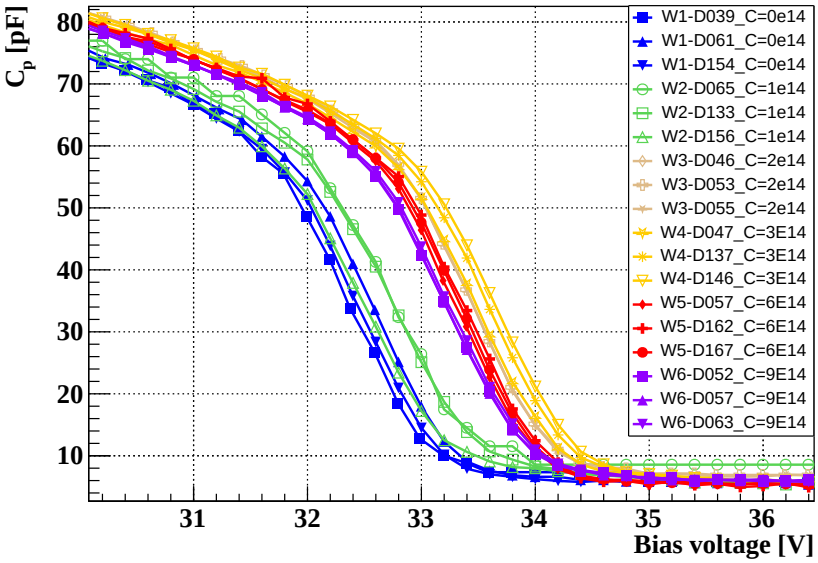

Fig. 6.21 Pad capacitance before irradiation as a function of the reverse bias for the standar CNM_SiSi_N and carbonated CNM_SiSi_N_CX samples of run #15973. Enlarged view of the gain layer region.

The pad capacitance of the samples after irradiation can be observed as CV curves in Figure 6.22 for the samples irradiated to $4 \times 10^{14}\,\mathrm{n_{eq}\,cm^{-2}}$, Figure 6.23 for the samples irradiated to $8 \times 10^{14}\,\mathrm{n_{eq}\,cm^{-2}}$, Figure 6.24 for the samples irradiated to $15 \times 10^{14}\,\mathrm{n_{eq}\,cm^{-2}}$ and Figure 6.25 for the samples irradiated to $25 \times 10^{14}\,\mathrm{n_{eq}\,cm^{-2}}$. We can observe the peaks described in subsubsection 4.3.2.2, which are only present in the irradiated samples and how the V_{GL} decreases with the irradiation fluence.

In addition to increasing the bias voltage to deplete the sensors after irradiation, it is important to observe the effect of carbon as the carbonated samples have higher V_{GL} compared to the standard samples, take for example plot (a) where V_{GL} of the carbonated devices is around 26.5 V whereas for the standard sensor it is around 22 V. The V_{GL} values for all the samples characterised are summarised in Table 6.7.

Acceptor removal coefficient: As previously stated, the LGADs from run#15973 demonstrate lower levels of inverse current, which has made it challenging to ascertain an objective definition of the V_{GL} from the IV curves for the various samples. Consequently, and given that the CV curves were measured with an adequate level of granularity and reproducibility, the acceptor removal coefficient was calculated exclusively based on the V_{GL} from the CV

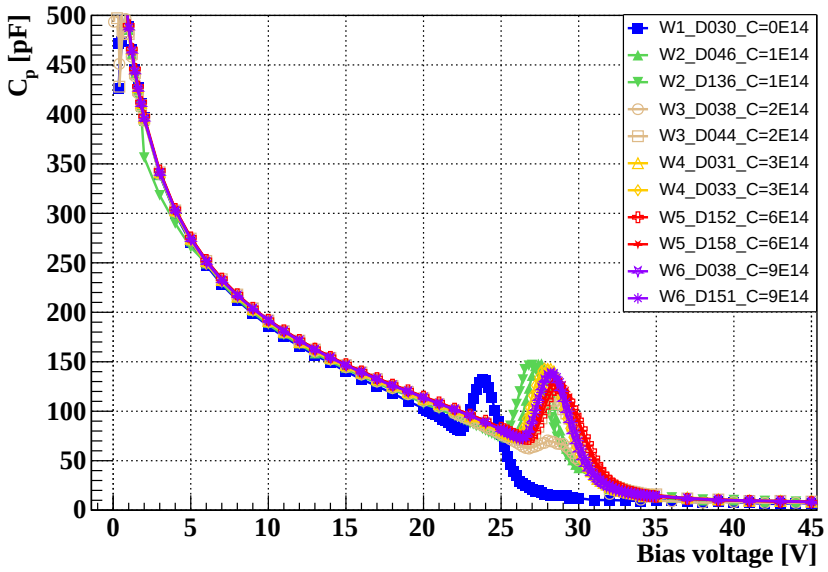

(a) Samples irradiated at $4 \times 10^{14}\,\mathrm{n_{eq}\,cm^{-2}}$

Fig. 6.22 Pad capacitance after irradiation as a function of the reverse bias. Standard CNM_SiSi_N and carbonated CNM_SiSi_N_CX devices irradiated to the fluence of $4 \times 10^{14}\,\mathrm{n_{eq}\,cm^{-2}}$.

characterization. Table 6.7 provides a summary of the V_{GL} values for the standard, low carbonated and high carbonated samples, as measured.

The V_{GL} values for the various standard (CNM_SiSi_N) and carbonated (CNM_SiSi_N_CX) samples are plotted against the irradiation fluence in Figure 6.26. The resulting acceptor removal coefficients per every carbon doses, are: $c[10^{-16}\,\mathrm{cm^2}] = 7.9$ for the standard samples, and $c[10^{-16}\,\mathrm{cm^2}] = 4.7$, $c[10^{-16}\,\mathrm{cm^2}] = 3.9$, $c[10^{-16}\,\mathrm{cm^2}] = 3.5$, $c[10^{-16}\,\mathrm{cm^2}] = 4.3$ and $c[10^{-16}\,\mathrm{cm^2}] = 4.4$, for the devices with 1×10^{14}, 2×10^{14}, 3×10^{14}, 6×10^{14} and 9×10^{14} at/cm^2 of carbon dose. These values can be seen in Figure 6.26.

Samples with a carbon dose of $3 \times 10^{14} at/cm^2$ (CNM_SiSi_N_C3) had the lowest acceptor removal coefficient, which a priori would indicate a superior radiation tolerance. Samples without carbon co-implantation had the highest acceptor removal coefficient. This result agrees with the findings of run #15246 (see subsection 6.2.2), which shows that devices with a carbonated multiplication layer exhibit enhanced radiation resistance. These results motivated the decision to select the CNM_SiSi_N_C3 (lowest acceptor removal coefficient) and CNM_SiSi_N_C9 (highest carbon dose) samples for the subsequent radioactive source characterization as we will review in the next sections.

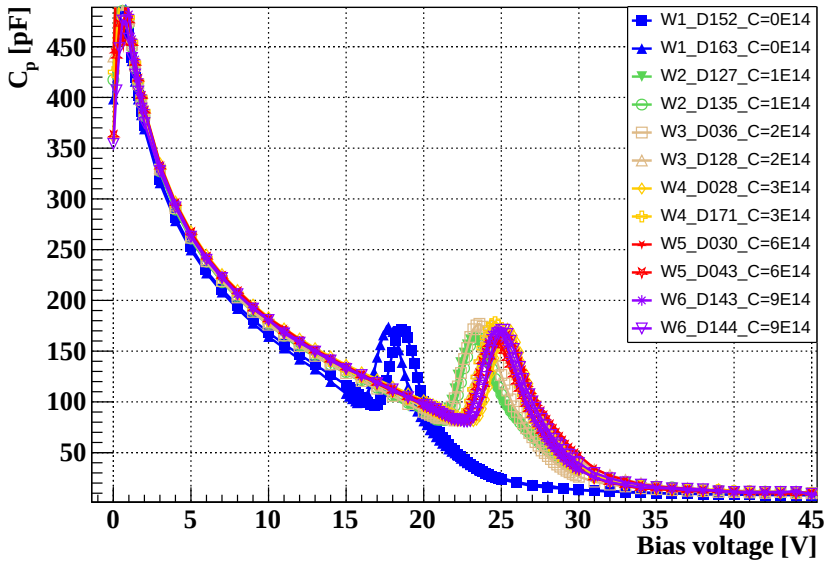

(a) Samples irradiated at $8 \times 10^{14}\,\mathrm{n_{eq}\,cm^{-2}}$

Fig. 6.23 Pad capacitance after irradiation as a function of the reverse bias. Standard CNM_SiSi_N and carbonated CNM_SiSi_N_CX devices irradiated to the fluence of $8 \times 10^{14}\,\mathrm{n_{eq}\,cm^{-2}}$.

Table 6.7 Summary of the V_{GL} values for the standard CNM_SiSi_N and the various carbon doses CNM_SiSi_N_CX sensors, extracted from the electrical characterization of capacitance before and after irradiation.

	V_{GL} from CV [V]					
Fluence ($\mathrm{n_{eq}\,cm^{-2}}$)	CNM_ SiSi_N	CNM_ SiSi_N_C1	CNM_ SiSi_N_C2	CNM_ SiSi_N_C3	CNM_ SiSi_N_C6	CNM_ SiSi_N_C9
0	31.6	32.6	33.4	32.7	33.1	32.5
0.4×10^{15}	22.3	25.1	26	26.7	25.9	26.5
0.8×10^{15}	15.8	19.8	21.2	23.1	22.5	22.6
1.5×10^{15}	9.4	14.8	16.3	17.9	16.2	17.5
2.5×10^{15}	4.5	9.5	11.6	12.7	10.5	9.9

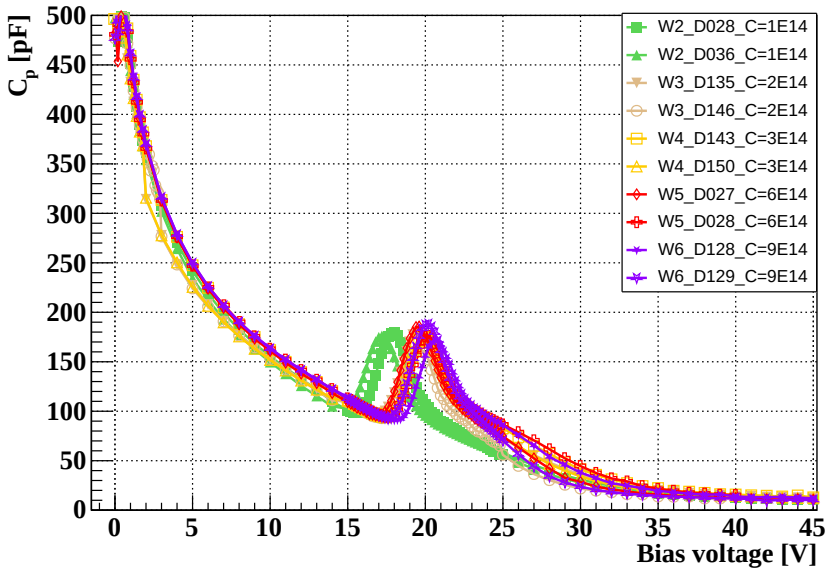

(a) Samples irradiated at $15 \times 10^{14}\,\mathrm{n_{eq}\,cm^{-2}}$

Fig. 6.24 Pad capacitance after irradiation as a function of the reverse bias. Standard CNM_SiSi_N and carbonated CNM_SiSi_N_CX devices irradiated to the fluence of $15 \times 10^{14}\,\mathrm{n_{eq}\,cm^{-2}}$.

Charge collection: After irradiation, samples from standard and carbonated with doses of $3 \times 10^{14} at/cm^2$ (CNM_SiSi_N_C3) and $9 \times 10^{14} at/cm^2$ (CNM_SiSi_N_C9) were measured with the radioactive source setup.

The collected charge as a function of the bias voltage applied to the samples from different fluences are shown in Figure 6.27 containing the CNM_SiSi_N_C3 and Figure 6.28 the CNM_SiSi_N_C9 samples, the doted lines are the limits for the ETL requirements: a collected charge above 8 fC at a bias voltage less than $12\,\mathrm{V/\mu m}$. As anticipated, the collected charge between samples of the same fluence and carbon dose is comparable, there is a difference in the voltage required to achieve the same level of collected charge between the two types of LGADs at a same fluence value, demonstrating the impact of radiation on the required bias voltage to collect a specific charge. The more irradiated samples exhibit a higher bias voltage required for charge collection.

For instance, CNM_SiSi_N_C3 samples irradiated to a fluence of $1.5 \times 10^{15}\,\mathrm{n_{eq}\,cm^{-2}}$ have a collected charge of 5 fC at 500 V and the samples of $2.5 \times 10^{15}\,\mathrm{n_{eq}\,cm^{-2}}$ require a bias voltage exceeding 540 V. Some CNM_SiSi_N_C3 samples were unable to be operated at higher voltages, unlike the CNM_SiSi_N_C9 samples, due to the presence of noise, particularly at the higher fluence.

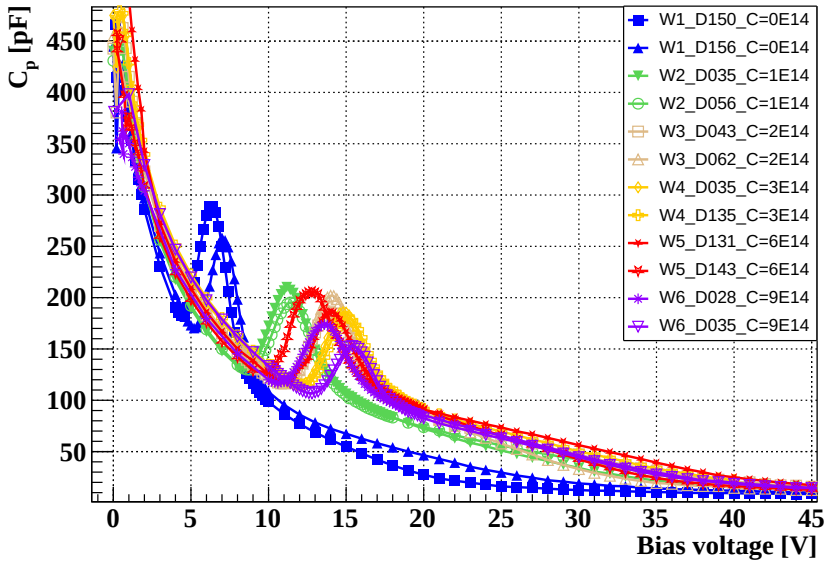

(a) Samples irradiated at $25 \times 10^{14}\,\mathrm{n_{eq}\,cm^{-2}}$

Fig. 6.25 Pad capacitance after irradiation as a function of the reverse bias. Standard CNM_SiSi_N and carbonated CNM_SiSi_N_CX devices irradiated to the fluence of $25 \times 10^{14}\,\mathrm{n_{eq}\,cm^{-2}}$.

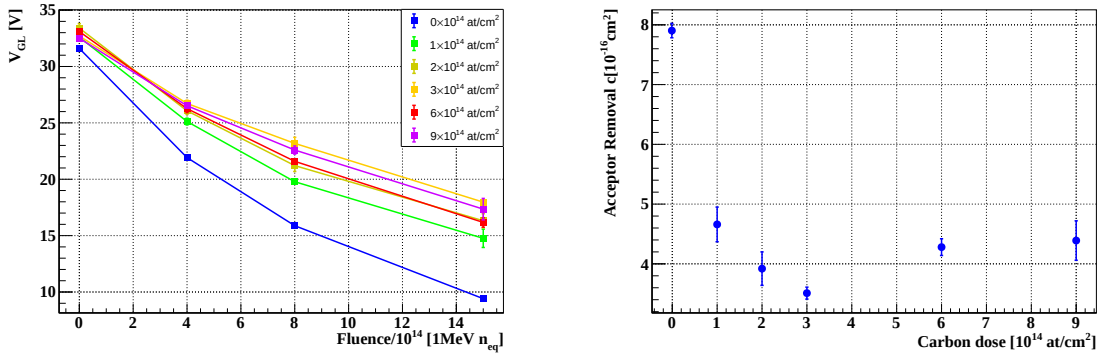

(a) V_{GL} values from CV

(b) Acceptor removal coefficients

Fig. 6.26 (a) contains the gain-layer depletion voltages from CV as a function of the fluence from where the acceptor removal coefficients are calculated. (b) shows the acceptor removal coefficients versus the carbon doses, being $c[10^{-16}\,\mathrm{cm^2}] = 7.9$ for the standard samples, and $c[10^{-16}\,\mathrm{cm^2}] = 4.7$, $c[10^{-16}\,\mathrm{cm^2}] = 3.9$, $c[10^{-16}\,\mathrm{cm^2}] = 3.5$, $c[10^{-16}\,\mathrm{cm^2}] = 4.3$ and $c[10^{-16}\,\mathrm{cm^2}] = 4.4$, for the devices with 1×10^{14}, 2×10^{14}, 3×10^{14}, 6×10^{14} and 9×10^{14} at/cm^2 of carbon dose.

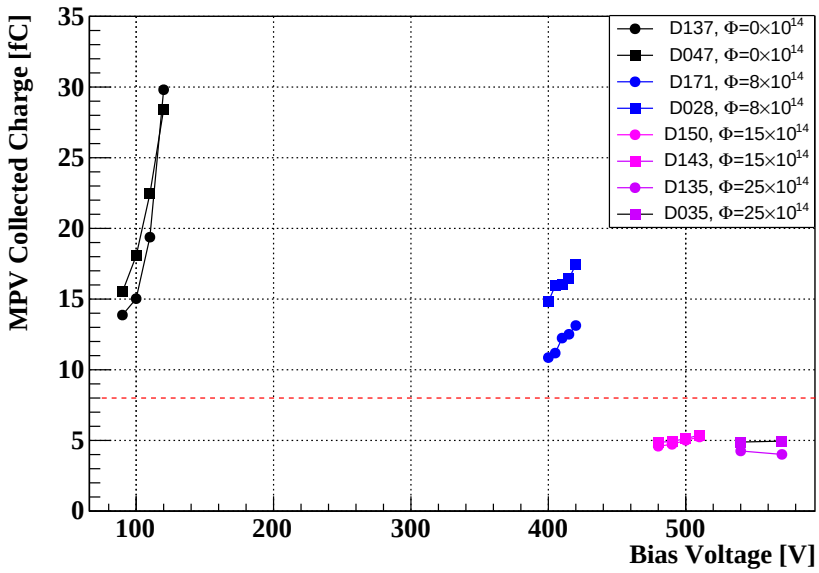

Fig. 6.27 Collected Charge as a function of the reverse bias voltage for CNM_SiSi_N_C3 samples. All these measurements were performed at $-25\,^{\circ}\mathrm{C}$. The doted lines are the limits for the ETL requirements: a collected charge above 8 fC at a bias voltage less than $12\,\mathrm{V}/\mu\mathrm{m}$.

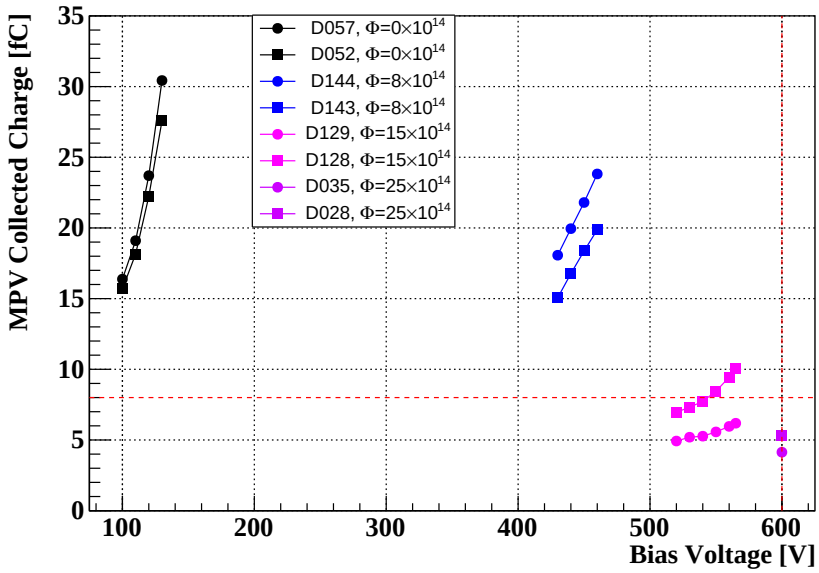

Fig. 6.28 Collected Charge as a function of the reverse bias voltage for CNM_SiSi_N_C9 samples. All these measurements were performed at $-25\,^{\circ}\mathrm{C}$. The doted lines are the limits for the ETL requirements: a collected charge above 8 fC at a bias voltage less than $12\,\mathrm{V}/\mu\mathrm{m}$.

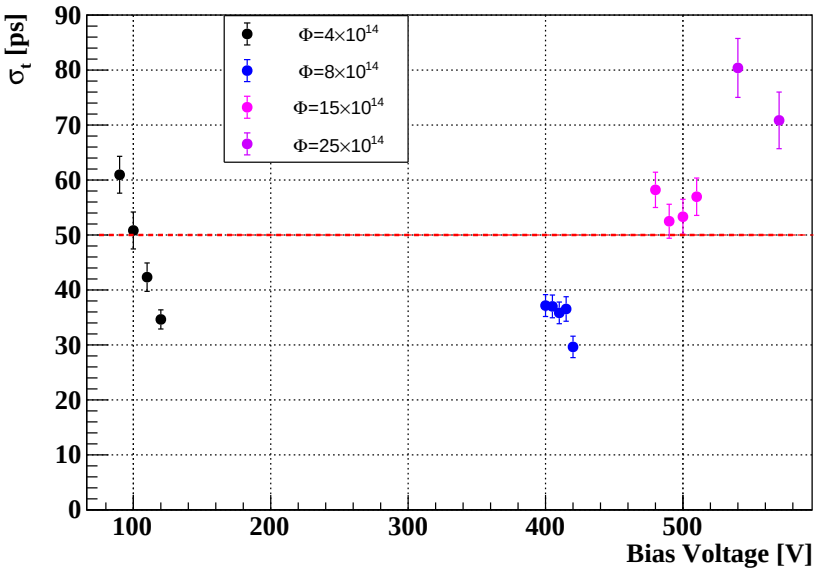

Fig. 6.29 Time resolution of the CNM_SiSi_N_C3 sensors, calculated using Equation 4.12 and errors with Equation 4.13. All these measurements were performed at $-25\,^{\circ}\mathrm{C}$. The doted lines are the limits for the ETL requirements: a time resolution below 50 ps at a bias voltage less than $12\,\mathrm{V}/\mu\mathrm{m}$.

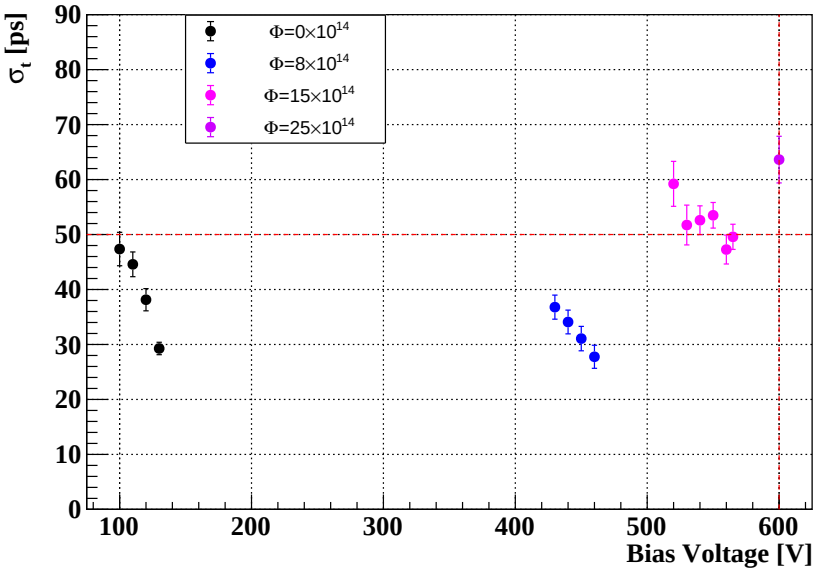

Fig. 6.30 Time resolution of the CNM_SiSi_N_C9 samples, calculated using Equation 4.12 and errors with Equation 4.13. All these measurements were performed at $-25\,^{\circ}\mathrm{C}$. The doted lines are the limits for the ETL requirements: a time resolution below 50 ps at a bias voltage less than $12\,\mathrm{V}/\mu\mathrm{m}$.

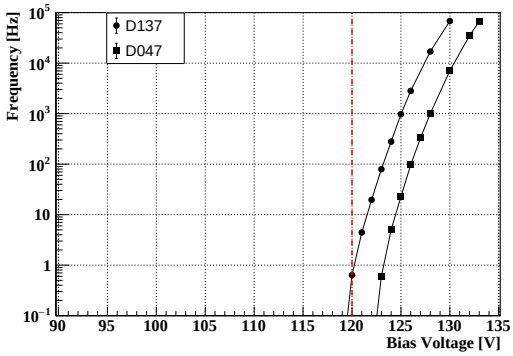

(a) Non-irradiated

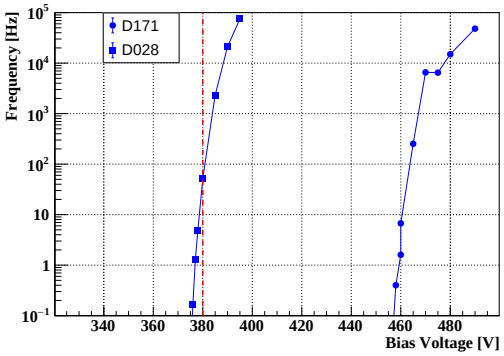

(b) $0.8 \times 10^{15}\,\mathrm{n_{eq}\,cm^{-2}}$

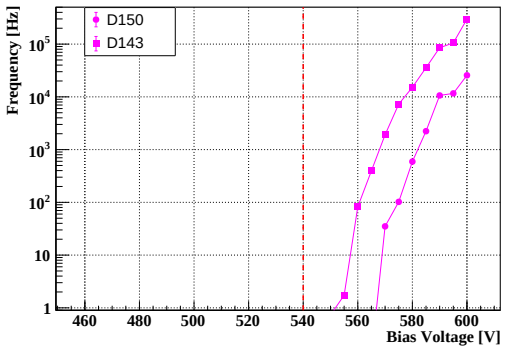

(c) $1.5 \times 10^{15}\,\mathrm{n_{eq}\,cm^{-2}}$

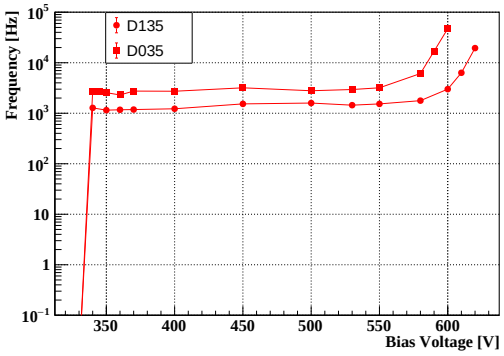

(d) $2.5 \times 10^{15}\,\mathrm{n_{eq}\,cm^{-2}}$

Fig. 6.31 Spurious pulse rate versus the bias voltage of the CNM_SiSi_N_C3 samples when fresh (a), and at $0.8 \times 10^{15}\,\mathrm{n_{eq}\,cm^{-2}}$ (b), $1.5 \times 10^{15}\,\mathrm{n_{eq}\,cm^{-2}}$ (c) and $2.5 \times 10^{15}\,\mathrm{n_{eq}\,cm^{-2}}$ (d) irradiation fluences. Doted lines indicates the working voltage. Measurements taken in the Radioactive Source setup with NIM electronics with a threshold of $-25\,\mathrm{mV}$.

Time resolution: The resulting time resolutions, σ_t, are plotted as a function of the bias voltage in Figure 6.29 for both CNM_SiSi_N_C3 sensors and Figure 6.30 for the CNM_SiSi_N_C9 sensors. It is evident that as the fluence increases, the requisite voltage for achieving an equivalent time resolution also rises, and the time resolution improves as the bias voltage rises. Both types of sensors are capable of achieving a time resolution below 50 ps at a fluence of $1.5 \times 10^{15}\,\mathrm{n_{eq}\,cm^{-2}}$. However, as previously discussed, the CNM_SiSi_N_C3 sensors were unable to be biased due to the presence of noise, while the CNM_SiSi_N_C9 sensors were able to be biased and reached comparable resolution values to those at lower fluences.

Spurious pulses: A noise study were conducted on carbonated CNM_SiSi_N_C3 and CNM_SiSi_N_C9 samples. The spurious pulses were observed in all samples in the

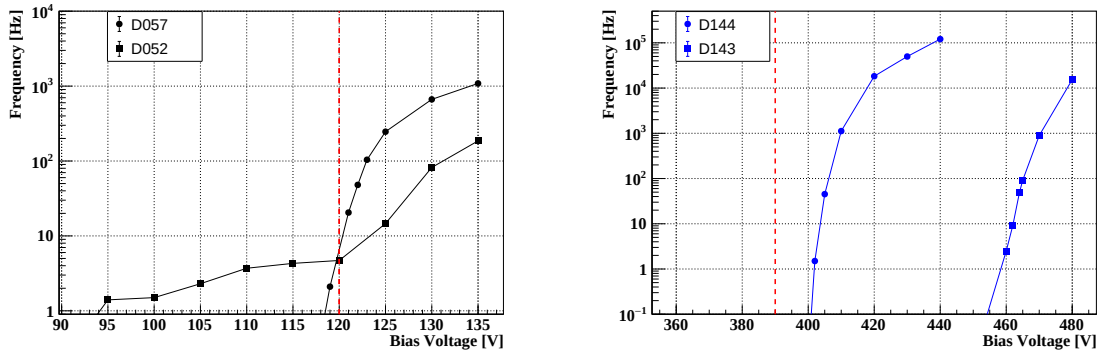

(a) Non-irradiated

(b) $0.8 \times 10^{15}\,\mathrm{n_{eq}\,cm^{-2}}$

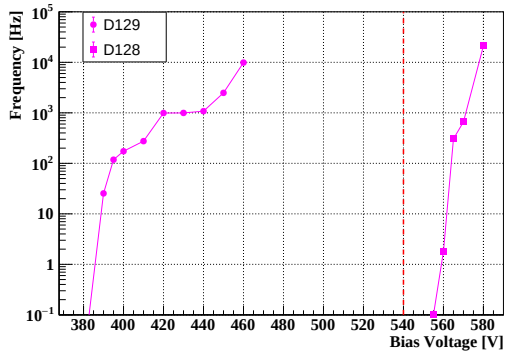

(c) $1.5 \times 10^{15}\,\mathrm{n_{eq}\,cm^{-2}}$

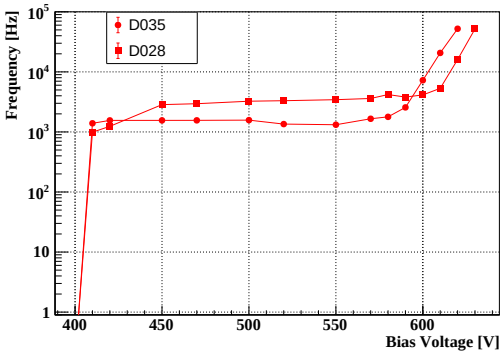

(d) $2.5 \times 10^{15}\,\mathrm{n_{eq}\,cm^{-2}}$

Fig. 6.32 Spurious pulse rate versus the bias voltage of the CNM_SiSi_N_C9 samples when fresh (a), and at $0.8 \times 10^{15}\,\mathrm{n_{eq}\,cm^{-2}}$ (b), $1.5 \times 10^{15}\,\mathrm{n_{eq}\,cm^{-2}}$ (c) and $2.5 \times 10^{15}\,\mathrm{n_{eq}\,cm^{-2}}$ (d) irradiation fluences. Doted lines indicates the working voltage. Measurements taken in the Radioactive Source setup with NIM electronics with a threshold of $-25\,\mathrm{mV}$.

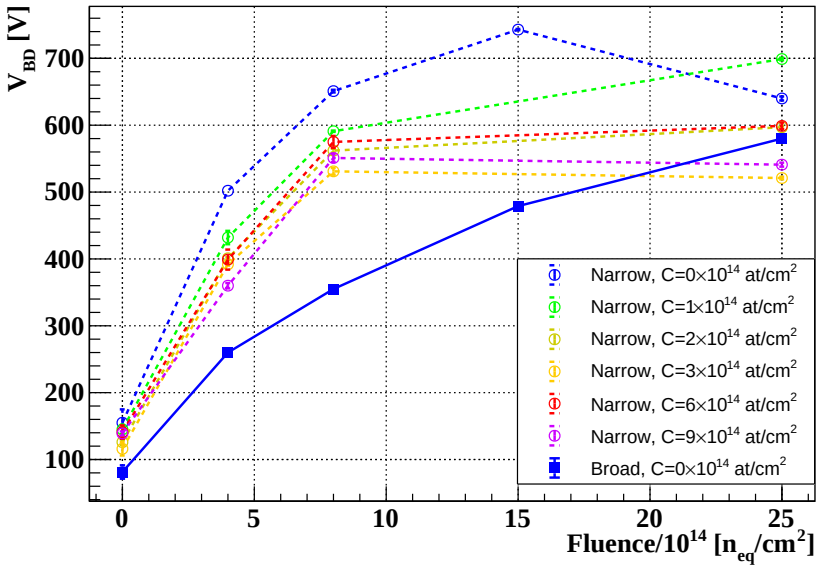

Fig. 6.33 Comparison of the V_{BD} before and after irradiation from run #15973 CNM_SiSi_N with narrow gain layer and for the different carbon doses CNM_SiSi_N_CX in empty markers and run #12916 CNM_SiSi_B with broad standard gain layer in filled markers.

vicinity of the breakdown voltage. The resulting rates for the different samples are presented in Figure 6.31 and Figure 6.32, which show the data for the CNM_SiSi_N_C3 and CNM_SiSi_N_C9 samples respectively. From these plots, it is possible to observe the frequency of the spurious pulses versus the bias voltage, with the operating voltage, that is the bias voltage needed to obtain a time resolution below 50 ps, indicated by dotted lines. For the CNM_SiSi_N_C3 sensors these operative voltages are: 120 V for non irradietd; 380 V for samples irradiated at $0.8 \times 10^{15}\,\mathrm{n_{eq}\,cm^{-2}}$ and 540 V for the samples at $1.5 \times 10^{15}\,\mathrm{n_{eq}\,cm^{-2}}$ of fluence. For the CNM_SiSi_N_C9 samples: 120 V, 390 V and 540 V are the operative voltages respectively to fresh, $0.8 \times 10^{15}\,\mathrm{n_{eq}\,cm^{-2}}$ and $1.5 \times 10^{15}\,\mathrm{n_{eq}\,cm^{-2}}$ fluences.

As the most irradiated samples were not operated at higher voltages, it is not possible to determine an operating voltage for this yield point for either device. The occurrence of spurious pulses in CNM_SiSi_N_C3 samples is observed to occur after the operative voltage, with the exception of one of the two devices irradiated at $0.8 \times 10^{15}\,\mathrm{n_{eq}\,cm^{-2}}$. In contrast, for the CNM_SiSi_N_C9 samples, the appearance of spurious pulses is observed to occur earlier than the operative voltage in one of the devices irradiated at $1.5 \times 10^{15}\,\mathrm{n_{eq}\,cm^{-2}}$.

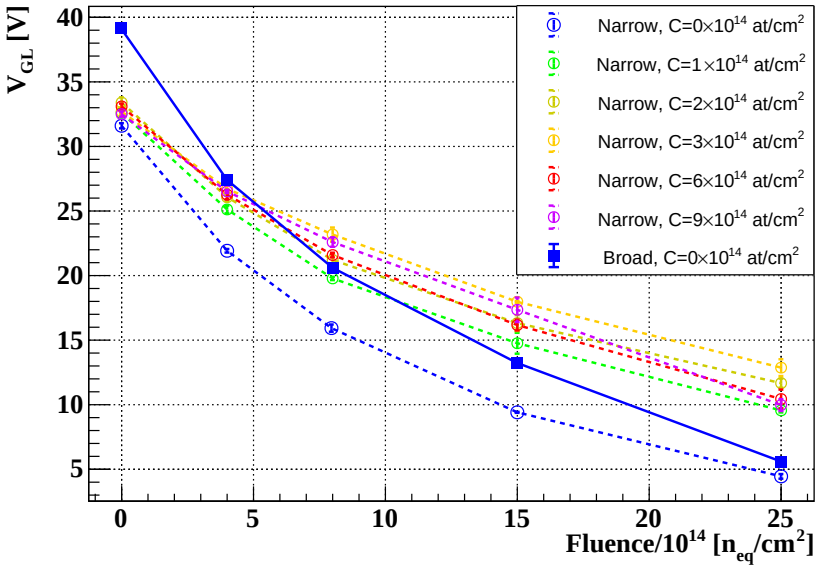

Fig. 6.34 Comparison of the V_{GL} values from run #15973 CNM_SiSi_N with narrow gain layer and for the different carbon doses CNM_SiSi_N_CX in empty markers and run #12916 CNM_SiSi_B with broad standard gain layer in filled markers. Both calculated from CV curves.

6.2.1.3 Comparative Analysis of Radiation Tolerance in Silicon-on-Silicon LGADs: Narrow, Broad, and Carbon-Enriched Gain Layers

Figure 6.33 presents a comparison of the mean of the V_{BD} before and after irradiation for both runs manufactured with Silicon-on-Silicon substrates. It compares the narrow gain layer samples (CNM_SiSi_N) with different carbon doses to the broad standard (no-carbonated) gain layer (CNM_SiSi_B) samples. As previously stated in section 6.2.1.2, the V_{BD} values obtained from the production process with a narrow gain layer (CNM_SiSi_N) are consistently larger than those obtained from the broad gain layer (CNM_SiSi_B). This is attributed to the reduced gain associated with the narrow gain layer.

The V_{GL} from these two runs together can be seen in Figure 6.34, Both calculations are derived from CV curves, with run #15973 CNM_SiSi_N and its different carbon doses CNM_SiSi_N_CX represented with doted lines and empty markers, and run #12916 CNM_SiSi_B represented with filled markers, the two standard non-carbonated wafers are marked in blue. From this comparison, it is evident that the carbonated samples exhibit reduced variability in V_{GL} across the irradiation fluences, suggesting diminished degradation due to irradiation. The standard gain layer samples demonstrate a comparable behavior.

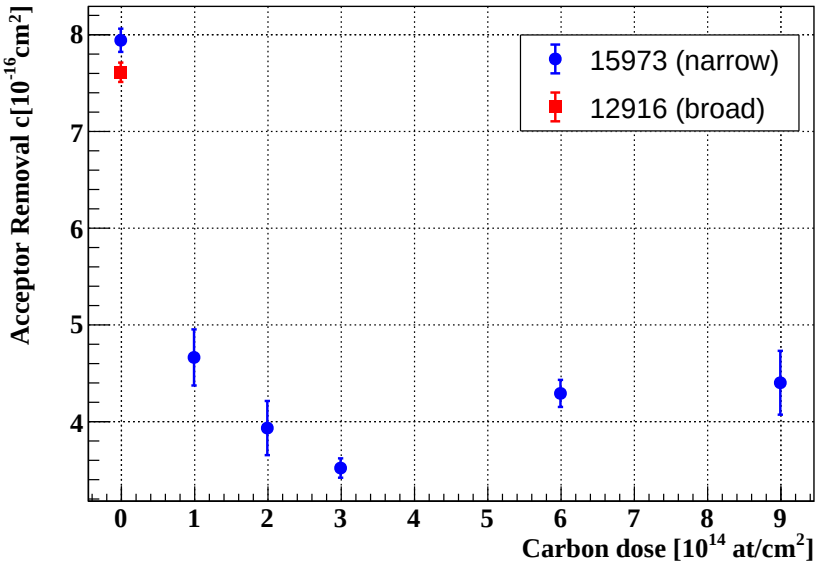

Fig. 6.35 Comparison of the accept removal coefficients from run #15973 with narrow gain layer (CNM_SiSi_N) and its different carbon doses (CNM_SiSi_N_CX) in blue markers and run #12916 with broad standard (CNM_SiSi_B) gain layer in red markers. Both calculated from CV curves.

Similarly, Figure 6.35 illustrates the acceptor removal coefficients obtained through the fitting of the preceding V_{GL} values as a function of the carbon dose for both experimental runs. The data set represented by the blue markers is from run the samples which features a narrow gain layer (CNM_SiSi_N) and varying carbon doses (CNM_SiSi_N_CX). The point represented by the red marker is derived from samples which employs a broad standard gain layer (CNM_SiSi_B). A comparison of the standard (non-carbonated) gain layer samples reveals that the run featuring a broad gain layer (run #12916, CNM_SiSi_B) displays slightly enhanced radiation resistance, though not to the same extent as the carbon-enriched samples from run #15973 (CNM_SiSi_N_CX), which exhibit significantly reduced acceptor removal coefficients.

6.2.2 LGAD on Epitaxial substrates

This run #15246 was a specialized production of LGADs with one of its specific objectives of investigating the impact of carbon co-implantation with the multiplication layer that has been utilized in its LGAD productions before. The LGADs were fabricated on epitaxial wafers with a diameter of 6 inches, featuring an active layer thickness of 55 µm and a support wafer thickness of 525 µm. The handle wafer exhibits a resistivity ranging from 0.001–1 Ω cm,

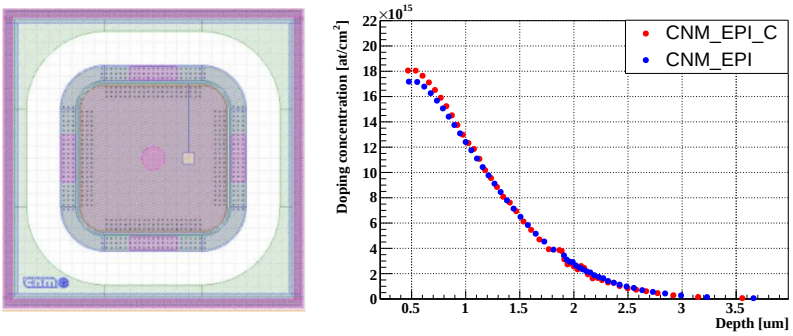

(a) LGAD top view (b) Doping profile of the GL

Fig. 6.36 (a) is the top view of a single pad sample characterized from run #15246. (b) is the doping profile obtained from the electrical characterization. In blue the doping profile of the standard (CNM_EPI) samples and in red the carbonated (CNM_EPI_C).

while the substrate resistivity is approximately 2 kΩcm. These sensors were designed with an inter-pad (IP) distance, which is the distance between the end of the $p+$ gain layer of two adjacent pads, of 47 µm.

Figure 6.36 shows in (a) a top view of a single pad device from this run, where the main central pad and the GR around it are visible. (b) is the layout of the samples characterized and (c) is the doping profile obtained from the electrical characterization.

The run #15246 are also intended to have different numbers of pads, including 1×1 (single diodes), 2×2, 5×5, 16×16 and 16×32 where each pad is $1.3 \times 1.3\,\mathrm{mm}^2$ of area. The single diodes are the size reported in this study, before and after being irradiated at the Jožef Stefan Institute (JSI) [123] in Ljubljana to fluences of $0.6 \times 10^{15}\,\mathrm{n_{eq}\,cm^{-2}}$, $1.0 \times 10^{15}\,\mathrm{n_{eq}\,cm^{-2}}$ and $1.5 \times 10^{15}\,\mathrm{n_{eq}\,cm^{-2}}$.

Table 6.8 Carbon and boron doses for the CNM_EPI_C (carbonated) and CNM_EPI (standard) devices per wafer from run #15246

Wafer	Carbonated	Standard
Boron dose ($1 \times 10^{13}\,\mathrm{cm^{-2}}$)	1.9	1.9
Carbon dose ($1 \times 10^{13}\,\mathrm{cm^{-2}}$)	10	-
Dry oxidation time DOT (min)	180	180

IV characteristics: The IV curves of the carbonated (CNM_EPI_C) and standard (CNM_EPI) sensors were taken before irradiation. A large number of single diode devices were available for this campaign and arrived at IFCA after being diced. 12 IV curves of carbonated sensors and 12 of standard samples were measured and are shown in Figure 6.37 and Figure 6.38

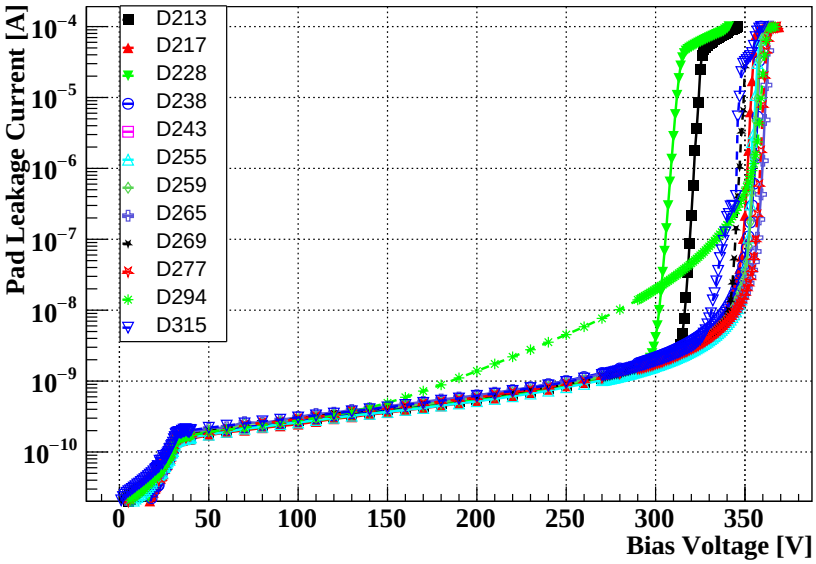

Fig. 6.37 The leakage current of the main diode are shown as a function of reverse bias before irradiation. Carbonated (CNM_EPI_C) gain layer sensors.

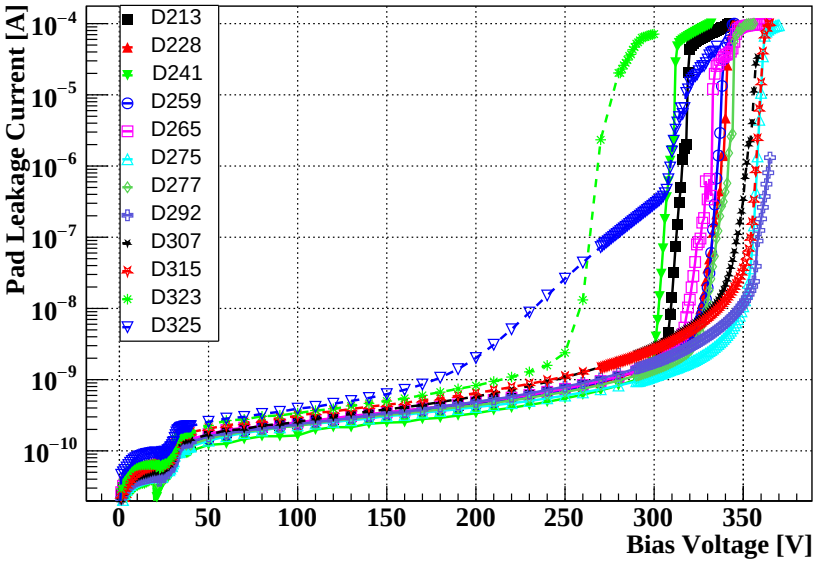

Fig. 6.38 The leakage current of the main diode are shown as a function of reverse bias before irradiation. Standard (CNM_EPI) gain layer sensors.

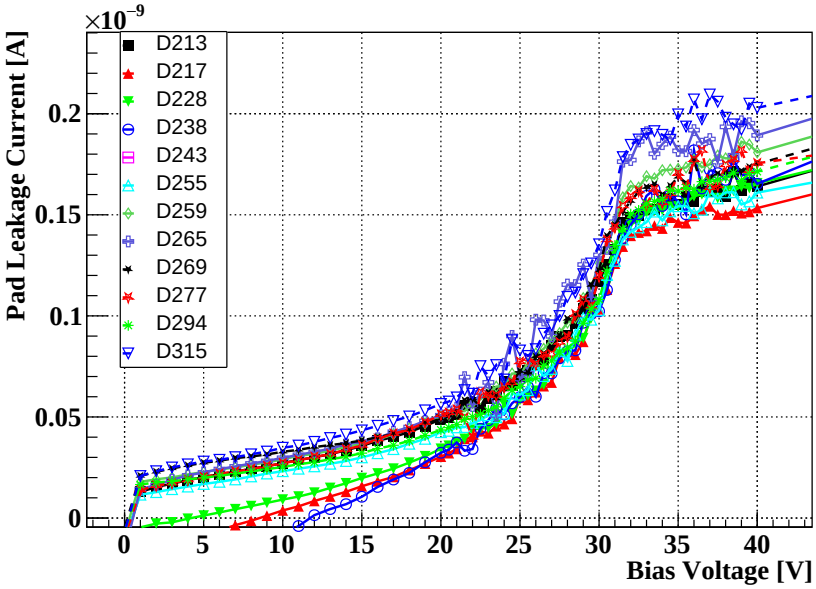

Fig. 6.39 The leakage currents of the main diode are shown as a function of reverse bias before irradiation. Zoomed-in view of the region where the gain layer is depleted for the carbonated (CNM_EPI_C) sensors.

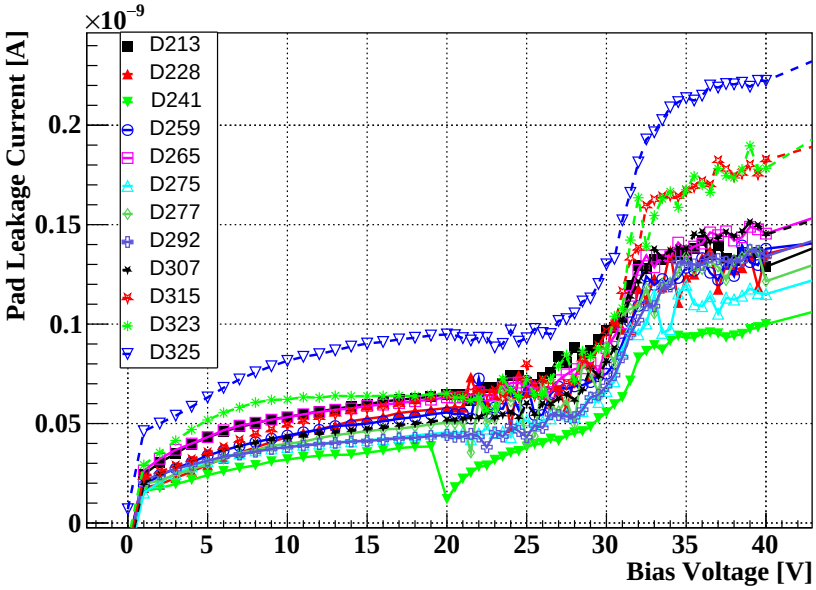

Fig. 6.40 The leakage currents of the main diode are shown as a function of reverse bias before irradiation. Zoomed-in view of the region where the gain layer is depleted for the standard (CNM_EPI) sensors.

respectively. The enlarged view of the region of the gain layer is shown in plots Figure 6.39 and Figure 6.40 for carbonated and standard sensors. Measurements were taken at room temperature with the GR connected to the HV.

In the region after V_{GL} and V_{BD} the current for both types of sensors is mostly below 1 nA and the V_{BD} was found to be in the range of 290–350 V for the carbonated sensors and 280–340 V for the standard samples. In general, the V_{BD} for both wafers has a low dispersion, with an RMS value of approximately 17 V for carbonated and 24 V for standard LGADs. The reverse current of the carbonated sensors in the V_{GL} region is higher, 150 pA, than for the standard sensors of about 100 pA.This increase in the carbonated samples is as expected [139] because the carbon enhancement increases the defects of the multiplication layer.

A second electrical characterization at $-25\,^{\circ}\mathrm{C}$ was performed after irradiation of the devices, but due to the limited number of irradiated devices, only two samples per irradiation fluence were measured. Figure 6.41 shows the IV curves for the carbonated (CNM_EPI_C) sensors in plot, the shift to higher voltage values for the V_{BD} regimes with increasing irradiation is clearly visible, starting from about 580 V for the sensors irradiated to $0.6 \times 10^{15}\,\mathrm{n_{eq}\,cm^{-2}}$ and between 690–710 V for the sensors of $1.5 \times 10^{15}\,\mathrm{n_{eq}\,cm^{-2}}$, which is in contrast to the initial 290–350 V range when fresh. The maximum applied voltage was not increased further to avoid SEBs.

In the case of the standard (CNM_EPI) sensors shown in Figure 6.42, their V_{BD} starts at 610 V for samples irradiated at the lowest fluence and at about 730 V for the remaining fluences. In both cases, the increase in V_{BD} indicates the degradation of the gain layer due to irradiation, but the breakdown itself cannot be observed from these measurements. The V_{GL} shift, which is another important indicator of this degradation due to irradiation, is shown in section 6.2.2.

CV characteristics: Prior to irradiation, the capacitance of the sensors was measured at room temperature with the GR connected to HV at a frequency of 1 kHz on the LCR-meter.

Figure 6.43 and Figure 6.44 show the CV curves for the carbonated (CNM_EPI_C) and standard (CNM_EPI) samples respectively. The first thing we notice is the high homogeneity and reproducibility of the curves, starting with a smooth decrease in capacitance, corresponding to the depletion of the gain layer region, which ends at approximately 30 V for both carbonated and standard samples, marking the depletion voltage of the multiplication layer. This is followed by another bend in the curve, indicating the depletion of the bulk, with a final capacitance (C_{end}) of about 4.0 pF for both types of wafer, at voltages above 32 V and

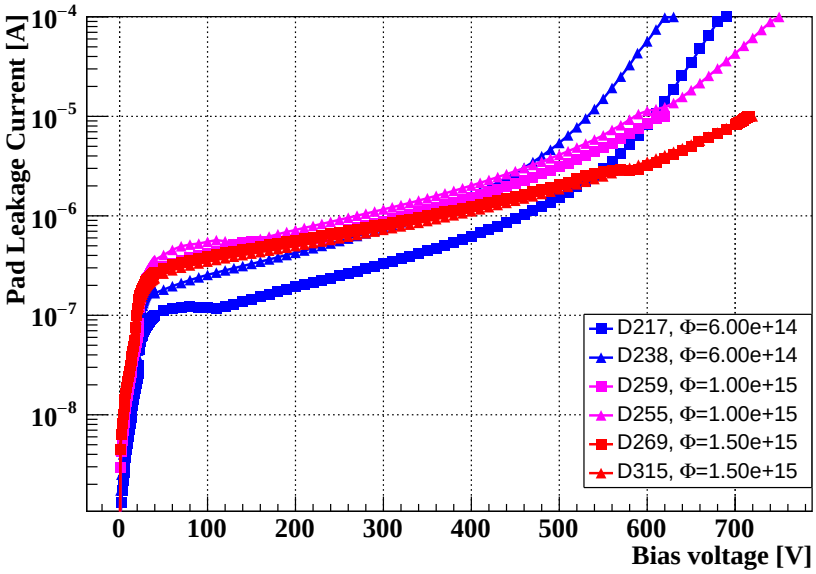

Fig. 6.41 Pad leakage current after irradiation as a function of the reverse bias of the carbonated (CNM_EPI_C) sensors. This plot is shown in log scale for Y axis.

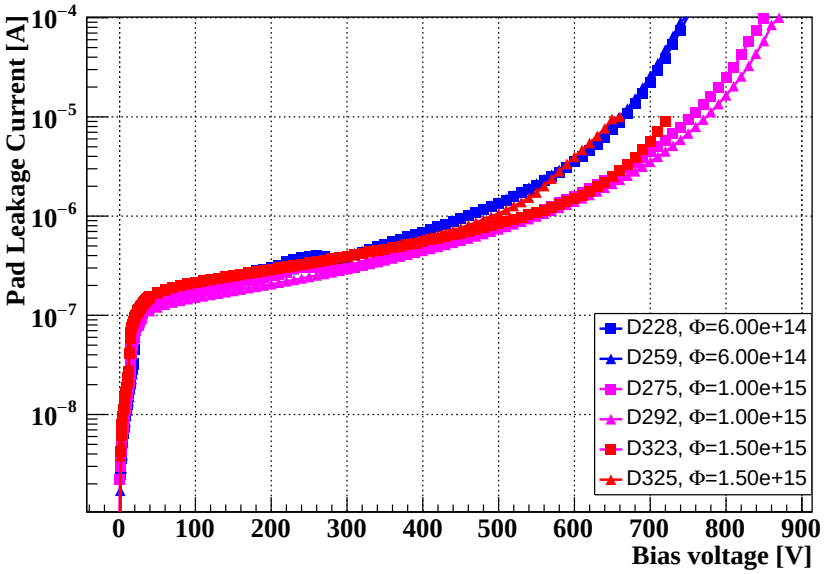

Fig. 6.42 Pad leakage current after irradiation as a function of the reverse bias of the standard (CNM_EPI) sensors. This plot is shown in log scale for Y axis.

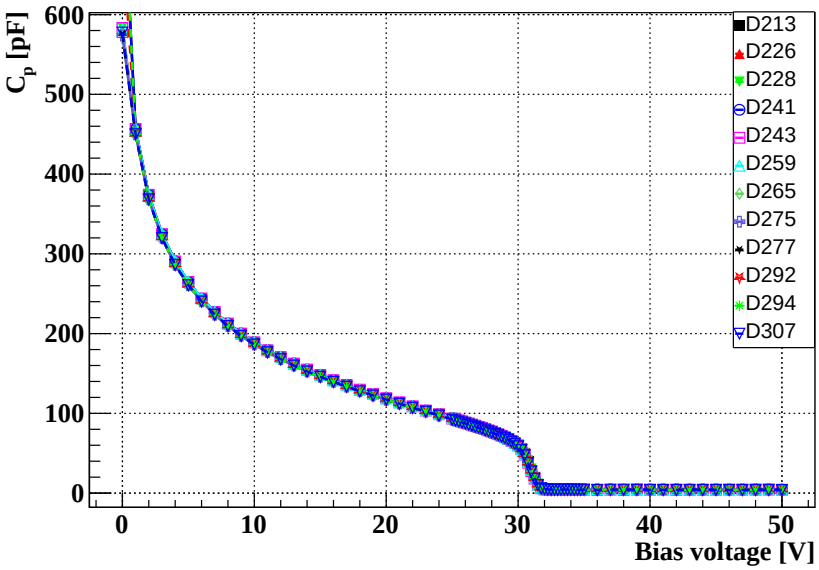

Fig. 6.43 Pad capacitance before irradiation as a function of the reverse bias for the carbonated (CNM_EPI_C) sensors.

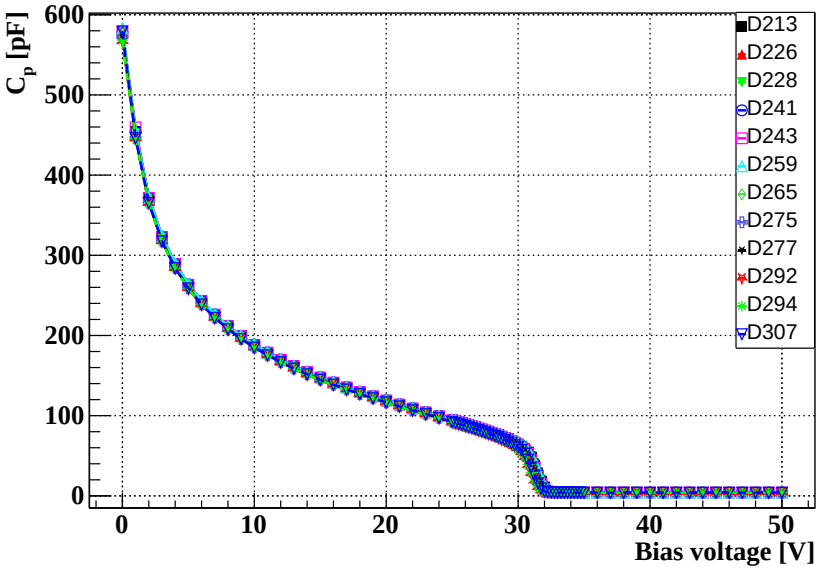

Fig. 6.44 Pad capacitance before irradiation as a function of the reverse bias for the standard (CNM_EPI) sensors are presented.

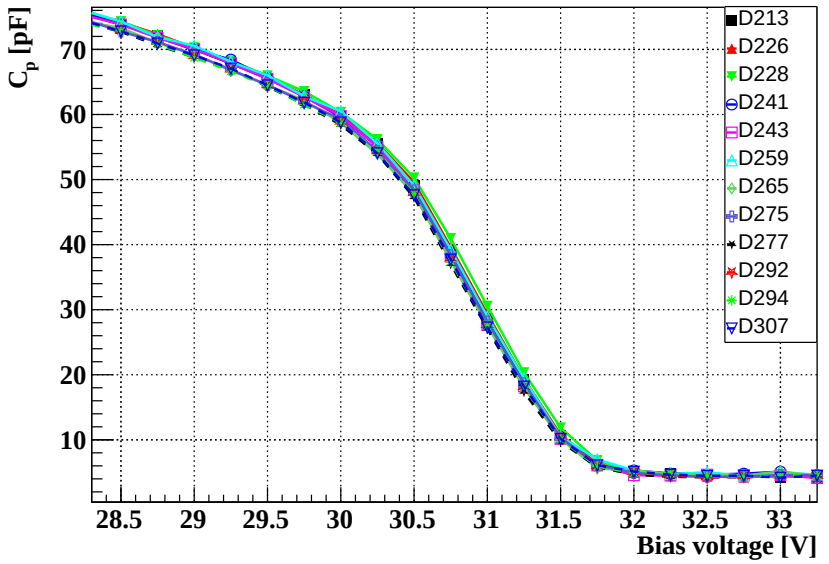

Fig. 6.45 Enlarged view of the gain layer region of the CV curve of the carbonated (CNM_EPI_C) sensors. The characteristic kinks in the curve due to the gain layer and bulk depletion transition can be observed.

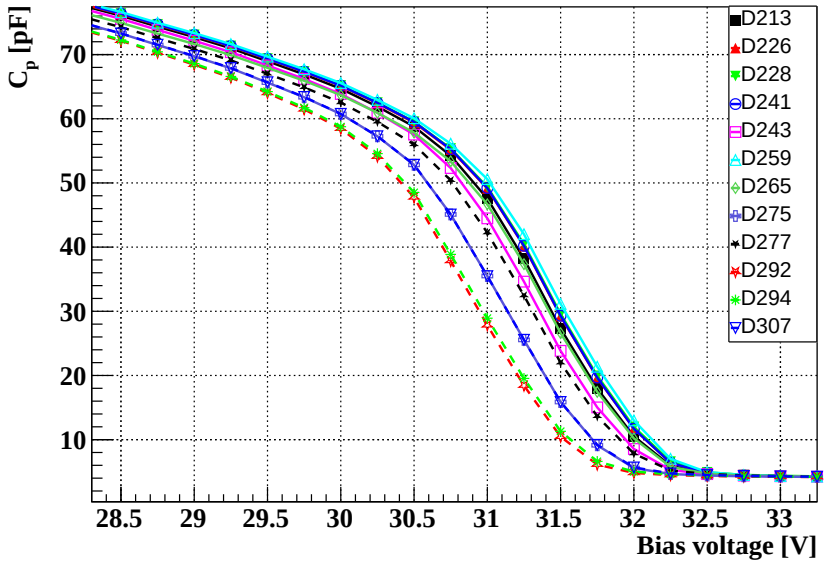

Fig. 6.46 Enlarged view of the gain layer region of the CV curve of the standard (CNM_EPI) sensors. The characteristic kinks in the curve due to the gain layer and bulk depletion transition can be observed.

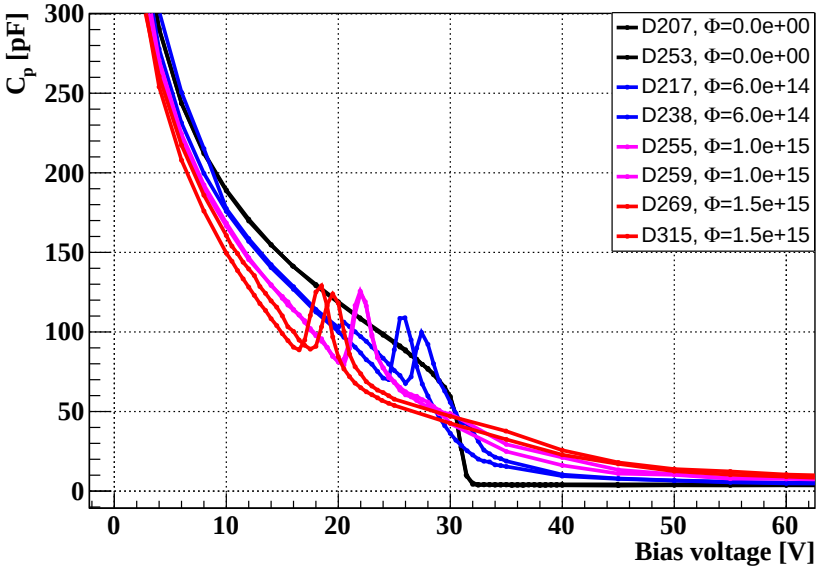

Fig. 6.47 Pad capacitance after irradiation as a function of the reverse bias of the carbonated (CNM_EPI_C) sensors. Non-irradiated samples added for comparison. Reduction of the V_{GL} as result of the irradiation at the three different fluences is observed.

32.5 V for carbonated and standard samples respectively. This C_{end} is consistent with the fact that all sensors have the same dimensions.

Figure 6.45 and Figure 6.46 show an enlarged view of the capacitance curves in the gain layer region, where it can be observed that in general the curves of all samples, carbonated and standard, have a similar shape, but the carbonated samples are less dispersed in the presence of carbon.

After irradiation a characterization was carried out at a temperature of 10 °C with a low frequency of 100 Hz as before irradiation. The CV curves after irradiation of the carbonated sensors can be seen in Figure 6.47. These carbonated (CNM_EPI_C) samples show a noticeable degradation of the gain layer due to irradiation, as evidenced by lower V_{GL}s at higher fluences. Figure 6.48 shows the curves of the standard (CNM_EPI) samples, where a reduction in V_{GL} is also evident, but these values are lower compared to the carbonated samples. For example, at the highest fluence, V_{GL} for the carbonated sensor is about 17 V, while for the standard sensor it is about 11 V.

Acceptor removal coefficient: As we saw in section 5.1, V_{GL} decreases in irradiated sensors compared to their pre-irradiation state. This reduction in V_{GL} provides an indication of the remaining active boron in the GL. A crucial aspect of this run #15246 is to study the

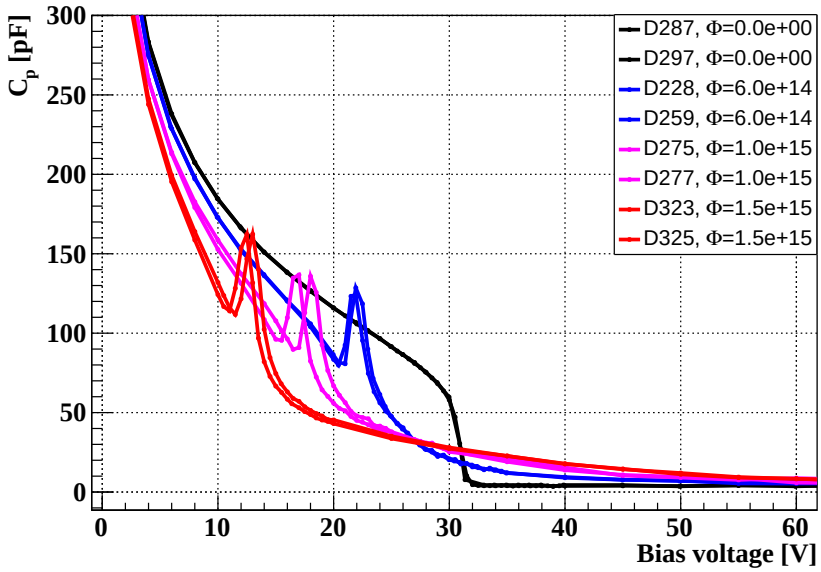

Fig. 6.48 Pad capacitance after irradiation as a function of the reverse bias of the standard (CNM_EPI) sensors. Non-irradiated samples added for comparison. Reduction of the V_{GL} as result of the irradiation at the three different fluences is observed.

effect of carbon enrichment in the GL compared to standard boron implantation and how it affects the acceptor removal coefficient for both types of sensors.

Table 6.9 Summary of the V_{GL} values for both type of sensors (CNM_EPI_C and CNM_EPI), extracted from the electrical characterization (IV and CV) before and after irradiation. The errors are the standard error of the mean (SEM) from the samples measured.

	V_{GL} from IV (V)		V_{GL} from CV (V)	
Fluence ($n_{eq}\,cm^{-2}$)	Carbonated	Standard	Carbonated	Standard
0	30.7 ± 0.2	29.1 ± 0.2	30.5 ± 0.1	30.5 ± 0.2
0.6×10^{15}	23.9 ± 0.9	19.4 ± 0.2	25.3 ± 0.2	20.8 ± 0.5
1.0×10^{15}	22.3 ± 0.5	14.2 ± 0.7	20.5 ± 0.3	15.7 ± 0.2
1.5×10^{15}	17.5 ± 0.5	12.8 ± 0.5	17.2 ± 0.2	11.3 ± 0.2

The resulting curve for V_{GL} versus fluence and its corresponding fit can be seen in Figure 6.49 for both carbonated and standard samples. The resulting coefficients are $c[10^{-16}\,cm^2] = 3.6$ and $c[10^{-16}\,cm^2] = 6.9$ for carbonated and standard samples respectively, calculated from the IV characteristics, and $c[10^{-16}\,cm^2] = 3.8$ and $c[10^{-16}\,cm^2] = 6.6$ calculated from the CV characterization.

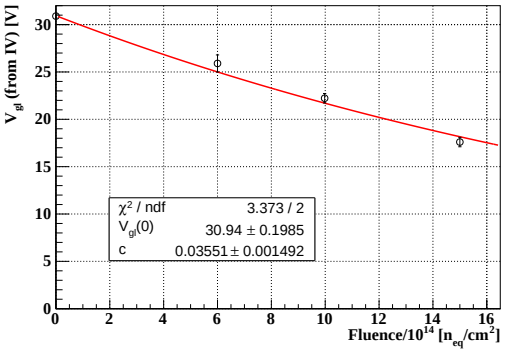

(a) CNM_EPI_C samples

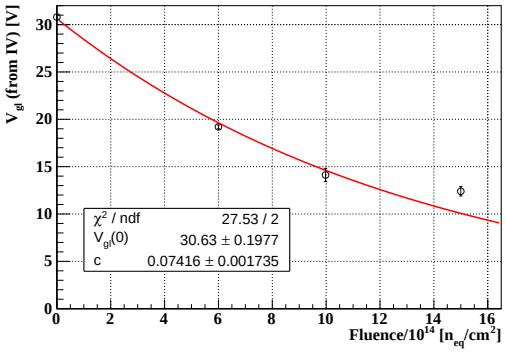

(b) CNM_EPI samples

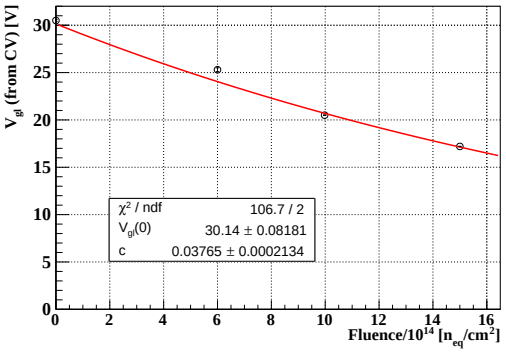

(c) CNM_EPI_C samples

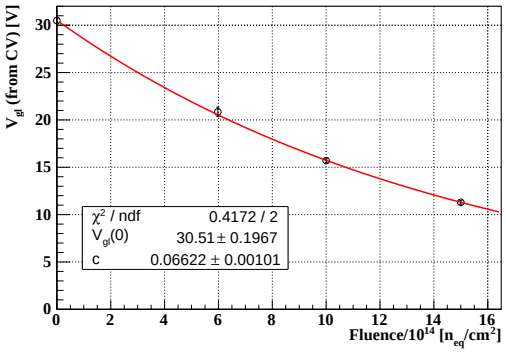

(d) CNM_EPI samples

Fig. 6.49 Gain-layer depletion voltage from IV (top plots) and CV (bottom plots) as a function of the fluence and the respective fit (red) from where the acceptor removal coefficient is calculated and being $c[10^{-16}\,\mathrm{cm}^2] = 3.6$ for carbonated (CNM_EPI_C) samples (a) and $c[10^{-16}\,\mathrm{cm}^2] = 7.4$ for the standard (CNM_EPI) samples (b) from IV calculation, and $c[10^{-16}\,\mathrm{cm}^2] = 3.8$ for carbonated samples (c) and $c[10^{-16}\,\mathrm{cm}^2] = 6.6$ for the standard samples (d) from CV.

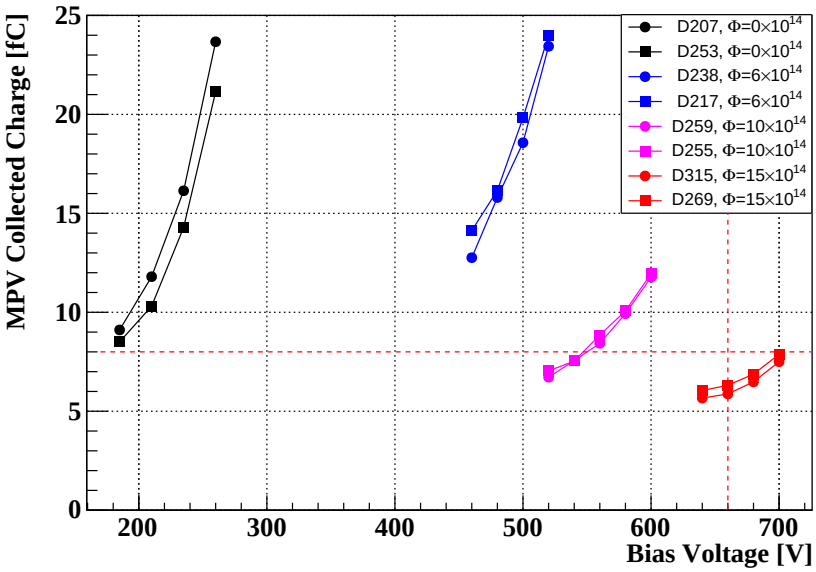

Fig. 6.50 Collected Charge as a function of the reverse bias voltage for the carbonated gain layer (CNM_EPI_C) samples. All these measurements were performed at $-25\,^{\circ}$C. The doted lines are the limits for the ETL requirements: a collected charge above 8 fC at a bias voltage less than 12 V/µm.

This difference in acceptor removal coefficient indicates that the addition of carbon in the co-implantation of the gain layer results in less boron depletion and consequently an improvement in the radiation stability of these LGADs. These results are also consistent with the evidence of better performance of carbonated sensors seen in the improvement of acceptor removal from other LGAD manufacturers. [140]

Charge collection: Figure 6.50 shows the charge collected as a function of bias voltage for the carbonated samples and Figure 6.51 for the standard samples, irradiated and non-irradiated. The damage caused by irradiation in terms of gain layer degradation is clear, e.g. samples irradiated at the higher fluence require a higher bias to achieve the same charge. There is good repeatability of the charge collected between samples from the same wafer irradiated at the same fluence.

It is also important to note that carbonated sensors can be operated with lower bias voltages than standard sensors. In this sense we can observe that 460 V is needed to collect 14 fC in a carbonated sample irradiated at a fluence of $6 \times 10^{14}\,\mathrm{n_{eq}\,cm^{-2}}$, while 600 V is needed for the standard samples at the same fluence. And since this difference is not too clear when comparing the non-irradiated sensors of both GL configurations, it is an indication that the carbon leads to a radiation resistance on these LGADs.

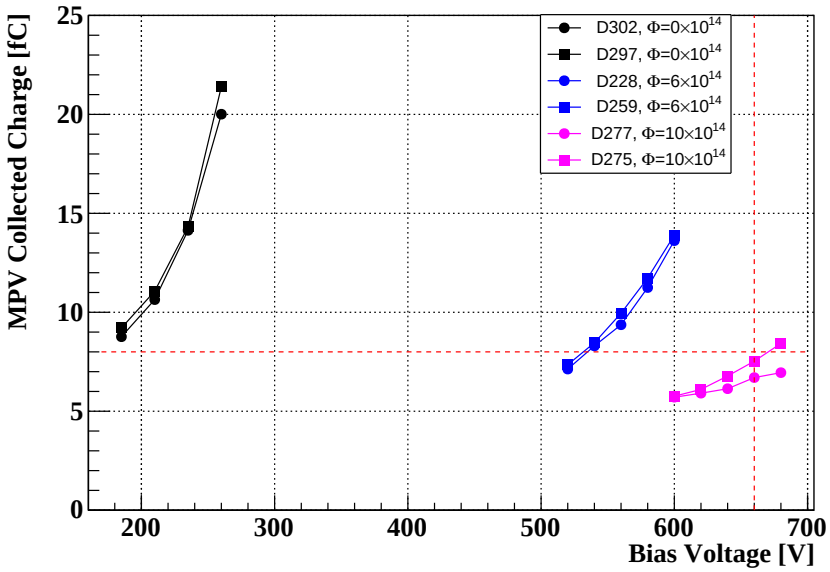

Fig. 6.51 Collected Charge as a function of the reverse bias voltage for the samples with standard gain layer (CNM_EPI). All these measurements were performed at $-25\,^{\circ}\mathrm{C}$. The doted lines are the limits for the ETL requirements: a collected charge above 8 fC at a bias voltage less than $12\,\mathrm{V}/\mu\mathrm{m}$.

Time resolution: The resulting time resolution σ_t of the carbonated and standard sensors measured at the radioactive source setup are shown in Figure 6.52 and Figure 6.53 respectively. According to the radiation damage, as the fluence increases, the voltage required to achieve the same time resolution also increases. For all fluences, the time resolution improves as the bias voltage increases. Again it can be seen that the bias voltage required to reach values below 40 ps of time resolution is lower for the carbonated sensors than for the standard sensors, and also that a better time resolution can be achieved with the carbonated sensors. This is even more obvious since the standard samples irradiated to $1.5 \times 10^{15}\,\mathrm{n_{eq}\,cm^{-2}}$ cannot be biased to a voltage in which measurements can be made, and the sensors began to enter in the breakdown regime. This is why Figure 6.53 only contains devices irradiated to $6 \times 10^{15}\,\mathrm{n_{eq}\,cm^{-2}}$ and $1.0 \times 10^{15}\,\mathrm{n_{eq}\,cm^{-2}}$.

Spurious pulses: These results are also consistent with the collected charge results, where the carbonated sensors have a larger charge than the standard samples after irradiation at the different fluences.

The resulting rates for the different samples are shown in Figure 6.54. The plot starts at the operating voltage for each detector, being the bias voltage required to obtain 8 fC (CMS requirement): $240\,\mathrm{V}, 460\,\mathrm{V}, 580\,\mathrm{V}$ and $690\,\mathrm{V}$ respectively for the fresh, $0.6 \times 10^{15}\,\mathrm{n_{eq}\,cm^{-2}}$,

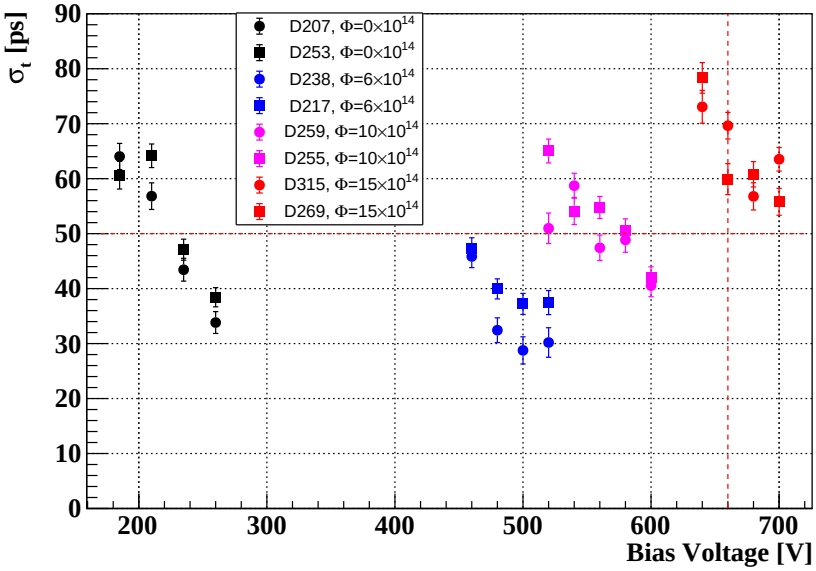

Fig. 6.52 Time resolution of the Carbonated (CNM_EPI_C) samples. All these measurements were made at $-25\,^{\circ}\mathrm{C}$. The doted lines are the limits for the ETL requirements: a time resolution below 50 ps at a bias voltage less than $12\,\mathrm{V}/\mu\mathrm{m}$.

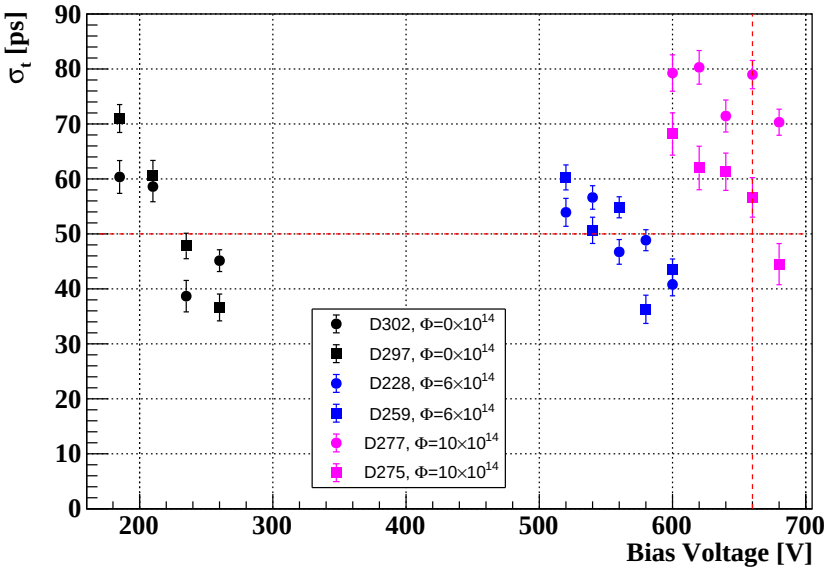

Fig. 6.53 Time resolution of the Standard (CNM_EPI) samples. The samples irradiated to $1.5 \times 10^{15}\,\mathrm{n_{eq}\,cm^{-2}}$ cannot be biased due to radiation damage. All these measurements were made at $-25\,^{\circ}\mathrm{C}$. The doted lines are the limits for the ETL requirements: a time resolution below 50 ps at a bias voltage less than $12\,\mathrm{V}/\mu\mathrm{m}$.

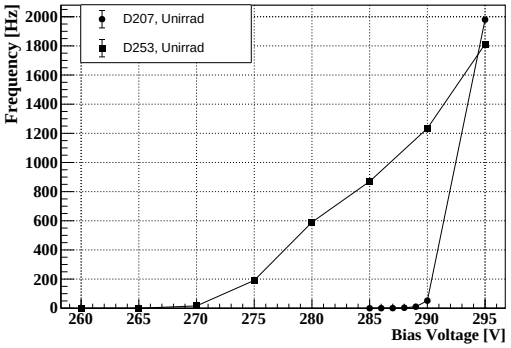

(a) Non-irradiated

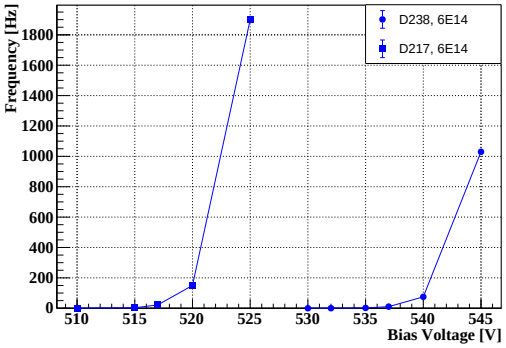

(b) $0.6 \times 10^{15}\,\mathrm{n_{eq}\,cm^{-2}}$

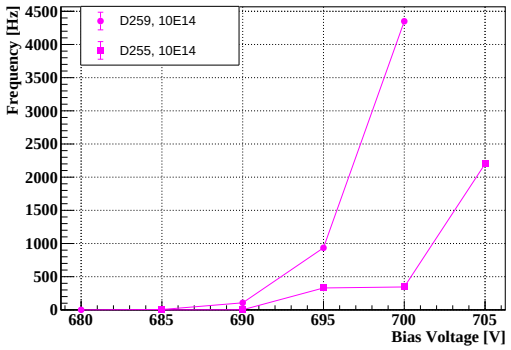

(c) $1.0 \times 10^{15}\,\mathrm{n_{eq}\,cm^{-2}}$

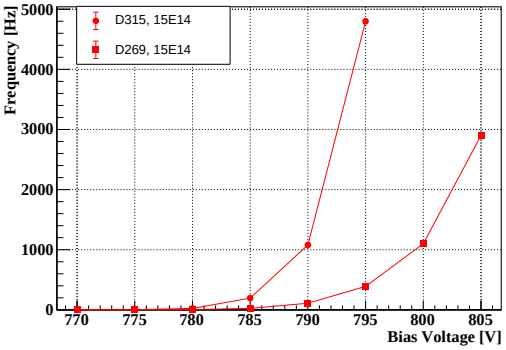

(d) $1.5 \times 10^{15}\,\mathrm{n_{eq}\,cm^{-2}}$

Fig. 6.54 Spurious pulse rate versus the bias voltage of the carbonated (CNM_EPI_C) samples when fresh (a), and at $0.6 \times 10^{15}\,\mathrm{n_{eq}\,cm^{-2}}$ (b), $1.0 \times 10^{15}\,\mathrm{n_{eq}\,cm^{-2}}$ (c) and $1.5 \times 10^{15}\,\mathrm{n_{eq}\,cm^{-2}}$ (d) irradiation fluences. Measurements taken in the Radioactive Source setup with NIM electronics with a threshold of $-25\,\mathrm{mV}$.

$1.0 \times 10^{15}\,\mathrm{n_{eq}\,cm^{-2}}$ and $1.5 \times 10^{15}\,\mathrm{n_{eq}\,cm^{-2}}$ irradiated samples. The presence of spurious pulses for this run was attributed to the short distance between the end of the $p+$ gain layer and the p-stop at the edge of the pad. This distance was 23.5 µm, which was designed to minimize the inter-pad distance in the multi-pad matrix type LGADs of this run. It is important to note that all the spurious pulses appears always after the working point of the V(8 fC), which indicates that these sensors have the best response against spurious pulses.

6.2.3 Comparative Analysis of Radiation Tolerance of Silicon-on-Silicon and Epitaxial LGADs with Standard and Carbon-Enriched Gain Layers

Figure 6.55 presents a comparison of the mean of the V_{BD} before and after irradiation for the three runs manufactured, with Silicon-on-Silicon CNM_SiSi_N (runs #15973) and CNM_SiSi_B (#12916) and with Epitaxial CNM_EPI (run #15246) substrates. The values are distinguished by the use of dotted lines for those sensors manufactured from SiSi substrates and simple lines for those derived from epitaxial wafers. The blue markers indicate the standard gain layer samples, while the black markers represent the carbonated gain layer. Lastly filled markers indicate sensors with a narrow gain layer, while empty markers indicate sensors with a broad gain layer. As previously stated, the V_{BD} values obtained from sensors with a narrow gain layer are consistently larger than those obtained from the broad gain layer. Furthermore the sensors from epitaxial wafers have larger values than those from SiSi wafers.

The V_{GL} from these three runs together can be seen in Figure 6.56, all derived from CV curves, with dotted lines for those sensors from SiSi substrates and simple lines for those sensors manufactured from epitaxial wafers. The blue markers indicate the standard gain layer sensors, while the black markers represent the sensors with carbonated gain layer. Filled markers indicate sensors with a narrow gain layer, while empty markers indicate sensors with a broad gain layer. From this comparison, it is clear that the carbonated samples across the three runs exhibit reduced variability in V_{GL} for all the irradiation fluences, suggesting diminished degradation due to irradiation.

Similarly, Figure 6.57 depicts the acceptor removal coefficients derived through the fitting of the preceding V_{GL} values as a function of the carbon dose for all the runs examined in this section. For the standard sensors (non-carbonated), the samples that display enhanced radiation resistance are those with an epitaxial substrate (run #15246) over the SiSi runs. Furthermore, a comparison between sensors with co-implantation of carbon in the multiplication layer, alongside the enhanced radiation resistance due to carbon, reveals that epitaxial

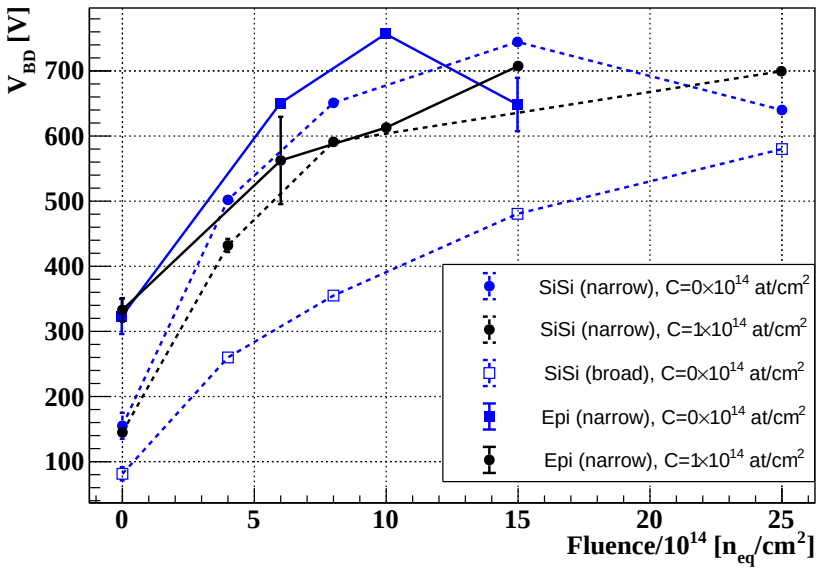

Fig. 6.55 Comparison of the V_{BD} before and after irradiation. The values are distinguished by the use of dotted lines for those derived from SiSi substrates (CNM_SiSi_B, CNM_SiSi_N and CNM_SiSi_N_C) and simple lines for those sensors manufactured from epitaxial wafers (CNM_EPI and CNM_EPI_C). The blue markers indicate the standard gain layer sensors, while the black markers represent the sensors with carbonated gain layer (CNM_SiSi_N_C and CNM_EPI_C). Filled markers indicate sensors with a narrow gain layer, while empty markers indicate sensors with a broad gain layer.

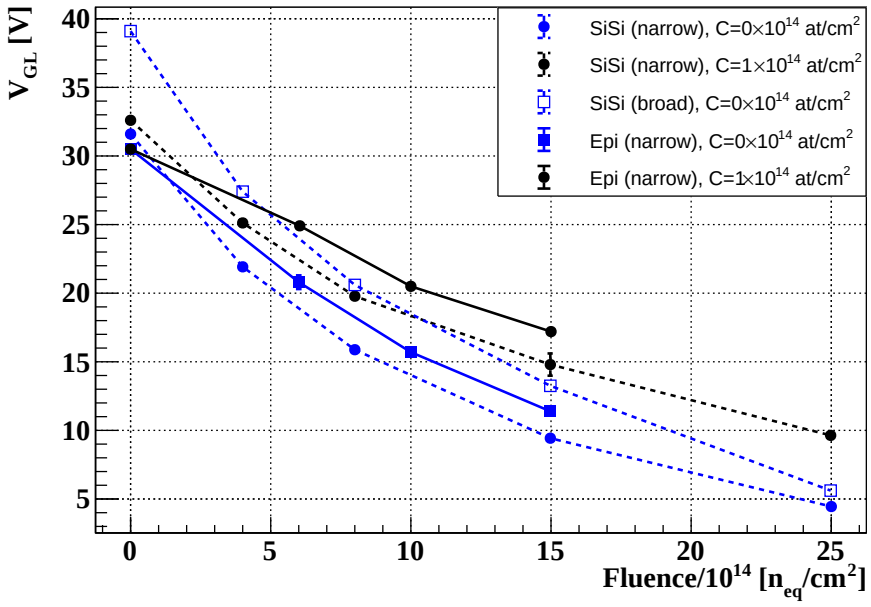

Fig. 6.56 Comparison of the V_{GL} values from the three runs, calculated from CV curves. The values are distinguished by the use of dotted lines for those derived from SiSi substrates (CNM_SiSi_B, CNM_SiSi_N and CNM_SiSi_N_C) and simple lines for those sensors manufactured from epitaxial wafers (CNM_EPI and CNM_EPI_C). The blue markers indicate the standard gain layer sensors, while the black markers represent the sensors with carbonated gain layer (CNM_SiSi_N_C and CNM_EPI_C). Filled markers indicate sensors with a narrow gain layer, while empty markers indicate sensors with a broad gain layer.

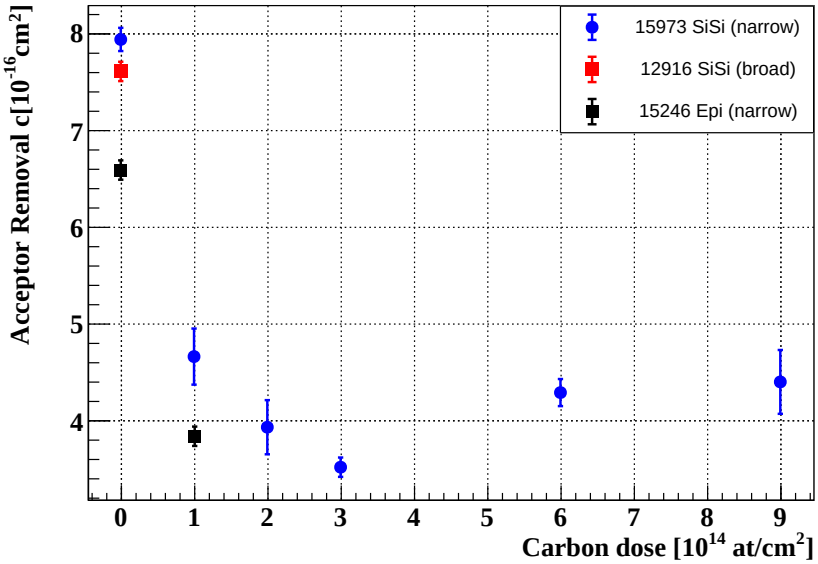

Fig. 6.57 Comparison of the accept removal coefficients from the three runs: #15973 (CNM_SiSi_N) with narrow gain layer for the different carbon doses (CNM_SiSi_N_CX) in blue markers, #12916 (CNM_SiSi_B) with broad standard gain layer in red marker and run #15246 standard (CNM_EPI) and carbonated (CNM_EPI_C) gain layer manufactured on epitaxial wafers. all values calculated from CV curves.

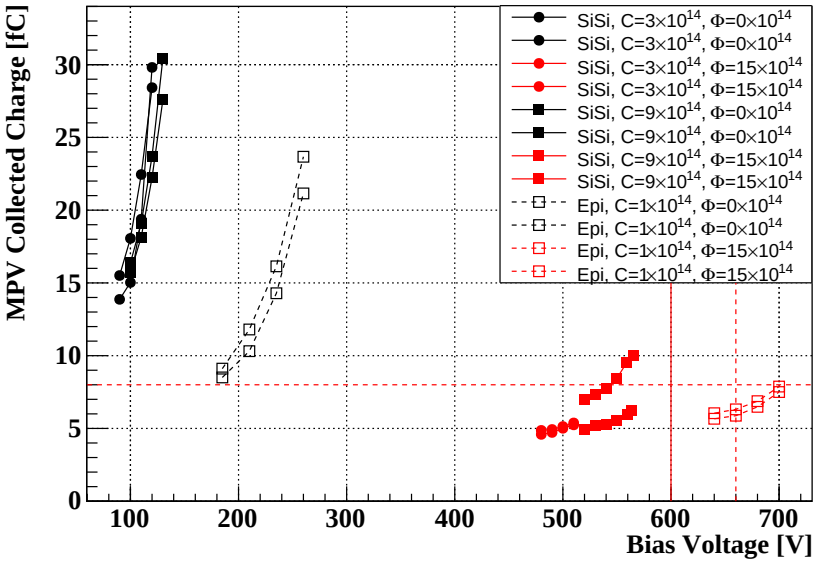

Fig. 6.58 Collected charge of the devices from run #15973 (filled markers) and run #15246 (empty markers), irradiated and non-irradiated as a function of the bias voltage. The limits for the ETL requirements of a collected charge above 8 fC at a bias voltage less than 12 V/µm are represented by red lines: vertical simple line is for run #15973 and doted for run #15246, horizontal is for both runs.

sensors exhibit reduced acceptor removal coefficients in comparison to sensors manufactured with SiSi wafers from run #15973.

A comparison is presented of the collected charge for both carbonated device runs with a narrow gain layer but different wafer type in Figure 6.58. The samples from run #15973 with different carbon doses are observed with filled markers. The carbonated devices from run #15246 are represented by empty markers with circles for the low carbonated samples and squares for the high carbonated samples. It can be observed that the samples from run #15973 exhibit a higher gain, as they generally require less voltage than the samples from run #15246. It should be noted that in the case of irradiated devices, there is only one common fluence point ($15 \times 10^{14}\,\mathrm{n_{eq}\,cm^{-2}}$) to be compared, and that the carbon doses are different between the runs under consideration.

Similarly, Figure 6.59 illustrates the time resolution obtained from both runs with a narrow gain layer, irradiated and non-irradiated. In this case, the filled markers represent samples from run #15973, fabricated with SiSi wafers, with circles indicating the carbonated samples with a dose of $3 \times 10^{14}\,\mathrm{at/cm^2}$ and squares indicating the carbonated samples with dose of $9 \times 10^{14}\,\mathrm{at/cm^2}$. The empty markers represent the carbonated sensors from run #15246, manufactured with epitaxial wafers. The sensors prior to irradiation from SiSi

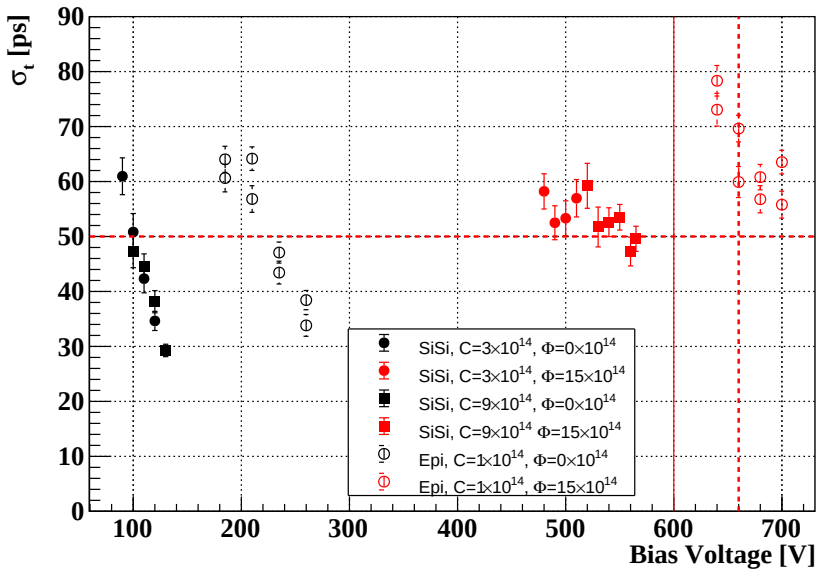

Fig. 6.59 Time resolution of the devices from run #15973 (filled markers) and run #15246 (empty markers), irradiated and non-irradiated as a function of the bias voltage. The limits for the ETL requirements of a time resolution below 50 ps at a bias voltage less than 12 V/µm are represented by red lines: vertical simple line is for run #15973 and doted for run #15246, horizontal is for both runs.

wafers (run #15973) exhibited a comparable operating voltage (independently of their carbon dose) and demonstrated the capacity to reach 50 ps at a bias voltage approximating 100 V, a value that is smaller than the 200 V necessary for the epitaxial sensors. The samples from run #15973 (SiSi) irradiated at 15×10^{14} $n_{eq}\,cm^{-2}$ exhibit superior time resolution in comparison to the preceding carbonated run #15246 (epitaxial), although it should be noted that these sensors have higher carbon doses.

6.3 Radiation tolerance studies of LGAD manufactured at HPK

Hamamatsu Photonics K.K. (HPK) is a company that develops a wide range of light sensors, such as photomultiplier tubes and photodiodes, and light sources such as lasers, LEDs, and measurement lamps. These sensors play a crucial role in various fields, from basic research to industrial quality control. In particular, Hamamatsu's semiconductor sensors are widely used in systems for distance measurement, imaging applications and radiation detection [141]. As the demand for silicon-based sensors continues to grow, Hamamatsu remains at the forefront of innovation, contributing significantly to the advancement of sensing technology worldwide.

6.3.1 HPK: HPK2 production

The LGADs studied from this manufacturer were sensors from the production run S10938-6130 that is also known as the HPK prototype 2 or simply HPK2, produced on a wafer of 50 µm of epitaxial layer over a support wafer of 150 µm thickness and low resistivity. For this production four splits were developed, each with a different gain value. These splits were labelled from S1, which had the highest gain, to S4, which had the smallest gain. This split classification according to the name of the wafer is presented in Table 6.10.

The samples for this study were only single pad devices with an active area of 1.3×1.3 mm^2 plus a guard-ring (GR) as well as all the LGAD studied in the present thesis. The samples have an optical window, of 100×100 μm^2 allowing direct illumination of the silicon with a laser for characterization with TCT.

At IFCA, measurements were conducted on all four splits of non-irradiated devices. However, after irradiation, only samples from W42 (S4) were available for fluences of 8×10^{14} $n_{eq}\,cm^{-2}$, 15×10^{14} $n_{eq}\,cm^{-2}$ and 25×10^{14} $n_{eq}\,cm^{-2}$.

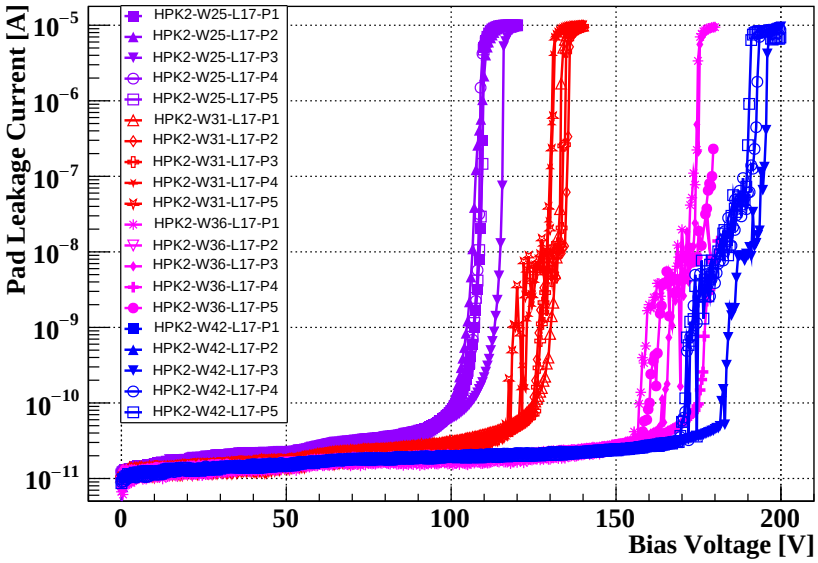

Fig. 6.60 The leakage current of the main pad is presented as a function of reverse bias prior to the irradiation of the LGADs from the different wafers from HPK (HPK2_EPI).

IV characteristics: The current-voltage characterization of the LGADs from this production was carried out on samples from the four available splits, and it was observed that the devices from the same wafer have similar characteristics. This finding is also confirmed by the gain level of each split, which gradually decreases from S1 to S4, as shown in Figure 6.60. The sensors of W25 (purple) had the highest gain, reaching V_{BD} before the other samples. W42 (blue) reached this point at a higher bias voltage and also has a relatively lower reverse current as shown in Figure 6.61, being the sensor with the better characteristics of the four wafers. In general, the reverse current of these sensors is very small, and the V_{BD} value of each wafer differs from wafer to wafer; these V_{BD} ranges are summarised in Table 6.10 but the V_{GL} was not possible to calculate properly from IV curves due to the very small currents.

Table 6.10 Summary of the V_{BD} values calculated from the IV curves for the various devices from wafers: W25, W31, W36 and W42. The gain level gradually decreases depending on the split, from S1 to S4.

V_{BD} for the different wafers (splits)			
W25 (S1)	W31 (S2)	W36 (S3)	W42 (S4)
90–105 V	115–130 V	155–175 V	175–190 V

Devices from the W42 wafer irradiated at $4 \times 10^{14}\,\mathrm{n_{eq}\,cm^{-2}}$, $8 \times 10^{14}\,\mathrm{n_{eq}\,cm^{-2}}$, $15 \times 10^{14}\,\mathrm{n_{eq}\,cm^{-2}}$ and $25 \times 10^{14}\,\mathrm{n_{eq}\,cm^{-2}}$, two samples per fluence, were characterised. The IV

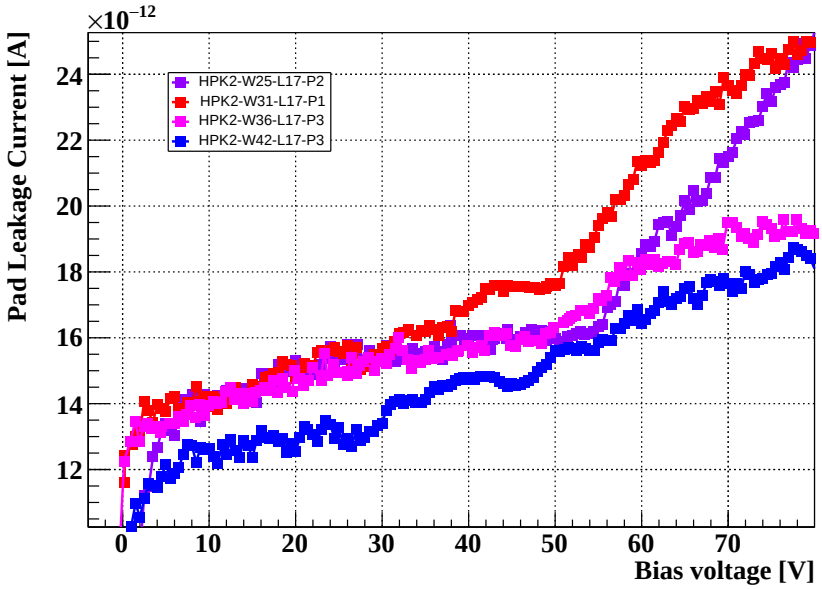

Fig. 6.61 Enlarged view of the gain layer region of the IV curves, with one sample per wafer for the HPK2_EPI. V_{GL} was not possible to calculate properly from IV curves due to the very small currents.

characteristics were measured using the methodology of subsection 4.3.1 and are shown in Figure 6.62 where the main behaviour is the grouping of the samples by their irradiation fluence: The less irradiated devices have a lower V_{BD} of around 300 V and this increases proportionally with fluence up to a higher V_{BD} of about 650 V for the samples at $25 \times 10^{14}\,\mathrm{n_{eq}\,cm^{-2}}$.

In Figure 6.63 we can see the range of V_{GL} where the effect is that the less irradiated samples have lower reverse current at a V_{GL} higher and with more fluence the current increases and the value of V_{GL} decreases, just as expected due to the effects of radiation. Table 6.12 summarises the V_{GL} values from the IV curves after irradiation.

CV characteristics: As with the IV characterization prior to irradiation, the CV measurements were taken over the four wafers available. These samples show a very good reproducibility between sensors from the same wafer split, which is easily visible. Figure 6.64 contains the CV curves, five samples for each wafer split. We can see the full curves, where their kinks corresponding to the depletion of the gain layer and bulk region are visible, and the V_{GL}s are around the 48–53 V as can be seen in Figure 6.65 which is an enlarged view of this region. Table 6.11 summarizes the V_{GL}s calculated from the CV characteristics.

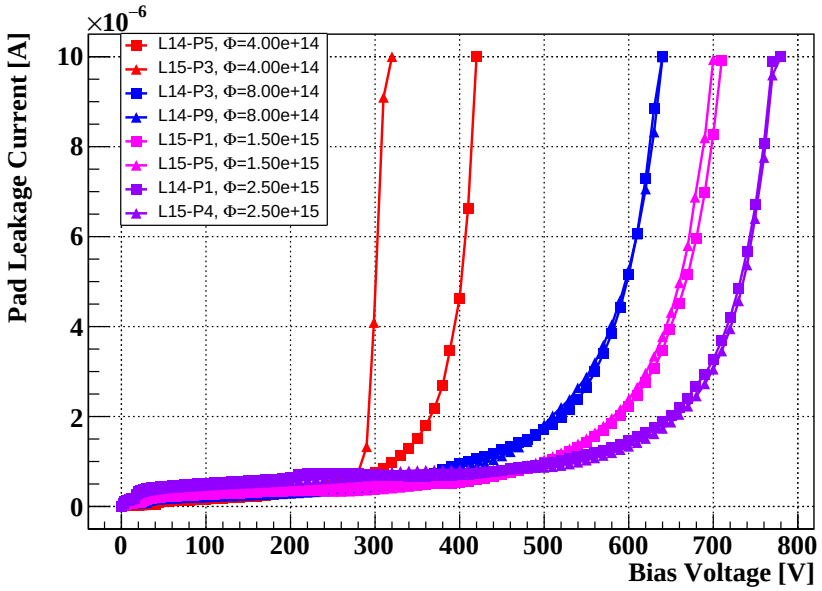

Fig. 6.62 IV curves of the samples irradiated to $4 \times 10^{14}\,\mathrm{n_{eq}\,cm^{-2}}$, $8 \times 10^{14}\,\mathrm{n_{eq}\,cm^{-2}}$, $15 \times 10^{14}\,\mathrm{n_{eq}\,cm^{-2}}$ and $25 \times 10^{14}\,\mathrm{n_{eq}\,cm^{-2}}$. The leakage current is shown as a function of reverse bias after irradiation of the LGDAs from W42 (HPK2_EPI_S4).

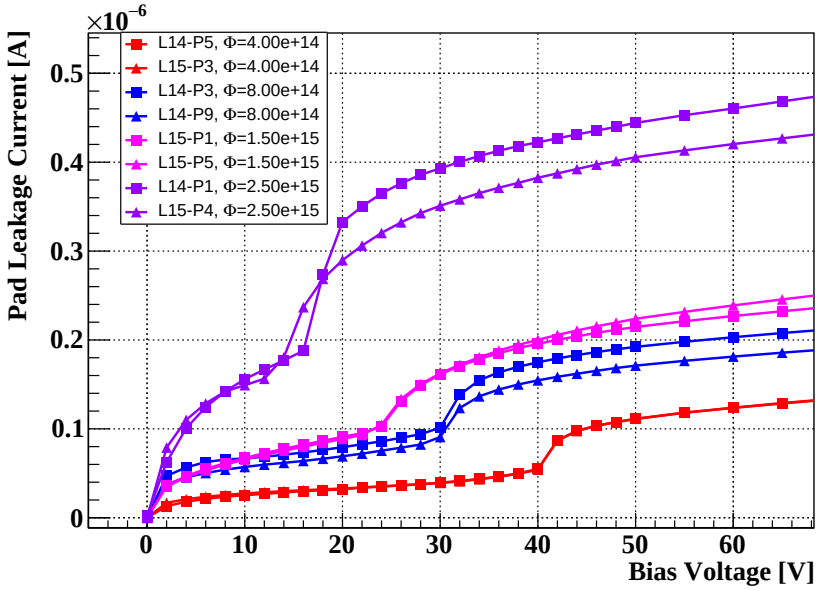

Fig. 6.63 Enlarged view of the gain layer region of the IV curves from the samples HPK2_EPI_S4 irradiated to $4 \times 10^{14}\,\mathrm{n_{eq}\,cm^{-2}}$, $8 \times 10^{14}\,\mathrm{n_{eq}\,cm^{-2}}$, $15 \times 10^{14}\,\mathrm{n_{eq}\,cm^{-2}}$ and $25 \times 10^{14}\,\mathrm{n_{eq}\,cm^{-2}}$.

Table 6.11 Summary of the V_{GL} values calculated from the CV curves for the various devices from wafers: W25, W31, W36 and W42 before irradiation.

V_{GL} for the different wafers (splits)			
W25 (S1)	W31 (S2)	W36 (S3)	W42 (S4)
53 V	52 V	49.5 V	49 V

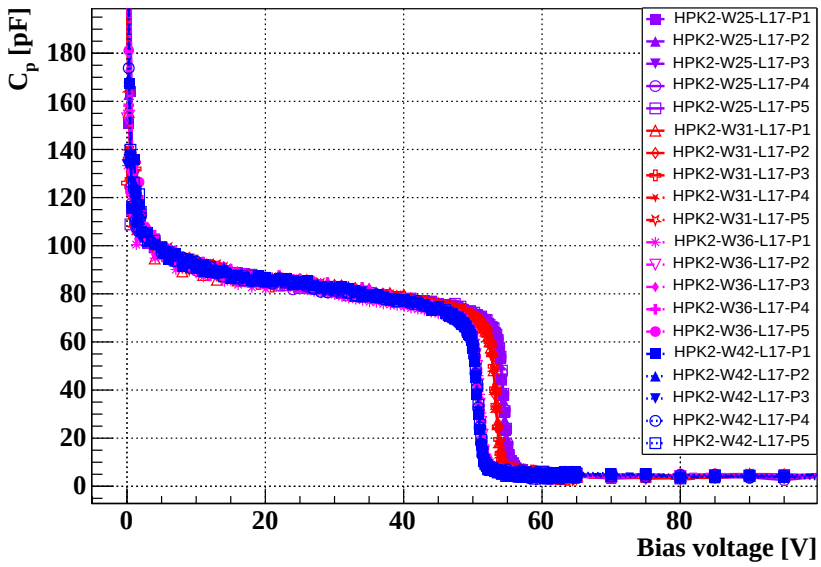

Fig. 6.64 The capacitance is shown as a function of reverse bias before irradiation for the HPK2_EPI LGADs from W25, W31, W36 and W42 wafers.

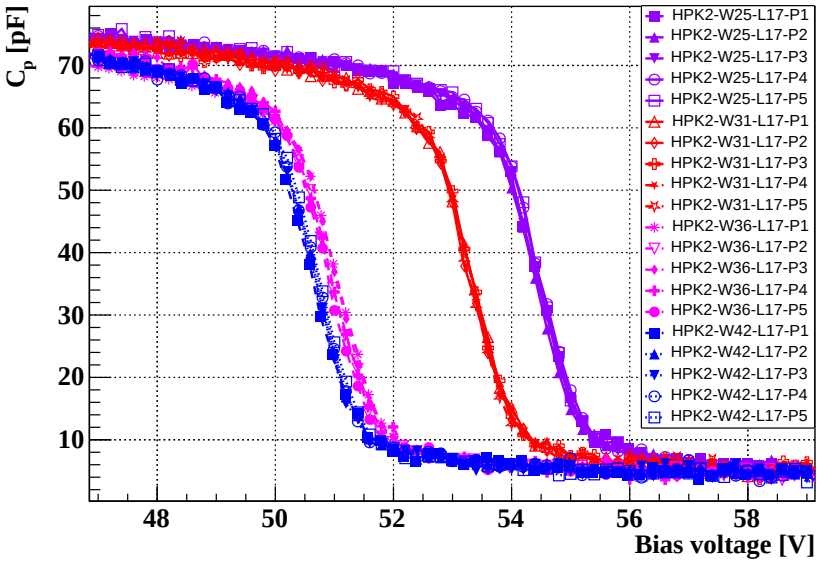

Fig. 6.65 Enlarged view of the gain layer regionfrom the CV curves before irradiation for the HPK2_EPI LGADs from W25, W31, W36 and W42 wafers.

Again, after irradiation only samples from W42 were available for CV characterization. As expected from the behaviour of the irradiated devices when measured to obtain their CV curves, these samples have a peak at the bias voltage corresponding to the gain layer, as discussed in subsubsection 4.3.2.2. The CV curves of these devices can be seen in Figure 6.66 and an enlarged view of the V_{GL} in Figure 6.67. The CV curves have a high reproducibility between sensors with the same irradiation fluence, the "peak" of the CV curves is located according to the irradiation of the samples: the higher the fluence, the lower the V_{GL} value, again due to the irradiation degradation of the multiplication layer. These V_{GL} values are summarised in Table 6.12 alongside the V_{GL} values calculated from IV characterization.

Acceptor removal coefficient: The acceptor removal coefficient was calculated by fitting the V_{GL} values summarized in Table 6.12 with Equation 5.1. The reported V_{GL}s and their fits are shown in Figure 6.68, in (a) the values calculated from the IV curves and (b) the values calculated from the CV curves. For the same samples, the acceptor removal coefficients are $c[10^{-16}\,\mathrm{cm}^2] = 4.8$ from the IV curves and $c[10^{-16}\,\mathrm{cm}^2] = 5.2$ from the CV curves. These coefficients are very good for standard (non-carbonated) LGADs, but not too small as achieved by carbonated samples as discussed in subsubsection 6.2.1.2 and subsection 6.2.2.

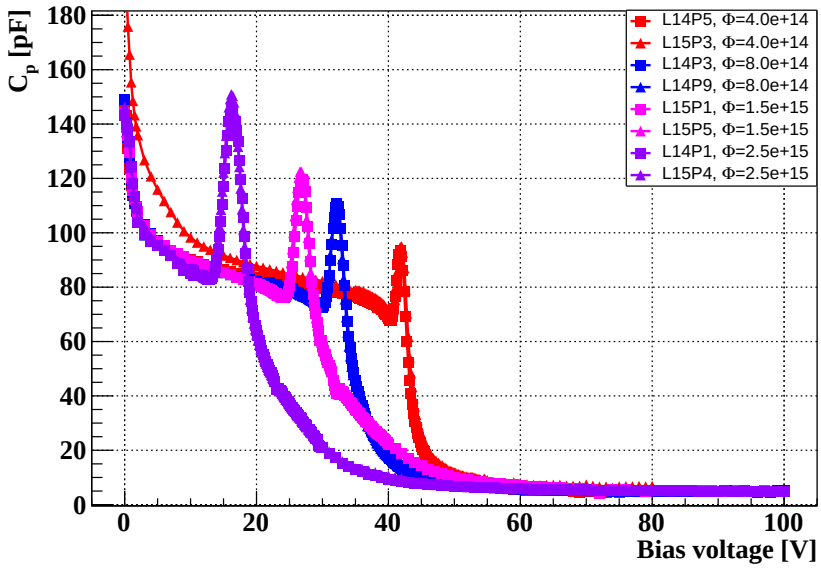

Fig. 6.66 CV curves of the HPK LGADs from wafer W42 (HPK2_EPI_S4). The capacitance is shown as a function of reverse bias after irradiation of the LGADs.

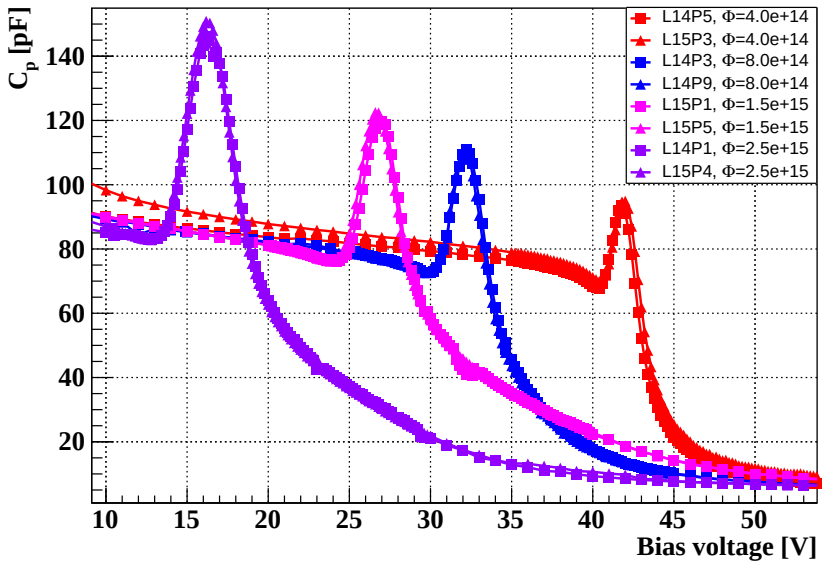

(a) GL region enlarged

Fig. 6.67 Elarged view of the gain layer region of the CV curves of the HPK LGADs from wafer W42 (HPK2_EPI_S4). The "peak" of the CV curves is located according to the irradiation of the samples.

Table 6.12 Summary of the V_{GL} values calculated from the electrical characterization of capacitance (CV) and current (IV), before and after irradiation of the HPK2_EPI_S4 sensors.

Fluence ($n_{eq}\,cm^{-2}$)	V_{GL} from IV	V_{GL} from CV
0	48 V	49 V
$4 \times 10^{14}\,n_{eq}\,cm^{-2}$	40 V	40.5 V
$8 \times 10^{14}\,n_{eq}\,cm^{-2}$	30 V	30 V
$15 \times 10^{14}\,n_{eq}\,cm^{-2}$	24 V	24 V
$25 \times 10^{14}\,n_{eq}\,cm^{-2}$	14 V	13 V

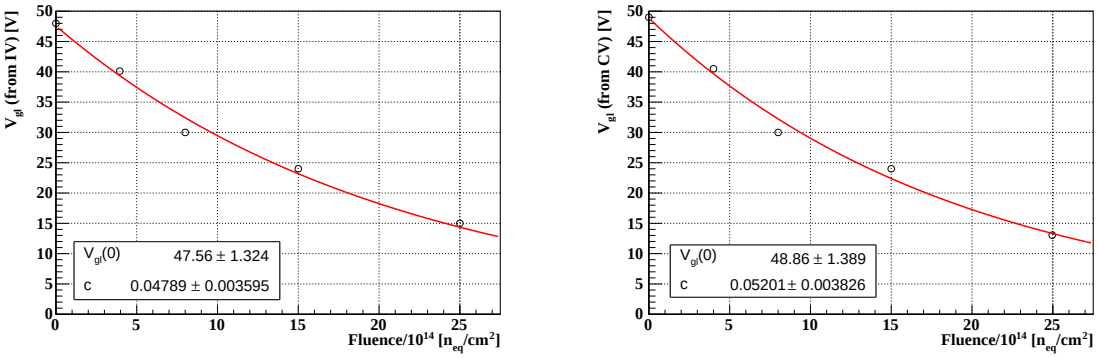

(a) From IV

(b) From CV

Fig. 6.68 Gain-layer depletion voltage from IV (a) and CV (b) as a function of the fluence and the respective fit (red) from where the acceptor removal coefficient is calculated and being $c[10^{-16}\,cm^2] = 4.8$ from IV calculation, and $c[10^{-16}\,cm^2] = 5.2$ from CV. HPK2_EPI_S4 sensors.

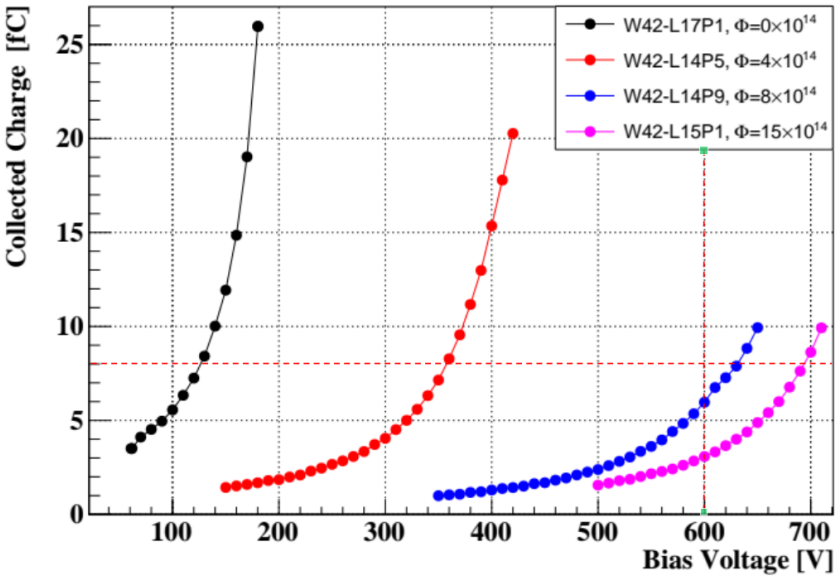

Fig. 6.69 Collected charge as a function of applied reverse bias of HPK LGADs (HPK2_EPI_S4), unirradiated and irradiated at different fluences. Calculated from the waveforms taken in the TCT setup at $-25\,°C$. The doted lines are the limits for the ETL requirements: a collected charge above 8 fC at a bias voltage less than $12\,V/\mu m$.

Collected charge: For this production, a TCT characterization was carried out in order to calculate the collected charge of these LGADs after irradiation, one sample per fluence, except for the $25 \times 10^{14}\,n_{eq}\,cm^{-2}$ which suffered physical damage and could not be measured. As the timing TCT setup was unfortunately not used for this campaign, only the collected charge was calculated by measuring the waveforms of each sample at different bias voltages as described in section 4.4 at $-25\,°C$, and the resulting collected charge is shown in Figure 6.69. Here, the LGADs after irradiation have an obvious degradation in the multiplication layer, requiring higher voltages compared to the unirradiated sample (black marker) to collect the same amount of charge.

The radioactive source setup was not available during this characterization campaign, which could be a better approach to estimate the collected charge and the possibility to make a timing characterization with the three sensors stack (section 4.5).

6.4 Radiation tolerance studies of LGAD manufactured at FBK

Fondazione Bruno Kessler (FBK) is a research centre focusing on highly integrated sensors and devices. Its work includes both state-of-the-art research and new frontier research in quantum sciences and technologies. FBK is engaged in research and industrial innovation, particularly in the field of silicon-based devices. These devices include micro-electro-mechanical systems (MEMS), complementary metal-oxide-semiconductor (CMOS) sensors, photonics and surface functionalisation techniques. In particular, FBK is a world reference in the production of silicon 3D detectors used in fundamental physics experiments [142].

Its ongoing research spans materials science, radiation detectors, photonics, life sciences, biotechnology and quantum technologies. The FBK facility, equipped with a 700 m^2 Class 10 clean room[143], enables the in-house development of various micron-scale devices. These range from silicon integrated microsensors to biosensors, BioMEMS and custom designed ASIC-CMOS.

6.4.1 FBK: UFSD4 production

FBK produced 18 wafers with different doping doses for Boron and for co-implanted Carbon. This production also includes different types of guard-ring and inter-pad designs to test them. This run is called UFSD4 ("Ultra Fast Silicon Detectors"). It consists of carbonated and standard gain layer wafers with two inter-pad layouts: Type 9, with a double p-stop and Type 10, implementing a guard-ring grid. This run also includes the denominated "shallow" and "deep" drive-in configurations. UFSD4 includes single pad, 1×2, 2×2, 5×5 and 16×16 arrays, all with 55 µm of active thickness. This was the first production of UFSD with devices specifically designed for the CMS ETL, unfortunately we cannot perform IV characterization on irradiated samples and only a few 2×2 samples have been measured with the radioactive source setup. This study focuses on wafers with shallow and deep drive-in gain layers. Their boron and carbon doses and drive-in configuration can be seen in Table 6.13.

IV characteristics: Single pad LGADs were measured to obtain their IV characteristics. The reverse current as a function of the applied bias voltage was obtained using the same methodology described in subsection 4.3.1. The resulting IV curves are shown in Figure 6.70 for the unirradiated sensors with the shallow drive-in LGAD sensors from W7 (red markers) and W8 (blue markers); Figure 6.72 contains the IV curves of the deep drive-in LGADs from W17 (purple markers) and W18 (pink markers). Figure 6.71 and Figure 6.73 are just

Table 6.13 Carbon and Boron dose and Drive-In configuration for the different wafers studied from the UFSD4 production of FBK. The doses are expressed in terms of "A" and "B" which, due to industrial secrecy is not publicly available.

Wafer	W7	W8	W9	W17	W18
Drive-In	Shallow	Shallow	Shallow	Deep	Deep
Boron dose (A)	0.98	0.98	0.98	0.79	0.79
Carbon dose (B)	0.8	0.8	0.8	0.6	0.6

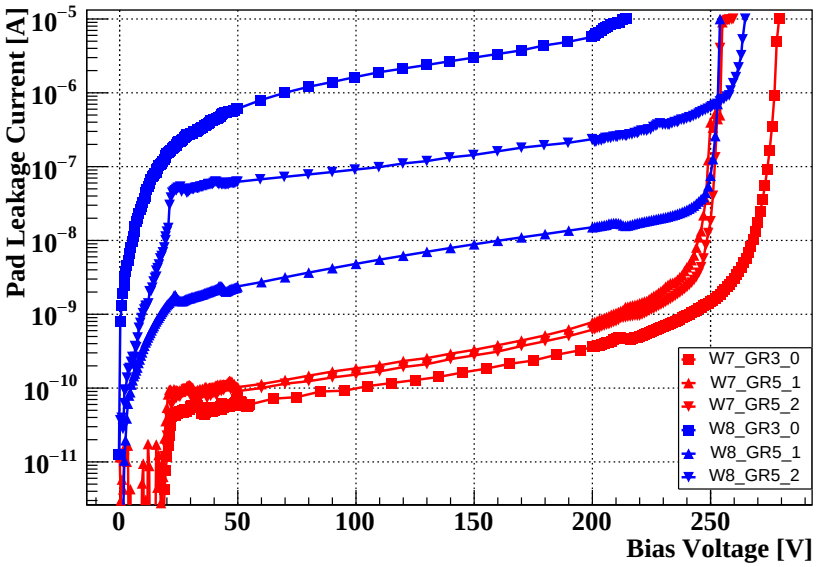

Fig. 6.70 IV curves of the LGDAs from the UFSD4 production are shown for the samples with an shallow drive-in. A high current can be seen in the shallow samples from wafer W8 compared to the rest of samples.

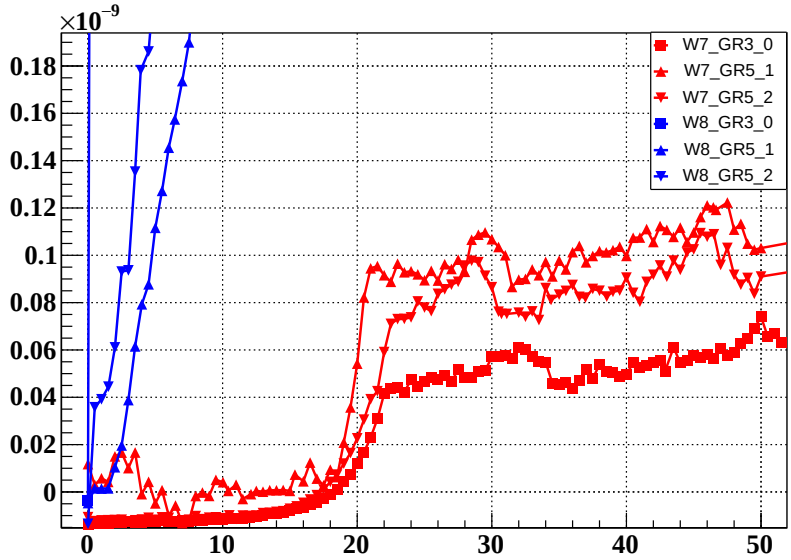

Fig. 6.71 Enlarged view of the gain layer region from the IV curves is shown for the shallow samples. A high current can be seen in the shallow samples from wafer W8 compared to the rest of samples.

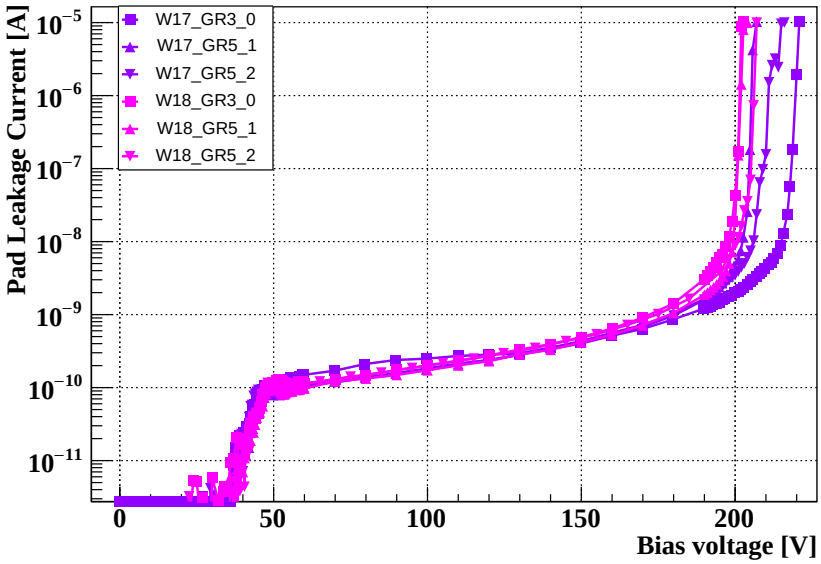

Fig. 6.72 IV curves of the LGDAs from the UFSD4 production are shown for the samples with a deep drive-in.

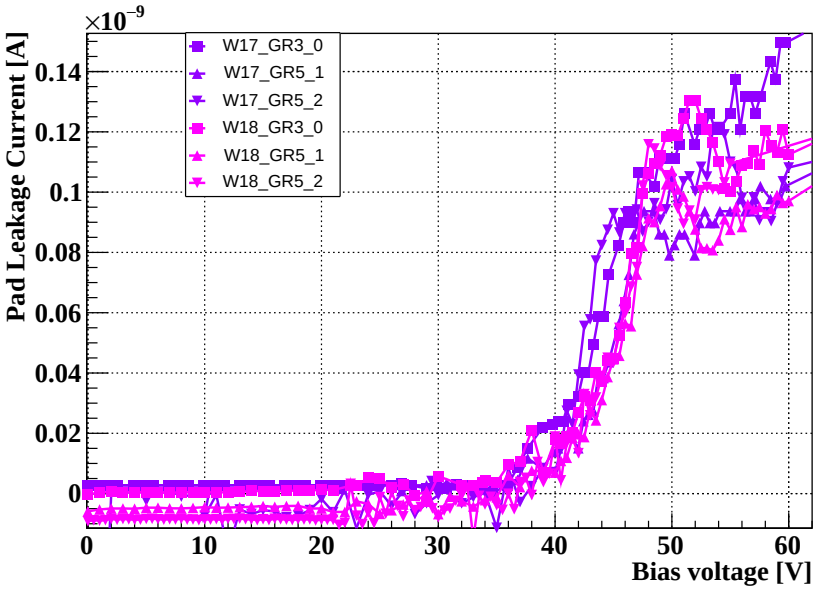

Fig. 6.73 Enlarged view of the gain layer region from the IV curves is shown for the deep samples.

the magnified view of the gain layer region of the IV curves for shallow and deep sensors, respectively.

One of the main differences we can observe is the fact that "shallow" samples from wafer W8 (blue) have a higher current than the rest of the samples (shallow and deep). This could be due to a defect in the manufacturing of the wafer that introduces an extra current, since the LGADs with the same design of GR, identified with the names GR3 and GR5, but from the other wafers, have reverse currents of a similar order of magnitude.

CV characteristics: The capacitance of the sensors non-irradiated was measured in the same way as for the other LGADs, with the GR connected to the HV and at a low frequency of 100 Hz. Figure 6.74 shows the CV curves of the sensors with shallow drive-in before irradiation; Figure 6.75 contains the CV curves of samples with deep drive-in before irradiation and Figure 6.76 and Figure 6.77 are the enlarged views of the CV curves in the GL region.

The shallow samples has a V_{GL} around the 21 V and the V_{GL} for the sensors with deep drive-in of around 45 V and with a lower capacitance value in the range of 80 pF, compared to the 200 pF for the V_{GL} of the shallow sensors. Both types of samples have a low scatter and a good reproducibility, regardless of the samples coming from different wafer numbers, since the shallow samples are from W7 and W8, and the deep sensors from W17 and W18. The final capacitance measured for both types of sensors was about $C_{end} = 3.5$ pF, which is

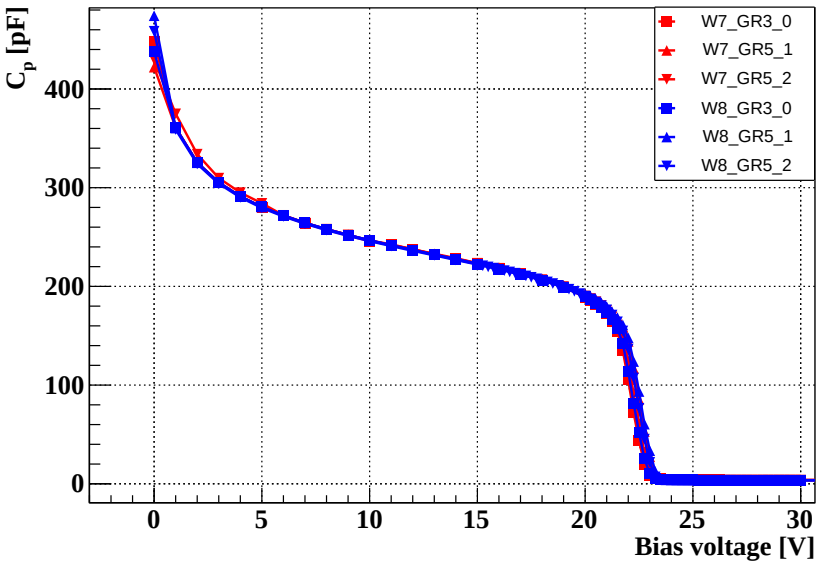

Fig. 6.74 CV curves from the LGADs with a Shallow drive-in before irradiation.

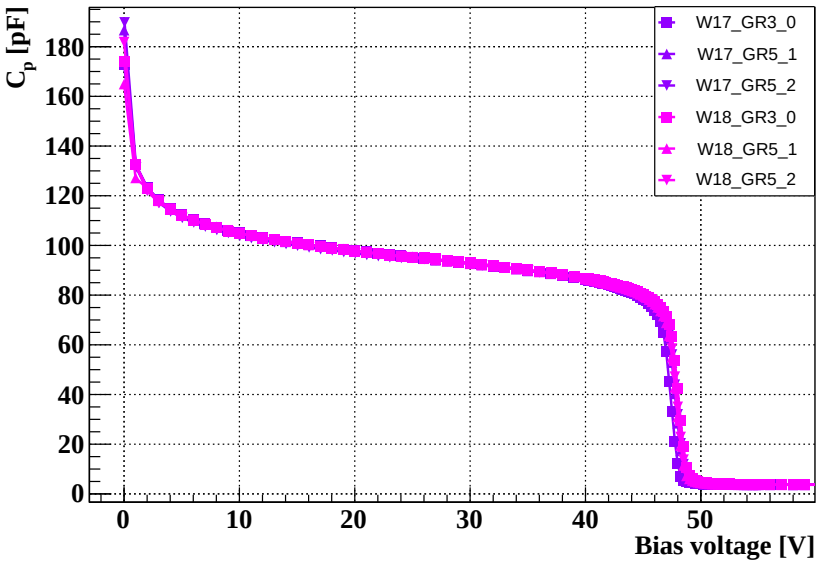

Fig. 6.75 CV curves from the LGADs samples with Deep drive-in before irradiation.

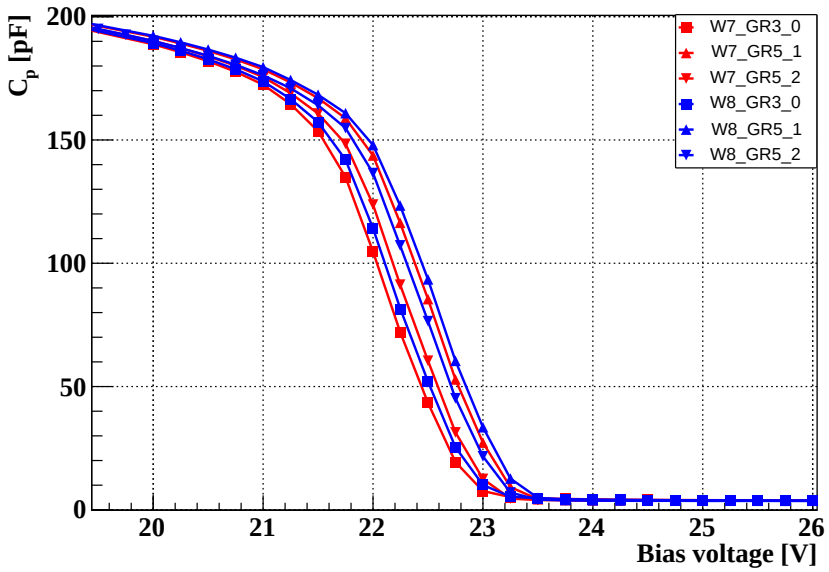

Fig. 6.76 Enlarged view of the gain layer region from the CV curves of the LGADs with a Shallow drive-in before irradiation.

less than the C_{end} of sensors with an active thickness of 50 µm, which is in agreement for these sensors of 55 µm active thickness. A better comparison of the CV curves for shallow and deep sensors can be seen in Figure 6.78.

Figure 6.78 shows the two types of drive-in, shallow (red and blue markers) and deep (purple and pink markers), used in these LGADs to better observe the regions where their V_{GL} are located and the different levels of capacitance across the applied reverse bias. In Figure 6.79 there are the doping profiles of the shallow (filled markers) and deep (empty markers) as a function of the depth of the sensor, calculated from their capacitance as described in subsection 4.3.3. It can be seen that the shallow diffusion is closer to the surface of the sensor and has a higher doping, while the deep diffusion is deeper (as expected) but has a lower doping level.

For the radiation tolerance study, only shallow drive-in samples with 1×2 and 2×2 arrays were available, and since our probe station was prepared to measure only single sensors, only one pad of each structure was measured, at a temperature of 10 °C with a low frequency of 100 Hz as before irradiation. The CV curves of these sensors after irradiation at 10×10^{14} $n_{eq}\,cm^{-2}$ and 15×10^{14} $n_{eq}\,cm^{-2}$ fluences can be seen in Figure 6.80. These carbonated shallow drive-in type sensors show a degradation of the gain layer due to irradiation, as evidenced by the difference in V_{GL}s from the two irradiation fluences, which

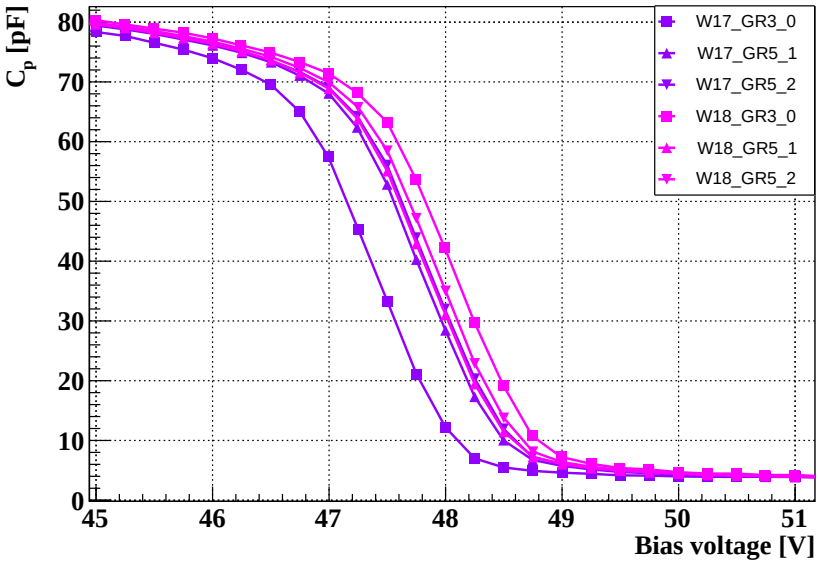

Fig. 6.77 Enlarged view of the gain layer region from the CV curves of the LGADs with a Deep drive-in before irradiation.

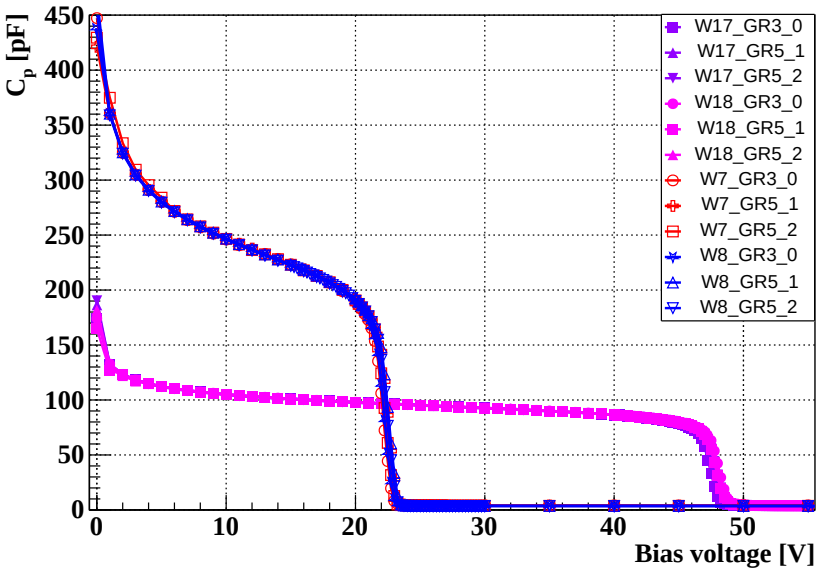

Fig. 6.78 Comparison of the samples with a different drive-in configuration of the gain layer: shallow (W7 in red and W8 in blue) and deep (W17 in purple and W18 in pink).

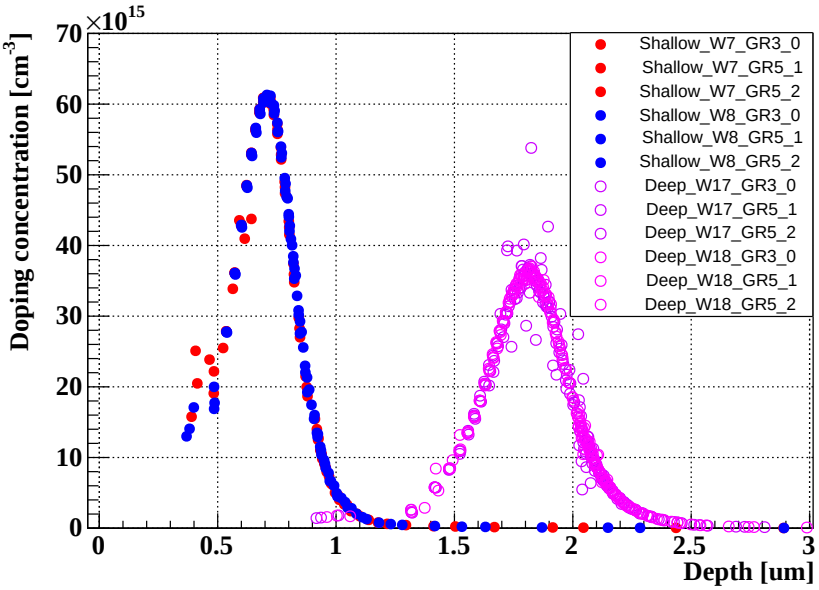

Fig. 6.79 Comparison of the doping profiles for both types of drive-in configuration of the gain layer: shallow (W7 in red and W8 in blue) and deep (W17 in purple and W18 in pink).

is about 18.6 V for the $10 \times 10^{14}\,\mathrm{n_{eq}\,cm^{-2}}$ fluence and 17.2 V for the $15 \times 10^{14}\,\mathrm{n_{eq}\,cm^{-2}}$ fluence.

Acceptor removal coefficient: The acceptor removal coefficient was calculated by fitting the V_{GL} values for the non-irradiated and irradiated sensors with a shallow drive-in configuration. These V_{GL}s and their fits are shown in Figure 6.81. This time, the acceptor removal coefficient was calculated from the CV characteristics only. The resulting acceptor removal coefficient is $c[10^{-16}\,\mathrm{cm^2}] = 1.5$ which is an indicator of the excellent radiation tolerance of these devices.

Charge collection: The shallow sensors of W7 and W9 were characterized using the radioactive source setup. Only sensors with 1×2 and 2×2 arrays were available and only one pad of each structure had to be connected in order to be measured in the setup designed for single pad sensors. Due to a problem with fluctuations in the baseline of the FBK sensor 2×2 irradiated at a fluence of $15 \times 10^{14}\,\mathrm{n_{eq}\,cm^{-2}}$, the sensor could not be properly characterized, for this reason and for comparison purposes, the results of three sensors from [144] were added, represented with triangle markers and with the difference that these measurements were made at a temperature of $-30\,^{\circ}\mathrm{C}$ instead of $-25\,^{\circ}\mathrm{C}$ of the measurements made at IFCA.

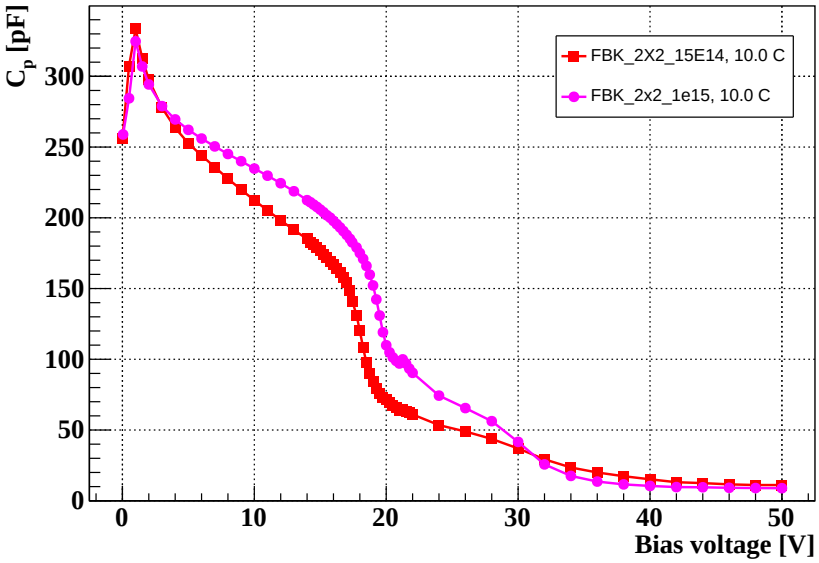

Fig. 6.80 CV curves from the LGADs with a Shallow drive-in after irradiation of 10×10^{14} $n_{eq}\,cm^{-2}$ (pink) and 15×10^{14} $n_{eq}\,cm^{-2}$ (red) fluences.

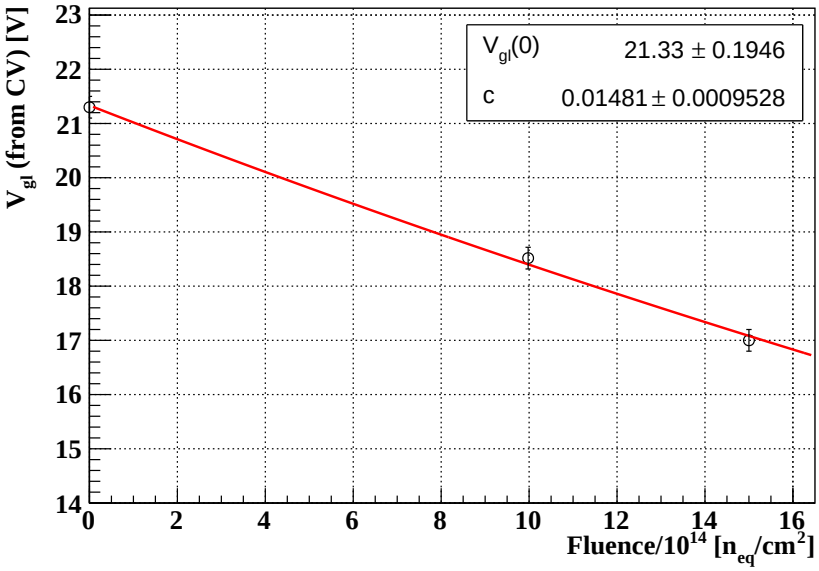

Fig. 6.81 Gain-layer depletion voltage from CV as a function of the fluence and the respective fit (red) from where the acceptor removal coefficient is calculated, resulting in $c[10^{-16}\,cm^2] = 1.5$.

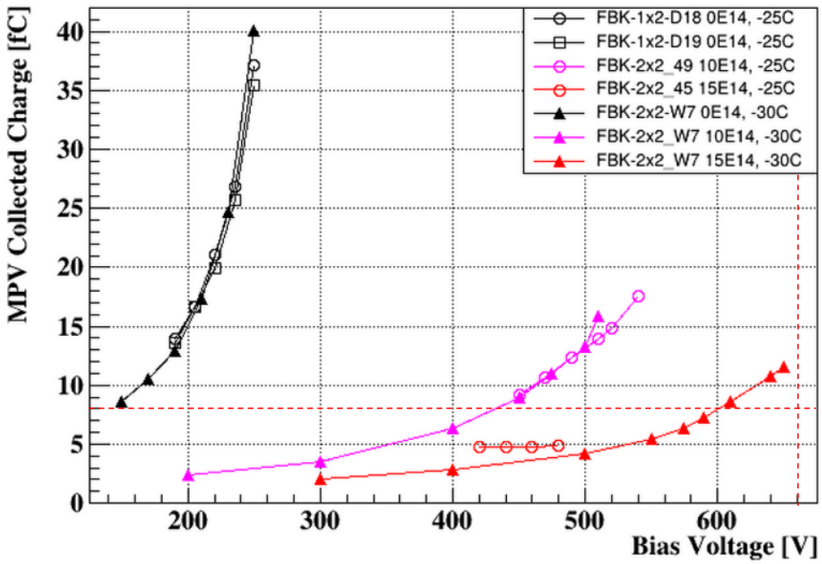

Fig. 6.82 Collected Charge as a function of the reverse bias voltage for the UFSD4 samples. Measurements with circle markers were performed at $-25\,^{\circ}\mathrm{C}$ at IFCA and measurements with triangle markers at a temperature of $-30\,^{\circ}\mathrm{C}$, added from [144] for comparison. The doted lines are the limits for the ETL requirements: a collected charge above 8 fC at a bias voltage less than $12\,\mathrm{V}/\mu\mathrm{m}$.

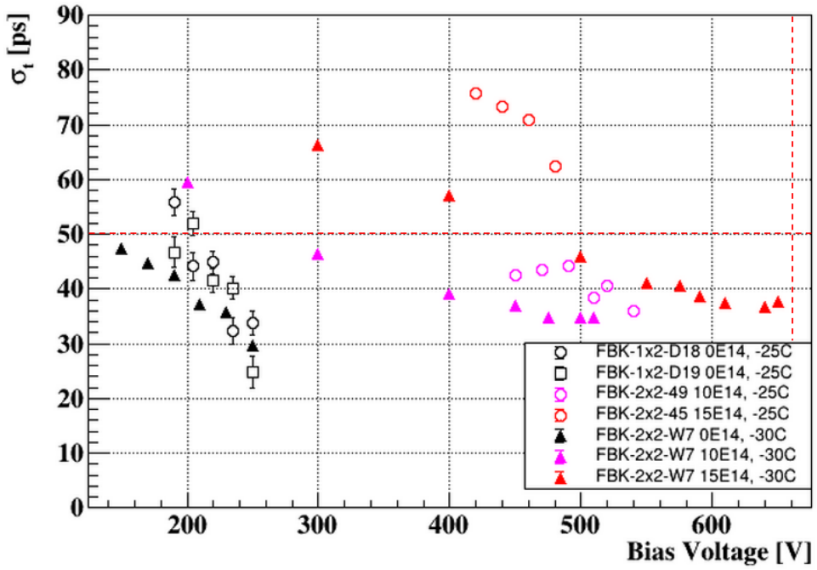

Fig. 6.83 Time resolution of the UFSD4 samples. Measurements with circle markers were performed at $-25\,^{\circ}\mathrm{C}$ at IFCA and measurements with triangle markers at a temperature of $-30\,^{\circ}\mathrm{C}$, added from [144] for comparison. The doted lines are the limits for the ETL requirements: a time resolution below 50 ps at a bias voltage less than $12\,\mathrm{V}/\mu\mathrm{m}$.

Figure 6.82 shows the charge collected as a function of bias voltage, irradiated and non-irradiated. The damage caused by irradiation in terms of gain layer degradation is evident, for example, the samples irradiated at the higher fluence of $15 \times 10^{14}\,\mathrm{n_{eq}\,cm^{-2}}$ require a higher bias, approximately 175 V to achieve the same charge of 8 fC compared to the sensors irradiated to $10 \times 10^{14}\,\mathrm{n_{eq}\,cm^{-2}}$. Both irradiated fluences required much more bias voltage compared to the non-irradiated devices.

Time resolution: The resulting time resolution σ_t of the sensors measured at the radioactive source setup are shown in Figure 6.83. Again, measurements from [144] was included. In the same way that with the others LGADs characterized, as the fluence increases, the voltage required to achieve the same time resolution also increases. To exemplified this, the bias voltage required to reach values below 40 ps of time resolution is lower for the non-irradiated sensors of about 230 V than after being irradiated that requires around 400 volt and around 580 V for the sensors irradiated to fluences of $10 \times 10^{14}\,\mathrm{n_{eq}\,cm^{-2}}$ and $15 \times 10^{14}\,\mathrm{n_{eq}\,cm^{-2}}$ respectively, both from wafer W7.

Chapter 7

Summary and Conclusions

The High-Luminosity Large Hadron Collider (HL-LHC) is set to be the flagship collider of particle physics in the coming decade, enabling unprecedented precision studies of the Higgs boson, searches for physics beyond the Standard Model (BSM), and exploration of rare processes. By increasing its instantaneous luminosity, the HL-LHC will deliver an integrated luminosity of 4000 fb^{-1}, enhancing the discovery potential of CERN's research program. However, these high luminosities introduce new technical challenges, particularly in tracking and vertex reconstruction, due to the extreme pile-up conditions expected in each bunch crossing. To maintain high reconstruction efficiency and physics sensitivity, the CMS experiment is undergoing a major upgrade, incorporating new timing layers to improve particle identification and vertex association.

Due to the increase in instantaneous luminosity, multiple pile-up collisions will occur at each bunch crossing, making it extremely difficult to disentangle the different particles originating from various vertices. To address this challenge, the introduction of a new detector concept, the MIP Timing Detector (MTD) has been proposed. The MTD will be able to determine the production times of the MIPs (Minimum Ionizing Particles) generated at the different primary vertices. The forward and backward parts of the MTD, named as the Endcap Timing Layer (ETL) sub-detetector uses as baseline sensor technology the Low Gain Avalanche Detectors (LGADs), which offer fast signal response, moderate internal gain, and excellent time resolution, making them ideal for high-precision tracking in the HL-LHC era. The ETL should provide a time resolution of few tens of picoseconds and a spatial resolution of several hundred microns, significantly improving upon previous time-of-flight detectors based on scintillator technologies.

Among the various technical challenges that LGAD sensors must overcome, radiation tolerance is the dominant one. In the CMS experiment, the maximum fluence in the innermost ETL region is $1.5 \times 10^{15}\,\text{n}_{\text{eq}}\,\text{cm}^{-2}$. However, for 80% of the detector area, the fluence

remains below 1.0×10^{15} n/cm^2, making radiation hardness a key factor in the sensor design. The contribution from other hadronic fluences is negligible, further reinforcing the need to optimize LGAD technology specifically for neutron-induced degradation.

Motivated by this challenging radiation environment, this thesis performed a comprehensive radiation tolerance study of LGAD sensors manufactured by three major production centers: IMB-CNM (Spain), FBK (Italy), and HPK (Japan). Special emphasis is placed on IMB-CNM sensors, investigating different technological implementations, including variations in substrate, Silicon-on-Silicon (SiSi) versus Epitaxial (Epi), gain layer designs with broad versus narrow implantation profiles, and multiplication layer doping with carbonated versus non-carbonated gain layers. These studies have been conducted within the framework of the above mentioned ETL detector collaboration of the CMS experiment, ensuring relevance to the HL-LHC upgrade program.

To assess the radiation tolerance of LGADs, two complementary methodologies have been considered. The first involves an expected more fundamental characterization by measuring the deactivation of the gain layer acceptors, quantified by the acceptor removal coefficient summarized in Table 7.1 The second focuses on operational performance by determining the minimum bias voltage required to achieve 8 fC charge collection, which is the threshold ensuring the readout ASIC achieves a 50 ps time resolution, see Table 7.2. Additionally, timing resolution measurements using a dedicated fast amplifier setup provide independent confirmation of the charge collection trends, further validating the analysis.

Among the various technological strategies explored to enhance radiation hardness, the most effective approach was the carbon co-doping of the gain layer. LGADs fabricated on Si-on-Si wafers with the highest carbon implantation dose exhibited the best post-irradiation performance, successfully reaching the 8 fC charge collection threshold at bias voltages well below the Single-Event Burnout (SEB) limit 12 V/µm. Other design parameters, such as gain layer width and substrate type, did not show a clear improvement in radiation tolerance, highlighting carbon co-implantation as the key factor in extending the operational lifetime of LGADs at HL-LHC. Notably, the FBK_UFSD4_S[1] and CNM_SiSi_N_C9 productions met the CMS requirements. More specifically, the CNM_SiSi_N_C9 LGAD production with Si-on-Si substrates, narrow implant, and the highest carbon implantation dose met the radiation tolerance requirements of the CMS ETL subdetector in terms of both timing resolution (Figure 7.1) and collected charge (Figure 7.2), as well as safe operating bias voltages. Also the spurious pulses are absent for one of the samples irradiated to 15×10^{14} $\mathrm{n_{eq}\,cm^{-2}}$ (Figure 7.3) and leakage current (Figure 7.4) and breakdown voltage (Figure 7.5) remain

[1]The radiation tolerance of the FBK_UFSD4_S LGADs, that present the smallest acceptor removal coefficient in agreement with previous studies[145], could only be assessed up to a fluence of $1.0 \times 10^{15} n_{eq}/cm^2$ since the samples irradiated at $1.5 \times 10^{15} n_{eq}/cm^2$ presented large baseline fluctuations.

Table 7.1 Summary of the Acceptor Removal Coefficients c achieved by the LGADs samples from different manufacturers, calculated from CV. The data set includes information on the boron and carbon doses when available and for the case of the FBK sensors, the doses are expressed in terms of "A" and "B" which, due to industrial secrecy, is not publicly available (see Table 6.13).

Production ID	B dose (width) $[10^{13} cm^{-2}]$	C dose $[10^{13} cm^{-2}]$	Acceptor removal coef. $[10^{-16} cm^{2}]$
CNM_SiSi_B	2.1 (broad)	0	7.8
CNM_EPI_C1	1.9 (narrow)	10	3.8
CNM_EPI	1.9 (narrow)	0	6.6
CNM_SiSi_N	1.9 (narrow)	0	7.9
CNM_SiSi_N_C1	1.9 (narrow)	10	4.7
CNM_SiSi_N_C2	1.9 (narrow)	20	3.9
CNM_SiSi_N_C3	1.9 (narrow)	30	3.5
CNM_SiSi_N_C6	1.9 (narrow)	60	4.3
CNM_SiSi_N_C9	1.9 (narrow)	90	4.4
HPK2_EPI_S4	-	0	5.2
FBK_UFSD4_S	0.98 (A)	0.8 (B)	1.5

inside the requirements (for the leakage current, the limit was scaled to one single pixel sensor assuming linearity with respect of the large sensors of 16×16, seesection 6.1).

Despite having a reduced acceptor removal coefficient, it was not the lowest among the tested CNM technologies, yet the overall performance under radiation conditions demonstrated its suitability for deployment in The CMS experiments.

These results indicate that the acceptor removal coefficient alone does not determine which LGAD doping profile is the most radiation-tolerant. The best-performing LGAD technology does not correspond to the device with the lowest acceptor removal coefficient. Other factors, such as the initial gain of the non-irradiated LGAD, may significantly impact its radiation tolerance. This suggests that a comprehensive evaluation considering other parameters is necessary to optimize LGAD designs for high-radiation environments.

Overall, the findings of this thesis confirm that radiation-hardened LGADs are viable for operation in HL-LHC conditions, ensuring that timing detectors will play a crucial role in maintaining tracking performance in the extreme pile-up environment of the HL-LHC.

Future activities

At the time of writing this thesis, several engineering runs at IMB-CNM are being processed with optimized parameters derived from characterization campaigns, incorporating a deep

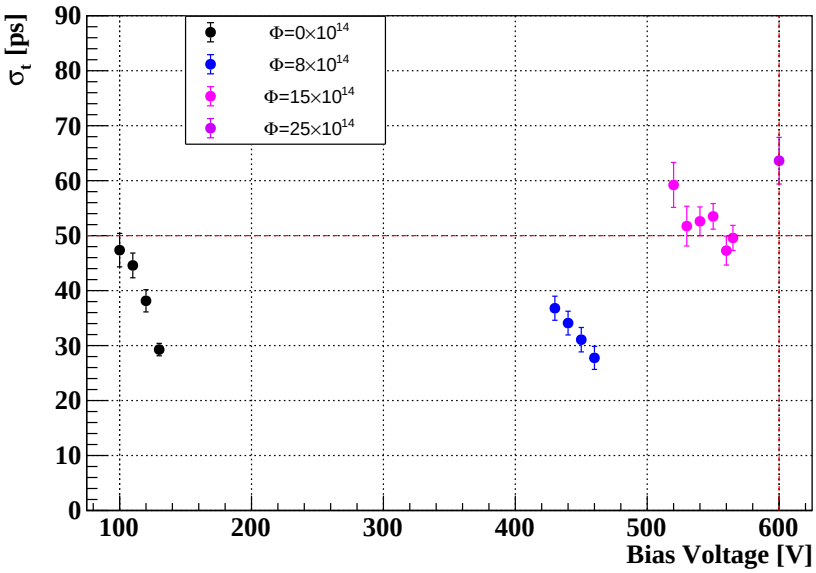

Fig. 7.1 Time resolution of the high carbonated samples, calculated using Equation 4.12 and errors with Equation 4.13. All these measurements were performed at $-25\,^{\circ}\mathrm{C}$. The doted lines are the limits for the ETL requirements: a time resolution below 50 ps at a bias voltage less than $12\,\mathrm{V}/\mu\mathrm{m}$.

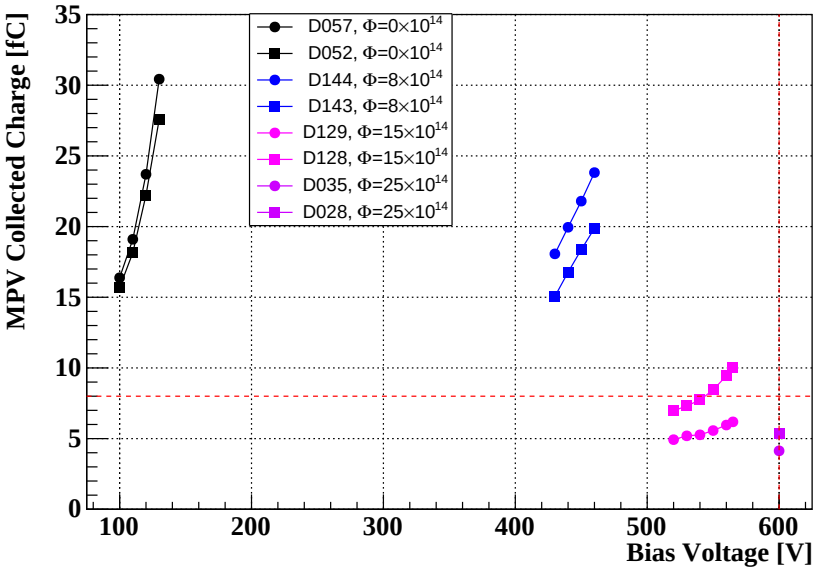

Fig. 7.2 Collected Charge as a function of the reverse bias voltage for low carbonated samples. All these measurements were performed at $-25\,^{\circ}\mathrm{C}$. The doted lines are the limits for the ETL requirements: a collected charge above 8 fC at a bias voltage less than $12\,\mathrm{V}/\mu\mathrm{m}$.

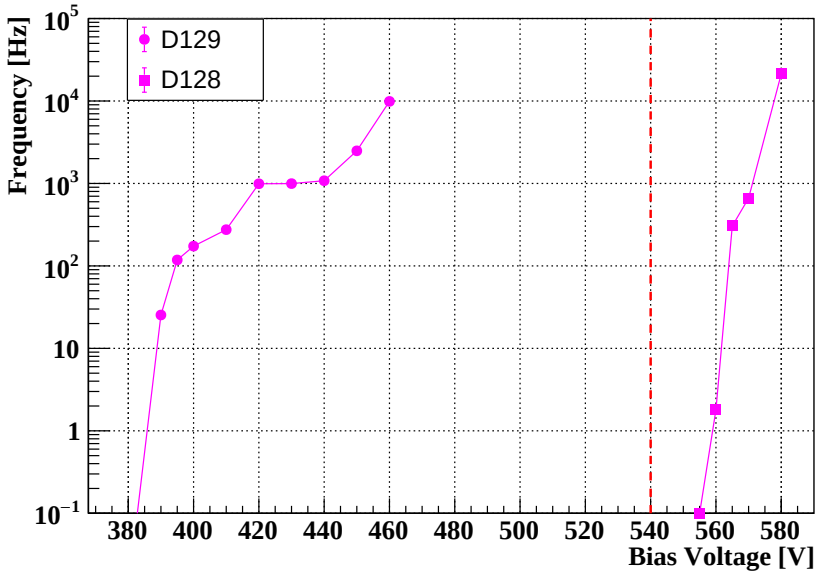

Fig. 7.3 Spurious pulse rate versus the bias voltage of the High Carbonated samples at $1.5 \times 10^{15}\,\mathrm{n_{eq}\,cm^{-2}}$ irradiation fluence. Doted lines indicates the working voltage. Measurements taken in the Radioactive Source setup with NIM electronics with a threshold of $-25\,\mathrm{mV}$.

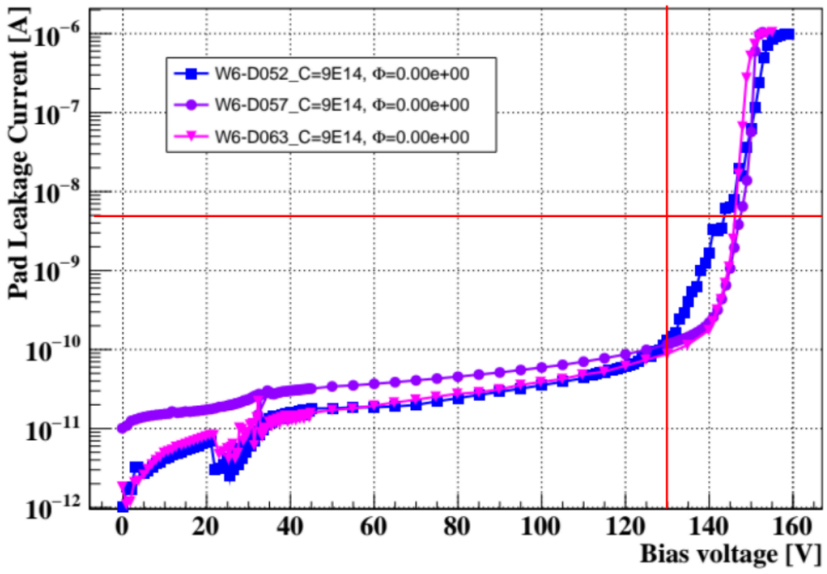

Fig. 7.4 Leakage current of the main diode as a function of the reverse bias voltage before irradiation. The vertical red line indicates the requirement for the breakdown voltage to be in the 130–250 V range, the horizontal red line is the leakage current limit, scaled to one single pixel sensor assuming linearity with respect of the large sensors of 16×16, see section 6.1.

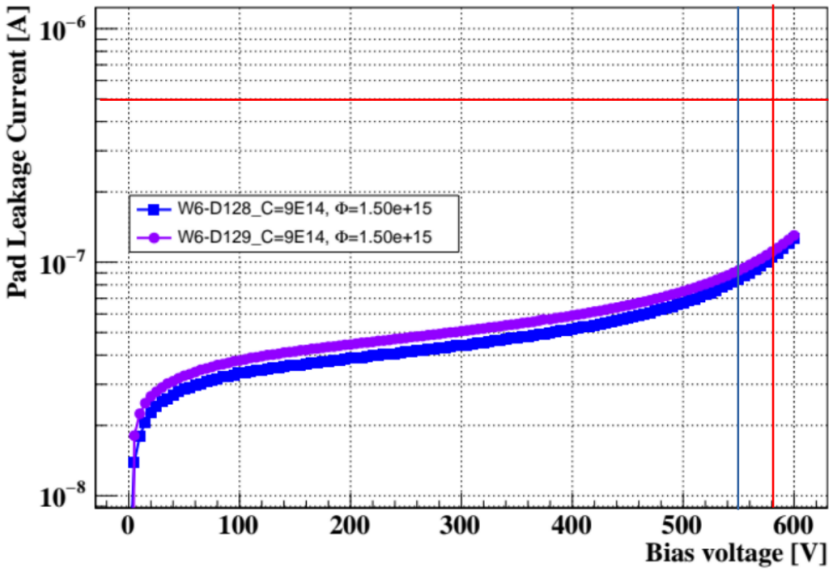

Fig. 7.5 The leakage current of the main pad after irradiation as a function of the reverse bias is shown. Samples irradiated at 15×10^{14} $n_{eq}\,cm^{-2}$ are shown. The blue line is the V(8 fC), the vertical red line indicates the requirement for the breakdown voltage to be >V(8 fC)+30 V and the horizontal red line is the leakage current limit, scaled to one single pixel sensor assuming linearity with respect of the large sensors of 16×16, see section 6.1.

Table 7.2 Summary of the bias voltage required to collect a charge of 8 fC (V(8 fC)) for the LGADs samples from different manufacturers, irradiated at the two fluences expected for the ETL of the CMS: 10×10^{14} $n_{eq}\,cm^{-2}$ and 15×10^{14} $n_{eq}\,cm^{-2}$. *Measurements taken from [144] for comparison (see subsection 6.4.1).

Production ID		V(8 fC) at:			σ_t at:	
	12 V/µm limit	8×10^{14} $n_{eq}\,cm^{-2}$	10×10^{14} $n_{eq}\,cm^{-2}$	15×10^{14} $n_{eq}\,cm^{-2}$	10×10^{14} $n_{eq}\,cm^{-2}$	15×10^{14} $n_{eq}\,cm^{-2}$
CNM_SiSi_B	600 V	590 V	-	Not reached	-	75 ps
CNM_EPI_C1	660 V	-	550 V	700 V	52 ps	60 ps
CNM_EPI	660 V	-	670 V	Not reached	65 ps	-
CNM_SiSi_N_C3	600 V	<400 V	-	Not reached	-	50 ps
CNM_SiSi_N_C9	600 V	<430 V	-	540 V	-	50 ps
HPK2_EPI_S4	600 V	640 V	-	700 V	-	-
FBK_UFSD4_S	660 V	-	440 V	600 V	42 ps	39 ps*

layer design combined with carbon enrichment. These new productions focus on improving the manufacturing yield of large matrix sensors (16x16), as required for the ETL subdetector, and on redesigning the interpad region to suppress the presence of spurious signals at bias voltages below the operational one.

Additionally, within the broader scope of research and development towards the 4D-tracking paradigm, ongoing studies and fabrications of LGAD-based technologies, such as Ti-LGADs and trench-iLGADs, are being pursued as follow-up activities. The results from this study will contribute to identifying the optimal technology capable of delivering superior time and spatial resolution while ensuring high operational performance and resilience in extreme radiation environments, relevant for potential second-phase upgrades and future high-energy physics experiments.

References

[1] C. J. Read. High-Luminosity Large Hadron Collider (HL-LHC): Technical design report. *CERN Yellow Reports: Monographs*, 2020. doi:10.23731/CYRM-2020-0010, https://cds.cern.ch/record/2749422.

[2] LHCb Collaboration. LHCb magnet : Technical Design Report. *Geneva : CERN, 2000. - 42 (Technical design report. LHCb; 1)*, 2000. http://cds.cern.ch/record/424338.

[3] The CMS Collaboration. The CMS experiment at the CERN LHC. *Journal of Instrumentation*, 3(08):S08004, aug 2008. https://dx.doi.org/10.1088/1748-0221/3/08/S08004.

[4] A. Tumasyan et al. The Phase-2 Upgrade of the CMS Tracker, 6 2017. https://doi.org/10.17181/CERN.QZ28.FLHW.

[5] The CMS Collaboration. The Phase-2 Upgrade of the CMS Endcap Calorimeter, 2017. https://doi.org/10.17181/CERN.IV8M.1JY2.

[6] T. Tomei. CMS Upgrades for the High-Luminosity LHC Era, 2025. https://arxiv.org/abs/2501.03412.

[7] CMS Collaboration. Technical proposal for a MIP timing detector in the CMS experiment phase 2 upgrade. *CERN Technical Report, CERN-LHCC-2017-027, LHCC-P-009*, Dec. 2017. https://cds.cern.ch/record/2296612.

[8] ATLAS Collaboration. Technical Proposal: A High-Granularity Timing Detector for the ATLAS Phase-II Upgrade. *CERN-LHCC-2018-023. LHCC-P-012, Geneva: CERN*, 2018. https://cds.cern.ch/record/2623663.

[9] F. Cossutti. Precision Timing with the CMS MIP Timing Detector for High-Luminosity LHC, 2025. https://doi.org/10.22323/1.476.0860.

[10] J. Butler and T. Tabarelli. A MIP Timing Detector for the CMS Phase-2 Upgrade, 2019. https://cds.cern.ch/record/2667167?ln=es.

[11] T. Hebbeker and A. Korytov. The Phase-2 Upgrade of the CMS Muon Detectors, 9 2017. https://cds.cern.ch/record/2283189?ln=es.

[12] A. Zabi, J. Berryhill, E. Perez, and A. Tapper. The Phase-2 Upgrade of the CMS Level-1 Trigger, 2020. https://cds.cern.ch/record/2714892?ln=es.

[13] CMS Collaboration. The Phase-2 Upgrade of the CMS Data Acquisition and High Level Trigger. Technical report, CERN, Geneva, 2021. https://cds.cern.ch/record/2759072.

[14] E. Navarrete Ramos. Characterization of Low Gain Avalanche Detectors (LGAD) for the timing detectors of the HL-LHC. Master's thesis, Universidad de Cantabria, 2019. https://digital.csic.es/handle/10261/230441.

[15] H. Spieler. *Semiconductor Detector Systems*. Oxford University Press, 2005.

[16] CAPLINQ Corporation. High Purity Silica Sand, Quartz, Crystalline & Spherical Micro Quartz Powder, 2024. https://www.caplinq.com/hb4s-high-purity-quartz-sand-99.995-qs-hb4s.html?filter=48704.

[17] R. Satpathy and V. Pamuru. Chapter 1 - Manufacturing of polysilicon. In Rabindra Satpathy and Venkateswarlu Pamuru, editors, *Solar PV Power*, pages 1–29. Academic Press, 2021. https://doi.org/10.1016/B978-0-12-817626-9.00001-0.

[18] N.E.B. Cowern. 1 - silicon-based photovoltaic solar cells. In John A. Kilner, Stephen J. Skinner, Stuart J.C. Irvine, and Peter P. Edwards, editors, *Functional Materials for Sustainable Energy Applications*, pages 3–22e. Woodhead Publishing, 2012. https://doi.org/10.1533/9780857096371.1.1.

[19] Masarykova Univerzita. Crystal Structure and Growth, 2024. https://www.physics.muni.cz/~jancely/teamCMV/Texty/RuzneTexty/Krystaly/CrystalStructure&Growth.

[20] G. Müller and J. Friedrich. Crystal Growth, Bulk: Methods. In Franco Bassani, Gerald L. Liedl, and Peter Wyder, editors, *Encyclopedia of Condensed Matter Physics*, pages 262–274. Elsevier, 2005. https://www.sciencedirect.com/science/article/pii/B0123694019004162.

[21] RAN Biotechnologies Inc. Silicon epitaxial growth process., 2005. https://www.eesemi.com/epi-deposition.htm.

[22] Semiconductor Engineering. Epitaxy. a method for growing or depositing mono crystalline films on a substrate., 2013. https://semiengineering.com/knowledge_centers/manufacturing/process/epitaxy/.

[23] IceMOS Technology Ltd. Sisi wafers., 2024. https://icemostech.com/sisi-wafers.html.

[24] N. Liaros and J. T. Fourkas. Ten years of two-color photolithography. *Opt. Mater. Express*, 9(7):3006–3020, Jul 2019. https://opg.optica.org/ome/abstract.cfm?URI=ome-9-7-3006.

[25] Y. Nishimura, K. Yano, M. Itoh, and M. Ito. *lat Panel Display Manufacturing*. Wiley, 2018. https://doi.org/10.1002/9781119161387.ch13.

[26] E. Currás, A. Doblas, M. Fernández, D. Flores, J. González, S. Hidalgo, R. Jaramillo, M. Moll, E. Navarrete Ramos, G. Pellegrini, and I. Vila. Timing performance and gain degradation after irradiation with protons and neutrons of Low Gain Avalanche Diodes based on a shallow and broad multiplication layer in a float-zone 35 µm and 50 µm thick silicon substrate. *Nuclear Instruments and Methods in Physics Research,*

A: Accelerators, Spectrometers, Detectors and Associated Equipment, pages 51–55, 2023. https://doi.org/10.1016/j.nima.2023.168522.

[27] CERN. RD50 - Radiation hard semiconductor devices for very high luminosity colliders, 2009. https://rd50.web.cern.ch/.

[28] E. Navarrete Ramos, J. Duarte-Campderros, M. Fernández, G. Gómez, J. González, S. Hidalgo, R. Jaramillo, P. Martínez Ruiz del Árbol, M. Moll, C. Quintana, A. K. Sikdar, I. Vila, and J. Villegas. Impact of Neutron Irradiation on LGADs with a Carbon-Enriched Shallow Multiplication Layer: Degradation of Timing Performance and Gain, 2024. https://arxiv.org/abs/2406.01267.

[29] IMB-CNM-CSIC. Instituto de Microelectrónica de Barcelona (IMB-CNM-CSIC), 2024. https://www.imb-cnm.csic.es/es.

[30] P. Fernández-Martínez, D. Flores, S. Hidalgo, V. Greco, A. Merlos, G. Pellegrini, and D. Quirion. Design and fabrication of an optimum peripheral region for Low Gain Avalanche Detectors. *Nuclear Instruments and Methods in Physics Research Section A: Accelerators, Spectrometers, Detectors and Associated Equipment*, 821:93–100, 2016. https://doi.org/10.1016/j.nima.2016.03.049.

[31] C. Gallrapp, M. Fernández, S. Hidalgo, I. Mateu, M. Moll, S. Otero Ugobono, and G. Pellegrini. Study of gain homogeneity and radiation effects of Low Gain Avalanche Pad Detectors. *Nuclear Instruments and Methods in Physics Research Section A: Accelerators, Spectrometers, Detectors and Associated Equipment*, 875:27–34, 2017. https://doi.org/10.1016/j.nima.2017.07.038.

[32] R. Nienhuis and C. Busselaar. Planar semiconductor device with scribe lines and channel stopper, 1973. https://patents.google.com/patent/US3772576A/en.

[33] M. Moll. Displacement Damage in Silicon Detectors for High Energy Physics. *IEEE Transactions on Nuclear Science*, 65(8):1561–1582, 2018. https://doi.org/10.1109/TNS.2018.2819506.

[34] M.S. Lazo, D.M. Woodall, and P.J. McDaniel. Silicon and Silicon dioxide neutron damage functions. Technical report, INIS, United States, 1987.

[35] R. Wunstorf. *A Systematic investigation of the radiation hardness of silicon detectors for high-energy physics experiments*. PhD thesis, Universität Hamburg, 10 1992. https://inspirehep.net/literature/341378.

[36] G. C. Messenger and M. S. Ash. The effects of radiation on electronic systems. *Van Nostrand Reinhold, New York*, 1992.

[37] H. Moser. Silicon detector systems in high energy physics. *Prog. Part. Nucl. Phys.*, 63:186–237, 2009. https://doi.org/10.1016/j.ppnp.2008.12.002.

[38] W. Adam et al. Evaluation of planar silicon pixel sensors with the RD53A readout chip for the Phase-2 Upgrade of the CMS Inner Tracker. *JINST*, 18(11):P11015, 2023. https://doi.org/10.1088/1748-0221/18/11/P11015.

[39] A. Doblas. *Low Gain Avalanche Detector (LGAD and iLGAD) for High-Energy Physics and Synchrotron applications.* PhD thesis, Universitat Autonoma de Barcelona, 2023. https://ddd.uab.cat/pub/tesis/2024/hdl_10803_689771/adm1de1.pdf.

[40] TPT GmbH Co KG. Wire bonding technologie, 2014. https://www.tpt-wirebonder.com/applications/#wirebonding.

[41] C. Broennimann, F. Glaus, J. Gobrecht, S. Heising, M. Horisberger, R. Horisberger, H. C. Kastli, J. Lehmann, T. Rohe, and S. Streuli. Development of an indium bump bond process for silicon pixel detectors at PSI. *Nuclear Instruments and Methods. A*, 565:303–308, 2006. https://doi.org/10.1016/j.nima.2006.05.011.

[42] A. Macchiolo, L. Andricek, M. Beimforde, H. G. Moser, R. Nisius, R. H. Richter, and P. Weigell. Performance of thin pixel sensors irradiated up to a fluence of 10**16 n(eq) cm(-2) and development of a new interconnection technology for the upgrade of the ATLAS pixel system. *Nuclear Instruments and Methods. A*, 650:145–149, 2011. https://doi.org/10.1016/j.nima.2010.11.163.

[43] M. Barreto. Anisotropic Conductive Film (ACF) developments, 2020. https://https://indico.cern.ch/event/850899/contributions/3767174/.

[44] E. Navarrete Ramos, J. Duarte-Campderros, M. Fernández, G. Gómez, J. González, S. Hidalgo, R. Jaramillo, P. Martínez Ruiz del Árbol, M. Moll, C. Quintana, A.K. Sikdar, I. Vila, and J. Villegas. Impact of neutron irradiation on LGADs with a carbon-enriched shallow multiplication layer: Degradation of timing performance and gain. *Nuclear Instruments and Methods in Physics Research Section A: Accelerators, Spectrometers, Detectors and Associated Equipment*, 1074:170309, 2025. https://doi.org/10.1016/j.nima.2025.170309.

[45] N. Alipour, M. Benoit, D. Dannheim, A. Fiergolski, D. Hynds, W. Klempt, A. Macchiolo, M. Munker, and A. Nürnberg. Performance evaluation of thin active-edge planar sensors for the CLIC vertex detector. *Nucl. Instrum. Meth. A*, 953:162850, 2020. https://doi.org/10.1016/j.nima.2019.162850.

[46] N. Moffat and R. Bates. Simulation of the small pixel effect contributing to a low fill factor for pixellated low gain avalanche detectors (lgad). *Nuclear Instruments and Methods in Physics Research Section A: Accelerators, Spectrometers, Detectors and Associated Equipment*, 1018:165746, 2021. https://doi.org/10.1016/j.nima.2021.165746.

[47] M. Tornago et al. Silicon sensors with resistive read-out: Machine Learning techniques for ultimate spatial resolution. *Nucl. Instrum. Meth. A*, 1047:167816, 2023. https://doi.org/10.1016/j.nima.2022.167816.

[48] N. Moffat, G. Pellegrini, J. Villegas, M. Manojlovic, and S. Hidalgo. Update of AC-LGAD at CNM, 2022. https://rd50.web.cern.ch/.

[49] A. Apresyan, W. Chen, G. D'Amen, K. Di Petrillo, G. Giacomini, R. Heller, H. Lee, S. Los, C. Moon, and A. Tricoli. Measurements of an AC-LGAD strip sensor with a 120 GeV proton beam. *JINST*, 15(09):P09038, 2020. https://doi.org/10.1088/1748-0221/15/09/P09038.

[50] M. Mandurrino et al. First demonstration of 200, 100, and 50 um pitch Resistive AC-Coupled Silicon Detectors (RSD) with 100% fill-factor for 4D particle tracking. *IEEE Electron. Dev. Lett.*, 40(11):1780, 2019. https://doi.org/10.1109/LED.2019.2943242.

[51] M. Tornago et al. Resistive AC-Coupled Silicon Detectors: principles of operation and first results from a combined analysis of beam test and laser data. *Nucl. Instrum. Meth. A*, 1003:165319, 2021. https://doi.org/10.1016/j.nima.2021.165319.

[52] L. Menzio et al. DC-coupled resistive silicon detectors for 4D tracking. *Nucl. Instrum. Meth. A*, 1041:167374, 2022. https://doi.org/10.1016/j.nima.2022.167374.

[53] G. Paternoster, G. Borghi, M. Boscardin, N. Cartiglia, M. Ferrero, F. Ficorella, F. Siviero, A. Gola, and P. Bellutti. Trench-Isolated Low Gain Avalanche Diodes (TI-LGADs). *IEEE Electron. Dev. Lett.*, 41(6):884–887, 2020. https://doi.org/10.1109/LED.2020.2991351.

[54] G. Paternoster et al. Novel strategies for fine-segmented Low Gain Avalanche Diodes. *Nucl. Instrum. Meth. A*, 987:164840, 2021. https://doi.org/10.1016/j.nima.2020.164840.

[55] M. Senger, A. Macchiolo, B. Kilminster, G. Paternoster, M. Centis, and G. Borghi. A Comprehensive Characterization of the TI-LGAD Technology. *Sensors*, 23(13), 2023. https://doi.org/10.3390/s23136225.

[56] G. Giacomini and C. W. Platte. Diffused trenches for high fill-factor Low-Gain Avalanche Diodes. *Nuclear Instruments and Methods in Physics Research Section A: Accelerators, Spectrometers, Detectors and Associated Equipment*, 1055:168497, 2023. https://doi.org/10.1016/j.nima.2023.168497.

[57] I. Velkovska, V. Gkougkousis, I. Vila, J. Duarte-Campderrós, M. Fernandez, P. Rezaei-Mianroodi, A. Hennessy, A. Macchiolo, B. Hiti, M. Senger, N. Moffat, E. Robutti, R. López, E. Navarrete Ramos, C. Gemme, and G. Kramberger. Performance of irradiated TI-LGADs at 160 GeV SPS pion beams, 2025. https://indico.cern.ch/event/1455346/contributions/6322682/.

[58] G. Pellegrini et al. Technology developments and first measurements of Low Gain Avalanche Detectors (LGAD) for high energy physics applications. *Nuclear Instruments Methods. A*, 765:12–16, 2014. https://doi.org/10.1016/j.nima.2014.06.008.

[59] A. Doblas, D. Flores, S. Hidalgo, N. Moffat, G. Pellegrini, D. Quirion, J. Villegas, D. Maneuski, M. Ruat, and P. Fajardo. Inverse Low Gain Avalanche Detector (iLGAD) Periphery Design for X-Ray Applications, 2 2022. https://doi.org/10.48550/arXiv.2202.01552.

[60] A. Doblas, D. Flores, S. Hidalgo, G. Pellegrini, D. Quirion, and Ivan Vila. Technology developments on iLGAD sensors at IMB-CNM, 2021. https://doi.org/10.1016/j.nima.2016.05.066.

[61] F. J. Muñoz Sánchez. *Study of New Silicon Sensors for Experiments at Future Particle Colliders*. PhD thesis, Universidad de Cantabria, 2014.

[62] R. Turchetta. Spatial resolution of silicon microstrip detectors. *Nuclear Instruments and Methods. A*, 335:44–58, 1993. https://doi.org/10.1016/0168-9002(93)90255-G.

[63] E. Butz. Operation and Performance of the CMS outer tracker. *PoS*, Vertex 2017:013, 2018. https://doi.org/10.22323/1.309.0013.

[64] S. Seif El Nasr. The CMS Outer Tracker Upgrade for the High Luminosity LHC, 2018. https://indico.cern.ch/event/666427/contributions/2880250/.

[65] S.I. Parker, C.J. Kenney, and J. Segal. 3D — A proposed new architecture for solid-state radiation detectors. *Nuclear Instruments and Methods in Physics Research Section A: Accelerators, Spectrometers, Detectors and Associated Equipment*, 395:328–343, 1997. http://inis.iaea.org/search/search.aspx?orig_q=RN:28076340.

[66] G.-F. Dalla Betta, M. Boscardin, G. Darbo, R. Mendicino, M. Meschini, A. Messineo, S. Ronchin, D.M.S. Sultan, and N. Zorzi. Development of a new generation of 3D pixel sensors for HL-LHC. *Nuclear Instruments and Methods in Physics Research Section A: Accelerators, Spectrometers, Detectors and Associated Equipment*, 824:386–387, 2016. https://doi.org/10.1016/j.nima.2015.08.032.

[67] M. Meschini, A. Cassese, R. Ceccarelli, L. Viliani, M. Dinardo, S. Gennai, D. Zuolo, A. Messineo, S. Parolia, A. Ebrahimi, D. Pitzl, G. Steinbrück, G.F. Dalla Betta, R. Mendicino, G. Alimonti, C. Gemme, M. Boscardin, and S. Ronchin. Radiation resistant innovative 3D pixel sensors for the CMS upgrade at the High Luminosity LHC. *Nuclear Instruments and Methods in Physics Research Section A: Accelerators, Spectrometers, Detectors and Associated Equipment*, 2020. https://doi.org/10.1016/j.nima.2020.164429.

[68] M. Trimpl, M. Koch, R. Kohrs, H. Krueger, P. Lodomez, L. Reuen, C. Sandow, E. Toerne, J. Velthuis, N. Wermes, L. Andricek, H. Moser, R. Richter, G. Lutz, F. Giesen, P. Fischer, and I. Perić. Status of a DEPFET pixel system for the ILC vertex detector. *Universitt Bonn*, 06 2006. https://doi.org/10.48550/arXiv.physics/0606104.

[69] L. Struder, P. Holl, G. Lutz, and J. Kemmer. Development of Fully Depletable Pn Ccd's. 1. Device Modeling of Fully Depletable Ccd's. *Nucl. Instrum. Meth. A*, 253:386, 1987. https://doi.org/10.1016/0168-9002(87)90521-3.

[70] J. Schieck. DEPFET pixels as a vertex detector for the Belle II experiment. *Nucl. Instrum. Meth. A*, 732:160–163, 2013. https://doi.org/10.1016/j.nima.2013.05.054.

[71] M. Garcia-Sciveres and N. Wermes. A review of advances in pixel detectors for experiments with high rate and radiation. *Rept. Prog. Phys.*, 81(6):066101, 2018. https://doi.org/10.1088/1361-6633/aab064.

[72] G. Contin et al. The STAR MAPS-based PiXeL detector. *Nucl. Instrum. Meth. A*, 907:60–80, 2018. https://doi.org/10.1016/j.nima.2018.03.003.

[73] A. Besson, A. Pérez Pérez, E. Spiriti, J. Baudot, G. Claus, M. Goffe, and M. Winter. From vertex detectors to inner trackers with CMOS pixel sensors. *Nucl. Instrum. Meth. A*, 845:33–37, 2017. https://doi.org/10.1016/j.nima.2016.04.081.

[74] H. Kolanoski and N. Wermes. *Particle Detectors: Fundamentals and Applications*. Oxford University Press, 06 2020. https://doi.org/10.1093/oso/9780198858362.001.0001.

[75] I. Perić et al. High-voltage pixel detectors in commercial CMOS technologies for ATLAS, CLIC and Mu3e experiments. *Nucl. Instrum. Meth. A*, 731:131–136, 2013. https://doi.org/10.1016/j.nima.2013.05.006.

[76] CIVIDEC Instrumentation. TCT Amplifier for Detector Physics, integrated Bias-Tee, 2024. https://cividec.at/electronics-C2-TCT.html.

[77] C. Wang, Y. Li, L. Jia, S. Zhang, and J. Ye. Design of charge-sensitive and current-sensitive preamplifiers for electrostatic sensor. *Journal of Electrostatics 105 103449*, 2020. https://www.sciencedirect.com/science/article/pii/S0304388620300334, https://doi.org/10.1016/j.elstat.2020.103449.

[78] Advanced Measurement Technology. Preamplifier Introduction, 2024. www.ortec-online.com.

[79] E. Coates. Amplifier Gain & Decibels, 2024. https://learnabout-electronics.org/Amplifiers/amplifiers13.php.

[80] AspenCore. Power gain of amplifiers and filters, 2024. https://www.electronics-tutorials.ws/filter/decibels.html.

[81] LISUN group. Understanding key specifications in digital oscilloscopes: Sampling rate, bandwidth, and resolution, 2023. https://www.lisungroup.com/news/technology-news/understanding-key-specifications-in-digital-oscilloscopes/sampling-rate-bandwidth-and-resolution.html.

[82] Y. Sugihara, S. Takezawa, S. Katou, and K. Morita. YOKOGAWA DL9000 Series of Digital Oscilloscopes, 2005. https://www.yokogawa.com/library/resources/yokogawa-technical-reports/dl9000-series-of-digital-oscilloscopes/.

[83] G. Kramberger. *Signal development in irradiated silicon detectors*. PhD thesis, University of Ljubljana, 2001. http://merlot.ijs.si/~gregor/GKpapers.html.

[84] Tektronix Inc. Digital and Mixed Signal Oscilloscopes: MSO/DPO70000 Series Datasheet, 2015. https://assets.testequity.com/te1/Documents/pdf/tektronix/Inside-MSODPO70000-Series.pdf.

[85] ROOT team. ROOT: data analysis framework, 2024. https://root.cern/.

[86] M. Fernández. TRICS: TCT Root-based IFCA-CERN Software, 2020. Used under author's consent.

[87] M. Fernández, P. Matorras, M. Petek, and A. Carrasco. 101: ROOT-based CV-IV analysis software, 2019. Used under author's consent.

[88] Instituto de Física de Cantabria IFCA. Experimental HEP and Instrumentation, 2024. https://ifca.unican.es/en-us/research/high-energy-physics-and-instrumentation/experimental-hep-and-instrumentation.

[89] European Southern Observatory (ESO). Noise Distributions, 1999. http://www.eso.org/midas/midas-support.html.

[90] T. Kuwano, K. Hara, S. Shinma, Y. Ikegami, T. Kohriki, S. Terada, and Y. Unno. Systematic study of micro-discharge characteristics of ATLAS barrel silicon microstrip modules. *Nuclear Instruments and Methods in Physics Research Section A: Accelerators, Spectrometers, Detectors and Associated Equipment*, 579(2):782–787, 2007. https://doi.org/10.1016/j.nima.2007.05.288.

[91] Levine and S. William. *The Control Handbook*. Boca Raton, FL: CRC Press, 1996.

[92] M. Fernández. TRICS tutorial, 2020. Used under author's consent.

[93] B. Fong, Murray D., and Pierre D. Timing resolution and time walk in SLiK SPAD - measurement and optimization. *Proceedings Volume 10353, Optical Sensing, Imaging, and Photon Counting: Nanostructured Devices and Applications 2017; 1035309*, 2017. https://doi.org/10.1117/12.2274073, https://www.spiedigitallibrary.org/conference-proceedings-of-spie/10353/2274073/Timing-resolution-and-time-walk-in-SLiK-APD--measurement/10.1117/12.2274073.short.

[94] P. McKarris, M. C. Vignali, and M. O. Wiehe. Commissioning of a beta setup for time resolution measurements, 2019. https://indico.cern.ch/event/840877/.

[95] Tektronix, Inc. Keithley 2400 Standard Series SMU, 2023. https://www.tek.com/en/products/keithley/source-measure-units/2400-standard-series-sourcemeter#.

[96] N. Bacchetta, D. Bisello, A. Candelori, M. Da Rold, M. Descovich, A. Kaminski, A. Messineo, F. Rizzo, and G. Verzellesi. Improvement in breakdown characteristics with multiguard structures in microstrip silicon detectors for CMS. *issn: 0168-9002, 204-206*, 2001. https://www.sciencedirect.com/science/article/pii/S0168900200012079, doi:10.1016/S0168-9002(00)01207-9.

[97] M. Fernández. Status report on the radiation tolerance assessment of CNM AIDA2020v2 and HPK-P2 LGADs. *16th Trento Workshop on Advanced Silicon Radiation Detectors, (2)*, 2021. https://indico.cern.ch/event/983068/contributions/4223223/.

[98] IET Labs, Inc. IET/QuadTech 1910/1920 1 MHz LCR Meter, 2023. https://www.ietlabs.com/1900-lcr-meter.html.

[99] IET Labs, Inc. Precision instruments for test and measurement: LCR Meter user and service manual, 2014. https://www.ietlabs.com/pdf/Manuals/1920_im.pdf.

[100] C. W. Gwyn. Calculated small signal characteristics for irradiated pn junctions. *IEEE Trans. Nucl. Sci. NS-19(355)*, 1972. https://doi.org/10.1109/TNS.1972.4326858.

[101] D. Campbell, A. Chilingarov, and T. Sloan. Frequency and temperature dependence of the depletion voltage from cv measurements for irradiated si detectors. *Nuclear Instruments and Methods in Physics Research Section A: Accelerators, Spectrometers, Detectors an Associated Equipment 492, (3), 402–410*, 2022. https://www.sciencedirect.com/science/article/pii/S0168900202013530.

[102] M. Wiehe, M. Fernández, S. Hidalgo, M. Moll, S. Otero, U. Parzefall, G. Pellegrini, A. Barroso, and I. Vila. Study of the radiation-induced damage mechanism in proton irradiated low gain avalanche detectors and its thermal annealing dependence. *Nuclear Instruments and Methods in Physics Research Section A: Accelerators, Spectrometers, Detectors and Associated Equipment 986, Article 164814*, 2021. https://www.sciencedirect.com/science/article/pii/S0168900220312110.

[103] M. Ferrero, R. Arcidiacono, M. Barozzi, M. Boscardin, N. Cartiglia, G. F. Dalla Betta, Z. Galloway, M. Mandurrino, S. Mazza, G. Paternoster, F. Ficorella, L. Pancheri, H-F W. Sadrozinski, F. Siviero, V. Sola, A. Staiano, A. Seiden, M. Tornago, and Y. Zhao. Radiation resistant LGAD design. *Nuclear Instruments and Methods in Physics Research Section A: Accelerators, Spectrometers, Detectors and Associated Equipment, 0168-9002*, 2019. https://www.sciencedirect.com/science/article/pii/S0168900218317741, https://doi.org/10.1016/j.nima.2018.11.121.

[104] Z. Galloway, V. Fadeyev, P. Freeman, E. Gkougkousis, C. Gee, B. Gruey, C. Labitan, Z. Luce, F. McKinney-Martinez, H. F. Sadrozinski, A. Seiden, E. Spencer, M. Wilder, N. Woods, A. Zatserklyaniy, Y. Zhao, N. Cartiglia, M. Ferrero, M. Mandurrino, A. Staiano, V. Sola, R. Arcidiacono, V. Cindro, G. Kramberger, I. Mandić, M. Mikuž, and M. Zavrtanik. Properties of HPK UFSD after neutron irradiation up to 6e15 n/cm2. *Nuclear Instruments and Methods in Physics Research, A: Accelerators, Spectrometers, Detectors and Associated Equipment, (10)*, 2019. doi:10.1016/j.nima.2019.05.017, https://www.sciencedirect.com/science/article/pii/S0168900219306278.

[105] PiLas. Picosecond Laser Diode Systems, 2015. http://www.optophase.com/als_laser.html.

[106] Tektronix, Inc. 3390 Arbitrary Waveform Generator, 2024. https://www.tek.com/en/products/arbitrary-waveform-generators/model-3390.

[107] CDC: Centers for Disease Control and Prevention. Radioisotope Brief: Strontium-90, 2018. https://www.cdc.gov/nceh/radiation/emergencies/isotopes/strontium.htm.

[108] Costrell and et. al. Standard NIM Instrumentation System. *DOE/ER-0457T; ON: DE90010387; TRN: 90-020017*, 1990. https://www.osti.gov/biblio/7120327, https://doi.org/10.2172/7120327.

[109] CAEN S.p.A. Quad Scaler And Preset Counter / Timer, 2024. https://www.caen.it/products/n1145/.

[110] CERN. The Super Proton Synchrotron: The second-largest machine in CERN's accelerator complex provides a stepping stone between the Proton Synchrotron and the LHC, 2024. https://home.cern/science/accelerators/super-proton-synchrotron.

[111] E. Gschwendtner. Overview on CERN Test Beam Facilities and Plans for Tests for Non-Collider Experiments, 2009. https://indico.cern.ch/event/51128/contributions/2032881/attachments/966402/1372336/test_beams_non-collider_Geschwendtner_200905.ppt.pdf.

[112] R. Diener, J. Dreyling-Eschweiler, H. Ehrlichmann, I.M. Gregor, U. Kötz, U. Krämer, N. Meyners, N. Potylitsina-Kube, A. Schütz, P. Schütze, and M. Stanitzki. The DESY II test beam facility. *Nuclear Instruments and Methods in Physics Research Section A: Accelerators, Spectrometers, Detectors and Associated Equipment*, 922:265–286, 2019. https://doi.org/10.1016/j.nima.2018.11.133.

[113] DESY. EUDET: Detector R&D towards the International Linear Collider, 2016. https://www.eudet.org/index_eng.html.

[114] J. Baudot, G. Bertolone, A. Brogna, G. Claus, C. Colledani, Y. Degerli, R. De Masi, A. Dorokhov, G. Dozière, W. Dulinski, M. Gelin, M. Goffe, A. Himmi, F. Guilloux, C. Hu-Guo, K. Jaaskelainen, M. Koziel, F. Morel, F. Orsini, M. Specht, I. Valin, G. Voutsinas, and M. Winter. First test results Of MIMOSA-26, a fast CMOS sensor with integrated zero suppression and digitized output. In *2009 IEEE Nuclear Science Symposium Conference Record (NSS/MIC)*, pages 1169–1173, 2009. https://doi.org/10.1109/NSSMIC.2009.5402399.

[115] Stanford University for the U.S. Department of Energy Office of Science. SLAC: National Accelerator Laboratory, 2023. https://www6.slac.stanford.edu/.

[116] F. Frommberger. The Electron Stretcher Accelerator, 2012. https://www-elsa.physik.uni-bonn.de/elsa-facility_en.html.

[117] D. Dannheim, K. Dort, L. Huth, D. Hynds I. Kremastiotis, J. Kröger, M. Munker, F. Pitters, P. Schütze, and S. Spannagel. Corryvreckan: a modular 4D track reconstruction and analysis software for test beam data. *Journal of Instrumentation, Volume 16*, 2021. https://iopscience.iop.org/article/10.1088/1748-0221/16/03/P03008.

[118] J. Gonzalez. Integration examples of EUDET Telescope with different DUTs, 2023. https://indico.cern.ch/event/1252057/.

[119] Y. Liu and et. al. EUDAQ2: A flexible data acquisition software framework for common test beams. *JINST*, 14(10):P10033, 2019. https://doi.org/10.1088/1748-0221/14/10/P10033.

[120] P. Baesso, D. Cussans, and J. Goldstein. The AIDA-2020 TLU: a flexible trigger logic unit for test beam facilities. *Journal of Instrumentation*, 14(09):P09019–P09019, sep 2019. https://doi.org/10.1088/1748-0221/14/09/p09019.

[121] M. Senger. Chubut 2: Readout board for LGADs, 2023. https://sengerm.github.io/Chubut_2/doc/testing/index.html#Equation:%20measured%20transimpedance%20number.

[122] CAEN S.p.A. 16+1 Channel 12 bit 5 GS/s Switched Capacitor Digitizer, 2024. https://www.caen.it/products/dt5742/.

[123] D. Žontar, V. Cindro, G. Kramberger, and M. Mikuž. Time development and flux dependence of neutron-irradiation induced defects in silicon pad detectors. *Nuclear Instruments and Methods in Physics Research, A 426, 51-55.*, 1999. https://www.sciencedirect.com/science/article/pii/S0168900298014685, https://doi.org/10.1016/S0168-9002(98)01468-5.

[124] European Nuclear Experimental Educational Platform (ENEEP). IJS Ljubljana, 2019. https://www.eneep.org/about/ijs/.

[125] G. Kramberger, M. Carulla, E.Cavallaro, V. Cindro, D. Flores, Z. Galloway, S. Grinstein, S. Hidalgo, V. Fadeyev, J. Lange, I. Mandić, G. Medin, A. Merlos, F. McKinney-Martinez, M. Mikuž, D. Quirion, G. Pellegrini, M. Petek, H. Sadrozinski, A. Seiden, and M. Zavrtanik. Radiation hardness of thin Low Gain Avalanche Detectors. *Nuclear Instruments and Methods in Physics Research, A: Accelerators, Spectrometers, Detectors and Associated Equipment, (5), issn: 0168-9002, 68-77*, 2018. doi:10.1016/j.nima.2018.02.018, https://www.sciencedirect.com/science/article/pii/S0168900218301682.

[126] M. Moll. Acceptor removal - Displacement damage effects involving the shallow acceptor doping of p-type silicon devices. In *The 28th International Workshop on Vertex Detectors - Vertex2019*, 2019. https://cds.cern.ch/record/2747752?ln=es.

[127] A. Nitescu, I. Pintilie, L. D. Filip, C. Besleaga, and G. Nemnes. On-going studies on diminishing the acceptor removal effect by tuning the charge state of Boron containing defects in p-type irradiated PAD samples, 2024. https://indico.cern.ch/event/1402825/contributions/5998116/.

[128] LW Song, XD Zhan, BW Benson, and GD Watkins. Bistable interstitial-carbon-substitutional-carbon pair in silicon. *Physical Review B*, 42(9):5765, 1990. https://doi.org/10.1103/PhysRevB.42.5765.

[129] L. Kimerling, M. Asom, J. Benton, P. Drevinsky, and C. Caefer. Interstitial defect reactions in silicon. In *Materials Science Forum*, volume 38, pages 141–150. Trans Tech Publ, 1989. https://doi.org/10.1063/1.98465.

[130] C. Besleaga, A. Kuncser, A. Nitescu, G. Kramberger, M. Moll, and I. Pintilie. Bistability of the BiOi complex and its implications on evaluating the "acceptor removal" process in p-type silicon, journal = Nuclear Instruments and Methods in Physics Research Section A: Accelerators, Spectrometers, Detectors and Associated Equipment, 2021. https://doi.org/10.1016/j.nima.2021.165809.

[131] G. Kramberger. LGADs for timing detectors at HL-LHC, 2021. https://indico.cern.ch/event/1088953/.

[132] G. Kramberger and V. Cindro and I. Mandić and M. Mikuž and M. Zavrtanik. Studies initial acceptor removal in p-type silicon, 2015. https://indico.cern.ch/event/381195/contributions/905665/.

[133] R. Lipton. LGAD Single Event Burnout Studies. *FERMILAB-FN-1141-CMS; oai:inspirehep.net:2010270; TRN: US2302630*, 2021. https://www.osti.gov/biblio/1841397/, https://doi.org/10.2172/1841397.

[134] Mika Huhtinen. Highly ionising events in silicon detectors. Technical report, CERN, Geneva, 2002. http://cds.cern.ch/record/687409.

[135] L.A. Beresford, D.E. Boumediene, L. Castillo García, L.D. Corpe, M.J. Da Cunha Sargedas de Sousa, H. El Jarrari, A. Eshkevarvakili, C. Grieco, S. Grinstein,

S. Guindon, A. Howard, G. Kramberger, O. Kurdysh, R. Mazini, M. Missio, M. Morenas, O. Perrin, V. Raskina, G. Saito, and S. Trincaz-Duvoid. Destructive breakdown studies of irradiated LGADs at beam tests for the ATLAS HGTD. *Journal of Instrumentation*, 18(07):P07030, jul 2023. https://dx.doi.org/10.1088/1748-0221/18/07/P07030.

[136] CERN. Market Survey - Technical Description Supply of LGAD sensors for the CMS MIP Timing Detector Endcap, 2021. https://cds.cern.ch/record/2777890/files/MS-4689_Technical_Description.pdf.

[137] L. Garcia, E. Gkougkousis, C. Grieco, and S. Grinstein. Characterization of Irradiated Boron, Carbon-Enriched and Gallium Si-on-Si Wafer Low Gain Avalanche Detectors. *Instruments*, 6(1):2, 2021. https://doi.org/10.3390/instruments6010002.

[138] J. Villegas, G. Pellegrini, M. Manojlovic, N. Moffat, and S. Hidalgo. Measurements on last IMB-CNM LGADs production, 2023. https://indico.cern.ch/event/1334364/contributions/5672080/.

[139] E. L. Gkougkousis, L. Castillo Garcia, S. Grinstein, and V. Coco. Comprehensive technology study of radiation hard LGADs. *JJ. Phys.: Conf. Ser. 2374 012175*, 2022. https://iopscience.iop.org/article/10.1088/1742-6596/2374/1/012175, https://doi.org/10.1088/1742-6596/2374/1/012175.

[140] K. Wu, X. Jia, T. Yang, M. Li, W. Wang, M. Zhao, Z. Liang, J. Guimaraes, Y. Fan, H. Cui, A. Howard, G. Kramberger, X. Shi, Y. Heng, Y. Tan, B. Liu, Y. Feng, S. Li, M. Li, C. Yu, X. Yang, M. Zhai, G. Xu, G. Yan, Q. Zhai, M. Ding, J. Luo, H. Yin, and J. Li. Design and testing of LGAD sensor with shallow carbon implantation. *Nuclear Instruments and Methods in Physics Research, A.*, 2023. https://doi.org/10.1016/j.nima.2022.167697.

[141] Hamamatsu Photonics K.K. Hamamatsu Photonics, 2024. https://www.hamamatsu.com/jp/en.html.

[142] FBK. Fondazione Bruno Kessler, 2024. https://www.fbk.eu/en/.

[143] FBK. New frontier technologies in the Clean Room, 2024. https://www.fbk.eu/en/initiative/new-frontier-technologies-in-the-clean-room/.

[144] F. Siviero. Status of the Market Survey on FBK UFSD4, 2023. ETL sensors and modules meeting.

[145] K. Wu, X. Jia, T. Yang, M. Li, W. Wang, M. Zhao, Z. Liang, J. Guimaraes, Y. Fan, H. Cui, A. Howard, G. Kramberger, X. Shi, Y. Heng, Y. Tan, B. Liu, Y. Feng, S. Li, M. Li, C. Yu, X. Yang, M. Zhai, G. Xu, G. Yan, Q. Zhai, M. Ding, J. Luo, H. Yin, and J. Li. Design and testing of LGAD sensor with shallow carbon implantation, 2023. https://www.sciencedirect.com/science/article/pii/S0168900222009895.

Summary of measured sensors

Table 3 Summary of the sensors that were measured in the various characterisation campaigns that were conducted as part of this thesis study.

	Sensor		Irradiation	Characterisation			
Vendor	Run	Wafer	Fluence	IV	CV	RS	TCT
CNM	12916	W2	0	15	15		2
CNM	12916	W2	4.00E+14	3	3		
CNM	12916	W2	8.00E+14	3	3		1
CNM	12916	W2	1.50E+15	3	2		1
CNM	12916	W2	2.50E+15	3	2		
HPK	V2	W25	0	5	5		
HPK	V2	W31	0	5	5		
HPK	V2	W36	0	5	5		
HPK	V2	W42	0	5	5		1
HPK	V2	W42	4.00E+14	2	2		1
HPK	V2	W42	8.00E+14	2	2		1
HPK	V2	W42	1.50E+15	2	2		1
HPK	V2	W42	2.50E+15	2	2		
FBK	UFSD4	W7	0	1			
FBK	UFSD4	W8	0	2			
FBK	UFSD4	W9	0	1			
FBK	UFSD4	W17	0	1			
FBK	UFSD4	W18	0	3			
FBK	UFSD4	W7	0	3	3		1
FBK	UFSD4	W8	0	3	3		1
FBK	UFSD4	W9	1.50E+15			2	
FBK	UFSD4	W17	0	3	3		2
FBK	UFSD4	W18	0	3	3		

Table 4 (Continuation)

CNM	15246	W8	0	12	14	2
CNM	15246	W8	6.00E+14	2	2	2
CNM	15246	W8	1.00E+15	2	2	2
CNM	15246	W8	1.50E+15	2	2	2
CNM	15246	W10	0	12	14	2
CNM	15246	W10	6.00E+14	2	2	2
CNM	15246	W10	1.00E+15	2	2	2
CNM	15246	W10	1.50E+15	2	2	2
CNM	15246	W8	0		12	
CNM	15246	W10	0		12	
CNM	15973	W1	0	2	3	
CNM	15973	W1	4.00E+14	2	1	
CNM	15973	W1	8.00E+14	2	2	
CNM	15973	W1	1.50E+15	2	0	
CNM	15973	W1	2.50E+15	2	2	
CNM	15973	W2	0	3	3	
CNM	15973	W2	4.00E+14	2	2	
CNM	15973	W2	8.00E+14	2	2	
CNM	15973	W2	1.50E+15	2	2	
CNM	15973	W2	2.50E+15	2	2	
CNM	15973	W3	0	3	3	
CNM	15973	W3	4.00E+14	2	2	
CNM	15973	W3	8.00E+14	2	2	
CNM	15973	W3	1.50E+15	2	2	
CNM	15973	W3	2.50E+15	2	2	
CNM	15973	W4	0	3	3	2
CNM	15973	W4	4.00E+14	2	2	
CNM	15973	W4	8.00E+14	2	2	2
CNM	15973	W4	1.50E+15	2	2	2
CNM	15973	W4	2.50E+15	2	2	2
CNM	15973	W5	0	3	3	
CNM	15973	W5	4.00E+14	2	2	
CNM	15973	W5	8.00E+14	2	2	
CNM	15973	W5	1.50E+15	2	2	
CNM	15973	W5	2.50E+15	2	2	
CNM	15973	W6	0	3	3	2
CNM	15973	W6	4.00E+14	2	2	
CNM	15973	W6	8.00E+14	2	2	2
CNM	15973	W6	1.50E+15	2	2	2
CNM	15973	W6	2.50E+15	2	2	2